INTERNATIONAL DOCTORAL
SCHOOL OF THE USC

Damián
García Castro

PhD Thesis

Cosmic Rays' study with a TRASGO detector

Santiago de Compostela, 2022

Doctoral Programme in Nuclear and Particles Physics

USC
UNIVERSIDADE
DE SANTIAGO
DE COMPOSTELA

TESE DE DOUTORAMENTO

COSMIC RAYS' STUDY WITH A TRASGO DETECTOR

Damián García Castro

ESCOLA DE DOUTORAMENTO INTERNACIONAL DA UNIVERSIDADE DE SANTIAGO DE COMPOSTELA

PROGRAMA DE DOUTORAMENTO EN FÍSICA NUCLEAR E DE PARTÍCULAS

SANTIAGO DE COMPOSTELA

2022

USC
UNIVERSIDADE
DE SANTIAGO
DE COMPOSTELA

DECLARACIÓN DE AUTOR DA TESE

D. Damián García Castro

Título da tese: **Cosmic rays' study with a TRASGO detector**

Presento a miña tese, seguindo o procedemento axeitado ao Regulamento, e declaro que:

1) A tese abarca os resultados da elaboración do meu traballo.
2) De selo caso, na tese faise referencia ás colaboracións que tivo este traballo.
3) A tese é a versión definitiva presentada para a súa defensa e coincide coa versión impresa presentada en formato electrónico.
4) Confirmo que a tese non incorre en ningún tipo de plaxio doutros autores nin de traballos presentados por min para a obtención doutros títulos.

E comprométome a presentar o Compromiso Documental de Supervisión no caso de que o orixinal non estea na Escola.

En **Santiago de Compostela**, 11 de Maio de 2022

Asdo. Damián García Castro

USC
UNIVERSIDADE
DE SANTIAGO
DE COMPOSTELA

AUTORIZACIÓN DO DIRECTOR DA TESE

D. **Juan Pablo Garzón Heydt**

En condición de: **Director**

Título da tese: **Cosmic rays' study with a TRASGO detector**

INFORMA:

Que a presente tese, correspóndese co traballo realizado por D. Damián García Castro, baixo a miña dirección, e autorizo a súa presentación, considerando que reúne os requisitos esixidos no Regulamento de Estudos de Doutoramento da USC, e que como director/titor non incorre nas causas de abstención establecidas na Lei 40/2015.

En **Santiago de Compostela**, 11 de Maio de 2022

Asdo. Juan Pablo Garzón Heydt

USC
UNIVERSIDADE
DE SANTIAGO
DE COMPOSTELA

AUTORIZACIÓN DO TITOR DA TESE

D. **Héctor Álvarez Pol**

En condición de: **Titor**

Título da tese: **Cosmic rays' study with a TRASGO detector**

INFORMA:

Que a presente tese, correspóndese co traballo realizado por D. Damián García Castro, baixo a miña titorización, e autorizo a súa presentación, considerando que reúne os requisitos esixidos no Regulamento de Estudos de Doutoramento da USC, e que como titor non incorre nas causas de abstención establecidas na Lei 40/2015.

En **Santiago de Compostela**, 11 de Maio de 2022

Asdo. Héctor Álvarez Pol

USC
UNIVERSIDADE
DE SANTIAGO
DE COMPOSTELA

This thesis was partially supported by the Spanish Ministry of Economy, Industry and Competitiveness, under the predoctoral grant BES-2017-081058, and the project CTM2016-77325-C2-2-P. Cofinanced by the European Social Fund.

USC
UNIVERSIDADE DE SANTIAGO DE COMPOSTELA

USC
UNIVERSIDADE
DE SANTIAGO
DE COMPOSTELA

AGRADECIMIENTOS

Que la vida sea corta o larga, todo depende de la manera en que se viva. Así son los agradecimientos. Llegados a este punto, es un privilegio que me encuentre escribiendo estas palabras, las cuales son muy necesarias, puesto que la gratitud en silencio no sirve de nada.

En primer lugar, quiero dar las gracias a Hans, mi director de tesis. Gracias por concederme la oportunidad de formarme en el mundo de la investigación y por poner todos los medios para que este trabajo saliese adelante. También mi agradecimiento a Héctor por asumir el papel de tutor durante el último año y por sus siempre constructivas críticas para mejorar la calidad de este trabajo.

Esta tesis ha sido posible gracias a la inestimable ayuda de Georgy. Sin todas esas conversaciones, discusiones y consejos no estaría en este punto en este preciso momento.

Me gustaría destacar a todos aquellos que forman o han formado parte de las colaboraciones TRISTAN y TRAGALDABAS. Gracias por todas las conversaciones y por los conocimientos que me habéis transmitido. En especial, Alberto, Georgy, João, Juanjo, Marcos, Pablo y Teresa.

Gracias al LIP Coimbra por acogerme durante la estancia y por resolver todas las dudas sobre RPCs que han surgido.

Mi más profundo agradecimiento a toda las excelentes personas de la BAE-JCI con las que he compartido estancia en la Antártida. Si os intento citar a todos seguro que me olvido de alguien.

Gracias a Diego por ofrecerme su apoyo desde el inicio de mi aventura investigadora y por el tiempo dedicado.

Quisiera agradecer también a Irma y J. Cuenca todas las discusiones y las charlas en la cafetería. Gracias por vuestra disposición en todo momento y por haber contribuido a este trabajo de una u otra forma.

USC DE COMPOSTELA

Por supuesto no olvidar a Cris, Dani F., Dani R., Juan, Marwan y Lucía por esos momentos de desconexión en el ratatorio.
Gracias a todos mis amigos y compañeros de Física por haber compartido todos estos años juntos, desde las comidas en mates a los festivales, partidos y deliciosos perros.
Mil gracias también a Jose y Josito por aguantarme todos estos años y por animarme en todo momento.
Una gran parte de este logro se lo debo a mi familia. Ni somos todos los que estamos ni estamos todos los que somos, pero su recuerdo es su mejor legado. Gracias a mis padres, por todo su apoyo en esta travesía, su dedicación y el trabajo duro de cada día. Gracias a mis hermanos por aguantarme siendo el jefe de casa. También, gracias a Hugo, que aunque no lea esto hasta dentro de unos años, ha hecho que los últimos meses hayan sido muy divertidos viendo como avanzaba su aprendizaje. Sin olvidarme de mi segunda familia, Loli, Manolo y Marta, gracias por todos estos años, por vuestra ayuda y por hacerme sentir uno más cada día.
Y por supuesto, gracias Vane. Alcanzar esta meta no hubiese sido posible sin tu compañía. De corazón, gracias por quererme como lo haces y por estar siempre dispuesta a resolver cualquier problema de esos que solo me pasan a mí (aunque sea a las 4 am y a 12.000 km de distancia). En definitiva, me has dado una vida con la que jamás hubiese podido soñar.

Gracias.

USC
UNIVERSIDADE DE SANTIAGO DE COMPOSTELA

USC
UNIVERSIDADE
DE SANTIAGO
DE COMPOSTELA

USC
UNIVERSIDADE
DE SANTIAGO
DE COMPOSTELA

TABLE OF CONTENTS

TABLE OF CONTENTS 1
ABBREVIATIONS i
INTRODUCTION 1
OBJECTIVES 5
1 COSMIC RAYS 9
1.1 DISCOVERING THE COSMIC RAYS 9
1.2 PROPERTIES 10
1.2.1 Energy spectrum 11
1.2.2 Composition 13
1.2.3 Sources and propagation 14
1.3 INFLUENCE OF MAGNETIC FIELDS 16
1.3.1 Intergalactic 17
1.3.2 Galactic 17
1.3.3 Heliospheric 17
1.3.4 Geomagnetic 18
1.3.4.1 South Atlantic Anomaly 19
1.3.4.2 Cutoff rigidity 20
1.3.4.3 Latitudinal effect 21
1.3.4.4 Atmospheric effect 21
1.4 SOLAR MODULATION 22
1.5 INTERACTION WITH THE EARTH'S ATMOSPHERE 24
1.5.1 EAS 24
1.5.1.1 Hadronic component 25
1.5.1.2 Muonic component 26
1.5.1.3 Eletromagnetic component 26
1.5.1.4 Time and density microestructure 27
1.5.2 Atmospheric effects 28
1.5.2.1 Pressure 28

USC
UNIVERSIDADE DE SANTIAGO DE COMPOSTELA

1.5.2.2 Temperature 29

1.6 DETECTION METHODS 32
1.6.1 Direct 33
1.6.2 Indirect 33

2 GASEOUS IONIZATION DETECTORS 35

2.1 RADIATION-MATTER INTERACTION 35
2.1.1 Interaction of charged particles with matter 36
2.1.1.1 Heavy particles 36
2.1.1.2 Electrons and positrons 40
2.1.2 Interaction of neutral particles with matter 42
2.1.2.1 Photons 42
2.1.2.2 Neutrons 42

2.2 OPERATION PRINCIPLE OF GAS DETECTORS 43
2.2.1 Working regimes 44
2.2.2 Avalanche multiplication 45

2.3 RESISTIVE PLATE CHAMBERS 47

3 TRASGO DETECTORS 53

3.1 THE TRASGO PROJECT 53

3.2 DETECTORS 54
3.2.1 TRAGALDABAS 55
3.2.2 TRISTAN 58
3.2.3 muTT 61
3.2.4 STRATOS 63

4 ELECTRONIC SYSTEMS 67

4.1 INTRODUCTION TO THE COMPONENTS 67

4.2 FRONT-END ELECTRONICS 68
4.2.1 DBO 68
4.2.2 MBO 69

4.3 DATA ACQUISITION SYSTEM 70
4.3.1 TRB 70
4.3.1.1 TRB version 2 71
4.3.1.2 TRB version 3 71
4.3.2 Trigger system 71

USC
UNIVERSIDADE DE SANTIAGO DE COMPOSTELA

4.4 ENVIRONMENTAL SENSORS 73
4.4.1 Presure 73
4.4.2 Relative humidity 74
4.4.3 Temperature 74

4.5 POWER SUPPLY 75
4.5.1 LV 75
4.5.2 HV 75

4.6 GAS SYSTEM 77
4.6.1 Bubbler 77

4.7 TRISTAN-TRAGALDABAS EQUIPMENT 78
4.7.1 TRISTAN 78
4.7.2 TRAGALDABAS 83

5 SLOW CONTROL AND MONITORING 89

5.1 OVERVIEW 89

5.2 PARAMETERS CONTROLLED BY THE SCMS 90

5.3 SENSOR READING 91
5.3.1 Environment 91
5.3.2 Gas system 92
5.3.3 HV 92
5.3.4 FEE 92
5.3.5 DAQ 93

5.4 ALARMS 94

5.5 VISUALIZATION 96
5.5.1 TRISTAN 96
5.5.1.1 Daily reports 96
5.5.1.2 Cell and multiplicity maps 98
5.5.2 TRAGALDABAS 99
5.5.2.1 Grafana with PNP4Nagios 99
5.5.2.2 Cell and multiplicity maps 100
5.5.2.3 Charge report 101
5.5.2.4 Cell Viewer 102

6 CALIBRATION AND RECONSTRUCTION 105

6.1 STRUCTURE OF UNPACKING AND CALIBRATION PROCESSES 105

6.2 GEOMETRIC ACCEPTANCE 107

USC
UNIVERSIDADE DE SANTIAGO DE COMPOSTELA

6.3 SIGNAL CALIBRATION 111
6.3.1 Charge 111
6.3.2 Time 114
6.3.3 Slewing correction 119

6.4 RANDOM COINCIDENCES 120

6.5 ACTIVE AND DEAD TIMES 121

6.6 EFFICIENCY 122
6.6.1 Tracking method 123
6.6.2 Principal component analysis 124
6.6.3 Charge study 129

6.7 EVENT RECONSTRUCTION 131

6.8 PERFORMANCE 136
6.8.1 Angular resolution 137
6.8.2 Time resolution 137
6.8.3 Position resolution 138

7 RESULTS 141

7.1 INTRODUCTION 141

7.2 DATA-TAKING CAMPAIGNS 142
7.2.1 TRISTAN 142
7.2.1.1 Latitudinal survey 2018 143
7.2.1.2 Latitudinal survey 2019-I 145
7.2.1.3 Latitudinal survey 2019-II 146
7.2.1.4 Santiago 2019 148
7.2.1.5 Antarctica 2020 149
7.2.2 TRAGALDABAS 151

7.3 RAW DATA PROCESSING 151
7.3.1 Event reconstruction 151
7.3.2 Calibration 153
7.3.3 Raw vs. calibrated data 159

7.4 ATMOSPHERIC CORRECTIONS 162
7.4.1 Barometric effect 163
7.4.2 Temperature effect 165
7.4.3 Calibrated vs. corrected data 169

7.5 INFLUENCE OF GEOMAGNETIC FIELD AND SOLAR ACTIVITY 171
7.5.1 Cutoff rigidity 171

USC UNIVERSIDADE DE SANTIAGO DE COMPOSTELA

7.5.2 Solar activity 178
7.5.3 SAA 182

7.6 EXTENDED MULTIPLICITY STUDY 183
7.6.1 Barometric effect 184
7.6.2 Cutoff rigidity dependency 185

CONCLUSIONS 189

RESUMO EN GALEGO 193

APPENDIX 203

BIBLIOGRAPHY 209

USC
UNIVERSIDADE DE SANTIAGO DE COMPOSTELA

USC
UNIVERSIDADE
DE SANTIAGO
DE COMPOSTELA

ABBREVIATIONS

AC	Air Conditioning system
ADC	Analog-to-Digital Converter
AEMET	Agencia Estatal de Meteorología
AGN	Active Galactic Nuclei
BAE-JCI	Base Antártica Española-Juan Carlos I
BIO	Buque de Investigación Oceanográfica
CDS	Copernicus Climate Data Store
CMB	Cosmic Microwave Background
CME	Coronal Mass Ejection
CR	Cosmic Ray
CSDA	Continuous Slowing Down Approximation
DABC	Data Acquisition Backbone Core
DACs	Digital-to-Analog Converters
DAQ	Data Acquisition System
DBO	DaughterBOard
DOY	Day Of the Year
DSA	Diffusive Shock Acceleration
Dst	Disturbance short-time index
DTC	Differential Temperature Coefficient
EAS	Extensive Air Shower
EBL	Extragalactic Background Light
ECMWF	European Centre for Medium-Range Weather Forecast
EGCR	Extragalactic Cosmic Ray
FD	Forbush Decrease
FEE	Front-End Electronics
FPGA	Field-Programmable Gate Array
FWHM	Full Width at Half Maximum
GCR	Galactic Cosmic Ray

USC UNIVERSIDADE DE SANTIAGO DE COMPOSTELA

GMDN	Global Muon Detector Network
GMF	Galactic Magnetic Field
GRBs	Gamma Ray Bursts
GSI	Gesellschaft für SchwerIonenforschung
GUI	Graphical User Interface
GWP	Global Warming Power
GZK	Greisen-Zatsepin-Kuzmin
HADES	High Acceptance DiElectron Spectrometer
HDD	Hard Disk Drive
HLD	HADES List Data
HMF	Heliospheric Magnetic Field
HPTDC	High-Performance TDC
HV	High Voltage
IGM	Intergalactic Medium
IGMFs	Intergalactic Magnetic Fields
IGRF	International Geomagnetic Reference Field
ISM	Interstellar Medium
Kp	Planetary k-index
LabCaF	Laboratorio Carmen Fernández
LAN	Local Area Network
LIP	Laboratório de Instrumentação e física experimental de Partículas
LSM	Least-Squares-Method
LV	Low Voltage
LVDS	Low Voltage Differential Signaling
MARTA	Muon Array with RPCs for Tagging Air showers
MBO	MotherBOard
MITO	Muon Impact-Tracer Observer
NEMO	Neutron Monitor
NH	Northern Hemisphere
NOAA	National Oceanic Atmospheric Administration
NTP	Network Time Protocol
ORCA	Observatorio de Rayos Cósmicos Antártico
PC	Principal Component
PCA	Principal Component Analysis

USC
UNIVERSIDADE DE SANTIAGO DE COMPOSTELA

PCB	Printed Circuit Board
PoE	Power over Ethernet
PS	Power Supply/ies
Q2W	Charge-to-Width
RPC	Resistive Plate Chamber
RMS	Root-Mean-Square
RMSE	Root-Mean-Square Error
RRD	Round Robin Database
RTC	Real Time Clock
SAA	South Atlantic Anomaly
Saeta	SmAllest sEt of daTa
SBC	Single-Board Computer
SCMS	Slow Control and Monitoring System
SCR	Solar Cosmic Ray
SDI	Serial Data Input
SDO	Serial Data Output
SFP	Small Form-Factor Pluggable
SF	Solar Flares
SH	Southern Hemisphere
SNRs	Supernova Remnants
SPI	Serial Peripheral Interface
SS	Solar System
TDC	Time-to-Digital Converter
TimTrack	Timing and Tracking
TOF	Time Of Flight
ToT	Time over Threshold
TRAGALDABAS	TRAsGo for the AnaLysis of the nuclear matter Decay, the Atmosphere, the earth B-field And the Solar activity
TRASGO	TRAck reconStructinG bOx
TRB	TDC Read-out Board
TRISTAN	TRasgo para InveSTigaciones ANtarticas
UDP	User Datagram Protocol
USC	University of Santiago de Compostela
UTM	Marine Technology Unit
WD	WatchDog

USC
UNIVERSIDADE DE SANTIAGO DE COMPOSTELA

USC
UNIVERSIDADE
DE SANTIAGO
DE COMPOSTELA

INTRODUCTION

Cosmic rays remain a permanent source of unknowns, despite being discovered by Victor Hess more than a hundred years ago. Primary cosmic radiation arrives evenly from all directions to Earth and gives a sample of matter from some of the most energetic astrophysical processes in nature. Chapter 1 introduces the reader to the topic of cosmic rays. It explains their properties and the influence that magnetic fields and the atmosphere exert on them.

Nowadays, a broad range of techniques is available to detect cosmic rays. The method used depends on both their energy and nature. Among all possibilities, gaseous ionization detectors such as resistive plate chambers are used widely in different experiments because of their tracking and timing capabilities. The development of a new generation of cosmic ray detectors based on this technology allows the study of the secondary particles produced due to the interaction of a primary cosmic ray with the Earth's atmosphere. These detectors are the so-called TRASGOs, whose main characteristics are high granularity and a good position-time resolution. TRASGOs permit multiparticle detection and particle identification. On the one hand, Chapter 2 presents the radiation-matter interaction mechanisms and the operation principle of the gaseous ionization detectors. On the other hand, Chapter 3 gives an overview of the TRASGO project.

The TRASGO project aims to offer information about cosmic rays that is usually absent in other kinds of detectors. The reconstruction of the registered events may allow the estimation of the energy of the primary incident particle and the evaluation of the effects of solar modulation and Earth’s magnetic field and atmosphere. Within this framework, the detectors TRISTAN and TRAGALDABAS were developed. TRISTAN performed a series of unprecedented latitudinal surveys before being installed in Antarctica. Its data is of exceptional interest for studies of

USC
UNIVERSIDADE DE SANTIAGO DE COMPOSTELA

the influence of the cutoff rigidity and Earth's atmosphere on the rate of secondary cosmic rays at different locations. TRAGALDABAS is a permanent station placed in Santiago de Compostela for the regular study of space weather events and the atmosphere. Chapter 4 describes, in detail, the electronic systems of which both detectors are composed and their logic and power diagrams.

As for any high-energy physics detector, the slow control and monitoring system is a fundamental part of the experiment to guarantee the detector stability and integrity. The correct operating conditions are required to ensure optimal data quality. For this reason, TRISTAN and TRAGALDABAS have many visualization tools that offer continuous monitoring of their status. Chapter 5 explains the tools we have elaborated for such a purpose.

Besides good monitoring or detector surveillance, reconstruction and calibration are necessary to interpret the measured data correctly. The first stages of the calibration process involve signal calibration, which consists of filtering the charge and synchronizing the times of the channels. Then, other effects are considered, for example, the active and dead times and the number of accidental coincidences. Moreover, the detector's efficiency depends on many factors, and it is not always constant, which affects the rate of cosmic rays we detect. Chapter 6 deals with the calibration and reconstruction algorithms we have implemented in TRISTAN and TRAGALDABAS.

A joint analysis of the calibrated data with external variables serves as a quality check. The most significant correction we have to apply is the pressure effect removal. Then, we can study the influence of the temperature at different layers in the atmosphere, the solar modulation, and the cutoff rigidity. Chapter 7 shows the coefficients that account for the dependency of TRISTAN rates with the pressure, temperature, and cutoff rigidity. Additionally, it includes the pressure correction applied to the TRAGALDABAS rate and the study of a powerful geomagnetic storm and their correlation with the rate.

Finally, the conclusions chapter summarizes the main results obtained in this thesis.

USC
UNIVERSIDADE DE SANTIAGO DE COMPOSTELA

USC
UNIVERSIDADE
DE SANTIAGO
DE COMPOSTELA

USC
UNIVERSIDADE
DE SANTIAGO
DE COMPOSTELA

OBJECTIVES

The main line of research of this thesis is the calibration and commissioning of TRISTAN and TRAGALDABAS detectors, as well as the analysis of the measured data for the study of showers of secondary cosmic rays at the Earth's surface. The aim of this work is:

1. Assembly, commissioning, and maintenance of the TRISTAN detector at the Spanish Antarctic Base JCI and during the multiple latitudinal surveys performed. Maintenance of the TRAGALDABAS detector and control of its operating conditions.

2. Develop the necessary software for slow control and monitoring, event reconstruction, and analysis of the data registered by both detectors, and by extension, for other TRASGO detectors.

3. Study and understand the response of both detectors with their internal variables (such as high voltage, background currents, relative humidity, etc.), besides determining the influence of the barometric pressure and the temperature at different layers of the Earth's atmosphere.

4. Develop the calibration software of the TRISTAN detector, and improve the existing one for TRAGALDABAS. Calibrate several data samples from the latitudinal surveys and the static measurements performed in Antarctica and Santiago de Compostela.

5. Correct the measured data by efficiency, barometric pressure, and temperature at different layers of the Earth's atmosphere.

USC
UNIVERSIDADE DE SANTIAGO DE COMPOSTELA

6. Study the influence of the geomagnetic field and solar activity in the cosmic ray data registered by both detectors, together with the analysis of neutron monitor data taken by ORCA detectors during the first latitudinal survey.

7. Extend the analysis of TRISTAN data to high multiplicities to obtain the barometric and rigidity coefficients.

TRASGO detectors are presented as an alternative to traditional technologies such as neutron monitors or muon detectors, which are bulkier and more expensive. The final impressions of the work developed in this thesis confirm the advantages of this technology compared to the aforementioned ones. The results will improve with the particle identification, muon-electron separation, and reconstruction of events with multiple particles, information only accessible with this kind of detectors.

USC
UNIVERSIDADE DE SANTIAGO DE COMPOSTELA

USC
UNIVERSIDADE
DE SANTIAGO
DE COMPOSTELA

USC
UNIVERSIDADE
DE SANTIAGO
DE COMPOSTELA

1 COSMIC RAYS

In the early years of the 20th century, not long after Antoine Henri Becquerel and the Curies were awarded the Nobel Prize in Physics for the discovery and research of natural radioactivity, scientists came up against another mystery: the origin, nature and properties of a new form of energy detected coming from outer space, afterward coined with the charming term cosmic rays.

1.1 DISCOVERING THE COSMIC RAYS

Up to the time that cosmic rays (CRs) were discovered, the source of natural radioactivity that cause the air, in a closed vessel, to be ionized was not known. Certainly, there was radiation coming from the Earth and the Sun, but the question was which of all sources was dominant and whether they were the only ones. The consensus in the scientific community was that the Earth's soil was the primary source and so its effects could be shielded. Various experiments showed that shielding did not reduce the ionization rate, while others suffered the effects of numerous experimental errors [1, 2].

It was in 1909–1910 when Theodor Wulf measured the ionization rate at different heights, on the ground and at the top of the Eiffel Tower, expecting an exponential decrease as the main assumption was that the Earth's soil was the main source. No conclusive evidence was found due to the small change of the ionization rate for such an increase in the height [3].

The breakthrough in the investigation of this phenomenon came thanks to Domenico Pacini in 1910. Pacini performed a series of experiments measuring the ionization rate at different altitudes and underwater. The hypothesis that the origin of the penetrating radiation was only the soil couldn't explain the obtained results [4].

USC
UNIVERSIDADE DE SANTIAGO DE COMPOSTELA

In 1912, Victor Hess during one of his flights aboard a hot air balloon reached 5 km height, improving previous results. In order to exclude the Sun as a source of incoming radiation, a flight was done during a near-total eclipse. Hess proved that ionization increased powerfully with height [5]. Therefore, he concluded that the origin of this penetrating radiation had to be extraterrestrial, which gained him the Nobel Prize in Physics in 1936.
In the following years and decades, multiple experiments were carried out to investigate the nature of this radiation that Robert Millikan referred to as CRs in 1925 [6]. All of this research generates the following picture: most of the CRs are relativistic charged atomic nuclei, primarily protons (~ 86%) along with α-particles (~ 11%), and a contribution of heavier nuclei and electrons, which are originated in outer space. The Earth's atmosphere is continuously bombarded by these highly energetic particles. The first interaction of CRs with an atmospheric target nuclei typically takes place between 10 and 30 km in height. The high-energy collisions produce lots of secondary particles like other protons, neutrons and pions, which can also interact again with the atmosphere forming an extensive air shower (EAS) (Section 1.5). An EAS consists of hadronic, muonic and electromagnetic components. They continue to grow as they go deeper into the Earth's atmosphere until the energy of the secondary particles is insufficient to continue the process. Consequently, the size of the shower decreases and eventually dies out. Only a part of the shower reaches the surface, depending on the energy of the primary particle. The discovery of CRs sets the stage for the exciting field known as astroparticle physics.

1.2 PROPERTIES

Since the identification of CRs, many scientists have examined the phenomenon and compiled a list of the properties of this new kind of radiation. Together with the energy spectrum, which gives us two physical puzzles that span a wide range of energy, we will discuss the composition, abundance, and propagation of CRs in this section.

USC UNIVERSIDADE DE SANTIAGO DE COMPOSTELA

1.2.1 Energy spectrum

The CR spectrum covers a wide range of energies that goes from around 10^9 eV up to 10^{21} eV, energies far above those reached in human-made particle accelerators with modern technology. The flux of observed CRs follows a remarkably smooth curve compatible with a power-law with minor deviations (Figure 1.1).

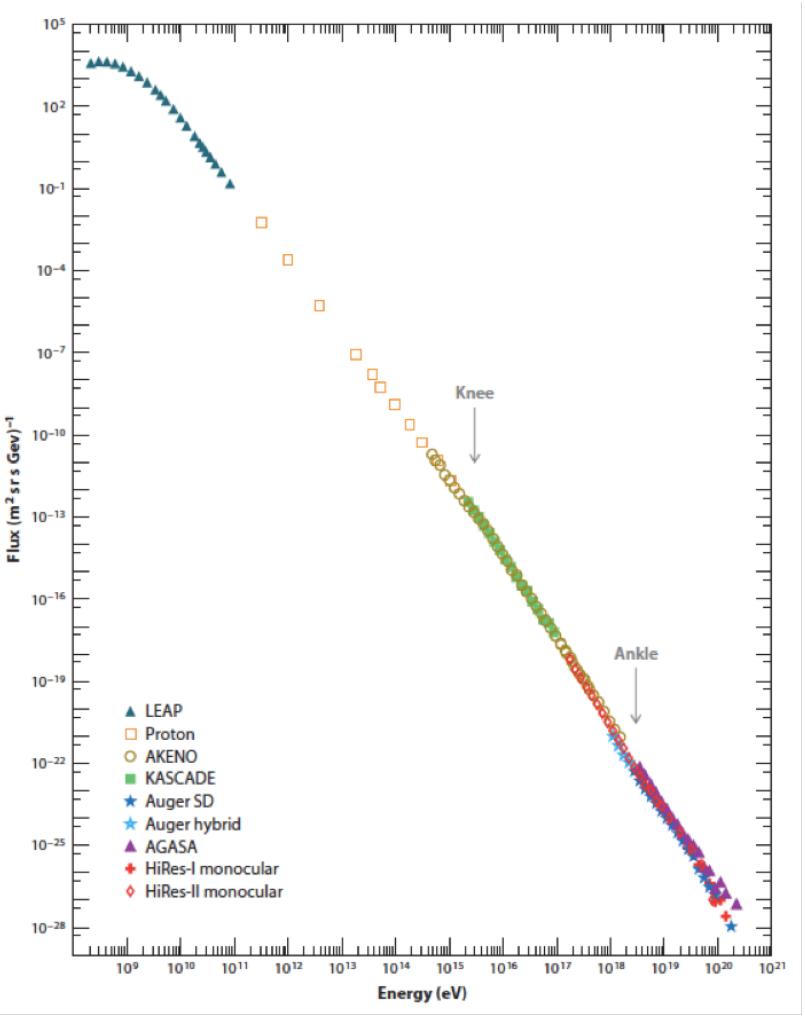

Figure 1.1: Overview of the CR spectrum. Different colors indicate different experiments. Deviations from the power-law known as the knee and the ankle are indicated by arrows. (Used with permission of Annual Reviews, Inc. from [7]; permission conveyed through Copyright Clearance Center, Inc.)

USC UNIVERSIDADE DE SANTIAGO DE COMPOSTELA

The spectrum contains different structures that are worthwhile to be described. Starting with the low-energy range, the deviation from the general behavior is due to the effect of the Sun and solar modulation, which is described in Section 1.4. Moreover, at higher energies, the spectrum is split up into two regions defined by the "knee" and the "ankle" (Figure 1.2). The differential energy spectrum is parametrized by:

$$\frac{dN}{dE} = C\,E^{-\alpha}\,, \tag{1.1}$$

where C is a constant and α is the differential spectral index. This index remains almost constant at approximately 2.7 starting from 10^9 eV to about 10^{15} eV. The so-called knee is the end of this region where the slope steepens from 2.7 to roughly 3.0. Beyond the knee there is a slight steeping around 10^{17} eV, sometimes referred to as the "second knee". The energy spectrum at 10^{18} eV flattens back to an index of 2.7 at the so-called ankle. Finally, for energies above 4×10^{19} eV, there is a softening of the spectrum. The significance of this reduction is determined by comparing the observed flux to the number anticipated for an unabated spectrum that follows the same power law as seen for low energy [8, 9].

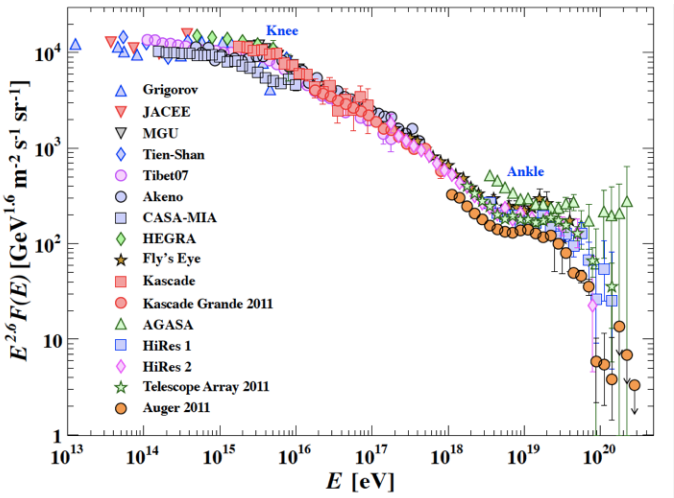

Figure 1.2: The all-particle spectrum of primary CRs in the high-energy region. Different colors correspond to different experiments. (Reprinted with permission from [9]. Copyright by the American Physical Society.)

Two models explain this flux suppression beyond 5×10^{19} eV. The Greisen-Zatsepin-Kuzmin (GZK) feature is caused by the interaction of energetic CRs with the cosmic microwave background (CMB) [10]. The second model explains the cut-off as the absolute maximum energy of the acceleration mechanism. Currently, the measurements are compatible with both models.

1.2.2 Composition

The origin of CRs can be either galactic (GCRs), including those of solar origin, or extragalactic (EGCRs). It was already stated that most but not all of the CRs are protons. Their chemical abundances reveal information about where they come from and how they propagate. Figure 1.3 shows a comparison of the relative abundances found in GCRs and the solar system (SS). At first sight, the important differences are in those elements with atomic numbers directly under C and Fe.

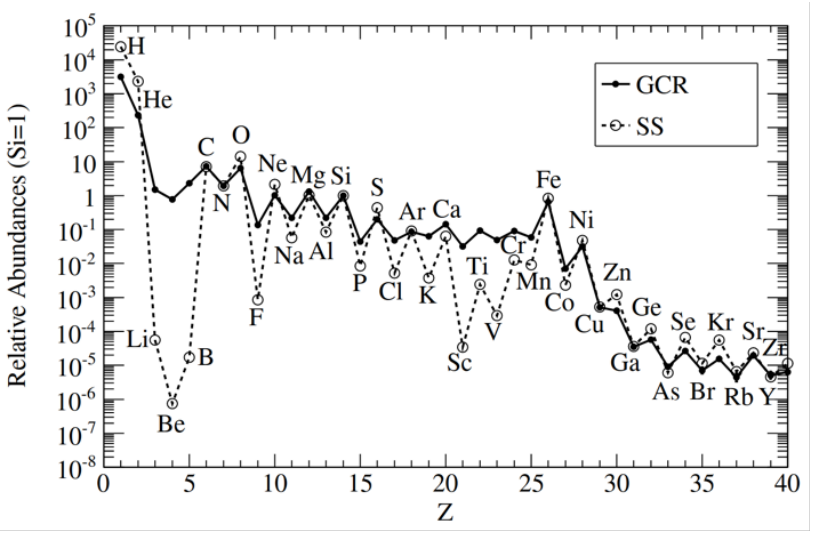

Figure 1.3: GCR and SS relative abundances normalized to ^{14}Si.
(Used with permission from [11], Creative Commons CC-BY-NC-ND 4.0.)

Significant proportions of the common heavier elements (such as carbon, oxygen, magnesium, silicon, and iron) travel the distance between their origins and the Earth without interacting significantly with the interstellar medium. This suggests that the elements are produced by nucleosynthesis like in the Sun. The enrichment in GCR

USC UNIVERSIDADE DE SANTIAGO DE COMPOSTELA

abundances, for the light elements (lithium, beryllium, and boron) and the sub-Fe group, are a result of spallation processes caused by carbon, oxygen, and iron near the Earth. Last but not least, the underabundance of hydrogen and helium is not really understood yet [12].

If the spallation cross-sections are known, it is then straightforward to deduce the quantity of matter traversed by CRs and their original composition.

1.2.3 Sources and propagation

Even though CRs arrive evenly from all directions, the sources of CRs are not necessarily spread uniformly. There are four categories of CRs according to their energy (Table 1.1):

Table 1.1: Energy ranges of CRs.

Energy / eV	CR type; origin and acceleration mechanism
$\sim 10^7 - 10^{10}$	- SCRs; galactic origin and shock acceleration
$< 3 \times 10^{15}$	- GCRs I; galactic origin and diffusive shock acceleration in supernova remnants (SNRs)
$\sim 10^{15} - 10^{18}$	- GCRs II; galactic origin and second stage acceleration of GCRs I by shocks
$> 10^{18}$	- EGCRs; extragalactic origin and diffusive shock acceleration in extragalactic sources

Diffusive shock acceleration (DSA), also known as first-order Fermi acceleration, is one of the most commonly accepted mechanisms for producing CRs. In Fermi's mechanism, CRs accumulate energy by being scattered by turbulence up and downstream of the shock, crossing the shock multiple times [13–17].

CRs have a broad range of possible sources, covering from solar cosmic rays (SCRs) ejected in solar flares (SF) and coronal mass ejections (CMEs), GCRs produced in supernova explosions, SNRs and Wolf-Rayet stars, and finally to EGCRs which origin might be the intergalactic medium (IGM), gamma-ray bursts (GRBs), blazars and active galactic nuclei (AGNs). In order to accelerate to a certain energy, CRs must be confined in the acceleration region, so the acceleration

USC UNIVERSIDADE DE SANTIAGO DE COMPOSTELA

physical site (R_S) must be about the order of Lamor radius (R_L) of a charged particle in a magnetic field:

$$R_L = \frac{E}{|q|\, c\, B} \leq R_S\,, \tag{1.2}$$

with E and q as the energy and charge of the particle, B as the strength of the magnetic field of the source. This is the famous Hillas Criterion that predicts the circumstances that must exist in an accelerator for particles to reach maximum energy [18]. In typical units, the maximum energy can be stated as follows:

$$E_{max}^{Hillas} = Z \times 10^{18}\ eV \left(\frac{B}{\mu G}\right)\left(\frac{R_S}{kpc}\right). \tag{1.3}$$

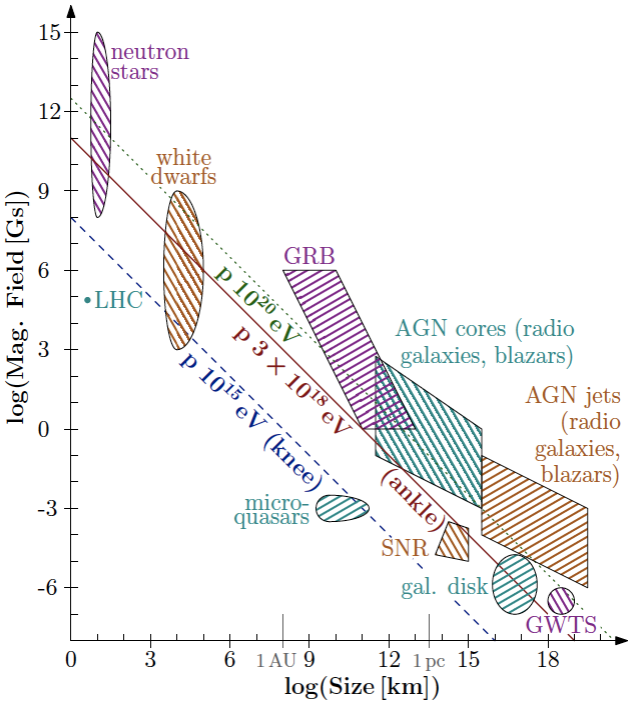

Figure 1.4: The Hillas plot represents the position of the acceleration sources in a double logarithmic scale of the magnetic field intensity vs. the source size. The knee (blue dashed), ankle (red solid) and maximum energy (green dotted) lines are shown. (Reprinted from [8], with permission from Elsevier.)

USC UNIVERSIDADE DE SANTIAGO DE COMPOSTELA

Hillas constructed his well-known diagram, in which astrophysical sources with non-thermal emission are displayed with respect to their magnetic field and size. The lines represent the maximum energy for protons to reach the knee, the ankle and the highest observed energies (Figure 1.4).

The propagation model of CRs through the galaxy, which must account for changes in energy, diffusion, convection, nuclear interactions, radioactive decay, and spallation processes, may be studied using relative abundances of cosmic-ray nuclei. The propagation equation of CRs in the general form is:

$$\begin{aligned}\frac{\partial\psi(\vec{r},\mathrm{p},\mathrm{t})}{\partial \mathrm{t}} - \vec{\nabla}\cdot\left(\mathrm{D_{xx}}\vec{\nabla}\psi - \vec{\mathrm{V}}\psi\right) - \frac{\partial}{\partial \mathrm{p}}\mathrm{p}^2\mathrm{D_{pp}}\frac{\partial}{\partial \mathrm{p}}\frac{1}{\mathrm{p}^2}\psi \\ + \frac{\partial}{\partial \mathrm{p}}\left[\dot{\mathrm{p}}\psi - \frac{\mathrm{p}}{3}\left(\vec{\nabla}\cdot\vec{\mathrm{V}}\right)\psi\right] + \frac{1}{\tau_{\mathrm{f}}}\psi + \frac{1}{\tau_{\mathrm{r}}}\psi \\ = \mathrm{q}(\vec{\mathrm{r}},\mathrm{p},\mathrm{t})\,,\end{aligned} \tag{1.4}$$

where $\partial\psi(\vec{r},p,t)$ is the CR density per unit of total particle momentum p at the position $\vec{r}$. D_{xx} is the spatial diffusion coefficient, $\vec{V}$ is the convection velocity, D_{pp} is the diffusion momentum that describes the diffusive reacceleration, $\dot{p}$ is the momentum gain, τ_f is the time scale for fragmentation loss, and τ_r the time scale for radioactive decay. $q(\vec{r},p,t)$ is the source term, which includes the contributions of primary, spallation and decay [19].

The propagation of CRs in the IGM is primarily influenced by astrophysical photon backgrounds, such as CMB and extragalactic background light (EBL), and magnetic fields in both the IGM and interstellar medium (ISM). Nonetheless, the global magnetic field of the universe is still unknown.

1.3 INFLUENCE OF MAGNETIC FIELDS

Due to their nature, CRs are continually scattered and deflected by the magnetic fields while traveling through space. Therefore, charged particles arrive isotropically to the Earth without any information of

USC UNIVERSIDADE DE SANTIAGO DE COMPOSTELA

their initial direction of motion and the locations of their sources. Only EGCRs with the highest energies have enough energy to travel through the magnetic field of the galaxy and continue unimpeded crossing the heliosphere and the Earth's magnetic field.

1.3.1 Intergalactic

The role of intergalactic magnetic fields (IGMFs) as possible seed fields for galaxies and clusters, as well as their likely link to structure formation in the early Universe, sets notable importance on their discovery. Several generation mechanisms have been proposed. In magnetohydrodynamic simulations, the strength of the turbulent field range between 0.1 μG and 0.01 μG, whereas regular fields are weaker. The magnetic field in galaxies is stronger than in the IGM [20, 21].

1.3.2 Galactic

The galactic magnetic field (GMF) in the galactic disk is well understood due to Faraday rotation measurements from galactic pulsars. Our galaxy has a spiral structure and the GMF may be explained in terms of the regular component, that seems to be linked to the spiral arms with a characteristic intensity in the microgauss range (~ 3 μG), and the turbulent or random component with at least the same strength or higher. The magnetic field lines in the regular component lay parallel to the plane of the galaxy and track azimuthal spirals coming out from the galaxy's core. Even though these magnetic field lines coincide with the spiral arms of the galaxy, some go toward the galactic center, whereas others point away from it. The GMF becomes weaker as you go away from the galactic plane. A field strength of a few microgauss means that significant scattering of CRs will occur at least up to 10^{17} eV [22].

1.3.3 Heliospheric

CRs breaking into the SS must overcome the heliospheric magnetic field (HMF). The penetration probability through the heliosphere is higher for CRs of high rigidity. The HMF is the component of the magnetic field of the Sun that is frozen into the flow of the solar wind as a result of the extremely high electrical conductivity of the solar wind plasma. Hence, the rotation of the Sun leads to the creation of an

USC UNIVERSIDADE DE SANTIAGO DE COMPOSTELA

Archimedes spiral, known as Parker's spiral. The average value of the HMF near the Earth is around ~ 6 nT (0.6 μG). At large distances, the radial component vanishes and the azimuthal dominates [23].

1.3.4 Geomagnetic

The Earth's magnetic field, also called the geomagnetic field, is mostly generated by the convective movement of liquid iron within the outer core and it forms the Earth's magnetosphere. The solar wind compresses its sunward side and drags out the night-side. Spherical harmonic analysis divides the field's contribution into different parts, being the dipole component the largest one. Thus, at the Earth's surface, the main field can be approximated by a dipole placed at the Earth's center and tilted about 10 degrees to the rotation axis, with strength varying from around 0.3 G to 0.6 G. The field lines flow into Earth in the northern hemisphere and out in the southern hemisphere. The geomagnetic field shields us from harmful solar and cosmic radiation, deflecting the trajectories of the charged particles, and preventing the low-rigidity ones from reaching the atmosphere. Hence, the flux of CRs on top of the atmosphere is not isotropic [24].

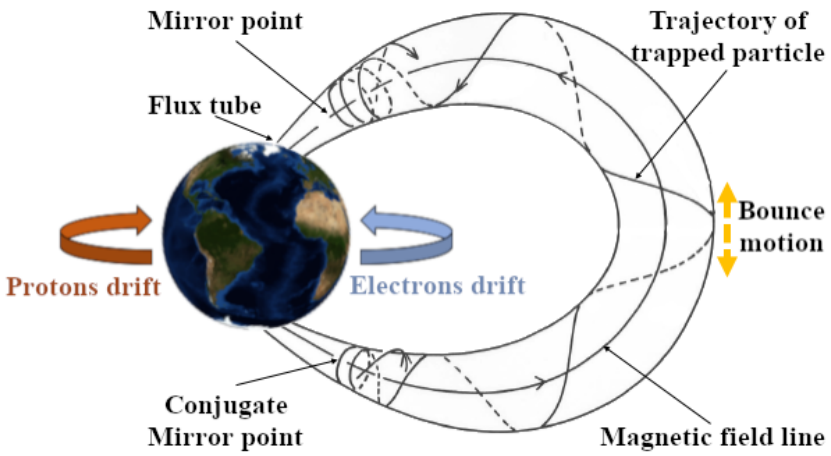

Figure 1.5: Schematic representation of the motion of particles in the geomagnetic field.

Incident particles can become trapped and held in the Van Allen Belts, which restrict particles to bounce back and forth between polar mirror points or drift around the planet. Protons drift to the west, whereas electrons to the east (Figure 1.5). Consequently, low-energy CRs arrive favorably from the west compared to the east since primary CRs are mainly positively charged nuclei. This is the well-known east-west effect [25, 26].

1.3.4.1 South Atlantic Anomaly

The South Atlantic Anomaly (SAA), located over South America and the South Atlantic, is one of the most distinctive features of the geomagnetic field. The field intensity at the Earth's surface has a weak minimum in the SAA region, which allows the inner Van Allen radiation belt to dip down closer to the atmosphere (Figure 1.6). This would allow a higher entrance of CRs causing an increase in the radiation, which in particular is very problematic at high altitudes because it could damage satellites' electronics. The origin of this region is the contribution of the quadrupole component to the main field [27].

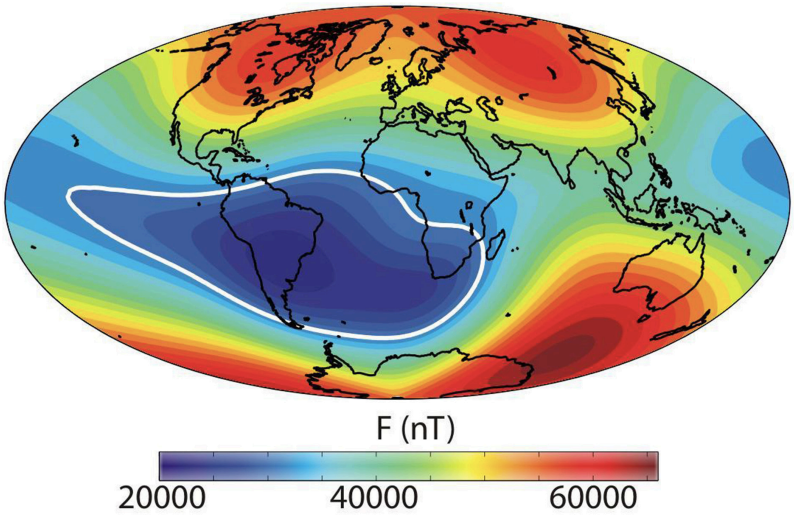

Figure 1.6: The total intensity of the geomagnetic field.
(Used with permission from [28], Creative Commons CC-BY 4.0.)

USC
UNIVERSIDADE DE SANTIAGO DE COMPOSTELA

1.3.4.2 Cutoff rigidity

The geomagnetic field near the Earth's surface has a significant impact on CRs trajectories and the values of the magnetic rigidity. The particle's magnetic rigidity is defined as follows:

$$R = \frac{p\,c}{|q|}, \tag{1.5}$$

where p and q are, respectively, the momentum and the charge of the particle. This parameter is exceptionally useful to describe the motion of charged particles in the geomagnetic field because particles with the same rigidity will follow the same path. There is a minimum value, called the cutoff rigidity, required to reach each point in the magnetosphere (Figure 1.7). CRs penetrate easier at high latitudes than near the equator as a result of the magnetic lines being more parallel to the trajectories of the incoming particles.

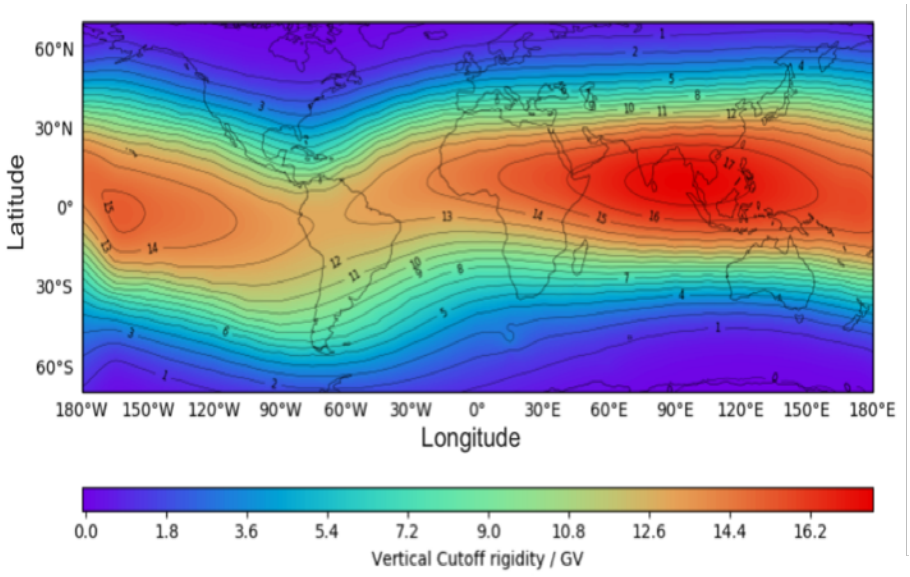

Figure 1.7: World map of the vertical CR effective cutoff rigidities. The data used for representation was obtained from [29].

Nevertheless, the impact of the geomagnetic field cannot accurately be described by only the cutoff rigidity. There is an upper cutoff above which all particle trajectories are allowed, a lower cutoff below which all are shielded, either by the solid body of the Earth or due to magnetic shielding, and a shadow region. The effective cutoff rigidity accounts for the shadow or penumbral region, where the transmission of cosmic radiation is chaotic with allowed and forbidden paths, and may be used for space weather applications [26].

1.3.4.3 Latitudinal effect

According to the aforementioned model of the geomagnetic field, the minimum intensity of CRs is where the value of the cutoff rigidity is maximal. Figure 1.8 shows the CR intensity as a function of the cutoff rigidity for a latitudinal survey. The main feature is the CR latitude knee in the low cutoff region, below which the latitude curve has a plateau. It exists for every CR secondary component.

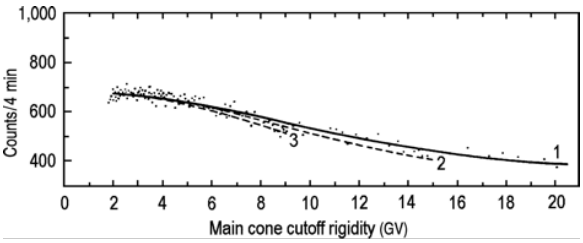

Figure 1.8: CR muon intensity measured by several inclined detectors as a function of the cutoff rigidity. (Reprinted with permission from [30]. Copyright by Springer Nature.)

The data from this kind of survey is of great importance for the study of the cutoff rigidity distribution, the coupling functions for neutron and muon components, and long-term CR modulations.

1.3.4.4 Atmospheric effect

Primary CRs lose energy propagating through the atmosphere which translates into an increase in the curvature of their trajectory due to the geomagnetic field. Therefore, the path length down to Earth's surface changes, and so does the probability to reach it.

USC
UNIVERSIDADE DE SANTIAGO DE COMPOSTELA

1.4 SOLAR MODULATION

The influence of the Sun upon the intensity of CRs is called solar modulation. The term "solar activity" accounts for all turbulences or non-stationary phenomena that are originated in the Sun's atmosphere and is dominated by the combination of magnetic and radiation activity. The main cause of solar modulation is the fluctuation in the magnitude of the solar wind, because of the solar activity. Generally, the solar activity is evaluated according to the number of black spots, called sunspots, on the Sun's surface. Sunspots are very strong magnetic fields that appear dark because they prevent some of the Sun's heat from reaching the surface. Their interaction with each other causes eruptions of energy in the form of SF and CMEs coming off the Sun, which perturb the solar wind and the HMF. In periods of high solar activity, the solar wind causes a decrease of the CR flux detected at Earth compared to the flux in the ISM [31].

The most remarkable modulation due to solar activity is the 11-year cycle, which is reflected in the CR intensity observed at Earth's surface since the 1960s and in the notes of the number of sunspots since the early 17th century. Figure 1.9 shows the negative correlation between the CR flux and the number of sunspots. This correlation was discovered by Forbush in 1954 [32]. It is well-known that the 11-year cycle is, in fact, a 22-year cycle, widely known as the Hale cycle, that is directly related to the reversal of the polarity of the HMF during each period of extreme solar activity [33]. This modulation is observed by all detectors that are sensitive to particles with rigidity lower than 20 GV, and the amplitude of the fluctuation increases with decreasing values of the rigidity.

In addition to long-term variations of the CR flux, there are considerable short-term periodicities that are relatively easy to distinguish during solar minima (solar activity minima): the 27-day variation caused by the rotation of the Sun. It is a quasi-periodic effect of 25–27 days due to the differential rotation of the Sun close to the equator; the daily variation owing to the Earth's rotation, and several oscillations due to the higher harmonics of the 27-day variation [34].

USC UNIVERSIDADE DE SANTIAGO DE COMPOSTELA

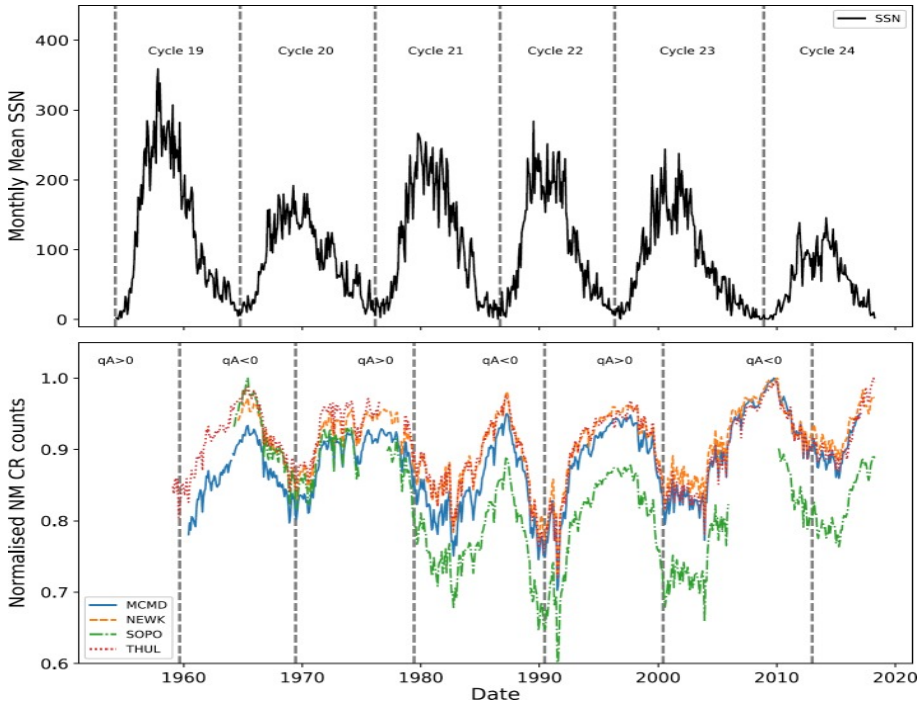

Figure 1.9: Top) Sunspot number. Vertical lines indicate the start of a new solar cycle. Bottom) CR intensity recorded by different neutron monitors. Vertical lines show approximately the solar magnetic field polarity reversal. (Used with permission from [35], Creative Commons CC-BY 4.0.)

It is also important to highlight the short-term effects of SF and CMEs in the CR intensity. SF and solar wind might cause magnetic storms when hitting the Earth's magnetosphere. If the arriving magnetic field direction is southward, it interacts powerfully with the geomagnetic field which is oppositely directed. The interaction causes a weakening of the Earth's magnetic field that will recover gradually over several days. Thus, energetic particles are streamed down the field lines and hit the Earth's atmosphere, normally at high latitudes, causing the auroras. The most intense SF are CMEs, which are massive emissions of x-rays and magnetized plasma into the ISM. The largest geomagnetic storms are a result of the interaction of this plasma with the Earth's magnetic field. The effect of the above-mentioned interactions on the CR flux is a sudden drop by 3–20%, followed by a progressive recovery to normal

USC UNIVERSIDADE DE SANTIAGO DE COMPOSTELA

intensity, called Forbush decrease (FD). A FD is caused by the sweeping of CRs by the plasma in the ISM and is registered by particle detectors in space and the Earth's surface [36–38]. The magnitude of the FD depends on the direction of propagation of the magnetized plasma and the strength of the CME that emitted it, and also on the energy of the CRs. The low-energy CRs experience larger drops than high-energy CRs.

1.5 INTERACTION WITH THE EARTH'S ATMOSPHERE

CRs hit the Earth's atmosphere continuously colliding with atmospheric target nuclei. If the energy of the primary CR is high enough, the collision produces many new energetic particles as secondaries. These new particles can interact again, adding more particles to the developing cascade until their energy is not enough to continue the process. The secondary particles are spread over large areas due to the interactions and they all arrive almost simultaneously. This phenomenon is known as EAS and the observed flux is affected by the barometric pressure and temperature of the atmosphere.

1.5.1 EAS

A detailed study of how an EAS develops in the atmosphere is relevant for the estimation of the energy and mass of the primary CR. All particles of an EAS undergo energy losses through hadronic and/or electromagnetic processes. As a result, the particle flux increases with increasing atmospheric depth, reaching a maximum in the first 100 g cm^{-2} ($\sim$ 30 km altitude over the sea level). Afterward, the flux decreases due to energy loss, absorption and decay processes. The shower eventually dies out before reaching the surface, if the energy of the primary CR is not enough. So that, the composition of the radiation changes at different altitudes over the sea level and it depends on where the first interaction of the primary CR took place. The interaction and decay probabilities depend on several factors such as particle's energy and mean lifetime, and atmospheric density. Three major CR components are distinguished in an EAS: hadronic, muonic and electromagnetic (Figure 1.10) [39].

USC UNIVERSIDADE DE SANTIAGO DE COMPOSTELA

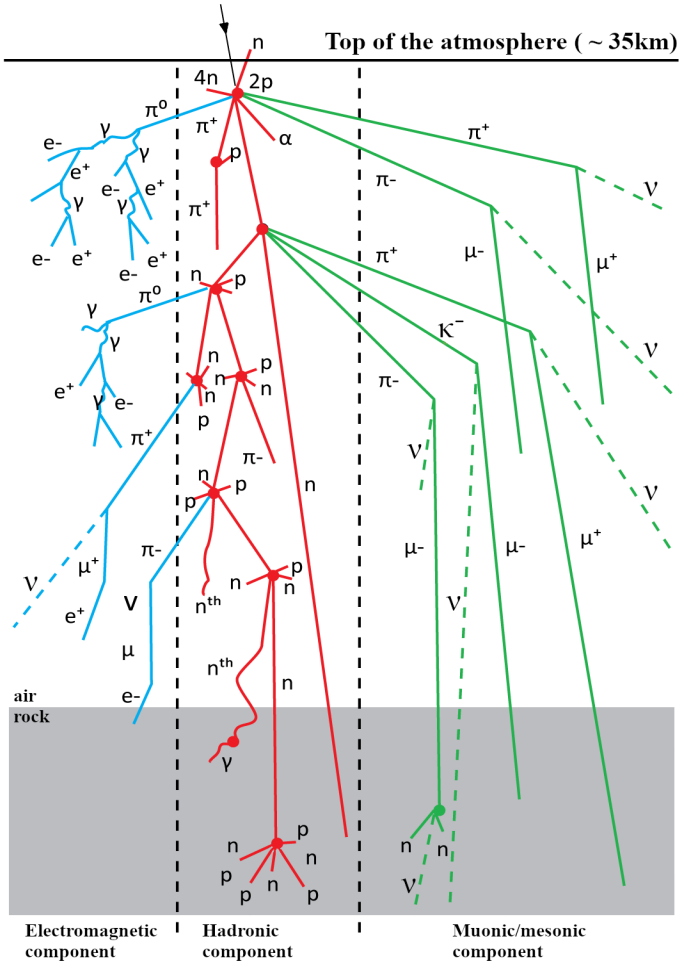

Figure 1.10: EAS schematic representation from top of the atmosphere. (Reprinted from [40], with permission from Elsevier)

1.5.1.1 Hadronic component

The hadronic component remains very close to the velocity vector of the primary CR and is the core of the shower. It contributes continually to the electromagnetic component producing mesons (mainly pions), which decay to muons, electrons and positrons. Charged pions, kaons, other mesons, hyperons and nucleon-antinucleon pairs resulting from strong interactions continue to propagate and feed the hadronic component.

USC UNIVERSIDADE DE SANTIAGO DE COMPOSTELA

1.5.1.2 Muonic component

The decays of charged pions, kaons, and other mesons into muons supply the muonic component. Kaon production has a low probability of about 10% in comparison to pions, so that, most of the muons originate from pion decays. The most important decay channels are:

$$\pi^{\pm} \rightarrow \mu^{\pm} + \nu_{\mu}\ (\overline{\nu_{\mu}})\ (\sim 100\%)$$
$$K^{\pm} \rightarrow \mu^{\pm} + \nu_{\mu}\ (\overline{\nu_{\mu}})\ (\sim 63.5\%)$$

The mean free path in air of charged pions is $\lambda_{\pi} \sim 120\ \mathrm{g\,cm^{-2}}$. Even though the mean lifetime of muons is approximately 2 μs, they easily penetrate the atmosphere reaching sea level because of the relativistic time dilation:

$$\tau(E) = \tau_0 \left(\frac{E}{m_o c^2}\right) = \tau_0\, \gamma\,, \qquad (1.6)$$

where τ_o and m_o are the mean lifetime and the mass of the particle at rest, E is the total energy and γ is the Lorentz factor. Muons and neutrinos are the dominant flux at the sea level, and only they can penetrate underground. Despite this, some of them may decay, helping to develop the electromagnetic component.

1.5.1.3 Eletromagnetic component

Neutral pions have a very short mean life and decay almost instantly. The dominant decay mode is into two photons:

$$\pi^0 \rightarrow \gamma + \gamma\ (\sim 98.8\%)$$

Photons can produce electron-positron pairs if their energy is higher than 1.02 MeV, which are subjected to produce bremsstrahlung photons leading again to pair production. The radiation length of electrons in air is $X_0 = 37\ \mathrm{g\,cm^{-2}}$. This process builds up the electromagnetic component of an EAS. In addition, at low energies the muon decay is also important:

$$\mu^{\pm} \rightarrow e^{\pm} + \nu_e\ (\overline{\nu_e}) + \overline{\nu_{\mu}}\ (\nu_{\mu})\ (\sim 98.6\%)$$

USC UNIVERSIDADE DE SANTIAGO DE COMPOSTELA

1.5.1.4 Time and density microestructure

The most representative properties of an EAS may be summarized by different parameterizations for the time profile, the density of particles and the energy of the primary CR (Figure 1.11). The use of these parameterizations was suggested by John Linsley in 1985 [41].

The time-width distribution of the particles in a shower is very narrow at short distances to the core and it becomes wider at long distances. The equation that describes this behavior is the following:

$$\sigma_t(r) = \sigma_{t_0}\left(1 + \frac{r}{r_t}\right)^{\beta}, \tag{1.7}$$

where r is the distance to the core, σ_{t_0} is the time width or time dispersion at time zero (2.6 ns), r_t is the dimension of the shower (30 m) and β is an empirical parameter (1.5) [41].

Another characteristic of an EAS is the density of particles or lateral density distribution. It depends on several variables such as the distance to the core (r), the shower size (N_0) and the mass of the primary CR as follows:

$$\rho(r, N_0) = \epsilon\, N_0\, r^{-n}, \tag{1.8}$$

where both ϵ and n changes for different primaries. For example, for a proton $\epsilon = 5.3 \times 10^{-4}$ and $n = 1.5$.

Finally, the energy of the primary CR is a function of the size of the EAS:

$$E_0(N_0) = \alpha\, {N_0}^{b}, \tag{1.9}$$

where $\alpha = 2.217 \times 10^{11}$ and $b = 0.798$ for a proton [42].

Using all these parameterizations, the energy of the primary CR can be written as:

$$E_0 = \alpha \left[\frac{\rho}{\epsilon}\left(r_t\left[\left(\frac{\sigma_t}{\sigma_{t_0}}\right)^{\frac{1}{\beta}} - 1\right]\right)^{n}\right]^{b}. \tag{1.10}$$

USC UNIVERSIDADE DE SANTIAGO DE COMPOSTELA

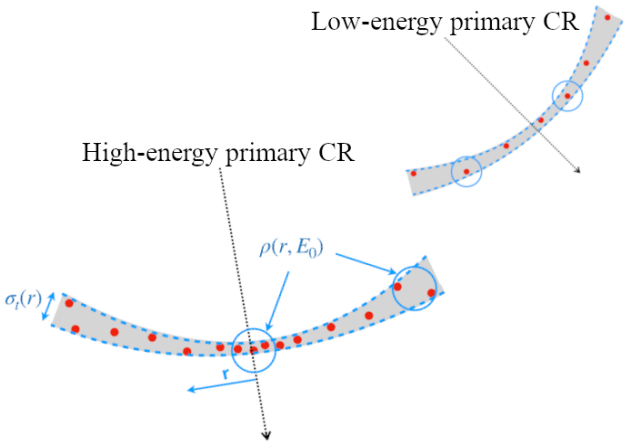

Figure 1.11: EAS front and lateral density distribution.

1.5.2 Atmospheric effects

Meteorological effects on secondary CRs are well known, with pressure and temperature effects being the dominant ones. The correction of the data by these effects increases the sensitivity to variations of the CR flux due to different processes of non-atmospheric origin. Both pressure and temperature cause perturbations in the effective thickness and height of the atmospheric layers.

1.5.2.1 Pressure

The barometric effect is determined experimentally by the following equation:

$$\ln\left(\frac{\delta I}{I}\right)_P = \beta\, \delta P\,, \qquad (1.11)$$

where $(\delta I/I)_P$ is the relative or normalized variation of the CR flux at the detection point, δP is the pressure variation which is calculated as $\delta P = P - P_{ref}$ being P and P_{ref} the current and reference pressure, respectively. The coefficient β, called barometric coefficient, depends on many factors including the kind of secondary particle and the altitude where the observation is performed. Hence, an increase (decrease) in

the pressure compared to the reference value means that secondary CRs suffer more (less) collisions on their way to the surface, and so that the flux detected decreases (increases). The barometric effect explains the effect of the atmospheric mass above the detector [39].

1.5.2.2 Temperature

In addition to the pressure effect, temperature changes in the atmosphere also modulate the CR flux at the surface. This modulation is very important, in particular for muon detectors. The temperature effect is mainly a result of two contributions, the so-called positive and negative effects. On the one hand, the positive effect is related to the interaction probability of kaons and charged pions with atmospheric nuclei in the high atmosphere. The decay of these particles is favored over their disintegration when the temperature increases, and that implies a higher production of high-energy muons [43]. On the other hand, the negative effect is associated with the path traveled by muons toward the surface. The higher the temperature, the further muons will travel. That benefits their decay before reaching the Earth's surface, causing a decrease of low-energy muons [44]. The temperature influence also affects neutron detectors, but this effect is less significant. Different methods can be used to describe the temperature effect. Some of them require the temperature profile of the entire atmosphere, whereas others use the temperature and altitude of the maximum muon production [45].

The theoretical or integral method takes into account the temperature profile along the whole vertical above a detector. The relative change of the flux of muons arriving with energy above E_{min} and zenith angle θ when the temperature changes by ΔT, can be written in the following way:

$$\left(\frac{\Delta N_T(E_{min}, X, \theta)}{N_0(E_{min}, X, \theta)}\right)_T = \int_0^X W_T\,(E_{min}, X, h, \theta)\,\Delta T(h)\,dh\,, \quad (1.12)$$

where h is the atmospheric depth in atm at the observation point (X) and W_T is the muon weighting function or differential temperature coefficient (DTC) [46–49].

USC UNIVERSIDADE DE SANTIAGO DE COMPOSTELA

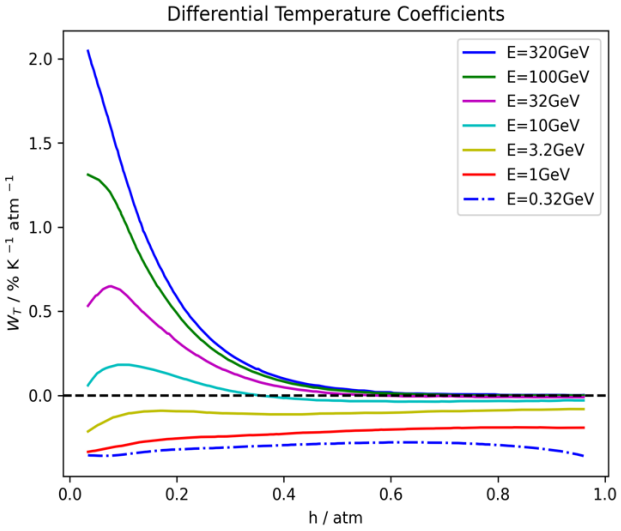

Figure 1.12: DTC for muons of different threshold energies arriving vertically at sea level. Values calculated by Dmitrieva in [49].

Figure 1.12 shows that high-energy muons are very sensitive to temperature variations in the stratosphere. A good and permanent monitoring of the muon flux and its correlation with the stratosphere temperature might improve the mid-long term weather forecast.

A new variable, defined as the weighted average of temperatures from the top of the atmosphere to the surface, can be derived from Equation 1.12:

$$\left(\frac{\Delta N_T(E_{min}, X, \theta)}{N_0(E_{min}, X, \theta)}\right)_T = \alpha_T \, T_{Eff}\,, \tag{1.13}$$

where α_T is the atmospheric temperature coefficient and T_{Eff} is the effective temperature defined as:

$$T_{Eff} = \frac{\int_0^X W_T\,(E_{min}, X, h, \theta)\,\Delta T(h)\,dh}{\int_0^X W_T\,(E_{min}, X, h, \theta)\,dh}, \tag{1.14}$$

The effective temperature takes into account the temperature at all pressure levels and approximates the atmosphere as an isothermal body. The contribution of each level is weighted, giving more importance to those where the muon production is more relevant. This parameter has been studied in multiple experiments like for instance Double Chooz, Daya Bay, IceCube, MINOS and Borexino, among others. The energy threshold varies from 22 GeV in Double Chooz to around 1.3 TeV in Borexino. The effective temperature and the temperature of the stratosphere are similar for such energies and the high-energy muon flux is strongly correlated with the temperature of the stratosphere. On the contrary, the flux of low-energy secondaries ($\sim$ 1 GeV muons, MeV electrons and gammas) showed a negative correlation. Figure 1.13 shows the α_T for various experiments. The lines represent the expected values for different assumptions of the ratio kaon-pion and the extreme cases of pure pion and kaon production [50–54].

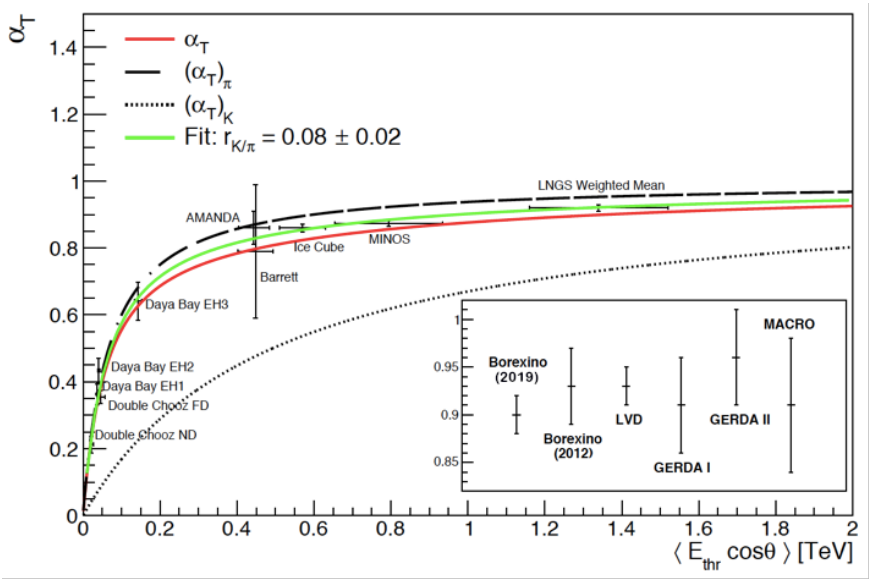

Figure 1.13: Measurements of the effective temperature coefficient α_T for different threshold energies and angles through $\langle E_{th} \cos\theta \rangle$. (Used with permission from [54], Creative Commons CC BY 3.0.)

USC UNIVERSIDADE DE SANTIAGO DE COMPOSTELA

1.6 DETECTION METHODS

The detection technique is determined by the nature and energy of the primary and secondary CRs (Figure 1.14). The energy spectrum of primary CRs was already described in Section 1.2, revealing that the flux decreases rapidly with the energy. The most abundant are the SCRs with a flux $\sim 1\ \mathrm{m^{-2}\ s^{-1}}$. Then, there is a broad energy band of GCRs, which flux is $\sim 1\ \mathrm{m^{-2}\ year^{-1}}$ in the knee region. Finally, for the EGCRs the flux is $\sim 1\ \mathrm{km^{-2}\ century^{-1}}$. As a consequence, the higher the energy, the larger area needs to be covered by a detector to measure a reasonable flux. CR detection methods can be roughly split into two categories: direct and indirect [55, 56].

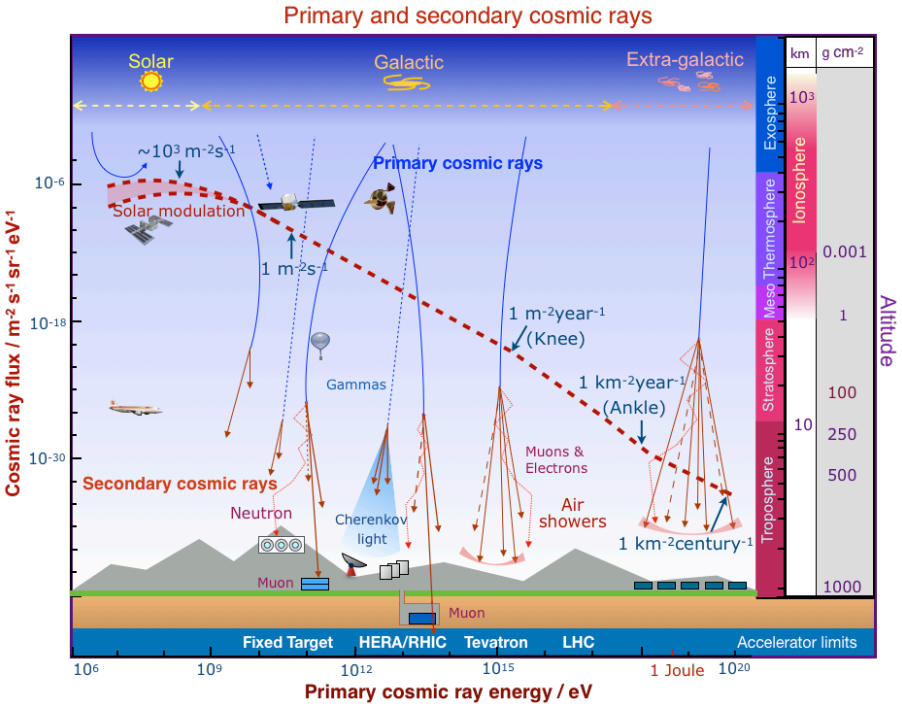

Figure 1.14: Main detection techniques used for the regular survey of primary and secondary CRs as a function of the energy of the primary. (Reprinted with permission of Physics of Atomic Nuclei from [79]. Copyright by Springer Nature.)

1.6.1 Direct

The direct measurements detect and identify directly the primary CRs in the energy range from 10^3 eV to 10^{15} eV. Since the atmosphere behaves as a shield, direct detection is assured mainly by space-based experiments and stratospheric balloons. Those carried out in space tend to follow near-equatorial orbits and suffer stronger geomagnetic shielding than balloons at high latitudes. Detectors placed in balloons undergo the effects of the residual atmosphere, such as the ionization loss. The small size of these detectors and the exposure time limit their energy range. Approaching the 10^{14} eV region, the boundary line between direct and indirect methods becomes more uncertain. A precise measurement of the CR flux by direct detection allows one to calibrate indirect experiments.

1.6.2 Indirect

EAS observation with ground-based experiments is the base of the indirect detection of CRs with energies above the knee. At the surface, different detectors are used to study different observables of an EAS. There is a wide choice of detectors including ionization, scintillators, calorimeters, Cherenkov, fluorescence, and radio emission detectors. The theoretical background of gaseous ionization detectors is introduced in the next section since this work is based on this kind of detection. Ground-based experiments can detect even the most energetic CRs for which the flux is very low. EAS originated by high-energy primary CRs may extend over very large areas at ground level, so big arrays of detectors distributed over a great area (typically 1 km^2 but it depends on the energy of the primary CR) are needed. Arrival times at several stations are very useful to determine the curvature of the shower front and the arrival direction of the primary.

USC
UNIVERSIDADE DE SANTIAGO DE COMPOSTELA

USC
UNIVERSIDADE
DE SANTIAGO
DE COMPOSTELA

2 GASEOUS IONIZATION DETECTORS

Radiation is the process by which energy is emitted, as particles or waves, or transmitted through a medium. According to its capability to ionize the medium in which it propagates, it can be classified into two large groups: ionizing and non-ionizing. This section is dedicated to ionizing radiation, which produces electron-ion pairs in matter, and gaseous ionizing detectors.

2.1 RADIATION-MATTER INTERACTION

Charged particles penetrate matter and lose energy by ionization or excitation of atoms and molecules. They are deflected or experience radiative energy loss due to the interactions with the Coulomb field of nuclei. Uncharged particles like neutrons or photons can interact with the medium liberating a charged particle. Then, the released particle losses energy due to electromagnetic interactions. Most particle detectors are based on the detection of the energy loss in the traversed material. The design of a detector depends on that energy and the interaction mechanism. The energy deposited in a gaseous detector may be enough to generate an electron-ion pair or produce a non-ionized excited state. Secondary fast electrons, or delta rays resulting from knock on processes, can also ionize or excite atoms within the detector's volume. Thus, a secondary ionization takes place. However, delta rays can be absorbed far away from the generation point or escape the medium because the energy lost by collisions is usually higher than the deposited energy per unit path in the medium. Depending on the mass and charge of the ionizing particles, the energy loss is due to different processes [57]. This section explains the main interaction mechanisms and gives the theoretical background needed to interpret the measurements.

USC UNIVERSIDADE DE SANTIAGO DE COMPOSTELA

2.1.1 Interaction of charged particles with matter

A relativistic charged particle loses discrete amounts of energy due to independent and stochastic collisions when interacting with the electrons and nuclei of the medium in which it propagates. In general, energy loss and deflection are the two main characteristics that describe the passage of a charged particle through matter. The interaction mechanisms are: inelastic collisions with atomic electrons, elastic scattering with atomic nuclei, nuclear reactions, Cherenkov radiation, and bremsstrahlung [58]. The following differentiation between heavy particles and electrons-positrons is motivated by the mass difference.

2.1.1.1 Heavy particles

The energy loss of particles heavier than the electron, like protons, pions, muons, α-particles, etc., is mainly through inelastic collisions with orbital electrons in matter. In these collisions, the energy is transferred and causes ionization or excitation of the atom. The amount of energy a particle transfers per collision is normally a very small fraction of its kinetic energy. However, in dense matter, the number of collisions per unit path is large enough. Thus, a considerable energy loss can be observed, even in thin materials. The average number of collisions per unit path (zeroth moment of the single-differential cross section ($d\sigma/dE$)) i.e., the inverse of the mean free path (λ), is obtained by multiplying the integral cross-section by the atomic density *N*:

$$\frac{1}{\lambda} = \mathrm{M}_0 = \mathrm{N} \int_{\mathrm{E_{min}}}^{\mathrm{E_{max}}} \frac{\mathrm{d}\sigma}{\mathrm{dE}} \mathrm{dE}\,. \tag{2.1}$$

The stopping power (or mass stopping power when divided by the density of the material) accounts for the energy loss per unit track length and is given by the first moment M_1 as follows:

$$-\frac{\mathrm{dE}}{\mathrm{dx}} = \mathrm{M}_1 = \mathrm{N} \int_{\mathrm{E_{min}}}^{\mathrm{E_{max}}} \mathrm{E} \frac{\mathrm{d}\sigma}{\mathrm{dE}} \mathrm{dE}\,. \tag{2.2}$$

USC UNIVERSIDADE DE SANTIAGO DE COMPOSTELA

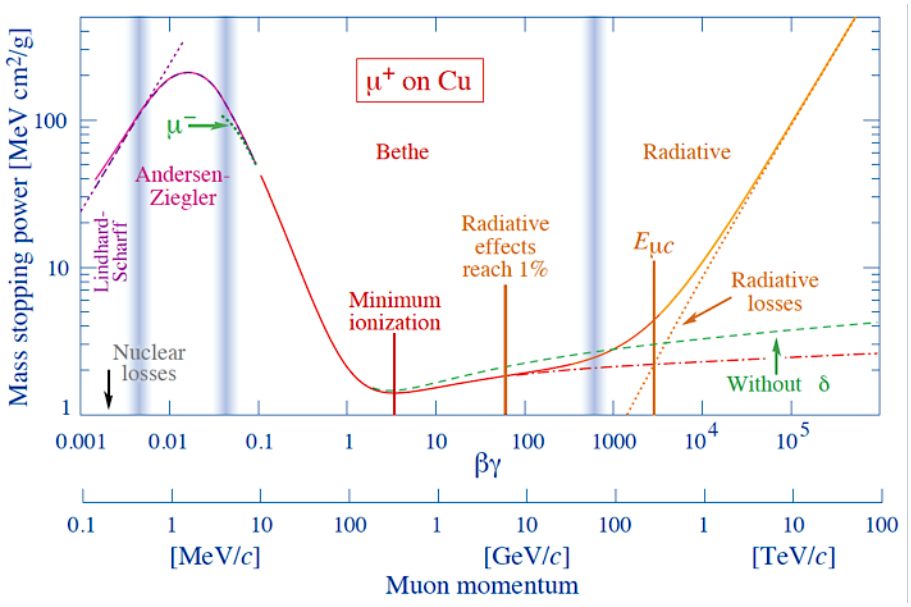

Figure 2.1: Mass stopping power of a μ^+ in copper. Bethe region together with other approximations separated by blue vertical bars are shown. (Reprinted with permission from [58]. Copyright by the American Physical Society.)

The Bethe formula (Figure 2.1) describes the mean stopping power for moderately relativistic heavy particles as a function of the maximum energy that can be transferred in a single collision (W_{max}); the mean excitation energy (I); the mass (M), ratio atomic/mass number (Z/A), charge in units of e (z), velocity ($\beta = v/c$) and Lorentz factor (γ) of the incident particle:

$$\left\langle -\frac{dE}{dx} \right\rangle = K z^2 \frac{Z}{A\beta^2}\left[\frac{1}{2}\ln\left(\frac{2m_e c^2\beta^2\gamma^2 W_{max}}{I^2}\right) - \beta^2 - \frac{\delta}{2} - \frac{C}{Z}\right], \quad (2.3)$$

where $K = 4\pi N_A r_e^2 m_e c^2$, N_A is Avogadro's number, m_e the electron mass and $r_e = e/4\pi\epsilon_0 m_e c^2$ the classical electron radius. The term $\delta/2$ is the density effect correction that takes into account the polarization present at high energies. The medium polarizes and limits the electric field extension and the energy loss for high-energy radiation. The last

USC UNIVERSIDADE DE SANTIAGO DE COMPOSTELA

term, *C*, accounts for the shell correction, noticeable when the velocity of the incident particle is low and close to the orbital velocity of the bound electrons of the target material. The maximum energy transferred per collision to an electron is given by:

$$W_{max} = \frac{2m_e c^2 \beta^2 \gamma^2}{1 + 2\gamma \frac{m_e}{M} \left(\frac{m_e}{M}\right)^2}. \qquad (2.4)$$

Equation 2.3 can be integrated between the initial energy and zero to find the continuous slowing down approximation (CSDA) range neglecting any kind of energy loss fluctuation and assuming it is continuous. Figure 2.2 shows the mean energy loss in several materials.

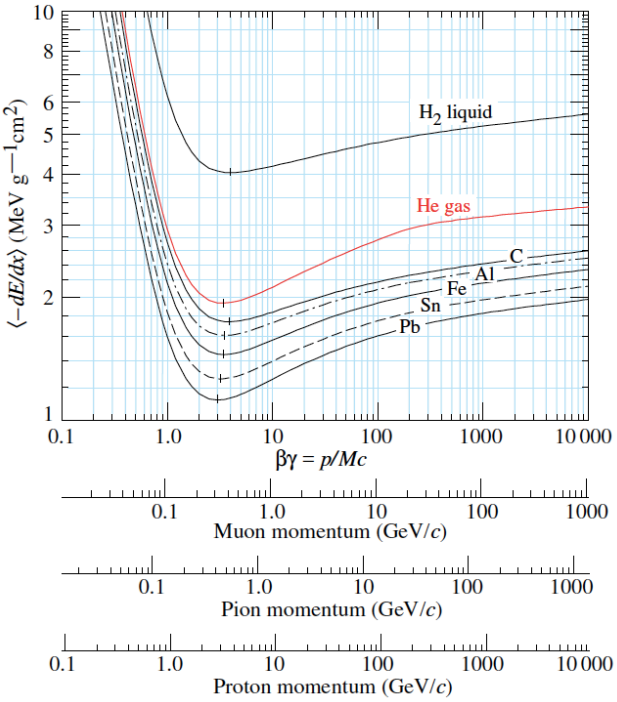

Figure 2.2: Mean stopping power as a function of βγ in different materials. (Reprinted with permission from [58]. Copyright by the American Physical Society.)

In the case of detectors with moderate thickness, the most probable energy loss is generally less than the given by Equation 2.3 for the mean energy loss (Figure 2.3). In this case, the energy loss is well-described by the Landau-Vavilov-Bichsel distribution, and it depends on the thickness of the material:

$$\Delta_p = \xi\left[\ln\left(\frac{2m_e c^2\beta^2\gamma^2}{I}\right) - \ln\left(\frac{\xi}{I}\right) + j - \beta^2 - \delta\right], \qquad (2.5)$$

where $\xi = (KZ/2A)\, z^2\, (x/\beta^2)$ MeV for a detector of thickness x in g cm^{-2} and $j = 0.200$.

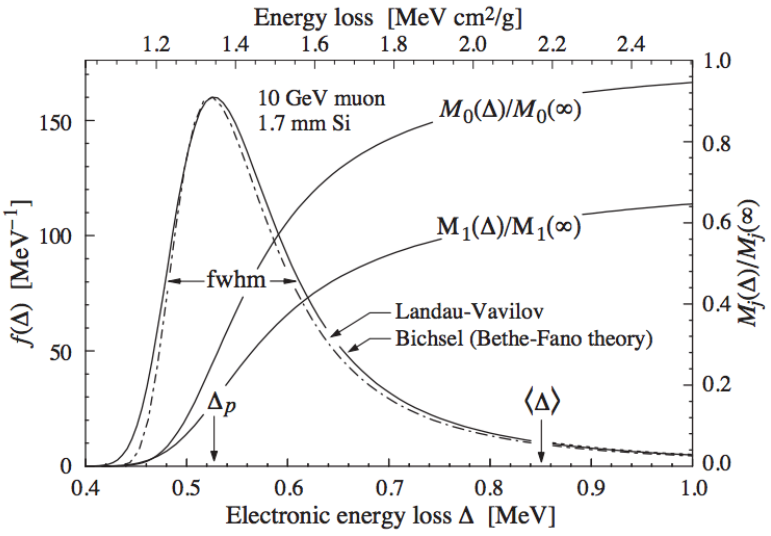

Figure 2.3: Energy loss distribution of a muon of 10 GeV crossing 1.7 mm of silicon. Comparison of Landau-Vavilov (dashed line) with Bichsel (solid line). Zeroth and first cumulative moments, full width at half maximum (FWHM), most probable energy loss Δ_p, and mean energy loss $\langle\Delta\rangle$ are shown. (Reprinted with permission from [58]. Copyright by the American Physical Society.)

USC
UNIVERSIDADE DE SANTIAGO DE COMPOSTELA

2.1.1.2 Electrons and positrons

Light particles, i.e., electrons and positrons, suffer energy loss as a result of two main processes: ionization and bremsstrahlung. However, at low energies, other mechanisms also play an important role such as positron annihilation and Moller and Bhabha scattering (Figure 2.4). The stopping power for electrons and positrons is slightly different, and both differ from heavy particles. Small mass, indistinguishability and deflection must be taken into account. Bremsstrahlung probability is inversely proportional to the squared mass of the particle, hence its importance for light particles. It is produced by the deceleration of the electron or positron, resulting in the emission of a real photon, when deflected in the Coulomb field of atoms. At energies of few MeV, bremsstrahlung is relatively small but, above a certain energy, called critical energy, it dominates completely. Regarding muons and pions, it becomes important at a few hundreds of GeV.

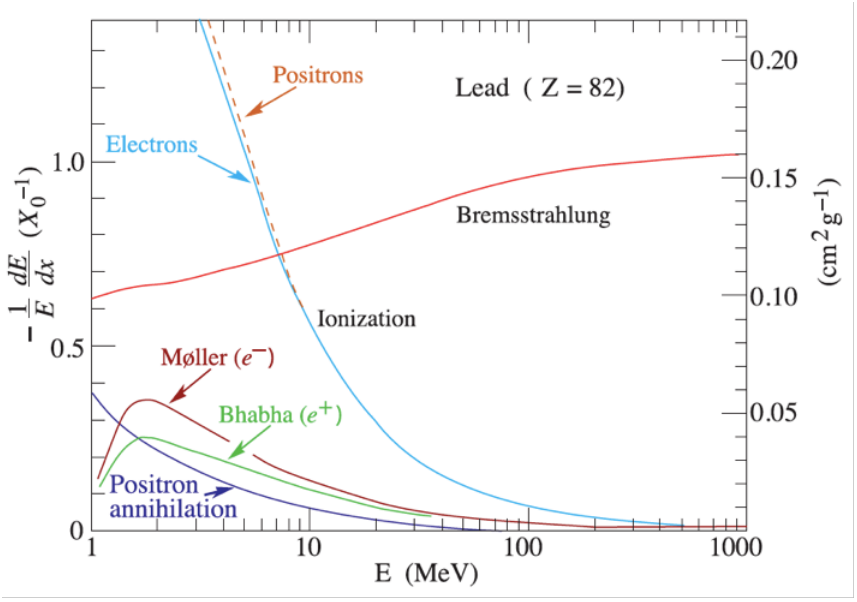

Figure 2.4: Contribution of the different processes to the fractional energy loss per radiation length as a function of the electron or positron energy. (Reprinted with permission from [58]. Copyright by the American Physical Society.)

The introduction of a new variable that characterizes the mean energy loss due to bremsstrahlung is needed. Considering the high-energy limit, where the radiative loss dominates and the screening effect is complete (Coulomb field of the nucleus screened by the electron cloud), the stopping power can be written as follows:

$$-\frac{dE}{dx} \approx \frac{E}{X_0} \rightarrow E(x) = E_0 \exp\left(-\frac{x}{X_0}\right), \quad (2.6)$$

where X_0 is the radiation length usually measured in $g\ cm^{-2}$. In such a way, the radiation length is the distance x an electron or a positron traverse losing all but 1/e of its initial energy E_0 by bremstrahlung. It can be approximated by:

$$\frac{1}{X_0} \approx \left(4Z(Z+1)\frac{\rho N_A}{A}\right) r_e^2 \alpha \left[\ln\left(183\ Z^{-1/3}\right) - f(Z)\right], \quad (2.7)$$

where Z and A are the atomic and mass numbers, N_A is Avogadro's number, r_e is classical electron radius and $\alpha = 1/137$ is the fine structure constant.

An useful approximation of the mass thickness as a function of the density (ρ) multiplied by the thickness leads to:

$$X_0 = \frac{A}{Z(Z+1)\ln(287/Z^{-1/2})} \times 716.4\ (g\ cm^{-2})\,. \quad (2.8)$$

Thus, radiation energy loss can be expressed in terms of the radiation length making it independent of the material. For chemical compounds and mixed materials, the radiation length can be calculated using the element mass fraction F_i and radiation length $X_{0,j}$:

$$\frac{1}{X_0} = \sum_j \frac{F_i}{X_{0,j}}\,. \quad (2.9)$$

USC UNIVERSIDADE DE SANTIAGO DE COMPOSTELA

2.1.2 Interaction of neutral particles with matter

Neutral particles such as photons and neutrons cannot interact through Coulomb forces within the detector's material, so they do it indirectly. They may release a charged particle that loses energy due to electromagnetic interactions.

2.1.2.1 Photons

The interaction of photons with matter may create or not secondary particles. The most important mechanisms of photon interaction with matter are the photoelectric effect, Compton and Rayleigh scatterings and pair production.

The photoelectric effect is the dominant process for low-energy photons in the keV range. A photon interacts with an atomic electron, transferring all its energy. As a consequence, one or more atomic electrons can escape the nucleus influence, whereas the photon is absorbed. In addition, lower energy photons, or fluorescence photons, might be emitted by the de-exciting atoms.

Compton and Rayleigh scatterings dominate at intermediate energies. In Compton scattering, an incident photon interacts with a free electron. If the energy of the photon is higher than the atomic binding energy, electrons are treated as free. The interaction can scatter an electron away in concurrence with a new and less energetic photon. In Rayleigh scattering, the interaction is with the atom, and the incident photon can be deflected. This is a coherent process, and the target atom is neither excited nor ionized.

Pair production is the most important process at high energies. To produce an electron-positron pair the energy of the photon must be at least 1.02 MeV, the energy equivalent to the rest mass of two electrons. The radiation length is also defined as a $\sim 7/9$ of the mean free path for pair production for photons [59].

2.1.2.2 Neutrons

Neutrons are highly penetrating particles that interact weakly with matter. They only deviate from their trajectory due to collisions with a nucleus. There are two major types of interaction: scattering and absorption.

USC UNIVERSIDADE DE SANTIAGO DE COMPOSTELA

Scattering can be elastic or inelastic depending on whether energy is transmitted or not between the neutron and the nucleus. The nucleus will have some recoil velocity. In the case of inelastic scattering, it may reach an excited level that leads to photon emission. A neutron loses energy due to scattering until a nucleus absorbs it.

Absorption involves the capture of the neutron by a target nucleus. This can lead to the emission of a wide range of radiations or induce fission. The target nucleus absorbs the neutron and emits a charged particle or a neutron. If the nucleus is left in an excited state, photon emission might occur [60].

2.2 Operation principle of gas detectors

Gaseous detectors are used to measure ionizing radiation. Electrons and ions move more freely in gas than in liquid or solid. Therefore, the space between electrodes is filled with gas. The operation principle is the collection of the ionization electrons and ions produced by radiation going through the detector. The distribution of electron-ion pairs follows a Poisson distribution with sigma equal to the square root of the number of pairs produced. Usually, the collection is done after some amplification. In absence of an electric field, the diffusion of pairs due to random thermal movement leads to collisions with gas molecules. Therefore, electrons and ions are not accelerated to the electrodes, and recombination may occur. To avoid that, a voltage is applied to the electrodes. The potential difference creates an electric field between them, and electrons and ions drift to the electrodes, resulting in an induced current that can be registered by an acquisition equipment. Electrons drift toward the anode and ions to the cathode, where they are collected. If they gain enough energy during the acceleration, they can produce secondary ionizations in the gas. The number of electron-ion pairs produced by constant incident radiation varies with the applied voltage, and the number of secondary ionizations is related to the mean free path and the energy transferred from the external field. Depending on the gas type, pressure, and geometry of the detector, a wide range of voltages can be applied. Gain is defined as the ratio between secondary and initial ionizations for a detector under specific conditions [61].

USC
UNIVERSIDADE DE SANTIAGO DE COMPOSTELA

2.2.1 Working regimes

Based on the applied electric field, there are different working regimes for a detector. Figure 2.5 shows the most important operating regions known as recombination, ionization, proportional, limited proportional, Geiger-Müller, and continuous discharge [62].

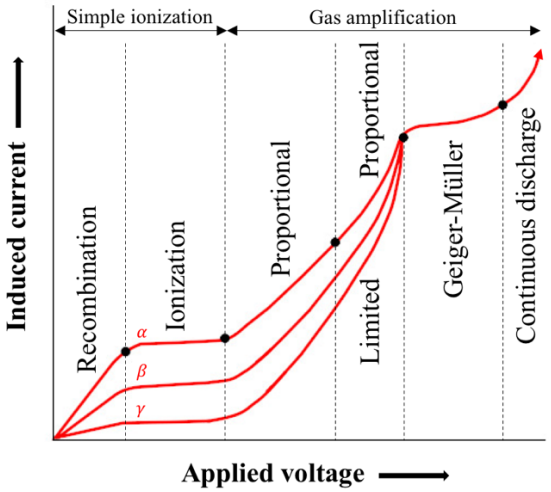

Figure 2.5: Total charge collected as a function of the applied electric field for different radiation.

At zero voltage, there is no charge collection due to the recombination of electron-ion pairs. The pulse size increases with increasing voltage, while the number of pairs that are lost due to recombination decreases to the point it becomes zero. The range from zero to this point is the recombination region.

Next is the ionization region, in which all pairs are collected. Thereby, a saturation zone is reached, and the charge collected does not change when increasing the electric field strength. This is the operating region of ion chambers. It is worth mentioning that the applied voltage is not enough to start an avalanche.

A further increase of field strength increments again the induced current, and the proportional region is entered. In this working regime, the field is high enough to accelerate electrons that produce secondary

ionizations in the gas. The avalanche or multiplication is proportional to the initial energy deposited.

The limit of the proportional region marks the start of the limited proportional region. Nonlinearities appear as a consequence of the growing voltage. Electrons drift faster than ions. So that, if the concentration of ions is high enough, it leads to electric field distortion about the anode.

Increasing the electric field even higher makes possible the appearance of discharge in the gas. Discharge refers to a chain of many secondary avalanches. To stop this effect a quenching gas must be present. This is the Geiger-Müller region which is characterized by a plateau and gives no direct information about the type and energy of the radiation.

Finally, the continuous discharge region must be avoided to prevent damage inside the detector.

The working regime determines the kind of measurements that can be performed with a detector. The transport of electron-ion pairs has already been summarized throughout this section. According to the type of detectors on which this work is based, it is necessary to study the physics of the avalanche in more detail.

2.2.2 Avalanche multiplication

Gas amplification occurs when the electrons resulting from the primary interaction gain sufficient energy to produce new ionizations in the gas. Secondary electrons moving toward the anode can also cause more ionizations and so on. The result is an avalanche that can continue growing until all electrons are collected [63, 64]. The probability per unit track length of a secondary ionization to happen is determined by the inverse of the ionization mean free path of electrons. This parameter is better known as the first Townsend coefficient (α), which depends on the electric field and the gas density [65]. In the simplest case of a uniform electric field in parallel plate geometry, one electron-ion pair is produced after $1/\alpha$. If there are n primary electrons, after a path ds there will be:

$$dn = n \alpha ds . \tag{2.10}$$

USC UNIVERSIDADE DE SANTIAGO DE COMPOSTELA

The total number of new electrons (n) integrated over a path (s) can be described mathematically by the following equation:

$$\mathrm{n(s)} = \mathrm{n_0}\ \exp\left(\alpha \mathrm{s}\right), \tag{2.11}$$

where n_0 is the original number of electrons. The gain or multiplication factor is the ratio between the total number of electrons and the initial number ($G = n/n_0$).

Nevertheless, an electron not only has a probability of being multiplied. There is also a probability of attachment by gas molecules. Normally, these molecules are present as impurities or contamination due to air, water, etc. Neglecting the contribution of the diffusion due to high electric fields, the gain equation can be written as follows [66]:

$$\mathrm{G} = \exp\left(\int_{\mathrm{s_1}}^{\mathrm{s_2}} \left(\alpha(\mathrm{s}) - \eta(\mathrm{s})\right) \mathrm{ds}\right), \tag{2.12}$$

where η is the attachment coefficient. In general, both α and η depend on the reduced electric field. These coefficients are constant in uniform electric fields. However, they are influenced by the electric field distortion caused by large avalanches. This is an important effect in resistive plate chambers (RPCs) and is called the space charge effect [67]. In addition, gas density, geometrical imperfections, and edge effects also alter the multiplication.

Besides ionization, excitation occurs, and so does photon emission. Ultraviolet photons that ionize gas molecules outside the radius of the electron avalanche generate delayed avalanches. The absorption of these photons requires a quenching gas that drains their energy.

A streamer may appear at high gain ($\sim 10^8$ electron-ion pairs), whose main characteristic is a fast increase of the charge. Its formation process is complex. The photons emitted in the avalanche create secondary electrons by photo-ionization of the gas molecules, which produce secondary avalanches that lead to charges moving forward and backward, originating a streamer. They may evolve to a spark if they are not damped [68].

USC UNIVERSIDADE DE SANTIAGO DE COMPOSTELA

2.3 RESISTIVE PLATE CHAMBERS

The first detector of this kind was developed in 1981 [69]. RPCs are one of the most used detectors in high-energy physics. They are used as trigger detectors and also for time-of-flight measurements [70–72]. A large detection area can be covered due to their relatively low cost per information channel. RPCs belong to the family of gaseous ionizing detectors, whose operation principle has already been described thus far.

An RPC consists of two parallel resistive plates separated by a gas volume (gas gap) of a few millimeters. The number of gas gaps may vary depending on the purpose of the detector. Increasing the number of gaps improves the efficiency and the time resolution. The thickness of the gap, and so the uniformity of the electric field, are preserved with the placement of a grid of spacers made of polycarbonate. Generally, the main used gas is tetra-fluorethane ($C_2H_2F_4$), commercially known as Freon R134-a, mixed with other gases (quenchers) to control the avalanche process [73]. A high voltage (HV) is applied to the electrodes, giving rise to a uniform electric field inside the gas gaps. At least one must be coated with a high-resistivity material to prevent sparks and discharges, limiting the available charge that can be evacuated instantaneously (Figure 2.6).

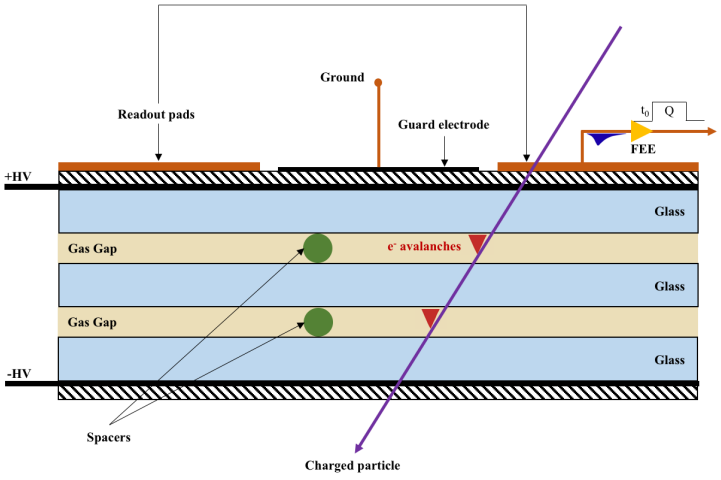

Figure 2.6: Schematic representation of the internal structure of an RPC made with three gaps, showing glass, spacers and read-out electrodes.

USC UNIVERSIDADE DE SANTIAGO DE COMPOSTELA

The charge collected on a resistive electrode Q_0 dissipates with time t:

$$Q(t) = Q_0 \exp\left(-\frac{t}{\tau}\right), \tag{2.13}$$

where τ is the relaxation time and depends on the properties of the resistive material such as resistivity (ρ), dielectric constant (ϵ_0), and relative permittivity (ϵ_r) [74]. It can be calculated as follows:

$$\tau = \rho\, \epsilon_0\, \epsilon_r\,. \tag{2.14}$$

Typical glass resistive plates of $10^{10}\ \Omega\,\text{cm}$ (bakelite) lead to a relaxation time (dead time) of about 10 ms. This is the time a local region of the electrode needs to recover from an avalanche or streamer. During this time, only that zone is blind to incoming particles while the remaining is still sensitive. As a result, if the rate of the incoming radiation is high compared to this time, the time resolution and the efficiency of the detector are both affected.

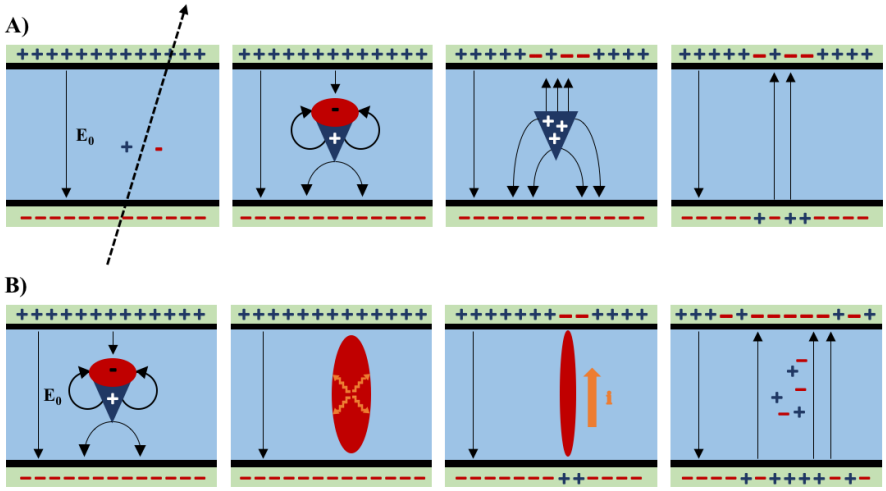

Figure 2.7: Development of two RPC processes and electric field distortions at high gain. A) Avalanche. B) Streamer.

Figure 2.7.A describes the avalanche formation inside an RPC. A charged particle ionizes the gas starting an avalanche. The electric field in the gas gap is influenced by the field originated by large avalanches. Electrons drift faster than ions. Finally, the charges collected in the resistive layers only modify the electric field in a small area. Figure 2.7.B shows the development from avalanche to streamer. Photons emitted in the avalanche might cause more ionizations and a fast spread of the charges. A streamer evolves, which might create a weak spark. Finally, the electric field in the resistive layers is strongly affected, and the detector has a blind zone until it recovers after the relaxation time.
The movement of charges inside the detector induces a current signal on the read-out electrodes. The induced signal is given by Ramo theorem [74, 75]:

$$\mathrm{i(t)} = \overrightarrow{\mathrm{E_w}}\big(\vec{\mathrm{x}}(\mathrm{t})\big) \cdot \vec{\mathrm{v}}_\mathrm{D}(\mathrm{t}) \cdot \mathrm{e}_0 \cdot \mathrm{N(t)}\,, \tag{2.15}$$

where $\overrightarrow{E_w}$ is the electrostatic weighting field (electric field at the position $\vec{x}(t)$ when an electrode is put to 1 V and the others to ground), $\vec{v}_D(t)$ is the drift velocity of a cluster of $N(t)$ charge carriers and e_0 the electron charge. For multiple clusters, the induced signal is the sum of each contribution. The induced charge is the integral of the induced current during the signal time.
Two modes of operation are possible in RPCs: avalanche or streamer. The first one is characterized by a lower charge and the need for an amplifier in the readout electronics to measure the signal. The latter occurs at very high electric fields (discharge mode), and the readout is more simple than in avalanche mode. Since the induced signal is strong enough for this mode, it implies that no amplification is needed.
The efficiency ϵ of the detector increases with the number of gaps *n as* follows:

$$\epsilon = 1 - (1 - \epsilon_\mathrm{n})^\mathrm{n}\,, \tag{2.16}$$

where ϵ_n is the efficiency of a single gap [76].

USC
UNIVERSIDADE DE SANTIAGO DE COMPOSTELA

Nowadays, RPCs are generally used in avalanche mode with multiple gas gaps that increase the signal on the read-out. This signal is the sum of the individual signals produced within each gap. Their good time resolution ($\sim$ 100 ps), together with good efficiency ($\sim$ 99%), make them suitable for particle identification through time-of-flight measurements.

USC
UNIVERSIDADE
DE SANTIAGO
DE COMPOSTELA

USC
UNIVERSIDADE
DE SANTIAGO
DE COMPOSTELA

3 TRASGO DETECTORS

A new generation of CR detectors, based on the latest technologies used in high-energy physics experiments, is presented in this thesis. The main characteristic of this new family of detectors is the use of RPCs as the main detection technology. RPCs offer a broad choice of designs with either sub-millimetric position sensitivity or time precision below 100 ps.

3.1 THE TRASGO PROJECT

TRASGO is the acronym of TRAck reconStructinG bOx, a new family of CR detectors intended for the observation of EAS. The development of these detectors was motivated by the analysis of the CR data taken during the commissioning of the RPC-TOF (time of flight) wall of HADES (High Acceptance DiElectron Spectrometer) at GSI (Gesellschaft für SchwerIonenforschung) Helmholtzzentrum in Germany [77–79]. TRASGOs are based on RPCs for timing purposes (t-RPC), a technology that offers an excellent compromise between performance and cost. Their main features are a good time resolution of about hundreds of ps, high granularity and position sensitivity. These properties enable excellent tracking and particle identification capabilities, which makes a TRASGO a good detector to perform studies of the CR properties. It can access CR information beyond the capacities of other detectors. The tracking capability makes possible to detect and reconstruct the arrival direction of clusters or bundles of particles. This family of detectors is sensitive to the charged particles produced in an EAS that can reach the observation point. The study of the number of particles detected per event or multiplicity, the direction, and the time profile may allow one to estimation the energy of the primary CR that caused the EAS. In general, RPCs used by TRASGOs are multi-gap, filled with

USC UNIVERSIDADE DE SANTIAGO DE COMPOSTELA

Freon R134-a. Even though this kind of detector is built to work as a stand-alone device, it can be arranged in sets covering large areas or pilling up on top of each other to improve the performance of the whole system (Figure 3.1).

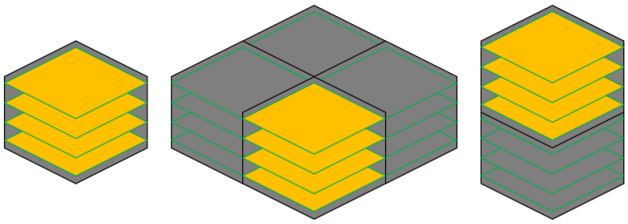

Figure 3.1: TRASGO with four RPC planes and some possible configurations.

3.2 DETECTORS

Nowadays, four TRASGOs are either operative or under development, and they have three different designs. The most important concept of the project is that all tools created can be used regardless of the design. The RPC structure and layout of the four detectors will be explained throughout this chapter. This thesis is based on the first two, thus, the remaining components will be described, in detail, in the next chapter. Figure 3.2 shows the current location of all TRASGO detectors.

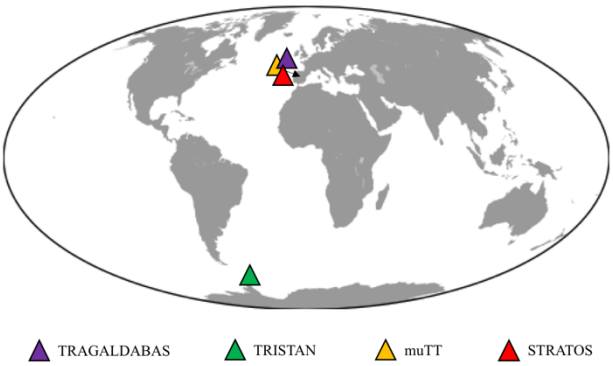

Figure 3.2: TRASGO detectors around the world.

3.2.1 TRAGALDABAS

The first TRASGO to be constructed has been TRAGALDABAS (TRAsGo for the AnaLysis of the nuclear matter Decay, the Atmosphere, the earth B-field And the Solar activity) [80, 81]. The detector is located at the Faculty of Physics of the University of Santiago de Compostela (USC), Spain (42º52'34" N, 8º33'37" W) since 2015. A very close to it weather station operated by MeteoGalicia provides the atmospheric data such as pressure, temperature and relative humidity, needed for the data corrections (Figure 3.3) [82].

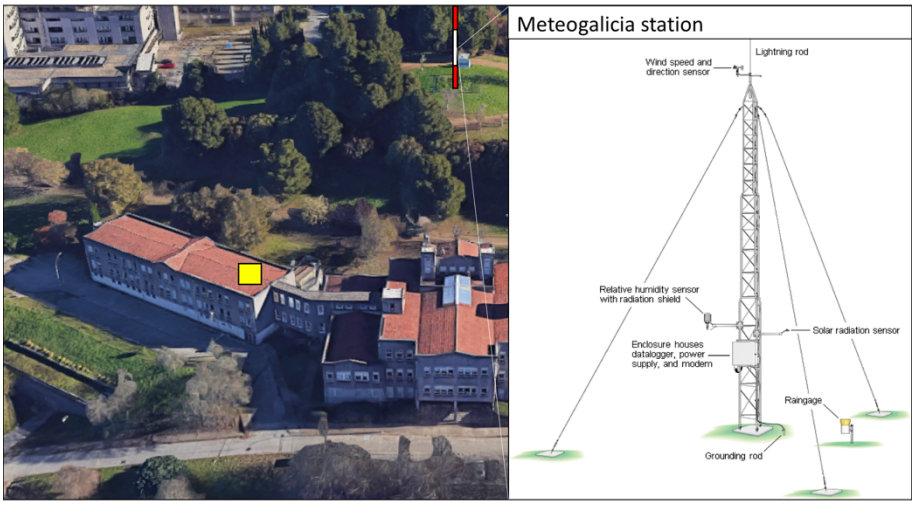

Figure 3.3: Left) TRAGALDABAS location in the Faculty of Physics of the USC (yellow box). Right) scheme of the weather station.

The detector has four active RPC planes and one layer of lead of 0.56 cm thickness or one radiation length, between the third and fourth (counting from top to bottom). These RPCs are based on the design developed by the Laboratório de Instrumentação e Física Experimental de Partículas (LIP) of Coimbra, in Portugal, for the MARTA (Muon Array with RPCs for Tagging Air showers) extension of Pierre Auger Observatory [83, 84]. Each plane has an active size of 150×120 cm^2 and is encapsulated by an aluminium box. An example of the internal layout of the RPCs was given in Section 2.3. These RPCs have two gas

USC UNIVERSIDADE DE SANTIAGO DE COMPOSTELA

gaps of 1 mm width filled with Freon R134-a and operate at a gas flow of ~ 8 cc min^{-1}. Three slides of glass of 2 mm thickness of high resistivity separate the gas gaps. The electric field inside the gas gaps is created by applying HV to the conductive coating of the external glass plates (~ 5.6 kV). Table 3.1 shows the different materials that compose each detection plane and the values of their radiation length. The foam is added for better isolation of the plane.

Table 3.1: Internal structure of the TRAGALDABAS RPCs.

RPC layer	X_0 / cm	z-thickness / mm
Aluminium	8.9	3.0
Polyethylene Foam	167.7	8.7
Copper	1.4	0.03
FR4 Printed circuit board (PCB)	15.9	1.57
Polymethylmethacrylate	34.1	1.0
Glass	9.5	1.9
Gas (Freon R134-a)	946.4	1.0
Glass	9.5	1.9
Gas (Freon R134-a)	946.4	1.0
Glass	9.5	1.9
Polymethylmethacrylate	34.1	1.0
Aluminium	8.9	3.0
Sum	-	26

The read-out is performed by 120 rectangular copper pads per plane, with a size of 116×111 mm^2 at a distance of 10 mm. Between pads, a guard electrode of 6 mm width has been added to prevent the cross-talk, which is almost negligible (Figure 3.4).

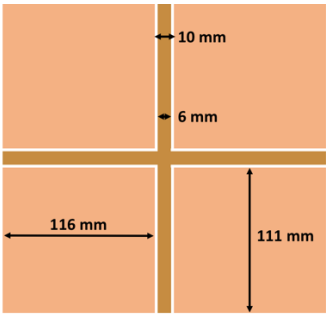

Figure 3.4: Sizes of TRAGALDABAS read-out pads and guard electrodes.

USC UNIVERSIDADE DE SANTIAGO DE COMPOSTELA

TRAGALDABAS is installed on the first of a two-floor building (~ 260 m a.s.l.) that partially rejects the low-energy particles of the electromagnetic component of the EAS. Additionally, electrons and gammas interacting with the walls of the building may produce low-energy secondary particles, whose contribution is hard to estimate. The detector is taking data at a constant rate of approximately 7–9 million events per day (~ 90 Hz) depending on the planes that are in the trigger. The acquisition trigger is done by a coincidence between two planes. Figure 3.5 shows the current layout of TRAGALDABAS and the effects of the walls on the incoming secondary particles.

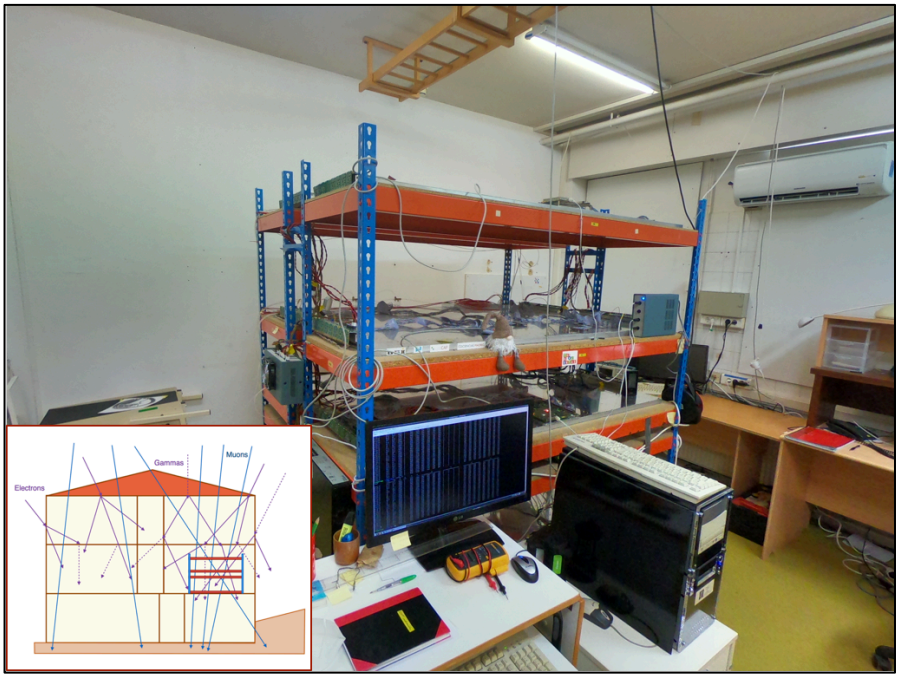

Figure 3.5: TRAGALDABAS in the current layout and the effects of the building.

As it was the first detector, it has been used to elaborate on some tools that future detectors of the TRASGO family might need. For instance, the ones used for calibration, monitoring or visualization, tracking, reconstruction, and particle identification, have been tested as part of the work done in this thesis.

USC UNIVERSIDADE DE SANTIAGO DE COMPOSTELA

3.2.2 TRISTAN

TRISTAN (TRasgo para InveSTigaciones ANtárticas), as its name states, is a detector intended for studying CRs in Antarctica [85, 86]. The principal objective is to improve the understanding of secondary CRs in a wide range of energies and study the correlation of their flux with different phenomena related to Earth's environment. Before being installed in Antarctica, the detector performed several latitudinal surveys onboard the Spanish oceanographic vessels Sarmiento de Gamboa and Buque de Investigación Oceanográfica (BIO) Hespérides (Figure 3.6) [87]. Onboard the Sarmiento de Gamboa, the detector performed, in late 2018 and early 2019, a two-way latitudinal CR survey from Vigo, Spain, (42º14'13" N, 8º43'59" W) to Punta Arenas, Chile, (53º09'17" S, 70º54'41" W). The last journey, on board of the BIO Hespérides, was performed in late 2019 from Cartagena, Spain, (37º36'00" N, 0º59'00" W) to Punta Arenas. Then, the data acquisition continued until the final destination, the Base Antártica Española-Juan Carlos I (BAE-JCI) (62º39'46" N, 60º23'20" W), where TRISTAN was finally installed. Between the second and the last latitudinal survey, the detector operated at the Faculty of Physics of the USC, located on the ground floor of the building, below TRAGALDABAS.

Figure 3.6: TRISTAN left) onboard of BIO Hesperides, right) in the BAE-JCI.

This thesis is based, essentially, on the tools created and tested for the data monitoring, calibration, reconstruction, and analysis of this detector. The RPCs were built in Coimbra with the expertise of the mechanical workshop of the LIP of Coimbra, including the HV power supplies and the gas system [83]. As the design of the RPCs is very

similar to the ones used for TRAGALDABAS, they share the internal layout, which can be found in Table 3.1 but uses polycarbonate instead of methacrylate. The electronics, provided by Hidronav Technologies, is described in detail in the next chapter together with the remaining components [88].

TRISTAN consists of three RPCs and one layer of lead of one radiation length enabling a better muon-electron separation. The lead covers the central area (40% of the total active area) and is placed between the second and third planes (counting from top to bottom). Each RPC plane has an active size of $150 \times 120\ \mathrm{cm}^2$, operating at a gas flow rate of $\sim 11\ \mathrm{cc\ min}^{-1}$. The HV ($\sim 5.9$ kV) applied to the conductive coating covering the external glass plates creates the uniform electric field inside the gas gaps. The read-out is done by 30 rectangular copper pads per plane, with a size of $242 \times 232\ \mathrm{mm}^2$, with each pair separated by a guard electrode of 6 mm width. The distance between pairs of pads is 10 mm, and the addition of the guard electrodes is to prevent the cross-talk between the read-out pads (Figure 3.7).

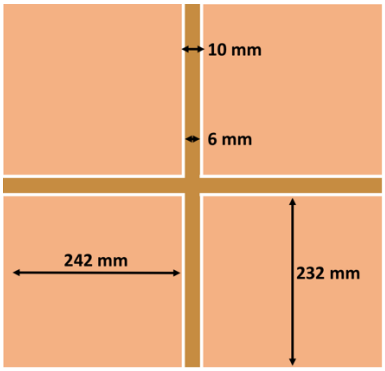

Figure 3.7: Size of TRISTAN read-out pads and guard electrodes.

The data acquisition registers a rate of about 11–13 million events per day ($\sim$ 130–160 Hz), depending on the cutoff rigidity of its location. The trigger scheme is based on coincidences between the first and third planes (counting from top to bottom). Figure 3.8 shows TRISTAN in the current layout in Antarctica.

USC
UNIVERSIDADE DE SANTIAGO DE COMPOSTELA

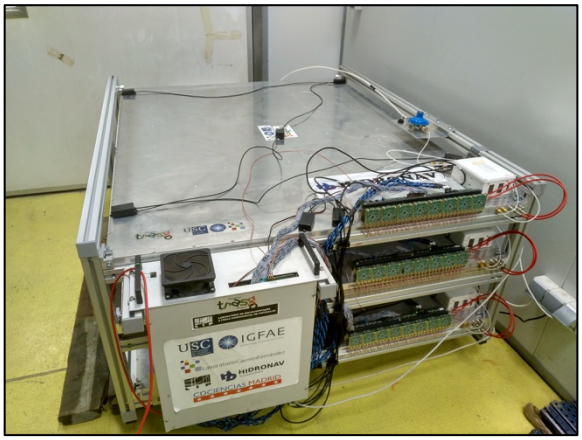

Figure 3.8: TRISTAN in the current layout, installed in the BAE-JCI.

This detector was conceived as a part of the Observatorio de Rayos Cósmicos Antártico (ORCA) set up in BAE-JCI in late 2018. ORCA is made up of a set of detectors with different properties that measure the flux of secondary CRs at ground level. Two blocks shape the whole observatory. On the one hand, TRISTAN, whose targets are all charged particles. On the other, NEMO (NEutron MOnitor) and MITO (Muon Impact-Tracer Observer), installed inside a 20 feet container thermally isolated (Figure 3.9) [89].

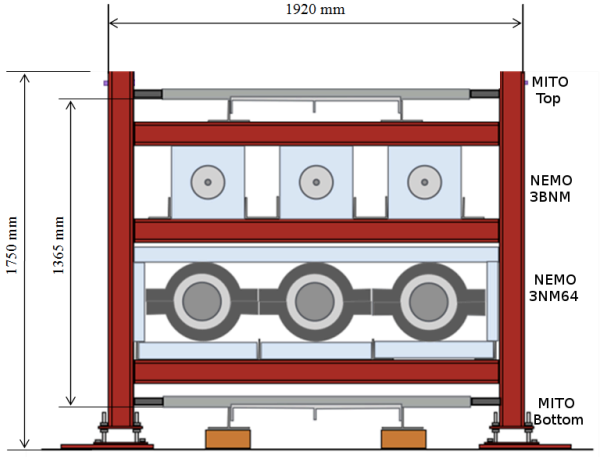

Figure 3.9: NEMO and MITO detectors.
(Used with permission from [120], Creative Commons CC-BY-NC-ND 4.0.)

3.2.3 muTT

MacroScanner project is a CR tomography project for security applications, and muTT is the prototype. Muon tomography can be exploited to effectively detect hidden and suspicious materials, especially those of high atomic numbers, in containers, vehicles, etc. The target is driven through the scanning device, formed by two groups of detectors: upper and lower (Figure 3.10). Both are used to reconstruct the trajectory of the incident muons. The lower detectors can detect a change in muons trajectory. The angular changes of the tracks depend on the material that muons traverse, being larger for denser materials.

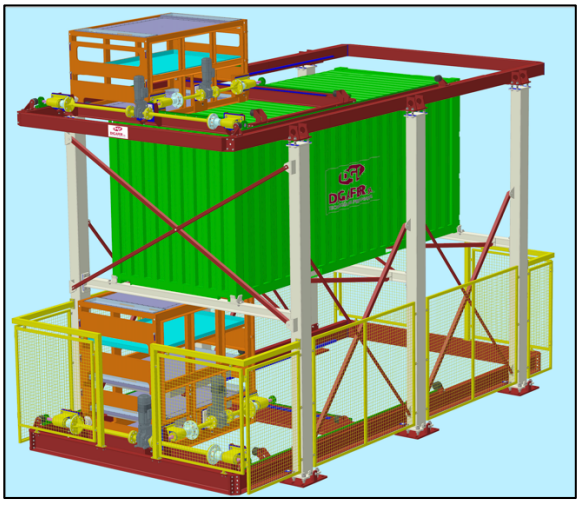

Figure 3.10: MacroScanner scheme.

muTT was mounted and tested in O Porriño, Spain, achieving the identification of materials with high atomic numbers. The detector has four RPC detection planes with an effective area of 150×120 cm^2. The RPCs were built by the LIP of Coimbra, and the electronics was provided by Hidronav Technologies [83, 88]. The main features are a high angular resolution (~ 1 degree), and sub-nanosecond time resolution (~ 100 ps) [90]. Table 3.2 shows the layers of each RPC, the materials, and their radiation length.

USC
UNIVERSIDADE DE SANTIAGO DE COMPOSTELA

Table 3.2: Internal structure of the muTT RPCs.

RPC layer	X_0 / cm	z-thickness / mm
Aluminium	8.9	3.0
Polyethylene Foam	167.7	3,1
PCB (FR4)	15.9	1.5
Copper	1.4	0.03
Polycarbonate	34.6	1.0
Glass	9.5	1.0
Gas (Freon R134-a)	946.4	0.3
Glass	9.5	1.0
Gas (Freon R134-a)	946.4	0.3
Glass	9.5	1.0
Gas (Freon R134-a)	946.4	0.3
Glass	9.5	1.0
Gas (Freon R134-a)	946.4	0.3
Glass	9.5	1.0
Gas (Freon R134-a)	946.4	0.3
Glass	9.5	1.0
Gas (Freon R134-a)	946.4	0.3
Glass	9.5	1.0
Polycarbonate	34.6	1.0
Copper	1.4	0.03
PCB (FR4)	15.9	1.5
Copper	1.4	0.03
Aluminium	8.9	3.0
Aluminium base	8.9	3.0
Sum	-	26

The need for a very good spatial and temporal resolution required a different configuration of the RPCs. In contrast to the aforementioned detectors, muTT replaces the rectangular read-out pads with read-out strips and the double-gap by multi-gap. Two layers of strips per plane, one up with 20 strips and one down with 25 strips, are placed perpendicularly to each other. The induced signal is collected by two layers of copper electrodes: top and bottom.

3.2.4 STRATOS

Continuous monitoring of the temperature changes in the stratosphere using a CR detector at ground level may lead to a new tool for a medium-long term weather forecast. For that purpose, Hidronav Technologies designed a new set of detectors as part of the STRATOS project. Two stations are being tested, one located in O Porriño, Spain, and the other in Coimbra, Portugal (Figure 3.11).

Figure 3.11: STRATOS-2 during the commissioning in Coimbra, Portugal.

The CR stations of STRATOS consist of four RPCs built by the LIP of Coimbra, and the electronics was provided by Hidronav Technologies [83, 88]. The RPCs have been designed to optimize the identification capability of clusters of particles. They offer a very good angular and temporal resolution of ~ 1 degree and ~ 300 ps, respectively, due to the high granularity (64 read-out strips). The external design of the detection planes is different from any other TRASGO detector as the pre-amplifying, acquisition electronics and power supplies are enclosed in a single Faraday cage. In addition, the gas consumption is lower (~ 5 cc min^{-1}) than for the other detectors because

USC UNIVERSIDADE DE SANTIAGO DE COMPOSTELA

of the low permeability of the tight box that encapsulates the RPCs. Table 3.3 shows the RPC structure of STRATOS stations, which have an active size of 150×120 cm^2.

Table 3.3: Internal structure of the STRATOS RPCs.

RPC layer	X_0 / cm	z-thickness / mm
Aluminium	8.9	2.0
Polystyrene	167.7	80.0
Aluminium	8.9	1.0
Polypropylene	49.5	1.0
Glass	9.5	1.9
Gas (Freon R134-a)	946.4	1.0
Glass	9.5	1.9
Polypropylene	49.5	1.0
Copper	1.4	0.018
Polyimide	28.6	0.085
Polypropylene	49.5	1.0
Glass	9.5	1.9
Gas (Freon R134-a)	946.4	1.0
Glass	9.5	1.9
Polypropylene	49.5	1.0
Aluminium	8.9	2.0
Sum	-	98.7

The detectors will be installed near the airport of Vigo, Spain, to perform measurements of the directional CR flux at the Earth's surface, and to study the correlation between clusters of secondary CRs and the temperature of the stratosphere. CR data will be correlated directly to the weather information given by balloon radiosondes.

USC
UNIVERSIDADE
DE SANTIAGO
DE COMPOSTELA

USC
UNIVERSIDADE
DE SANTIAGO
DE COMPOSTELA

4 ELECTRONIC SYSTEMS

High-energy physics detectors require the interconnection of many advanced electronic systems, all working together within the same system. From recording to processing, the correct operation of all systems is fundamental. The principal devices present on TRISTAN and TRAGALDABAS detectors are described throughout this chapter.

4.1 INTRODUCTION TO THE COMPONENTS

The instrumentation of TRISTAN and TRAGALDABAS detectors requires the interconnection of multiple electronic systems. These systems cover all the needs of a detector such as the reading, processing, and signal transport, the start of the acquisition of the events based on specific trigger conditions, the supply of electrical power, and the recording of the environmental and gas information. The reading of the induced signal, produced by the propagation of the charges to the electrodes, is done on the read-out copper pads (pick-up electrodes). These pads can read the distorted induction signals due to avalanches from a neighbor pad, an effect that is known as cross-talk. A guard electrode/strip is added between pads to avoid or minimize this effect. The quality of the signal is fundamental for achieving a good timing performance and depends on the properties of the RPCs and the electronic systems. All signals from the pick-up electrodes are sent to the RPC electronics chain, and only the data corresponding to valid events is sent via Ethernet to storage. All electronic systems and their functionalities will be described, in detail, in the following sections.

USC
UNIVERSIDADE DE SANTIAGO DE COMPOSTELA

4.2 FRONT-END ELECTRONICS

The front-end electronics (FEE) is one of the systems that determine the final time resolution, which is given by the quadratic sum of the electronics and RPC intrinsic resolutions. FEE is made up of two boards that are responsible for signal amplification, digitalization and transport. These boards are known as Daughterboard (DBO) and Motherboard (MBO), and have been designed for HADES [91, 92].

4.2.1 DBO

DBOs carry out the first stages of signal processing, amplification and digitalization. Each pad reads a signal and sends it to one of the input channels of a DBO (4 channels per DBO that can read up to 4 pads). Signals' rise-time is of nanosecond thus, the amplifying electronics requires a bandwidth up to 1–2 GHz. DBOs feed a dual discriminator with a constant threshold and an amplifier that performs charge measurements. The first produces the rising edge when the signal is over a certain threshold, through a leading-edge comparator with Low Voltage Differential Signaling (LVDS) output. The second gives the trailing edge of the pulse, shaped by an integrator and another comparator. The charge is measured by a time over threshold (ToT) algorithm in which the signal width is proportional to the deposited energy [93]. Figure 4.1 shows a diagram of the process.

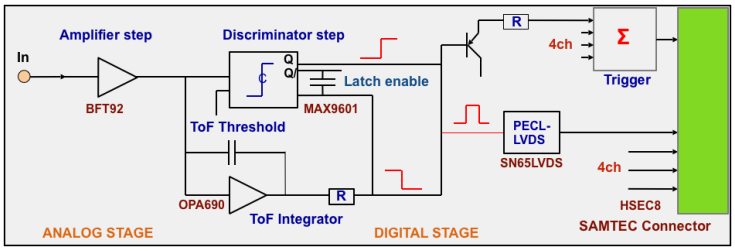

Figure 4.1: DBO logic diagram.

The information about the arrival time of the RPC signal is provided by the leading edge or start of the LVDS digital pulse. The charge is given by its width. The DBOs are connected to the RPC pads through a short MMCX cable at the bottom of the board (Figure 4.2).

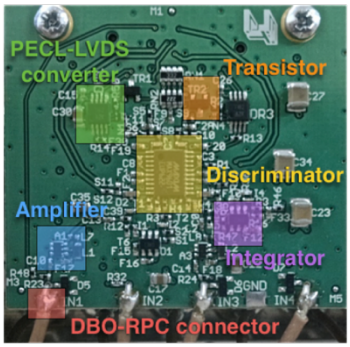

Figure 4.2: Main components of a DBO (6 cm × 5.5 cm).

4.2.2 MBO

MBOs connect the DBOs to the acquisition board. Each MBO is a 32-channel board and has room for 8 DBOs. Nevertheless, only 31 are available for TOF and ToT measurements, and the remaining one is used for synchronization purposes. The MBO is multitasking and provides different services such as signal transport from the DBOs to the acquisition system, low-level trigger signal generation, threshold voltages setting, test signals distribution to the DBOs, and generation of the low ripple/noise voltages that DBOs need.

Figure 4.3 shows the 8 blocks for the DBOs, the DBO-MBO connectors, the test signal distribution, trigger logic, power supply regulators, and the connection with the acquisition system.

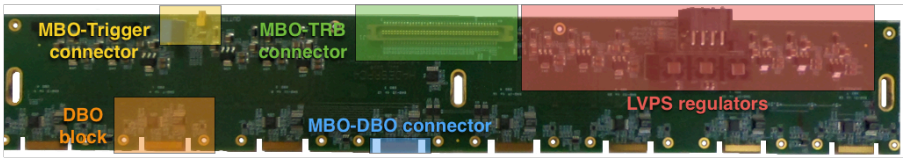

Figure 4.3: Connectors in an MBO (40 cm × 6 cm).

The low-level trigger signal is a combination of all DBO channels. It gives information about the number of cells fired (multiplicity) to the acquisition.

The threshold voltages are set via digital-to-analog converters (DACs) by the read-out boards explained in Section 4.3.1.

USC
UNIVERSIDADE
DE SANTIAGO
DE COMPOSTELA

4.3 DATA ACQUISITION SYSTEM

The data acquisition system (DAQ) and the FEE are the most important electronic systems. They determine the final time resolution of the detector, being the intrinsic resolution the limiting factor. The DAQ is based on the time-to-digital converter board (TDC read-out board), better known as TRB [95]. The signal from the FEE is transmitted to the TRB, where each MBO is connected via a flat cable. The acquisition starts after an external trigger signal is registered. The trigger is based on coincidences between planes within a certain time window. After a valid trigger, the TRB collects the data of the fired channels and applies several algorithms to decide whether an event is stored or not. Events that pass the filters are moved to external massive storage for offline analysis.

4.3.1 TRB

The TRB has been developed at GSI for the HADES experiment. The design and main features have been improved with the release of the different versions. Until now, there are three versions, but only the last two are installed in the two detectors of the TRASGO project described throughout this chapter. The schematic of the TRB versions 2 and 3, which are explained in this section, is displayed in Figure 4.4.

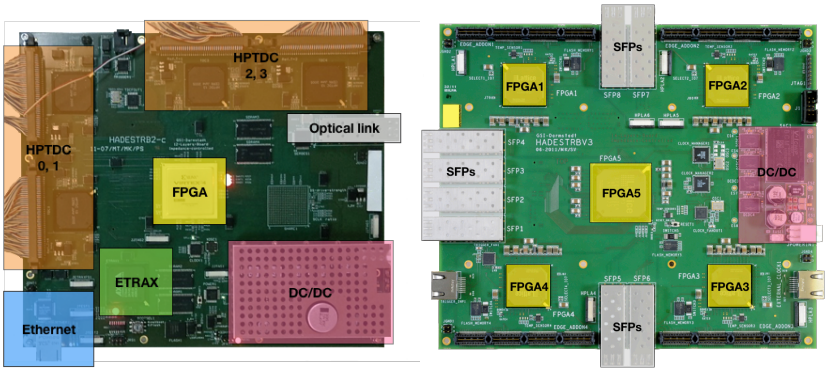

Figure 4.4: TRB layout left) TRBv2, right) TRBv3. Size: 20 cm × 23 cm.

4.3.1.1 TRB version 2

The DAQ and slow control of the TRBv2 are done by an ETRAX-FS processor running Linux and connected via ethernet of 100 Mb s^{-1}. All components are fed by a 48 V DC/DC converter.

The TRBv2 has four 32-channel High-Performance TDC (HPTDC) where the MBOs are connected [94]. Each HPTDC has 31 LVDS timing signals among other inputs and outputs for general purposes. An external time signal, used as the reference for synchronization, is connected to the 32nd channel of an HPTDC per plane. The TDCs have multi-hit capabilities that offer the possibility to differentiate simultaneous signals in multiple cells.

The data selection in the HPTDCs is started by an external trigger signal. Then, the board-controller field-programmable gate array (FPGA) initiates the read-out. The event-builder receives the date, formatted date via User Datagram Protocol (UDP) internet protocol, collects, and orders the individual sub-events from all read-out chains. In addition, the optical link of the TRBv2 offers high-speed data transfer of 2 Gb s^{-1}. The time resolution of the TRBv2 is 40 ps per channel [95].

4.3.1.2 TRB version 3

The TRBv3, like its predecessor, is a multi-purpose device with on-board DAQ functionality. The TRBv3 replaces the HPTDCs with ECP3-150 FPGAs, which improves the time resolution per channel to below 15 ps. Each one of them can support up to 64 high-rate multi-hit TDC channels, allowing up to 256 in total with add-on cards. FPGAs have all required algorithms implemented [96].

The central FPGA gathers and sends all data via 8 small form-factor pluggable (SFP) transceivers that support data transmission at speeds up to 3 Gb s^{-1}. Slow control information is transferred over the same links. A 48 V DC/DC provides power to all components.

4.3.2 Trigger system

The trigger logic is configurable and implemented in an FPGA-based system. The low-level trigger signal is transported from the MBOs to the trigger logic via MMCX cable (Figure 4.5). The system is programmed

USC UNIVERSIDADE DE SANTIAGO DE COMPOSTELA

with a single-board computer (SBC) running Linux (ODROID, Raspberry Pi, …) and programs *ctsrun, ctslog* and *ctschk*.

ctsrun is used to program the operating mode of the trigger system, which is done by defining the acquisition time window, the number of planes in coincidence, the trigger width and dead time, the synchronization frequency, and the logic gates. This program calls also the *ctschk*, which checks the correct programming of the hardware of this system.

ctslog is used to start the DAQ and is also used to read and store the information given by the counters in log files. The low-level trigger signals from the MBOs (i.e., the number of cells fired per MBO and plane, even if they are not enabled for trigger generation), the total trigger signals generated by the system, and the trigger signals successfully sent to the TRBs, are the counters in this case.

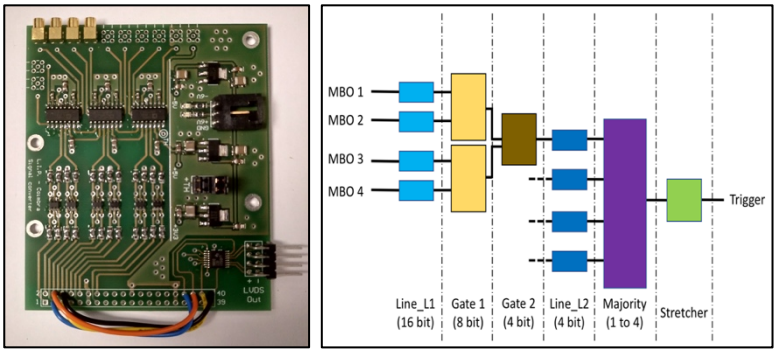

Figure 4.5: Left) Trigger board (8 cm × 10 cm). Right) Trigger logic.

The scheme of the system is shown in Figure 4.5. Each line (L1 and L2) is fully programmable (coded in decimal) so it can be enabled/disabled, and also its polarity can be changed. The gates (1 and 2) can be configured as "and/or". The condition that starts the acquisition is based on coincidences between the number of planes determined by the majority block. If there is a coincidence, the signal passes the stretcher and the trigger system generates a signal that is sent to the TRBs. A new output trigger signal will not be generated until the trigger dead time has expired. Even though the DAQ records all data of events

USC UNIVERSIDADE DE SANTIAGO DE COMPOSTELA

satisfying the trigger condition, the log file of the *ctslog* shows the counts in Hz (averaged over a custom time window). Additionally, a synchronization trigger signal with a custom frequency is sent to all TRBs simultaneously to ensure the correct data taking.

4.4 ENVIRONMENTAL SENSORS

Measuring the environmental variables (pressure, temperature and relative humidity) of the RPCs gives information about the gas conditions, enables the HV dynamic correction explained in Section 5.5, and allows one to do the CR data correction. RPCs are manufactured in a broad variety of layouts. Some include the environmental sensors inside the aluminium boxes, whereas others are installed outside. For both designs, all sensors are connected to an i2c-bus of an i2c-board controlled by an SBC which runs a Python code via cron. The data is saved in log files for analysis. The sensors used for the different variables are described in this section (Figure 4.6).

4.4.1 Presure

The pressure is measured by one MPL115A2 sensor per plane with an operative range from 50 to 115 kPa. The main features are an accuracy of ± 1 kPa and a resolution of 0.15 kPa (10 bits). The sensor also gives the temperature used to calculate the compensated pressure, a barometric pressure value compensated for changes in the sensor linearity. The 10-bit compensated pressure is calculated as follows:

$$\mathrm{P_{comp}} = \mathrm{a_0} + (\mathrm{b_1} + \mathrm{c_{12}}\,\mathrm{T_{ADC}})\,\mathrm{P_{ADC}} + \mathrm{b_2}\,\mathrm{T_{ADC}}\,, \qquad (4.1)$$

where P_{ADC} is the 10-bit pressure analog-to-digital converter (ADC) output, T_{ADC} is the 10-bit temperature ADC output, a_0 is the pressure offset coefficient, b_1 is the pressure sensitivity coefficient, b_2 is the temperature coefficient of offset, and c_{12} is the temperature coefficient of sensitivity. Pressure in kPa is obtained by Equation 4.2 (the maximum for 10-bit is 1023 decimal).

$$\mathrm{P} = \mathrm{P_{comp}}\left(\frac{115-50}{1023}\right) + 50\,. \qquad (4.2)$$

USC UNIVERSIDADE DE SANTIAGO DE COMPOSTELA

4.4.2 Relative humidity

SHT21 is the sensor that reads the information of relative humidity (RH). There is one sensor for each RPC plane. The most important properties are its accuracy of ±2% (from 20% to 80% RH) and its resolution of 0.04% (12 bits). The functional range goes from 0 to 100% RH. The ADC output signal S_{RH} is converted to relative humidity (result in % RH) by the following equation independently of the resolution:

$$\mathrm{RH} = -6 + 125\left(\frac{\mathrm{S_{RH}}}{2^{16}}\right). \tag{4.3}$$

Furthermore, this sensor measures the temperature within the limits of –40 and 125 ℃, with an accuracy of ±0.3 ℃ and a resolution of 0.01 ℃ (14 bits). The temperature conversion of the ADC output signal S_T is done as follows (result in ℃), regardless the resolution:

$$\mathrm{T} = -46.85 + 175.72\left(\frac{\mathrm{S_T}}{2^{16}}\right). \tag{4.4}$$

4.4.3 Temperature

Multiple TMP75 sensors are settled on all RPCs to measure the temperature. The operating regime extends from 40 to 125 ℃, with an accuracy of ±1 ℃ and a resolution of about 0.0625 ℃ (12 bits). The output-to-temperature ratio depends on the chosen resolution, but it is always a power of two in the denominator. In the 12 bits resolution, each output "unit" equals 1/16th of ℃ (for 11 bits, equals 1/8th and so on).

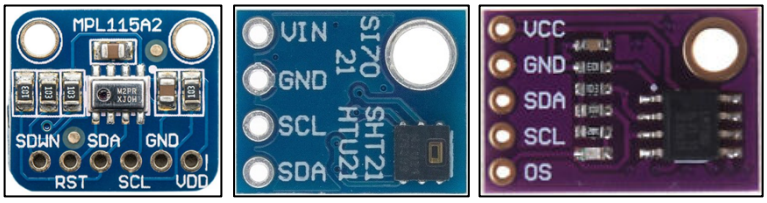

Figure 4.6: MPL115A2, SHT21 and TMP75 i2c sensors. Size: 19 mm × 18 mm.

4.5 Power supply

The power supply (PS) regulates and gives a smooth voltage to the components of a detector. Diverse PS devices bring the low voltage (LV) to the FEE and the DAQ, and the HV to the RPCs.

4.5.1 LV

The FEE and the DAQ are connected to individual LV PS that convert the 220 V input to 48 V. The LV provided to the FEE is about 5 V per MBO, so a maximum of 8 MBOs can be fed by a unique PS of this kind (Figure 4.7) [92]. Each TRB is supplied with 5 V by a different LV PS.

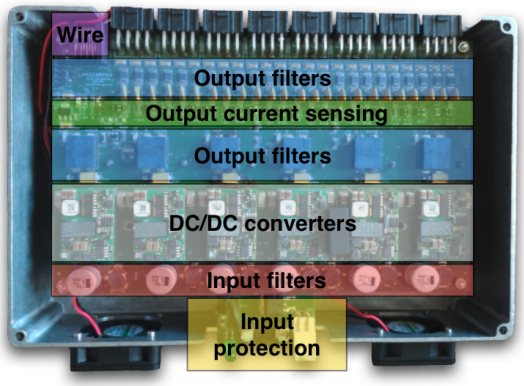

Figure 4.7: Components of the LV PS of the FEE.

4.5.2 HV

RPCs operate at HV to generate the avalanches inside the gas gaps. Each RPC plane is connected to a PS that sets the desired HV values (Figure 4.8). All HV PS of the detector are connected to an i2c-board. The voltage is set passing the information through an Ethernet cable. The same cable also carries the electrical power to the PS, what is called power over ethernet (PoE).

The input voltage of an HV PS is 5 V. Then, it is converted to a value determined by the mode of operation of the RPC (around 5–6 kV for the avalanche mode). HV and background currents are monitored

USC UNIVERSIDADE DE SANTIAGO DE COMPOSTELA

every minute via the i2c-bus, and the data is recorded in log files for online and offline analysis.

Figure 4.8: HV PS (44 cm × 16 cm).

A dynamic adjustment of the HV values is managed by an SBC (ODROID, Raspberry Pi, …) to compensate for the variations of temperature and pressure that modify the reduced electric field applied inside the gas gaps. The gain of the RPC is kept constant during the whole period of data taking by adapting the HV to the environmental conditions as follows:

$$\mathrm{V_{set}} = \frac{\mathrm{E_{red}\ d_{gap}\ P}}{0.0138068748\ \mathrm{T}}\ (\mathrm{V})\,, \tag{4.5}$$

where $E_{red} = E/N$ is the reduced electric field in Townsend (Td) being E the applied electric field and N the gas density, d_{gap} is the thickness of the gas gap in cm, P is the pressure in hPa, and T the temperature in K [97]. The data (P, T) of the environmental sensors, described in Section 4.4, is taken from the log files and averaged over a number n of measurements by a Python script. Then, the voltage is set to a value that keeps the $\mathrm{E_{red}}$ constant, whose value is calculated to operate within the efficiency plateau.

This method is the HV dynamic correction and is performed via cron. The limits or minimum and maximum voltages are calculated for extreme conditions of 900 hPa and 328 K and 1100 hPa and 273 K, respectively.

USC UNIVERSIDADE DE SANTIAGO DE COMPOSTELA

4.6 GAS SYSTEM

The gaps of the RPC are filled with pure Freon R-134a. Freon is an electronegative gas, so the majority of the free electrons in the gas are attached to its molecules. Only a small fraction of them contributes to the avalanche process. Moreover, other gases (quenchers) can be mixed with Freon to control the formation of secondary avalanches and streamers by absorbing the emitted photons. The gas is continuously flowing in an open loop. At the end of the loop, there is a one-way valve or bubbler partially filled with liquid vaseline. The gas from the RPC bubbles through the vaseline before being vented to the atmosphere.
In recent years, many studies have been carried out to find a gas with similar properties to R-134a and an acceptable Global Warming Power (GWP) [98]. Tetra-fluorethane has a GWP around 1430 being the reference the carbon dioxide with a GWP equal to 1. Nevertheless, none of the findings achieved the needed performances in terms of efficiency, time resolution, rate capability and aging. The gas emission can be reduced for indoor experiments by gas recirculation, while outdoor experiments, with stations covering large areas, are not suitable for such a technique [99].

4.6.1 Bubbler

The equipment of the bubblers has been improved considerably since the first version. First designs are used only as visual indicators of the number of bubbles produced at the gas outlet. Thus, to keep the gas flow constant, the bubblers needed regular on-site observations. Newest versions are more sophisticated and implement two different sensors that enable remote or online supervision of the gas conditions. Pressure and optical sensors quantify the flow at the gas outlet (Figure 4.9). The gas is introduced into the bubbler through a dip pipe, immersed at a fixed depth into vaseline. A pressure sensor installed at the gas inlet gives information of the gas flow and temperature. At the gas outlet, optical or photoelectric sensors detect the light changes when a bubble is produced. Since in the absence of bubbles the light reaches the photogate through vaseline with no interference, there is a reduction of the light intensity when a bubble is created. The pressure at the gas outlet is measured by the changes in the vaseline level a bubble causes.

USC UNIVERSIDADE DE SANTIAGO DE COMPOSTELA

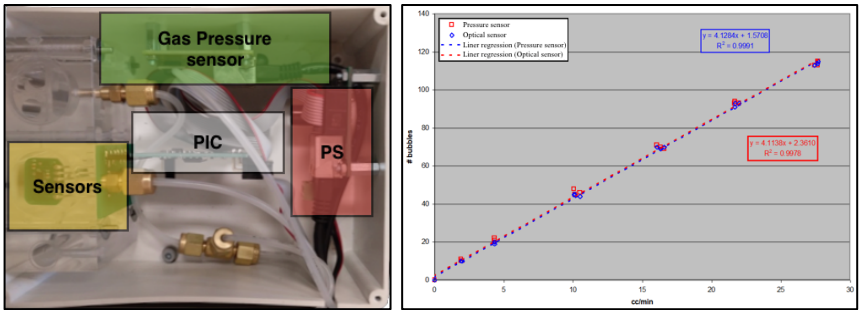

Figure 4.9: Left) Bubbler sensors. Right) Linear correlation between the number of bubbles registered and the gas flow in cc $\mathbf{min^{-1}}$.

4.7 TRISTAN-TRAGALDABAS EQUIPMENT

The equipment of the TRISTAN and TRAGALDABAS detectors is slightly different, being the latter the one with the newest versions of the aforementioned electronic devices. For both detectors, the size of the pads and the dimensions of the guard electrode were explained in Chapter 3. The active size per plane is the same for both detectors, and only the cell size changes. Both detectors work in avalanche mode, so the induced signal needs to be amplified by the FEE.

4.7.1 TRISTAN

The RPC planes of TRISTAN have 30 cells each, so 8 DBOs are needed for the read-out. The threshold of the DBOs is set to 40 mV by the TRB. Figure 4.10 presents the DBO channel configuration and cell mapping. The channels of the DBO start counting from the left, if we look at them from the front, and their corresponding number is written inside the rectangular pads. The cells are divided into groups of 30 as it is the maximum number of cells a single MBO can connect. Therefore, TRISTAN requires one MBO per RPC plane.

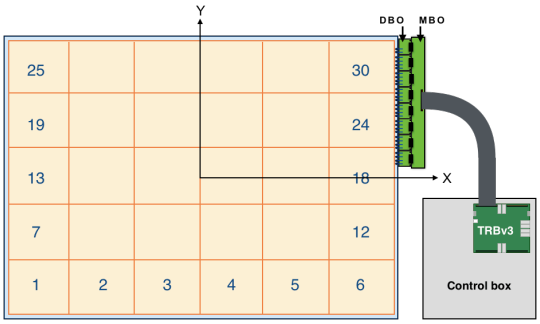

Figure 4.10: TRISTAN cell mapping and DBO-MBO-TRB connection.

TRISTAN is an almost completely autonomous detector designed to operate in Antarctica. In case of failure, the multiple programmed alarms give precise information about the cause via email. Hence, these alarms allow one to have a fast and effective response to guarantee the correct data taking and save the components in case of a major failure.

The DAQ is fully autonomous and based on a single TRBv3, to which the MBOs and the trigger logic are connected via TDC add-on cards. For the trigger logic, several frequencies have to be defined apart from the line-gate configuration, such as the window size (40 ns), trigger dead time (0.1 ms), trigger width (300 ns), synchronization frequency (1 s), and acquisition time (10 s). The first and third planes of TRISTAN measure in coincidence, so the majority value in the trigger system is set to 2. Event data recording starts when a coincidence occurs and the TRB gets the trigger signal. In addition to the data taken in coincidence, every RPC runs in self-trigger mode every six hours. Self-trigger enables a good diagnostic of the status of the RPCs. In this mode, the DAQ registers all signals originated in an RPC, independently of others. It takes three minutes to run the self-trigger in all planes, one minute each.

Concerning the alerts and the self-controlled DAQ, a watchdog (WD) reboots the entire system in case of a computer crash or communication failure. A reboot is performed weekly to check the detector status, keeping the HV PS at the operating value. Besides, a daily analysis of all log files searches for out-of-range values. Lastly,

USC UNIVERSIDADE DE SANTIAGO DE COMPOSTELA

a real-time clock (RTC) provides the event timestamp in case of the unavailability of the Network Time Protocol (NTP) server.

LV PS for all components of the detector are located in an aluminiun box, together with the DAQ and the router that allows wired and wireless connections. In Figure 4.11, the content inside the box and the linkages are shown.

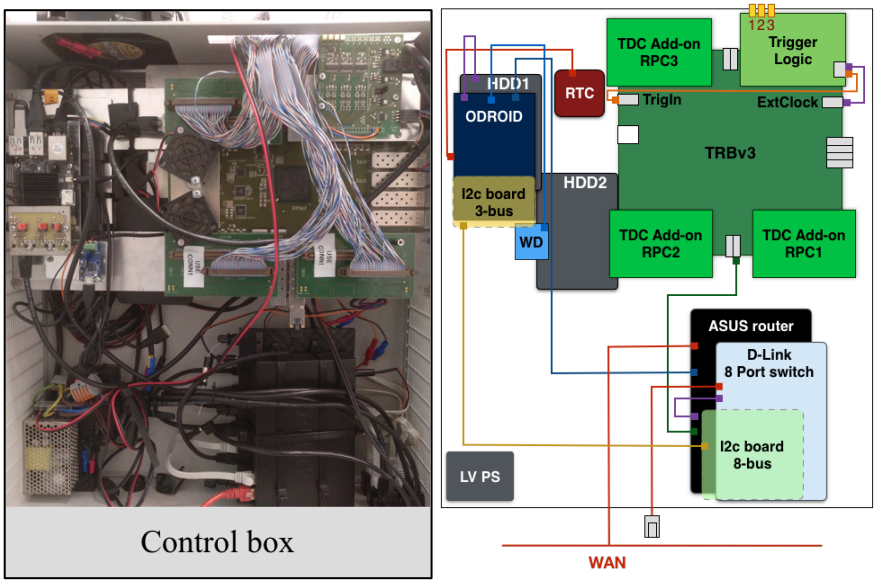

Figure 4.11: TRISTAN control box and schematic of the connections.

The detector is managed by a quad-core SBC ODROID-C2 that controls all devices and processes the data before being stored in the Hard Drive Disk (HDD). The computer communicates with all sensors of the three RPC planes via i2c-protocol (Figure 4.11). The HV PS (1 per plane), the chain of environmental sensors (1 per plane), and the gas system (1 for the gas pressure and 1 for the bubblers) are plugged into an 8-bus multiplexer by i2c connectors. The HV PS is dynamically adjusted to around 5.8–6.0 kV, according to a reduced electric field of 236 Td. After two read-outs out of range, an alert is sent by email, and the HV is set to a nominal value (5 kV). A set of seven environmental sensors are placed evenly all over the surface of each RPC aluminium

box, as it can be seen in Figure 4.12, with five measuring the temperature (numbers 3 to 7), one the pressure (number 1), and one both the temperature and the relative humidity (number 2).

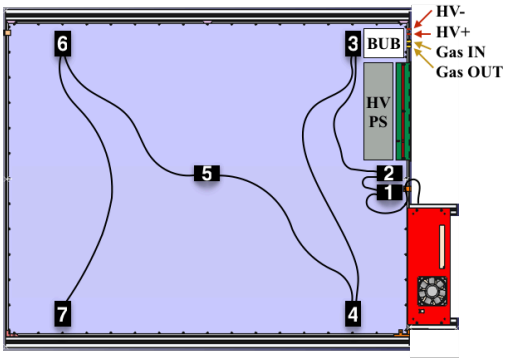

Figure 4.12: Top view of the location of the environmental sensors (1-7) and the connections of the HV PS and the bubbler.

The gas system consists of several gas flow regulators and one bubbler per plane. The detector operates at a gas flow rate of ~ 11 cc min^{-1}. The gas conditions (pressure, relative humidity and temperature) and the gas flow rate are registered in multiple log files.

The electrical power is supplied by various LV PS to all the electronic systems previously described. The LV PS that supplies the FEE is screwed to the cover of the control box. The HV PS converts the voltage given by an LV PS and sets the HV inside the RPCs.

CR data acquisition starts in the FEE and ends with the storage of the data, packed in files of around 15–20 MB, in the HDD. A file is created every five minutes, approximately (self-trigger data is stored in one-minute files). The packed files include the information of the events like the time and the charge of the cells fired within a temporal interval defined by the trigger coincidence signal. TRISTAN scripts are scheduled via cron. The data needs to be unpacked and calibrated before performing any analysis. Data calibration is discussed later in this manuscript. Finally, the power and data flow diagrams are shown, for a better comprehension of the detector's equipment, in Figures 4.13 and 4.14, respectively.

USC
UNIVERSIDADE DE SANTIAGO DE COMPOSTELA

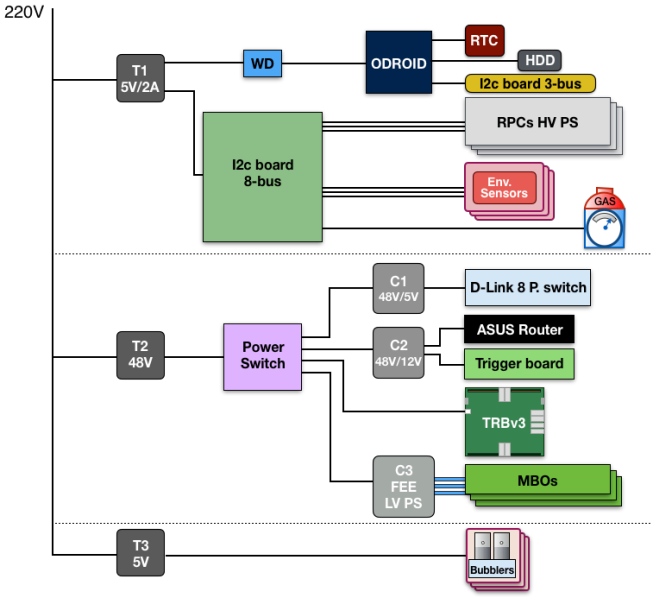

Figure 4.13: TRISTAN power diagram.

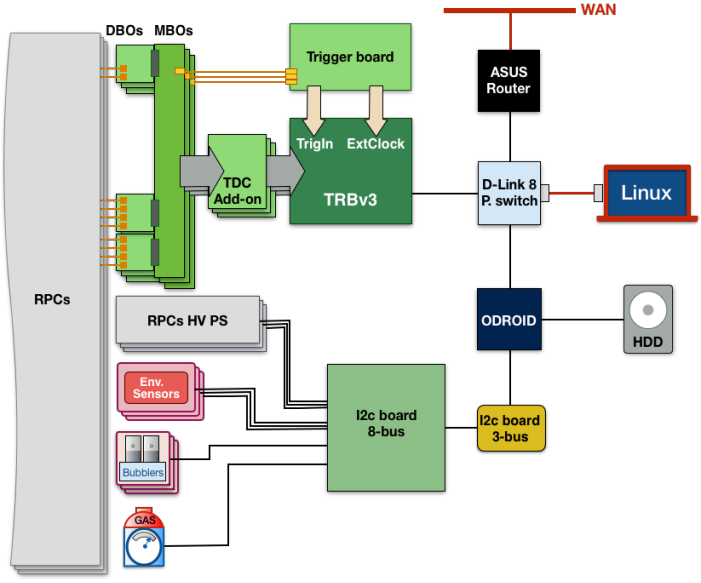

Figure 4.14: TRISTAN data flow diagram.

4.7.2 TRAGALDABAS

The size of the pads in TRAGALDABAS is smaller than in TRISTAN, which gives, for the same RPC active size, 120 read-out cells. All cells of each plane are divided into groups of 30 because the maximum DBOs that can be connected to a single MBO is eight. Hence, the detector requires a total of 4 MBOs and 32 DBOs per plane with each MBO covering a quadrant. The threshold in the DBOs is the same as for TRISTAN and is set to 40 mV by the TRB. Figure 4.15 shows the DBO channel configuration and cell mapping. The DBO channels start counting from the left, looking at them from the front, and the number of the channel is displayed inside the rectangular pads.

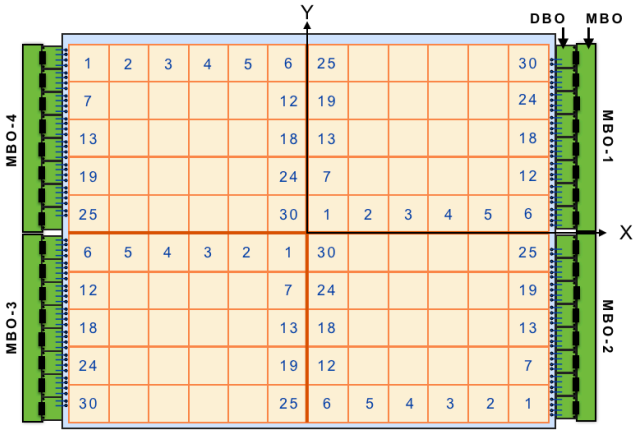

Figure 4.15: TRAGALDABAS cell mapping and DBO-MBO connection.

TRAGALDABAS is supervised by the Laboratorio Carmen Fernández (LabCaF) of the USC. The detector has operated in numerous configurations since the installation of the first two RPC planes in 2015. The instrumentation of the fourth plane started in late 2021 and finished in early 2022. Continuous monitoring provides vital information that is sent via email if a parameter goes out of range.

The DAQ is fully autonomous and based on one TRBv2 per plane due to the number of cells and the limited number of TDC channels that this TRB version offers. All MBOs of a plane are connected via flat cable to the TRBv2. The trigger logic is programmable and controlled

USC UNIVERSIDADE DE SANTIAGO DE COMPOSTELA

by an FPGA-based system built by the LIP of Coimbra. A Raspberry Pi communicates with the system and establishes the desired trigger settings. For any logic configuration, lines and gates have to be configured in addition to some important variables. These variables are frequencies for the window size (50 ns), trigger dead time (0.1 ms), trigger width (the values depend on the distance between planes in coincidence), synchronization frequency (1 s), and acquisition time (10 s). All inputs have the default polarity of true logic, and all Lines L1 are enabled. Line L2 enabling value is also a binary word coded in decimal which size is the number of bits shown in Figure 4.5. Table 4.1 shows the parameters used for the data taking based on coincidences between the first and third planes. In this scenario, the word is 0101, which is equal to 5 since planes start counting from the right.

Table 4.1: Trigger logic configuration.

Parameter	Value
Window size	10 = 50 ns
Line L1 enabling	65535
Line L1 polarity	65535
Gate 1	0
Gate 2	0
Line L2 enabling	5
Majority	2
Output polarity	4095
Trigger dead time	1 E-4 s
Synchronization frequency	1 s
Trigger width	3 E-7 s
Acquisition time	10 s

Event data recording starts when a coincidence occurs and the TRB receives the trigger signal from the FPGA system. Additionally, the acquisition runs every RPC in self-trigger mode at midnight for a minute (150 MB files). Self-trigger allows one to perform a good diagnostic of the status of the RPCs and the noisy cells. An NTP server gives the event timestamp. In case of a major failure of any component, except the gas system which is not monitored, the predefined alarms are sent via email, and the detector can be shut down or rebooted remotely.

USC UNIVERSIDADE DE SANTIAGO DE COMPOSTELA

Apart from the LV PS that feed the electronic systems inside the control box, a set of another three brings the electrical power to the FEE and the TRBs. TRAGALDABAS is split vertically in two (in terms of LV supply chain), and each half (8 MBOs) is supplied by an independent LV PS. A separate LV PS accommodates the four TRBs. In Figure 4.16 the control box and the connections are displayed.

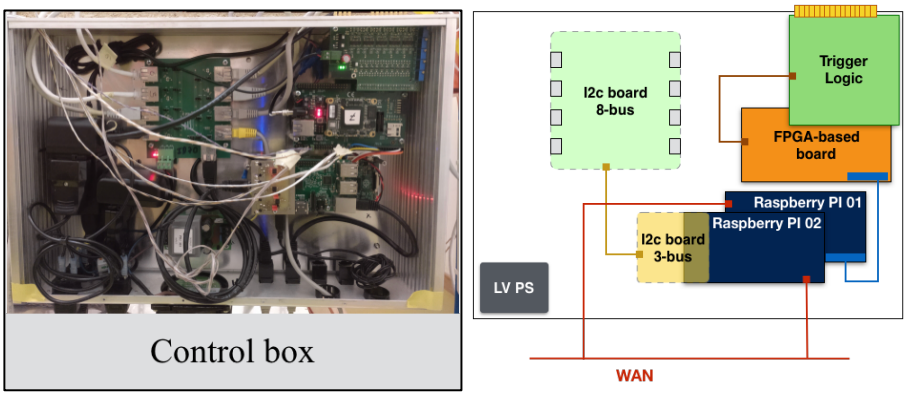

Figure 4.16: TRAGALDABAS control box and schematic of the connections.

The detector is controlled by an FPGA-based board and two Raspberry Pi. Raspberry01 is connected to the FPGA board and manages the trigger. Raspberry02 communicates with the HV PS and the environmental sensors of the four RPC planes via i2c-protocol (Figure 4.16). Environmental sensors (4) and HV PS (4) are plugged into an 8-bus i2c-board. After the successful configuration for TRISTAN, the HV dynamic correction was implemented in TRAGALDABAS. The HV is dynamically adjusted to a value around 5.6 kV according to a reduced electric field of 228 Td. This applied reduced field is enough to ensure the RPCs are working well within the plateau. After two unsuccessful read-outs, an alert is sent via email, and the HV is set to a nominal value (5 kV) to prevent damage. A set of seven environmental sensors, whose placement can be seen in Figure 4.17, are encapsulated in the same aluminium box as the RPCs. One of them registers the relative humidity and temperature (number 1), five measure

USC
UNIVERSIDADE DE SANTIAGO DE COMPOSTELA

the temperature independently (numbers from 2 to 6), and the last one gives the pressure (number 7).

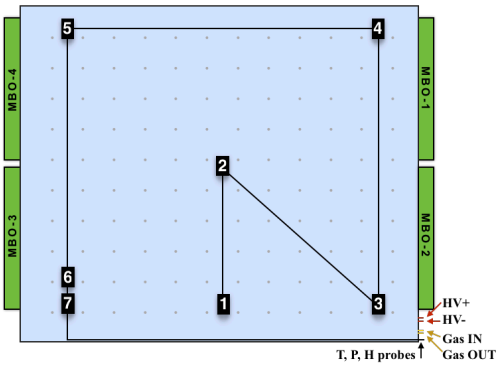

Figure 4.17: Top view of the location of the environmental sensors (1-7) and the connections of the HV PS and the bubbler.

The gas system consists of two gas flow regulators and one bubbler per plane. TRAGALDABAS operates at an almost constant gas flow rate of ~ 8 cc min^{-1}. Nevertheless, the gas system is not monitored because the bubblers don't have an integrated digital system. Even though the gas control has to be done in situ, some parameters, like the background currents, may give information about the gas conditions.

The power is supplied to the remaining electronic components by various LV PS placed inside the control box. The HV PS gets the power via PoE and converts it to the value requested by the script of the dynamic adjustment.

TRAGALDABAS CR data taking follows the same chain as for TRISTAN, from the FEE to the HDD. A new file is created for every 50 MB of data, and it needs to be unpacked and calibrated before performing any analysis. Data calibration is explained later in this manuscript. Besides local HDD storage, a copy of the data is sent to the Centro de Supercomputación de Galicia (CESGA) [100]. Figures 4.18 and 4.19 show the power and data flow diagrams for a better understanding of the equipment.

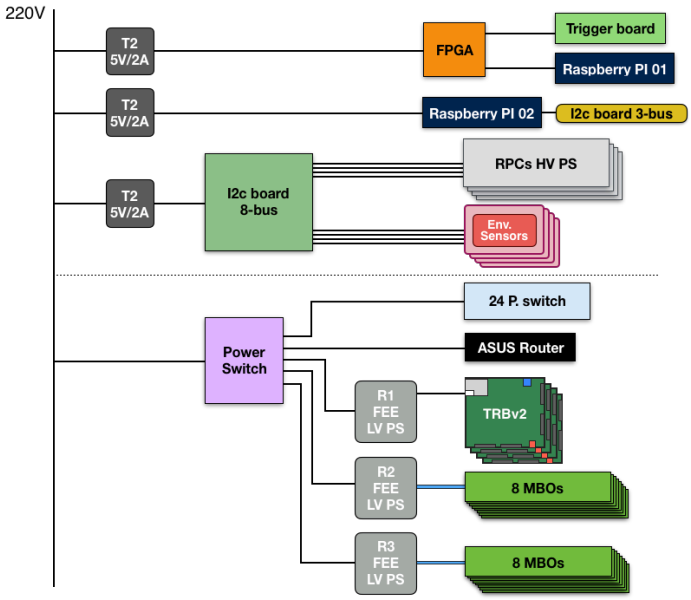

Figure 4.18: TRAGALDABAS power diagram.

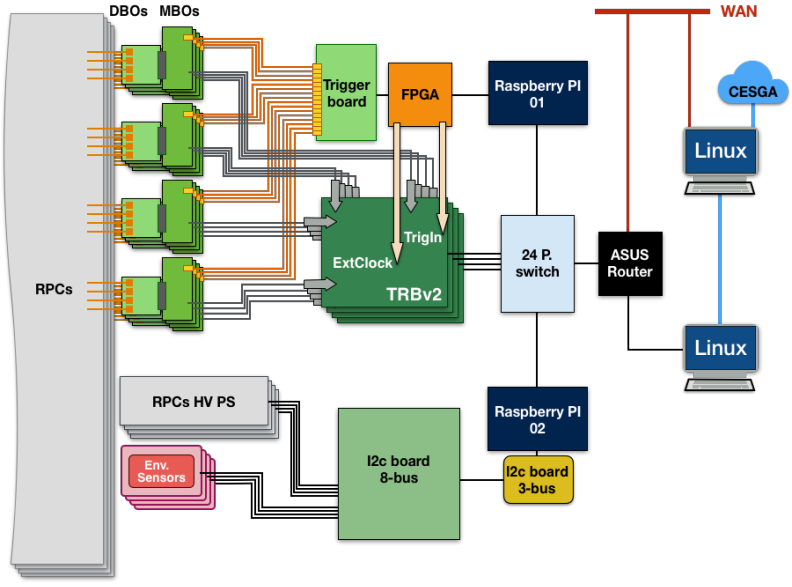

Figure 4.19: TRAGALDABAS data flow diagram.

USC
UNIVERSIDADE
DE SANTIAGO
DE COMPOSTELA

USC
UNIVERSIDADE
DE SANTIAGO
DE COMPOSTELA

5 SLOW CONTROL AND MONITORING

Since particle physics detectors have become progressively more sophisticated and demanding, the interest in monitoring the numerous system variables has been increased to guarantee detectors' integrity and stability. In this chapter, the slow control and monitoring systems of TRISTAN and TRAGALDABAS will be described in detail.

5.1 OVERVIEW

Reliable control and monitoring of the operational status is very important to guarantee detector's integrity and stability by early detection of system failures. The slow control and monitoring system (SCMS) refers to a fully autonomous system that controls different processes and gives information about their operational status. The SCMS is responsible for the periodic verification and display of the variables of the multiple systems that make up a detector. The experimental conditions are of special interest for future knowledge and offline data correction. For such a purpose, the SCMS controls, periodically, variables such as pressure, relative humidity, temperature, background currents, gas flow, disk space, and communication, among many others. Deviations from the predefined parameter range require immediate maintenance either with an automatic procedure or by operator-driven action. The SCMS also issues an alarm via email if any of the monitored variables exceed a preset acceptable working range. The SCMS of the detectors TRISTAN and TRAGALDABAS will be described in detail in the following sections. The detectors have been designed to operate under different conditions. Hence, the SCMS differs slightly concerning the visualization and control of some specific parameters.

USC
UNIVERSIDADE DE SANTIAGO DE COMPOSTELA

5.2 PARAMETERS CONTROLLED BY THE SCMS

The SCMS provides information about the conditions in which the experiments have been carried out. One or several parameters are controlled/monitored for each sub-system of the detectors. Depending on the sub-system, the monitoring is done via different processes. Some of them are fully monitored, whereas others require checking the log files manually. A summary of all sub-systems and parameters controlled by the SCMS for both detectors is given in Table 5.1.

Table 5.1: Summary of the sub-systems controlled in the detectors.

Sub-system	Parameters	TRISTAN	TRAGALDABAS
Environment	Pressure, relative humidity, and temperature	Yes	Yes
Gas system	Gas flow, temperature, relative humidity, and pressure	Yes	No
LV	-	No	No
HV	Voltage and background currents	Yes	Yes
FEE	Threshold setting and read-out	Yes	Yes
DAQ	Data recording, rates and charges	Yes	Yes

The data acquired from the multiple sub-systems are delivered to the SBC that controls every detector via the i2c-protocol and local area network (LAN). Only one sub-system is not implemented in the SCMS yet, which is the LV. LV control requires operator-driven action to check that the correct voltage is applied to the different devices. The LV PS status can be given indirectly by the status of the connected components because a failure of the PS causes the lack of their operability, and the SCMS issues an alert.

Client programs are used to check the experimental parameters, look for alarm situations and provide a graphical output of the progression of the variables. The core of the SCMS was implemented on a computer running Linux for both detectors. Several codes run periodically to verify the optimal working range of the parameters. Visualization is done via either daily report or continuous display at the laboratory facilities, depending on the detector (Section 5.5).

USC UNIVERSIDADE DE SANTIAGO DE COMPOSTELA

5.3 SENSOR READING

Data from each sub-system is stored in log files and transmitted to the computer in which the SCMS codes run systematically. The recording frequency of the log files depends on the variable impact on the detector's performance, and it can be seen in Table 5.2. This section gives an overview of the SCMS integration in every sub-system listed in Table 5.1. The electronic components of each sub-system have been explained in detail in Chapter 4.

Table 5.2: Recording frequencies of the log data used by the SCMS.

Sub-system	Parameters	TRISTAN	TRAGALDABAS
Environment	Pressure, relative humidity, and temperature	5 min	1 min
Gas system	Gas pressure at the gas inlet	5 min	-
Gas system	Gas flow, temperature, and relative humidity at gas outlet	5 min	-
LV	-	-	-
HV	Voltage and background currents	1 min	1 min
HV	HV dynamic setting	15 min	15 min
FEE	Threshold setting and read-out	DAQ start	DAQ start
DAQ	Self- and concidence trigger rates	2 min	1 min
DAQ	Data recording	5 min	5 min

5.3.1 Environment

Environmental sensors provide information about the pressure, relative humidity, and temperature of the RPCs via the i2c-protocol. Sensor reading and digital signal output conversion have been programmed in Python following the specifications of each device. The equations used for the signal conversion can be found in Chapter 4. The control computer runs the code via cron on a five and one-minute basis for TRISTAN and TRAGALDABAS, respectively. Several measurements are performed for each sensor to avoid a possible reading failure. The averaged values over the total number of measurements are stored in log files line-by-line.

USC UNIVERSIDADE DE SANTIAGO DE COMPOSTELA

5.3.2 Gas system

The gas system maintenance requires operator-driven action to replace the gas cylinder, modify the gas flow, and fill the bubblers with liquid vaseline. Gas flow monitoring is limited to on-site observation due to the version of the bubblers installed in TRAGALDABAS. The gas conditions are fully monitored in TRISTAN. Two independent sensors provide information about the gas pressure, gas flow, temperature, and relative humidity via the i2c-protocol. The gas flow is given by the number of bubbles produced per unit time. Sensor reading is programmed in Python. The code runs via cron every 5 minutes, and the data is stored line-by-line in a unique log file per day for the whole gas system.

5.3.3 HV

HV PS are controlled via i2c-connectors by the computer, which sets the operational voltages and registers the information in daily log files. The SCMS has access to the minute information about the positive and negative voltages and background currents, set voltages, set maximum current, and several control flags. The HV dynamics performs, every 15 minutes, a series of new measurements of the environmental sensors to adapt to the new conditions. The data from all measurements are registered in a log file together with the command used to set the HV.

5.3.4 FEE

Threshold setting is done by the TRBs via LTC2600 DACs with Serial Peripheral Interface (SPI) implemented in the MBOs. Eight DACs are connected in Daisy Chain per MBO. The TRB processor communicates with the DACs via a set of three differential-pair-pins plus ground. The data is sent to the first DAC via Serial Data Input (SDI) pins and clocked over the remaining DACs. After each programming operation, the data is clocked out via Serial Data Output (SDO) pins and read back by the TRB processor to verify the correct setting of the threshold voltages. TRBs are initialized at the start of the data acquisition. The information about the threshold writing and reading is registered in a log file for control purposes.

USC UNIVERSIDADE DE SANTIAGO DE COMPOSTELA

5.3.5 DAQ

Data acquisition programs provide information about the detected events. The data is transported via Gbit-Ethernet UDP from the TRBs to event-builder processes. TRISTAN DAQ operates with Data Acquisition Backbone Core (DABC) [101, 102]. DABC replaces the previous HADES building software hadaq, which is currently used in TRAGALDABAS. Data from the MBOs connected to the TRB are combined with an UDP frame and sent to the event-builder. The event building consists of the combination of Ethernet packets received by one or many TRBs, to coherent events based on the event identification generated in the first place by the trigger system. The resulting events are written in the standard HADES list data (HLD) format to an external HDD. Log files with self-trigger and coincidence trigger rates are created for monitoring purposes. Figure 5.1 illustrates the event building and storage chain.

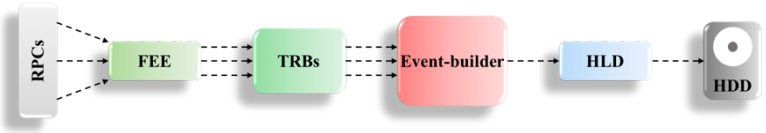

Figure 5.1: The acquisition chain from read-out to storage.

The data in the HLD files created by the DAQ contains the event information (Figure 5.2). Events consist of a header and sub-events. Sub-events are the signals sent by each TRB and consist of a header and the data, whose format is defined by the sub-event decoding.

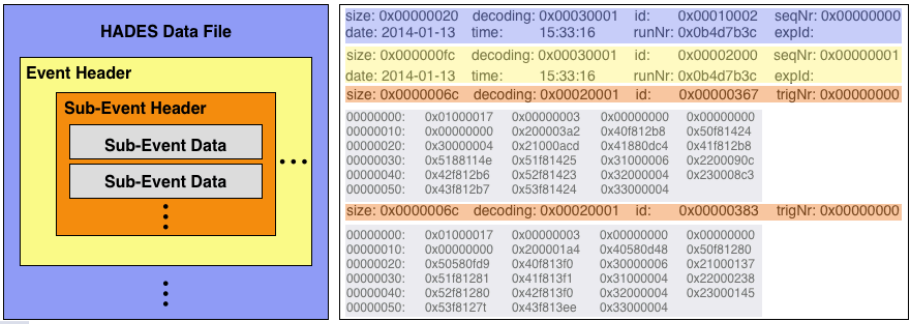

Figure 5.2: Structure of an HLD file.

USC UNIVERSIDADE DE SANTIAGO DE COMPOSTELA

In order to process the event information, the data is unpacked and calibrated before the analysis. Data calibration, reconstruction, and analysis are described in the next chapters. The unpacking is done either with the existing C++ (TRAGALDABAS) or MATLAB (TRISTAN) classes and methods. Time and charge signals of all cells in a detector are stored in units of TDC. Therefore, before recovering the information, the TDC bin units are converted to time units (ns) by multiplying by the TDC conversion factor. FEE channels behave slightly differently, so the ToT pedestal is substracted to homogenize the response. The SCMS reads the unpacked raw data to check its quality and also gives information about the operative, noisy and inactive channels.

5.4 ALARMS

Alarm programs periodically check the parameters from the log files of the aforementioned sub-systems and create a status report. Check intervals depend on the parameter and range from a few seconds to around one hour. The upper and lower limits of the working range of any parameter are predefined in a local configuration file. Alarms are issued via email either if a variable falls outside the allowed range, if the connection to a device cannot be established, or if a sub-system log file is not updated. TRISTAN and TRAGALDABAS alarms are configured in two different ways, but both have been implemented in the Python programming language.

TRISTAN SCMS runs a check of all log files every half an hour via cron. If everything is correct or within the optimal range, the averages are written in a daily log file, which is the reference for the next day. In case of error, the information about the issue is sent via email. Occasionally, emails are not sent due to communication failures, so the email sending success is checked via cron every hour, and the system retries to send the alert.

TRAGALDABAS is connected to a LAN with no band-width limits at the USC. Data from the sub-systems are delivered via LAN to a workstation. The SCMS of this detector is based on Nagios, which is an open-source software used for continuous monitoring and sending

USC UNIVERSIDADE DE SANTIAGO DE COMPOSTELA

of alerts [103]. A series of Nagios sensors (Python scripts) have been implemented to gather the data from the sub-system log files like pressure, relative humidity, temperature, HV, background currents, and trigger rates. The data is extracted periodically using regular expressions. Nagios connects to Raspberry01 to obtain the coincidence trigger rates and the self-trigger rates of each MBO and RPC. Environmental and power data access is done simultaneously via Raspberry02.

Host	Status	Last Check	Status Information
localhost	UP	02-25-2022 11:22:03	PING OK - Packet loss = 0%, RTA = 0.09 ms
fpcastor	UP	02-25-2022 11:19:07	PING OK - Packet loss = 0%, RTA = 0.31 ms
fppolux	DOWN	05-25-2020 13:02:39	CRITICAL - Host Unreachable (172.16.23.11)

Figure 5.3: Nagios alarms and host status.

Host	Service	Status	Last Check	Attempt	Status Information
tragaldabas	T1 triggers	CRITICAL	02-24-2022 20:10:16	1/3	Trigger is Critical: 0
	T2 triggers	CRITICAL	02-24-2022 20:10:16	3/3	Trigger is Critical: 0
	T3 triggers	WARNING	02-24-2022 20:10:16	3/3	Trigger Warning: 8346
	T4 triggers	WARNING	02-24-2022 20:10:16	3/3	Trigger Warning: 28374
	coincidence triggers	CRITICAL	02-24-2022 20:06:29	3/3	Trigger is Critical: 0
T4	Currents	OK	02-24-2022 20:09:47	1/3	Current is OK: ['0.332', '0.321']
	HighVoltage	OK	01-01-1970 01:33:42	1/3	High Voltage is OK:[5.599, 5.638]
	Humidity	OK	02-24-2022 20:08:45	1/3	Humidity is OK:37
	Pressure	OK	02-24-2022 20:08:47	1/3	Pressure is OK:99.9366
	Temperature	OK	02-24-2022 20:07:27	1/3	Temperature is OK:19.1
T3	Currents	OK	02-24-2022 20:07:17	1/3	Current is OK: ['0.404', '0.378']
	HighVoltage	OK	02-24-2022 20:08:31	1/3	High Voltage is OK:['5.605', '5.651']
	Humidity	OK	02-24-2022 20:07:17	1/3	Humidity is OK:41
	Pressure	OK	02-24-2022 20:07:16	1/3	Pressure is OK:99.5053
	Temperature	OK	02-24-2022 20:08:48	1/3	Temperature is OK:19.4
T2	Currents	OK	01-01-1970 01:33:42	1/3	Current is OK: [0.281, 0.266]
	HighVoltage	OK	01-01-1970 01:33:42	1/3	High Voltage is OK:[5.640, 5.581]
	Humidity	OK	01-01-1970 01:33:42	1/3	Humidity is OK:42
	Pressure	OK	01-01-1970 01:33:42	1/3	Pressure is OK:99.6592
	Temperature	OK	01-01-1970 01:33:42	1/3	Temperature is OK:17.9
T1	Currents	OK	02-24-2022 20:08:02	1/3	Current is OK: ['0.264', '0.244']
	HighVoltage	OK	01-01-1970 01:33:42	1/3	High Voltage is OK:[5.610, 5.599]
	Humidity	OK	02-24-2022 20:08:17	1/3	Humidity is OK:40
	Pressure	OK	02-24-2022 20:07:19	1/3	Pressure is OK:99.7322
	Temperature	OK	02-24-2022 20:07:15	1/3	Temperature is OK:19.7

Figure 5.4: Nagios alarms and sub-system status.

USC UNIVERSIDADE DE SANTIAGO DE COMPOSTELA

Screenshots of host and service status on Nagios web interface are shown in Figures 5.3 and 5.4. TRAGALDABAS SCMS also checks the available disk space, localhost communication, and DAQ status. Sub-system status is defined as ok, warning, critical or unknown, whereas host states are up or down/unreachable. To prevent false alarms due to transient problems, hosts and services are (re)checked a maximum of three times before considering an alarm as a real problem. Nagios detects status changes and suppresses notifications if a system is changing too frequently until it stabilizes. The frequency of service checks is five minutes, and re-checks are every minute. An email notification is sent when the maximum number of retry attempts is reached or the status changes. The notification interval avoids the emission of new alarms if the state is still non-ok. Alert messages and visualization tools guarantee detector integrity and stability.

5.5 VISUALIZATION

The main purpose of the SCMS can be divided into two main tasks: safety management of the detectors and monitoring of the experimental conditions. Visualization tools used to display the monitoring system's data depend on the conditions under which the detector operates.

5.5.1 TRISTAN

Limited human and network resources in Antarctica reduced the visualization of TRISTAN parameters to a daily report of 250 KB sent by email. Besides that, multiplicity maps are produced and used to check the quality of the data stored in the HLD files.

5.5.1.1 Daily reports

The detector's status and performance are summarized in a daily report that includes data of the previous three days as a reference. The document provides information about all sub-systems, together with a fast data quality analysis. Figure 5.5 shows the monitored parameters of the central plane, and all RPCs are controlled likewise.

USC UNIVERSIDADE DE SANTIAGO DE COMPOSTELA

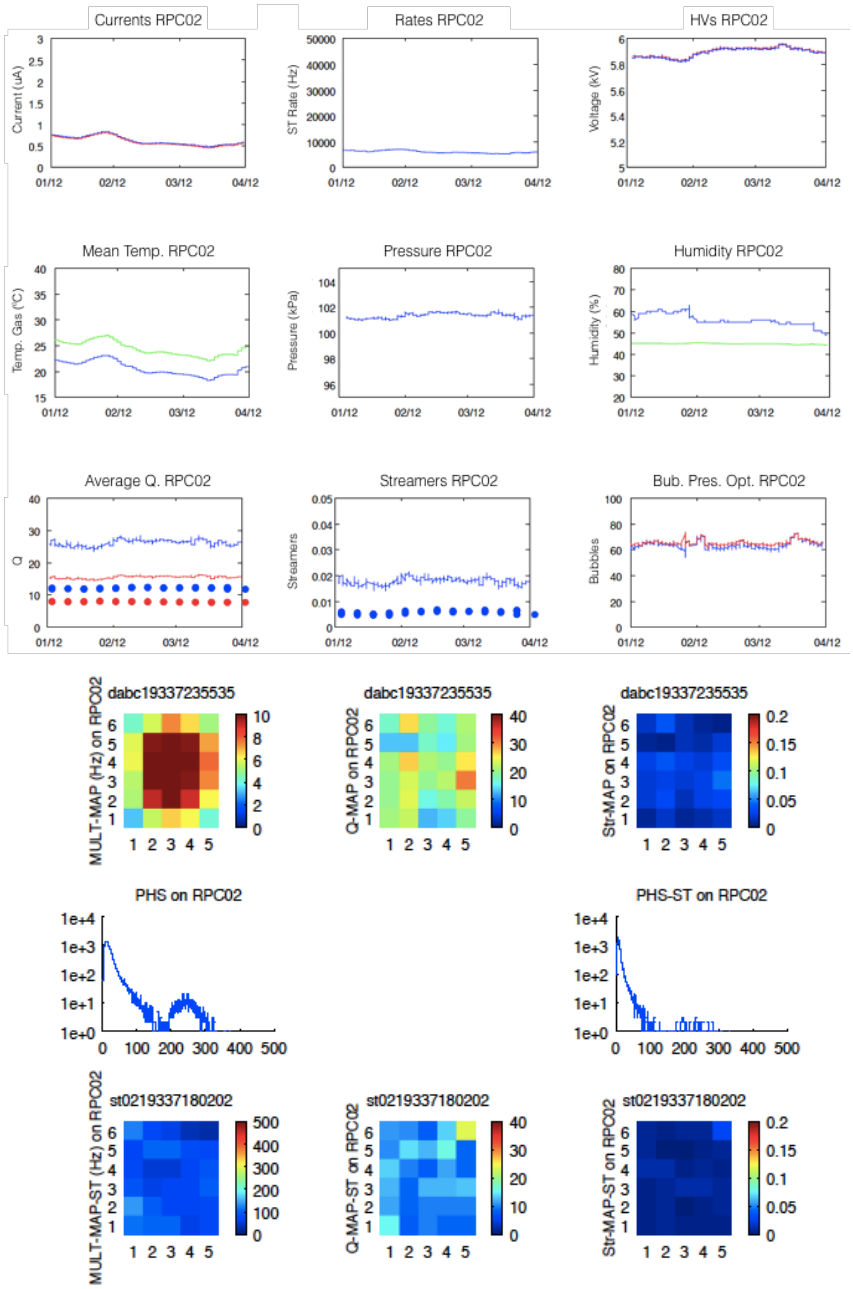

Figure 5.5: TRISTAN daily report. Overview of the working conditions on the top and the multiplicity, charge and streamer maps on the bottom.

The cell maps in Figure 5.5 show the multiplicity in coincidence and self-trigger configurations, respectively. Charge and streamer fractions provide information about the working conditions in the RPCs (PHS histograms). TRISTAN works in avalanche mode, so the streamer percentage must be kept very low. Daily reports keep track of parameters' behavior and experimental conditions.

5.5.1.2 Cell and multiplicity maps

Cells of each RPC form a 6×5 array. Observations of the self-trigger rates allow identifying problematic cells that need to be replaced. Cell identification is done via look-up tables, which contain the channel information, i.e., TDC-MBO-DBO channel connections. To produce cell and multiplicity maps data have to be unpacked. Figures 5.6 and 5.7 show raw data maps and multiplicity differences between planes. Multiplicity stands for the number of cells fired in an event, being the maximum equal to the total number of cells.

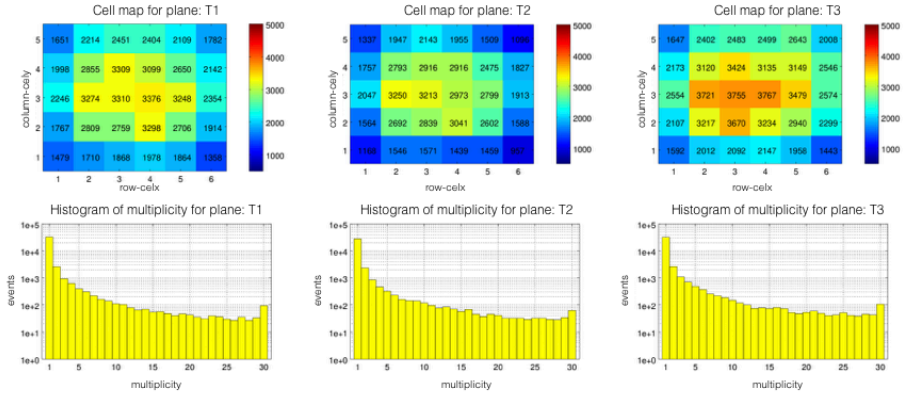

Figure 5.6: TRISTAN cell (top) and multiplicity (bottom) maps.

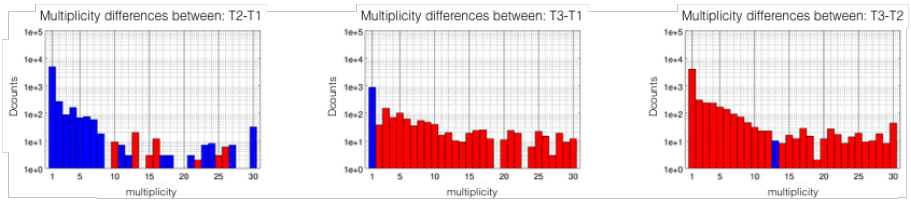

Figure 5.7: Multiplicity differences are shown in red (positive) or blue (negative) for all RPC combinations.

5.5.2 TRAGALDABAS

LabCaF laboratory counts with the necessary equipment to display TRAGALDABAS data for on-site experts. Operators have access to the log data from all sensors through graphical interfaces. In addition, every HLD file is unpacked and the data quality checked by the multiplicity maps.

5.5.2.1 Grafana with PNP4Nagios

Visualization can be done either using Nagios web interface or Grafana software. Nagios core receives the performance data formatted following strict guidelines and passes it to an external program. The performance data is the output of the services that read the sensors defined in Nagios. PNP4Nagios is the external program used for TRAGALDABAS [104]. PNP4Nagios processes and stores the performance data in Round Robin Database (RRD) files, and offers a graphical user interface (GUI) to display the data from Nagios Core. RRD is a special storage system for large amounts of time-series information with a constant disk footprint.

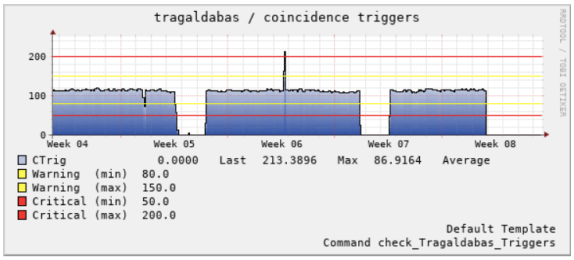

Figure 5.8: Example of the visualization via Nagios web interface. Warning and critical limits are given by yellow and red lines.

Grafana is an open-source platform that has been configured for running data analytics over a period of time with the help of customizable dashboards [105]. To generate the performance graphs, Grafana connects with the RRD files produced by PNP4Nagios. Dashboards are separated into two categories: one shows a detector's overview containing the key parameters over the last hours, and the other is for the conditions of each plane.

USC UNIVERSIDADE DE SANTIAGO DE COMPOSTELA

Grafana queries each sensor's value every 30 seconds and displays them over a 6-hour time span. The choice of parameters and time periods is fully configurable.

Figure 5.9: Visualization of the detector's overview dashboard with Grafana.

5.5.2.2 Cell and multiplicity maps

TRAGALDABAS cells form a 12 × 10 array for each RPC. Self-trigger rate maps and multiplicity histograms are produced to monitor the cell conditions by online unpacking of HLD data files. An existing bash program checks for a new HLD file every 10 seconds. If a new file is detected, the code runs the online unpacker and draws the maps. The bash program has been adapted to the different detector configurations. Like for TRISTAN, cell identification is done via look-up tables that contain the channel information.

An example of the cell maps and multiplicity histograms produced for every HLD file is shown in Figure 5.10. The number of cells fired per event is represented in multiplicity histograms, being 120 the maximum possible value. Operator-driven action is required when a problematic cell is found. The color maps allow operators to identify the inactive and noisy cells.

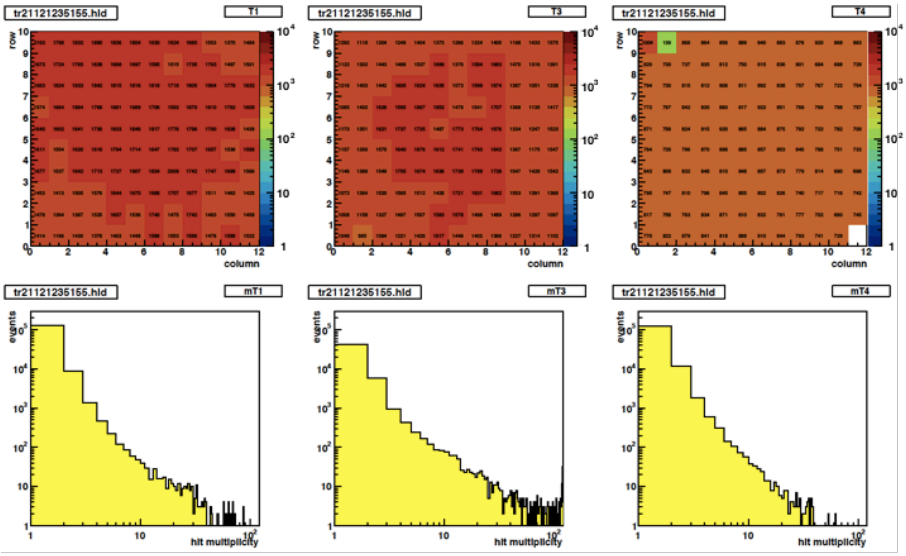

Figure 5.10: TRAGALDABAS cell (top) and multiplicity (bottom) maps.

5.5.2.3 Charge report

Monitoring the charges is fundamental for understanding cells response and helps to detect oscillating channels that require maintenance. Data is unpacked daily to obtain the charge spectra, and a charge report is created with the information of all cells via cron. Figure 5.11 shows the charge in nanoseconds for two cells.

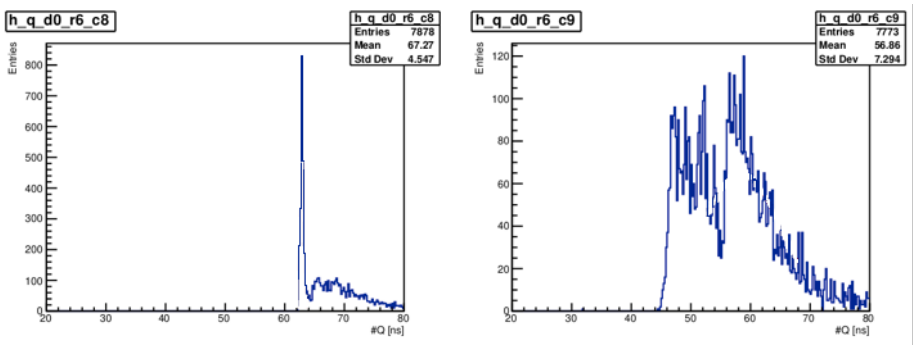

Figure 5.11: Charge report of a correct (left) and anomalous (right) cell.

USC UNIVERSIDADE DE SANTIAGO DE COMPOSTELA

5.5.2.4 Cell Viewer

A custom GUI, called Cell Viewer, has been developed within the LabCaF group to display stats about TRAGALDABAS. Nevertheless, it can be adapted to any detector of the TRASGO family. Cell Viewer is programmed in Python with ROOT libraries to extract the data from the different Trees. ROOT is a high-performance software for data analysis widely used in the particle physics field [106]. Data quality can be checked after the unpacking and/or reconstruction have been performed. Cell Viewer displays the cell rate for the different data levels, from raw to reconstructed tracks, and the time period is customizable. The detector is divided into four sections according to the number of MBOs. Figure 5.12 shows Cell Viewer GUI and cell and MBOs counting rates.

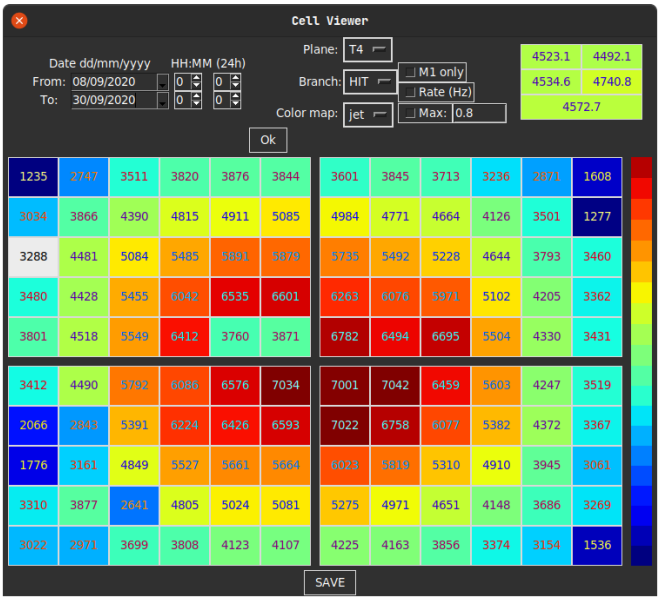

Figure 5.12: Cell Viewer interface.

USC
UNIVERSIDADE
DE SANTIAGO
DE COMPOSTELA

USC
UNIVERSIDADE
DE SANTIAGO
DE COMPOSTELA

6 CALIBRATION AND RECONSTRUCTION

Particle identification requires well-calibrated data to provide reliable information about CRs. Calibrating detectors ensure their operation in the best possible conditions giving the best performance. The calibration and validation of TRISTAN and TRAGALDABAS data have been assessed in this research. This chapter is dedicated to the calibration and reconstruction algorithms and methods.

6.1 STRUCTURE OF UNPACKING AND CALIBRATION PROCESSES

The correct understanding of the physics behind the CR data taken by the two detectors relies on a good characterization and calibration of the registered signals. Before performing any analysis, CR data stored in HLD files are unpacked with the existing C++ or MATLAB classes and methods. The unpacked data contains the event information like the event header and the signals measured by the TDCs. Events have at least as many signals as MBOs are connected to the TRBs. These signals are the trigger reference on channel 32 of each TDC. The appearance of more signals indicates that CR particles crossed the cells of the RPC, producing the so-called hits. A hit is a fired cell whose detected signal passed all thresholds. The time signals expected in a hit are the leading and trailing edges of the pulses. Hits with just one of those signals are rejected a posteriori. Times are in TDC bin units, and the TDC conversion factor converts them to nanoseconds. One TDC bin corresponds to 0.098 ns. Charge (in ns) is obtained by the difference between leading and trailing and times, and the algorithm is called charge-to-width (Q2W) [107]. The calibration process converts the raw data into hits for which the calibration constants, like time and charge, are needed. These constants are obtained by calculating the pedestals, which are subtracted from the original data to homogenize the response

USC UNIVERSIDADE DE SANTIAGO DE COMPOSTELA

of each FEE channel. Due to the fact that threshold voltages are set and fixed in the DBOs, the differences in rise-time or amplitude of the pulses can lead to differences in the digitizing time (Figure 6.1). This effect is known as amplitude or rise walk, and the walk correction is needed to generate the hits.

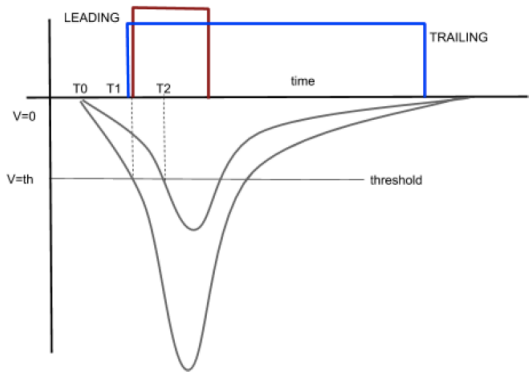

Figure 6.1: Walk correction effect. Signals with the same shape but different amplitude cross the threshold at nonidentical times T1, and T2.

Unpacked data also contains information about the TRB number, the channel, and the number of hits. The channel information used to unpack and calibrate the CR data is given by the look-up tables. These tables consist of one row per channel and the eight following columns: TDC channel number (1–128), MBO number (1-total number of MBOs), DBOs channel (1–32), MBO channel (1–30), Kx (1-RPC rows), Ky (1-RPC columns), and the x- and y-coordinates of the cell center, respectively. In TRAGALDABAS, the interconnection of multiple TRBs implies the addition of an external synchronization signal from the FPGA-based system (Table 4.1). This signal is used to check that all TRBs are synchronized and recording the same event. The script called *checksync* reads the event information to find that signal on channel 32 of the second TDC in all TRBs.

The arrival direction of the primary particle to the Earth's atmosphere can be derived from events of high hit-multiplicity (number of hits). Hence, it is essential to perform an accurate time calibration, whose

algorithms account for several effects such as fixed time delays due to cables, configurations, etc., in a unique constant per cell. The relative arrival times, together with the recorded charge, are important to determine the position of the shower axis on the ground. The calibration of the detectors includes the estimation of the efficiency and the noise rate of each RPC plane. Detectors' performance has a direct relation to the operation parameters. Thus, the production techniques can not guarantee the same performance and long-term stability. RPC performance varies from chamber to chamber and from time to time. Currently, calibration is generally performed once per day, and the calibration constants are stored in ASCII files. These constants have to be subtracted from the measured values to study the CR data. The calibration algorithms and methods developed in this work will be explained in the following sections.

6.2 GEOMETRIC ACCEPTANCE

Primary CRs can be assumed that arrive isotropically at the top of the Earth's atmosphere. At sea level, muons are the most abundant charged particles in secondary CRs. The general angular distribution of CR muons at a certain distance from the sea level depends on several factors, such as the incident zenith angle and energy as follows [39]:

$$\mathrm{I}(\theta) = \mathrm{I}_0 \cos^{\mathrm{n}} \theta \,, \tag{6.1}$$

where I_0 is defined as the integrated vertical muon flux in $\mathrm{cm}^{-2}\ \mathrm{s}^{-1}\ \mathrm{sr}^{-1}$ and θ is the zenith angle of the muon. The exponent n varies over a wide range depending on the latitude, altitude, muon cutoff momentum, etc. Integrating the angular distribution in the downward direction or vertical component of the velocity vector over the solid angle gives the downward flux as:

$$\mathrm{J}(\theta, \phi) = \int \mathrm{I}(\theta) \cos\theta \, \mathrm{d}\Omega = \int_0^{2\pi} \int_0^{\theta} \mathrm{I}(\theta) \cos\theta \sin\theta \, \mathrm{d}\theta \mathrm{d}\phi. \tag{6.2}$$

USC UNIVERSIDADE DE SANTIAGO DE COMPOSTELA

The acceptance of the detector depends on the active area, the zenith-angle distribution of the incident muons, and the solid angle subtended by the RPC planes. The steepest angle between the planes that are in coincidence is determined by the path from one edge of the top plane to the opposite edge of the bottom plane. A flat detector of active area *A* will see a muon spectrum approximately proportional to $\cos^2\theta$ at sea level. To estimate the muon flux, a couple of simplifying assumptions have to be made. On the one hand, we assume that all cells of the RPC planes see the same solid angle, which is equal to the angle seen by the element at the center of the bottom cells. On the other hand, we assume that cells of rectangular shape can be modeled as circular cells with the same area. This assumption makes the calculation of the flux per unit area easier because of the cylindrical geometry, for which the solid angle is subtended by a cone. Therefore, the estimated muon flux is modulated by the $\cos^4\theta$ and given by the following equation:

$$J(\theta) \approx \frac{\pi}{2} I_0 \left(1 - \cos^4\theta\right). \qquad (6.3)$$

A simulation using Monte Carlo techniques has been carried out to determine the acceptance of both detectors. The trigger is based on coincidences between the first and third planes for both cases. A random position is generated in the top trigger plane. Similarly, the zenith angle of the incident CR is generated using a $\cos^2\theta$ distribution, and the azimuth angle is generated randomly between 0 and 2π. The generated particle is extrapolated to the bottom trigger plane and the acceptance is computed. Basically, the Python script that performs the calculation determines if a CR passing through the active region of the top trigger plane is also detected by the bottom plane or not. The program *tacceptance* takes the name of the detector as an argument and imports its geometry from *tdetectors* class. The required geometric parameters are the number of cells and their size in both directions of the RPC plane, the width of the guard electrodes to compute the dead zones, and the vertical distance between the trigger planes. Table 6.1 shows the geometry of TRISTAN and TRAGALDABAS detectors used to obtain the acceptance and angular distribution of the particles that are accepted.

USC UNIDADE SANTIAGO COMPOSTELA

Table 6.1: Geometric parameters.

Parameter	TRISTAN	TRAGALDABAS
Cells x-axis	6	12
Cells y-axis	5	10
Cell size x-axis	242 mm	116 mm
Cell size y-axis	232 mm	111 mm
Width of dead zones	10 mm	10 mm
Vertical distance	484 mm	902 mm

In Table 6.2, the distances between RPC planes for both detectors are presented. Trigger configuration allows any combination of planes, and it was set to the first and third planes, counting from top to bottom, for this work. Hereinafter, planes are labeled starting from the top of the detectors as T1, T2, etc.

Table 6.2: RPCs z-coordinate in mm.

Plane	TRISTAN	TRAGALDABAS
T1	484	1739
T2	271	1217
T3	0	837
T4	-	0

Ten million CR particles have been generated. The zenithal angular distributions of generated and accepted events are shown in Figure 6.2. The acceptance, or the percentage of particles that crossed both planes over the total generated, is $57.89 \pm 0.02(\text{stat})$ for TRISTAN and $34.18 \pm 0.02(\text{stat})$ for TRAGALDABAS. Uncertainties have been calculated by taking the square root of the accepted events.

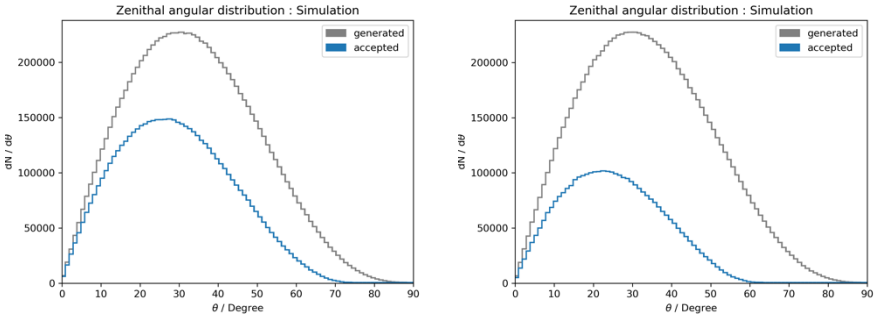

Figure 6.2: Zenithal angular distribution of generated and accepted events for left) TRISTAN and right) TRAGALDABAS.

USC UNIVERSIDADE DE SANTIAGO DE COMPOSTELA

Acceptance cell maps show the events with a hit in the active area of the top trigger plane, that have been detected also in the bottom trigger plane. The lower the incident zenith angle, the higher the acceptance. Central cells have a higher acceptance rate due to the detector's geometry (Figure 6.3).

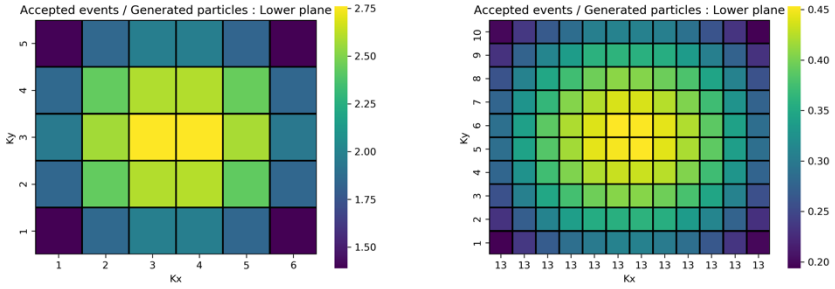

Figure 6.3: Acceptance cell maps left) TRISTAN and right) TRAGALDABAS. Colorbar shows the percentage of accepted events.

The acceptance or accepted CR fraction for a given zenith angle is plotted together with the zenith-angle distribution of the accepted events in Figure 6.4. TRISTAN cells have around four times the area of TRAGALDABAS cells. Therefore, a particle crossing the same cell in the upper and lower trigger planes can have a maximum zenith angle of about 35 degrees, whereas for TRAGALDABAS the maximum zenith is around 10 degrees.

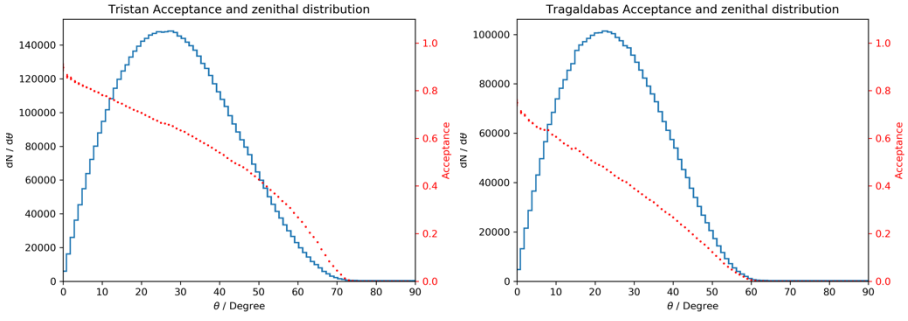

Figure 6.4: Theta distributions and acceptance of the detectors left) TRISTAN and right) TRAGALDABAS.

An important test is to verify the $\cos^2 \theta$ distribution of CRs arriving at the Earth's surface using the real reconstructed data from both detectors. Reconstruction algorithms will be described in Section 6.7.

6.3 SIGNAL CALIBRATION

Correct calibration of the CR data involves both charge and time-of-flight signals. In this section, the algorithms and results used for the signal calibration will be discussed. TRISTAN programs have been developed in MATLAB, whereas for TRAGALDABAS the already existing C++ classes within the ROOT framework have been used.

6.3.1 Charge

The charge spectrum of raw data is characterized by four regions (Figure 6.5). The first is the low-charge region, with no signals due to the fixed threshold on the FEE, which is delimited by the pedestal peak. The charge pedestal region separates the low and intermediate charge regions. Signals with a charge higher than a certain value obtained by fitting the pedestal peak correspond to CR particles, and the signals below that value are mainly noise. Finally, the high-charge region is associated with streamers produced in the detector due to the interaction of high ionizing particles. It is important to bear in mind that the measured charge is given in nanoseconds so that, to perform a detailed charge analysis it must be converted to femtocoulomb.

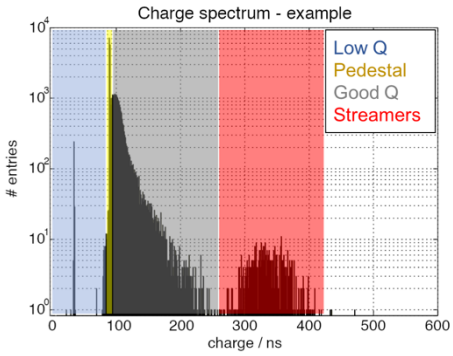

Figure 6.5: Charge measured in a cell. Vertical lines separate different regions.

USC UNIVERSIDADE DE SANTIAGO DE COMPOSTELA

Charge calibration is performed daily for both detectors, and the calibration constants are stored in ASCII files, which are one of the inputs of the efficiency programs described in the next section. Essentially, calibration constants consist of a charge threshold below which the charges are filtered, a process known as pedestal fitting and removal. This low-charge cut is obtained for every cell independently since they have a different response. Even though the tail of the pedestal peak follows a Lorentzian distribution, a Gaussian approximation has been considered. Pedestal and charge peaks of TRISTAN are fitted to a double Gaussian within a window of 20 ns centered at 95 ns. The best fit out of ten, the one that minimizes the residuals, is taken into account. Figure 6.6 shows the double fit results and the residual plot.

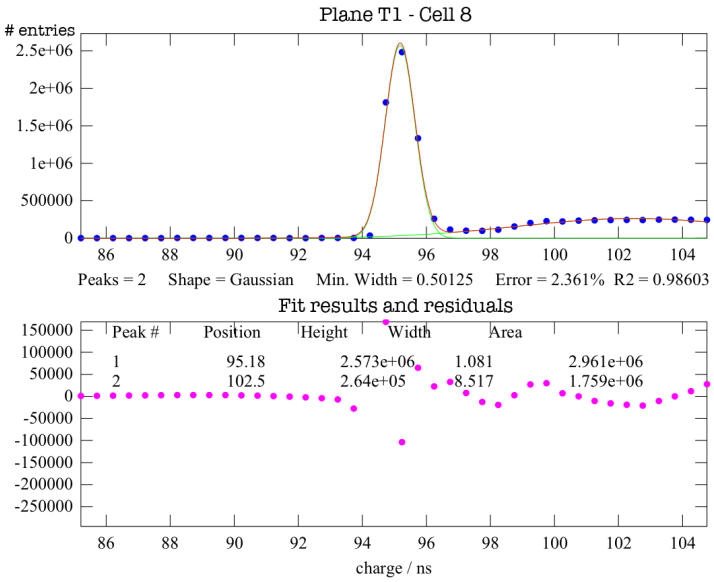

Figure 6.6: Top) Double Gaussian fit to the pedestal and CR charge peaks. Bottom) Residual plot and peak information obtained for TRISTAN.

Even though the residuals are very high for the pedestal peak, because of the Gaussian approximation, this method provides a good estimation of the calibration constants. The mean and sigma of the pedestal peak are stored in ASCII files. Charges within six sigma from

the mean value are rejected, reducing the noise to charge ratio to the minimum. In Figure 6.7, an example of the charge spectrum for cell number 8 of plane T1, the pedestal position, and the six sigma cut applied are shown.

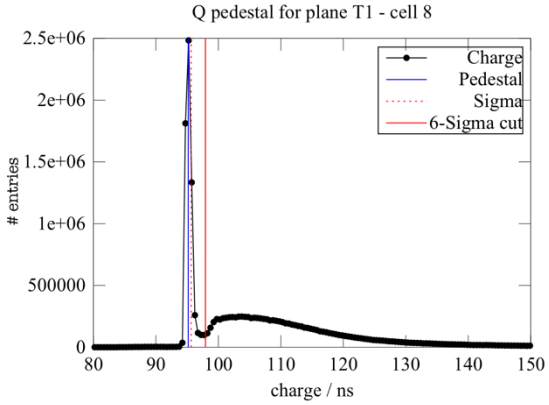

Figure 6.7: Pedestal position and six sigma cut of TRISTAN.

In TRAGALDABAS the pedestal is obtained by following a similar process assuming a gaussian peak. The program searches for the maximum of the charge histogram and extracts the bin center. Then a Gaussian fit is performed to obtain the charge calibration constant per cell (Figure 6.8).

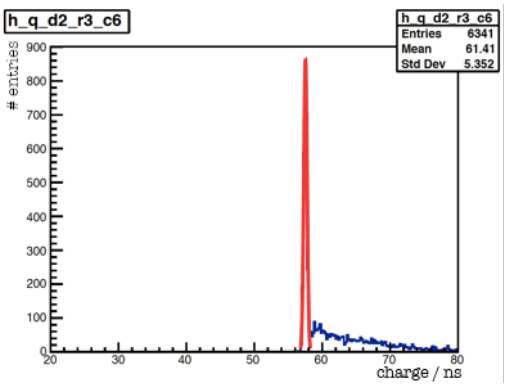

Figure 6.8: Gaussian fit to the pedestal peak for one cell of TRAGALDABAS.

USC UNIVERSIDADE DE SANTIAGO DE COMPOSTELA

A new set of charge calibration constants is produced daily. These constants are applied to filter the hits according to their charge when calculating the efficiency or reconstructing the CR events. The obtention of the calibration parameters is automatic, and it might happen that for some reason, the peak finder or fitting programs fail (failing rate is lower than 1%). In that case, the detector requires maintenance, and cells failing must be checked and replaced. If cells work properly and the issue is produced due to the non-convergence of the fit, a program searches for the previously acceptable calibration constant and corrects the problematic value. Programs called *tqcalibration* and *tqparscor* have been developed for TRISTAN charge calibration purposes. The streamer fractions in TRISTAN and TRAGALDABAS detectors are lower than 4% of the total charge.

6.3.2 Time

Time-of-flight measurement is the main characteristic of the t-RPCs. The primary role of time is to distinguish between incident particles according to their velocity. Hence, it is essential to have a very accurate time calibration. For such a purpose, it is necessary to synchronize all cells of the detector because of the design and the different lengths of the cables transporting the signal. Assuming that a cell measures the exact time, the time shifts or delays of the remaining cells are estimated. The obtention of the time calibration constants is accomplished in several stages. In contrast to the daily charge calibration, the time is calibrated only once using a few hours of data.

The time calibration process starts by filtering the hits according to their charge using the charge calibration constants and is carried out in pairs of RPC planes. The time differences between the hits of the top and bottom RPC planes are computed as follows:

$$dt_{DU} = t_D - t_U - \frac{1}{c}\left(\sum_{i=x,y,z}(i_D - i_U)^2\right)^{\frac{1}{2}}, \qquad (6.4)$$

where *i* refers to the pad coordinates of the hits, and *D* and *U* refer to bottom and top planes respectively.

USC UNIVERSIDADE DE SANTIAGO DE COMPOSTELA

TRISTAN consists of RPCs with 30 cells so that the number of cell combinations grows up to 900 for two planes considering that one hit per plane is taken at the same time. Histograms of the time difference, with a bin size of 100 ps, are fitted to a sum of two Gaussians, and the best fit out of ten is taken into account (Figure 6.9). Composed model information like peak position, sigma, and root-mean-square (RMS) are obtained and exported to an ASCII file by the MATLAB program *ttimecalbration*.

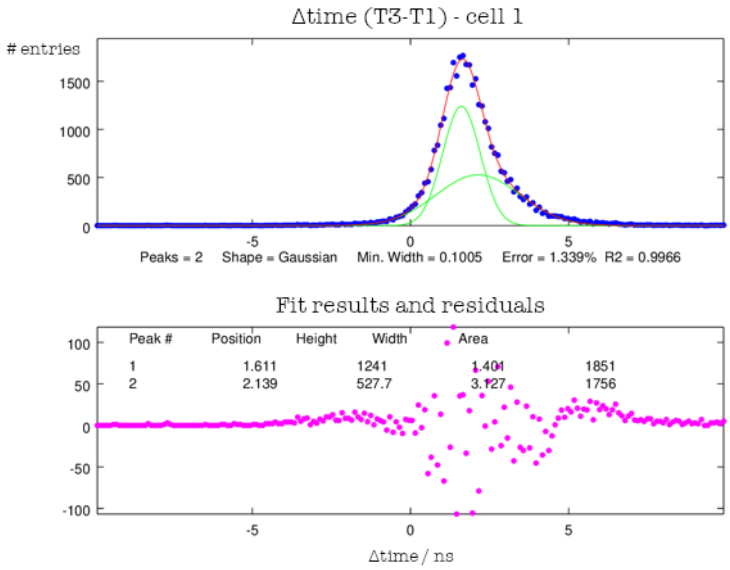

Figure 6.9: Top) Double Gaussian fit to the time difference peak. Bottom) Residual plot and peak information obtained for TRISTAN.

The centroids resulting from the composed fit are the input for the iterative process developed to find the 60 calibration parameters that minimize the system of 900 equations. Minimization is carried out by the Python code *ttimeitercal*. The iterative process is divided into the four steps outlined below.

1) Input centroids are stored in a data frame where the indices (rows) and columns refer to the cells of the top and bottom planes, respectively. The times of the bottom plane are centered with respect to one cell of the top plane. Input

USC UNIVERSIDADE DE SANTIAGO DE COMPOSTELA

parameters of the combinations of the top cell number 15 with all the bottom cells are selected. These constants are subtracted to the corresponding cells setting the entire row of the data frame to zero. Setting the combinations of one cell to zero reduces the calibration parameters to 59. Figures 6.10 and 6.11 show the original distribution and the resulting after the first step of the minimization process is performed.

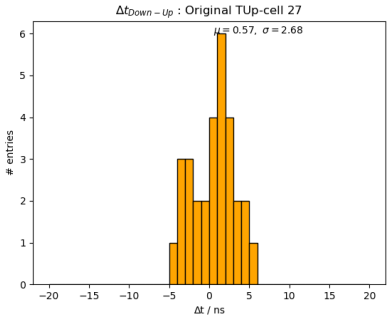

Figure 6.10: The original distribution of the time differences between all bottom cells and the top cell number 27.

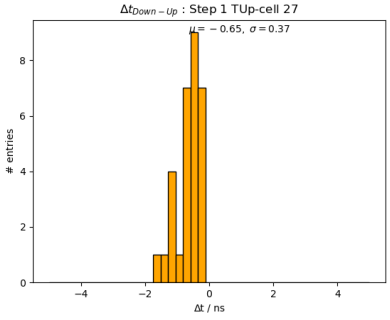

Figure 6.11: Time distribution of the top cell number 27 after the first step of the process.

2) Computation of the median of the time distribution, for the combination of each cell in the top plane with all cells in the bottom plane. The new constants are subtracted to the corresponding cells, in this case, to each column of the data frame as we refer to the top plane. The time distribution after the second step is shown in Figure 6.12.

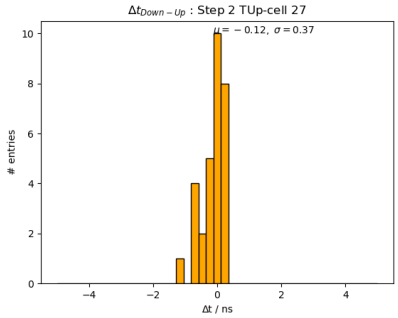

Figure 6.12: Time distribution of the top cell number 27 after the second step of the process.

3) Step 2 is repeated interchanging planes and calculating the median for the time distributions of each cell in the bottom plane with respect to all cells in the top plane. In this case, the constants are subtracted to each row of the data frame, giving the distribution displayed in Figure 6.13.

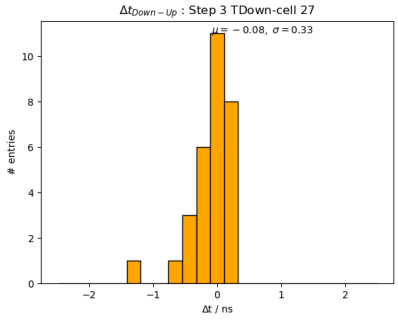

Figure 6.13: Time distribution of the top cell number 27 after the third step of the process.

USC UNIVERSIDADE DE SANTIAGO DE COMPOSTELA

4) The iterative process consists of repeating the aforementioned steps until it converges. Convergence is achieved once the constants of both planes differ less than 1% with respect to the previous iteration.

The result of the iterative process is a narrow time distribution centered at 0 ns. Normally, the process converges in no more than three iterations. Figure 6.14 shows the comparison of the distribution before and after the calibration process.

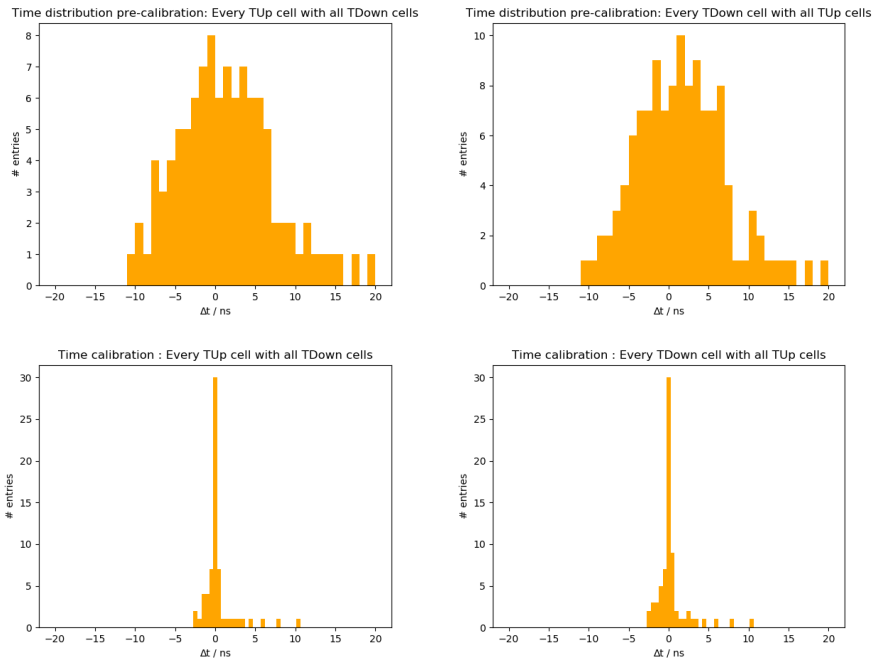

Figure 6.14: Comparison between the distributions before and after the calibration for all cells of left) top and right) bottom planes.

In TRAGALDABAS, the time calibration is performed using the C++ classes and methods already developed. The process followed is the same as for TRISTAN. A Gaussian fit is applied to the time differences distributions for all combinations of cells between two

planes. The mean and bin center of the histogram are extracted and then subtracted to the time differences of the measured data, which centers the distribution. Repeating the same steps a few times makes the distribution narrower after each step until it converges. Figure 6.15 presents an example of TRAGALDABAS time calibration.

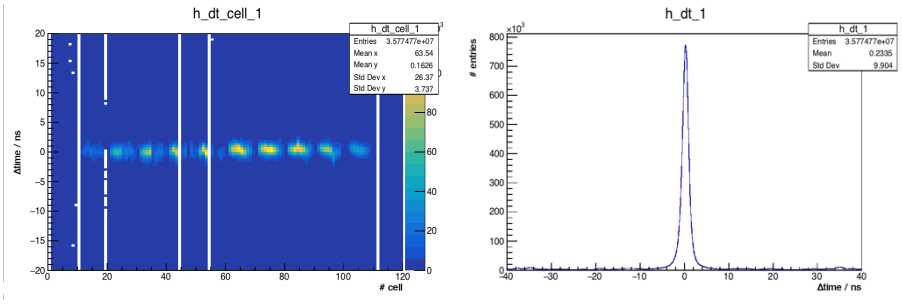

Figure 6.15: Time differences left) 2D map and right) projection.

The time calibration parameters of the detectors are stored in ASCII files. These constants are subtracted online from the measured times before performing the analysis of a CR shower.

6.3.3 Slewing correction

Signals produced when a CR particle interacts within the detector's active volume are sent to the read-out electronics. The charge integrated on the pads is related to the amplitude of the signals. As it was mentioned in Section 6.1, the differences in rise-time or amplitude can lead to differences in the digitizing time. This time shift depends on the ratio between the charge and amplitude of the signal, being the large signals the ones arriving first. The slewing correction is then an effect produced by the read-out electronics. The correction of the charge to time correlations can improve the time resolution considerably [108, 109]. Slewing correction consists of the mean deviation in time for each charge value, and its application to particles with different masses could improve the time resolution because the charge is also related to the mass and the velocity of the incident particle. Slewing effect is removed in TRAGALDABAS by fitting the two regions of the spectrum to two polynomials [108]. Due to the large size of TRISTAN pads this effect don't improve considerably the time resolution.

USC UNIVERSIDADE DE SANTIAGO DE COMPOSTELA

6.4 RANDOM COINCIDENCES

Accidental or random coincidences occur when unrelated pulses coincide by change, and they affect the rate of CRs measured by the detectors. The effect of the accidental coincidences has to be taken into account when correcting the rates because the efficiency correction, as will be explained in Section 6.6, is not enough when the environmental conditions suffer dramatic changes. An estimation of the expected random coincidence rate can be done by using simple probability arguments [110, 111]. If we assume a time window of size t_w within which the acquisition is open after a trigger signal is sent, a pulse arriving within a time interval of $2t_w$ represents a coincidence. The trigger configuration of TRISTAN and TRAGALDABAS is based on coincidences between two planes. However, the analysis will be extended to three planes in order to compare the results. In the simplest case of two RPCs in coincidence, an RPC producing r_A pulses per second means that the available time for the second RPC to produce a coincidence is the fraction $2r_A t_w$ of a second. If the rate of the second RPC is r_B, then the rate of accidental coincidences r_{Ac} after a long period is determined the following equation:

$$\mathrm{r_{Ac}} = \mathrm{r_A} \times \mathrm{P(t_w; B)} + \mathrm{r_B} \times \mathrm{P(t_w; A)}, \tag{6.5}$$

where $P(t_w; B)$ is the probability of plane B delivering a pulse within t_w when a pulse is sent by plane A, and $P(t_w; A)$ is the probability of plane A delivering a pulse within t_w when a pulse is sent by plane B.

$$\mathrm{P(t_w)} = 1 - \exp(-\mathrm{r\,t_w}) \approx \mathrm{r\,t_w}\,. \tag{6.6}$$

The probability when the window size t_w is much shorter than the individual rates is given in first order by Equation 6.6. Therefore, the rate of accidental coincidences is calculated as follows:

$$\mathrm{r_{Ac}} = 2\,\mathrm{r_A}\,\mathrm{r_B}\,\mathrm{t_w}\,. \tag{6.7}$$

Extending the argument to three planes it is easy to demonstrate that the rate is given by:

$$r_{Ac} = 3\, r_A\, r_B\, r_C\, t_w\,. \tag{6.8}$$

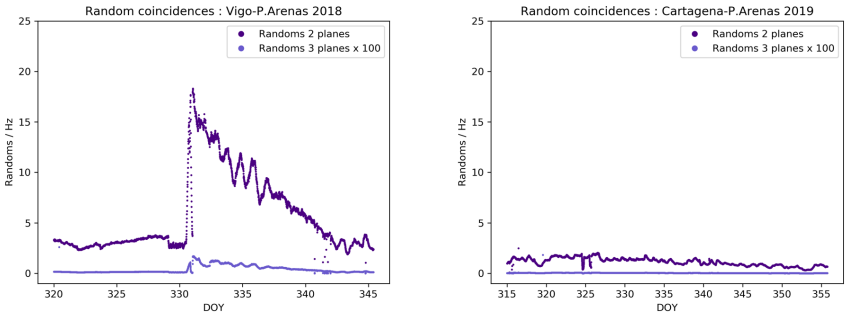

Figure 6.16: Random coincidences for two samples of TRISTAN data left) unstable and right) stable environmental conditions.

TRISTAN window size is set to 40 ns, whereas for TRAGALDABAS, it is 50 ns. The effect of the random coincidences is dominant under unstable environmental conditions such as extreme temperature changes. An increase in the temperature also produces an increase in the electronic noise in the detector.

In Figure 6.16, the left plot corresponds to a period of TRISTAN data where the working conditions changed from stable to unstable due to a drastic temperature increase caused by an air conditioning issue. The average trigger rate for such period was about 110 Hz, which makes the effect of the random coincidences very important, reaching 18%. On the other side, a period of stable conditions is shown, and the effect of the random coincidences is below 3% of the total coincidences rate for a trigger rate of around 120 Hz.

6.5 Active and Dead Times

Additional corrections to the data due to active and dead times might be required. The active time accounts for the seconds the detector takes data without any interruption. Data averaging over certain periods

USC UNIVERSIDADE DE SANTIAGO DE COMPOSTELA

require the active time correction due to the fact that the acquisition time might differ per interval. The dead time correction becomes important when operating at very high trigger rates. The relationship between real and measured counting rates, considering that the non-dead time disturbed distribution is Poissonian, is given by the next equation for the non-paralyzable dead time case:

$$R_r = \frac{R_m}{1 - \tau R_m}, \tag{6.9}$$

where R_r and R_m are the real and measured counting rates, respectively, and τ is the dead time [111]. In this case, its effect is less than 0.5% for a measured trigger rate of around 100 Hz and a dead time of 4 μs, making it almost negligible.

6.6 EFFICIENCY

RPCs are used in high-energy physics experiments due to their high efficiency. The peak of the efficiency distribution aims to be around 99%, while the tail at lower efficiency values is due to RPCs working out of the range of the optimal parameters. Normally, the efficiency drops are originated by dramatic temperature changes. These changes cause the saturation of the HV and the background currents, which may increase the number of streamer signals, and so the recovery time of the electrodes. TRISTAN and TRAGALDABAS RPCs operate in avalanche mode at the edge of the voltage plateau. Thus, HV changes cause major changes in the working conditions affecting the measured CRs rate. RPCs at their optimum involves a high efficiency and low noise level.

Several methods, labeled as *tefficiency*, have been developed to study the detection efficiency. The efficiency of the whole detector is calculated by multiplying the individual efficiencies of each RPC. Comparing the different methods described in this section the information about the systematic uncertainties can be inferred.

USC UNIVERSIDADE DE SANTIAGO DE COMPOSTELA

6.6.1 Tracking method

Usually, the CR detection efficiency is calculated by the tracking method. This method consists of finding the particles going through an RPC plane that is not in trigger using the information given by the RPCs that are in coincidence trigger. Hence, the reason why the random coincidences effect is important. The efficiencies for each plane can be obtained by changing the coincidence trigger configuration, but we assume that all RPC planes behave similarly. Therefore, all RPCs have the same efficiency given by the tracking method (ϵ_{Tr}) for the plane T2 when T1 and T3 are in coincidence.

To determine the efficiency of unpacked HLD files, the look-up table, and the charge and time calibration constants are needed. CR events are processed individually, starting by filtering the hits according to the charge calibration constants. A second filter using the time calibration constants can be added to reduce noise contamination. However, the charge filter is enough to remove most of the random coincidences, which probability for three planes is less than 2%, as it was shown in Section 6.4. For events with a hit multiplicity equal to one in T1 and T3, the algorithm searches for hits in T2. The information of the fired cells in T1 and T3, i.e., the Kx and Ky coordinates, defines the searching grid in T2. T2 efficiency, for the incident angles defined by T1-T3 cell centers, is given by the ratio between the number of events with and without at least one hit in T2 during a certain time. TRISTAN and TRAGALDABAS efficiencies are calculated on a two-hour basis. Data averaging over a certain period requires a correction related to the active time of the detector. The tracking method of TRISTAN has been developed in MATLAB whereas for TRAGALDABAS it was implemented in C++.

In Figure 6.17, a comparison between the efficiency for vertical incident particles with and without the random coincidences correction is presented. This correction is of special interest for the period of the first latitudinal survey performed by TRISTAN, which will be described in Chapter 7, due to the air conditioning issues that caused extreme temperatures where the detector was located. For other periods the correction is included but is less significant.

USC
UNIVERSIDADE DE SANTIAGO DE COMPOSTELA

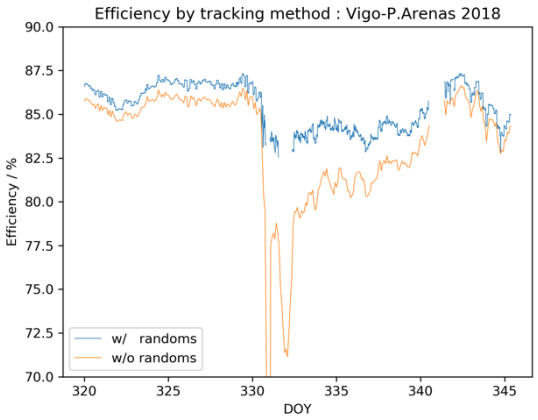

Figure 6.17: Efficiency for vertical incident particles with and without the random coincidences correction. TRISTAN data sample.

6.6.2 Principal component analysis

RPC performance depends on many factors such as HV, background currents, environmental conditions, gas flow, among others related to the building process. Changes in the conditions have a different impact on RPC efficiency. Knowing the efficiency of T2, we can estimate the efficiency of the remaining planes by performing a principal component analysis (PCA) [112]. The main goal of the PCA is to understand the relationship between a group of slow control variables and the efficiency calculated by the tracking method for the T2 plane. This technique consists of a dimensionality reduction by linearly transforming the original variables into a new set of uncorrelated variables, which are called principal components (PCs). The first PC accounts for the maximum variance and so on.

Taking the HV, background currents, pressure, temperature, and humidity of T2 as inputs or features, the PCA provides their relationship with the target variable, which is the efficiency of the T2 plane. The resulting equations that describe the target variable as a function of the slow control variables are used to obtain the efficiency of the other planes. PCA algorithm has been implemented in Python from scratch, and the steps will be described below.

Since the majority of optimization or machine learning algorithms, like PCA, perform better when all the features are along the same scale, data has to be standardized. It makes sense because the feature subspace given by the PCA maximizes the variance along the axis. Standardization of a feature value is given by the following calculation:

$$x_{std}^{i} = \frac{x^{i} - \mu_x}{\sigma_x}, \tag{6.10}$$

where μ_x and σ_x are the mean and the standard deviation of the feature variable. As a result of the standardization, feature values have a mean of 0 and standard deviation of 1 so they have the same parameters as a normal distribution.

Correlation between pairs of feature variables measures how they vary with each other. The covariance σ_{jk} for two features x_j and x_k with n values is obtained as follows:

$$\sigma_{jk} = \frac{1}{n-1}\sum_{i=1}^{n}\left(x_j^i - \mu_j\right)\left(x_k^i - \mu_k\right). \tag{6.11}$$

As a consequence of the standardization, the means are zero, and the covariance matrix of the standardized data ($\boldsymbol{X}$) can be calculated by Equation 6.12.

$$\boldsymbol{\Sigma} = \frac{1}{n-1}\mathbf{X}^{T}\mathbf{X}. \tag{6.12}$$

Directions and magnitudes of maximum variance, or the PCs, are represented by the eigenvectors and eigenvalues of the covariance matrix. Eigenvector v and eigenvalue λ of the covariance matrix, satisfy the condition $\Sigma v = \lambda v$. The eigenvalues of $\boldsymbol{\Sigma}$ are the roots of the following characteristic equation:

$$\det(\boldsymbol{\Sigma} - \lambda\mathbf{I}) = 0, \tag{6.13}$$

and the eigenvectors are calculated for the correspondent eigenvalues.

USC UNIVERSIDADE DE SANTIAGO DE COMPOSTELA

Eigenpairs are sorted based on the magnitude of their eigenvalues to find the PCs with the highest variability. Eigenvectors of symmetric matrices are orthogonal which means that the first PC explains most of the variance and is orthogonal to the second, and so on. The number of PCs selected for the dimensionality reduction is based on the cumulative explained variance. An example of a data set of TRISTAN is shown in Figure 6.18. The first two PCs are selected to reduce a 5-dimensional feature space to a 2-dimensional feature subspace, as they explain almost 90% of the variance.

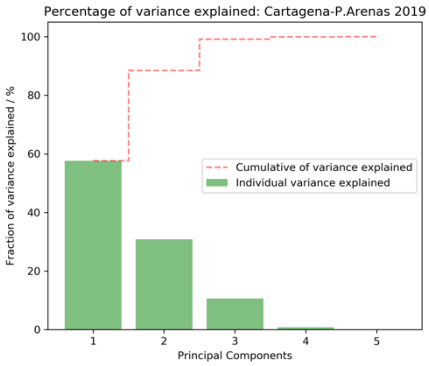

Figure 6.18: PCs individual and cumulative explained variance representation.

Correlation matrices before and after performing the PCA are shown in Figure 6.19 for the same data set.

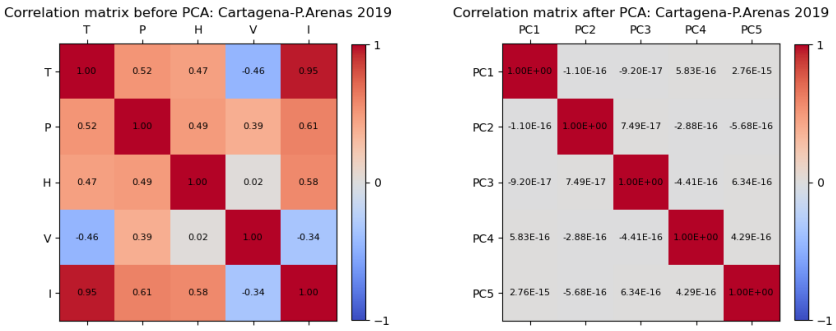

Figure 6.19: Correlation matrices left) before, and right) after the PCA. Inputs: temperature (T), pressure (P), humidity (H), HV (V), and currents (I).

The projection matrix $\boldsymbol{W}$ is constructed with the eigenvectors of the highest explained variance and is used to transform the original feature data onto the new reduced feature subspace. The transformation is done via Equation 6.14.

$$\mathbf{Y} = \mathbf{X} \cdot \mathbf{W}\,, \tag{6.14}$$

where $\boldsymbol{Y}$ is the matrix of the transformed feature data. Figure 6.20 presents the PCs corresponding to the aforementioned set of data. In this case, the 5-dimensional subspace is plotted to show the importance of the first two PCs and how higher components account for small oscillations or short-term variability.

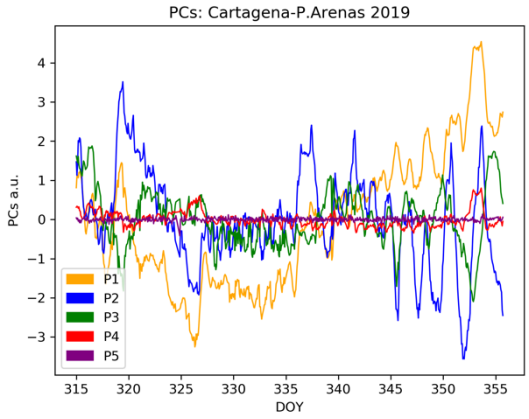

Figure 6.20: Example of PCs behavior for the above-mentioned data set.

The first two components describe almost 90% of the feature data variability. It is important to bear in mind that the target variable for the PCA is the efficiency of T2 from the tracking method. Several methods have been developed to find the best criteria for estimating the efficiency of the remaining planes. The best results are given by a 2-dimensional fit of the first two PCs as a function of the efficiency (Figure 6.21) and a running PCs linear regression method. The running method consists of a first linear regression of PC1 and efficiency,

USC
UNIVERSIDADE DE SANTIAGO DE COMPOSTELA

followed by *n* fits of the residuals, with *n* equal to the dimensions of the transformed subspace. This method is useful when more than two components are taken into account.

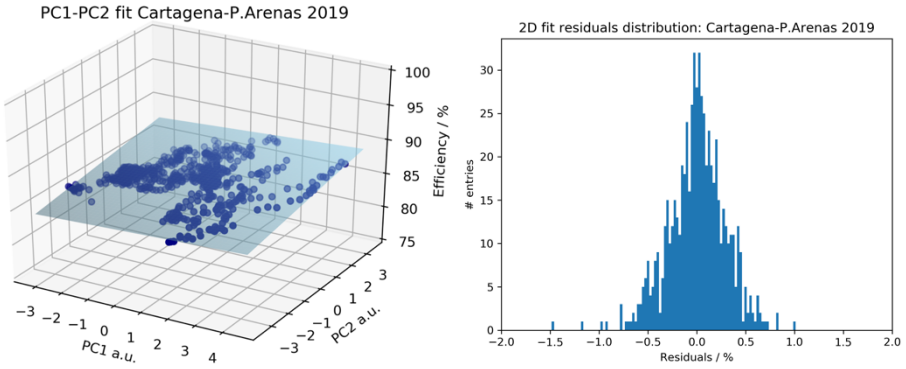

Figure 6.21: Example of the 2-dimensional fit of PC1 and PC2. Left) 3D plot with the efficiency. Right) Residuals distribution.

Finally, the PCA produces a set of efficiency values (ϵ_{PCA}) for all planes based on the relationship between the slow control variables and the efficiency of T2. In contrast to the efficiency obtained through the tracking method, the values obtained by the PCA method differ for each plane due to the different RPC conditions (Figure 6.22). For such analysis, we assume that the efficiency of all planes behaves similarly with the feature variables.

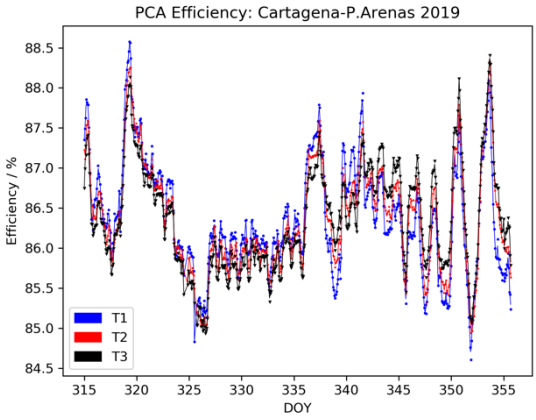

Figure 6.22: The efficiency of T1, T2, and T3 given by the PCA method.

6.6.3 Charge study

Measurements of the charge of CR events provide important information not only about the median charge and the streamer fraction but also about the efficiency [108]. The charge distribution of hits that pass the threshold of the charge calibration is highly asymmetrical, so the median is a better estimator than the mean in this case. Figure 6.23 shows the total charge distribution of T1 for a certain time.

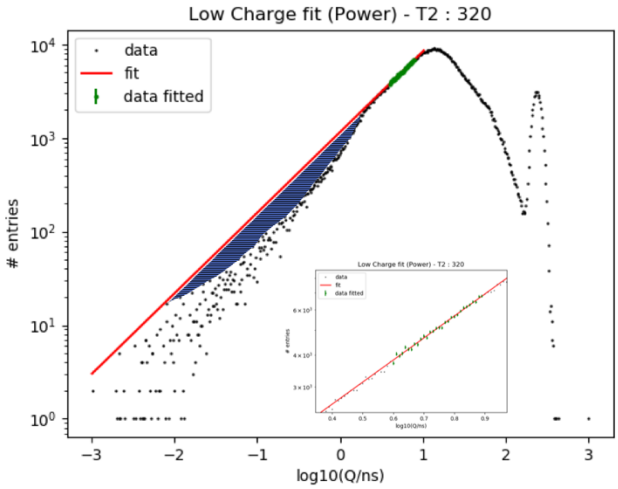

Figure 6.23: Example of the linear regression used to calculate the inefficiency.

The function enclosing the blue dashed area provides the inefficiency of the RPC plane by fitting to the left side of the peak:

$$f_\epsilon(q, a, b) = a\, q^b\,, \tag{6.15}$$

where q is the charge, and b is the slope of the exponential as it is represented in logarithmic scale. The efficiency is calculated as follows:

$$\epsilon_{QFit} = 1 - \frac{\int_{-\infty}^{1} f_\epsilon(q, a, b)}{\int_{-\infty}^{1} f_\epsilon(q, a, b) + \int_{q_{min}}^{q_{max}} q}\,. \tag{6.16}$$

USC UNIVERSIDADE DE SANTIAGO DE COMPOSTELA

The streamer fraction was not studied in detail, however, the method developed to obtain the efficiency has been extended to enable its calculation for future analysis. Equation 6.17 represents the function used to separate streamers from large avalanches.

$$f_\epsilon(q, a, b, c) = a\, q^b \exp(-q/c)\,. \qquad (6.17)$$

The number of streamers is given by the enclosed red dashed area between the charge spectrum and the fitted curve. Like for determining the efficiency, the ratio between extrapolated and total areas yields the streamer fraction (Figure 6.24).

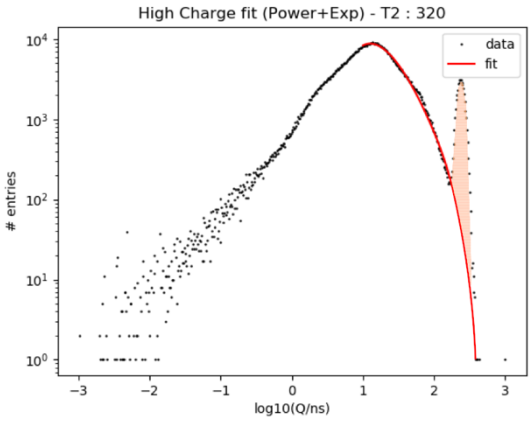

Figure 6.24: Streamer fraction estimation.

Efficiency by the charge method (ϵ_{QFit}) is calculated in 2-hour intervals. The points entering the linear regression, as the charge distribution is shown in the logarithmic scale, are those that minimize the chi-square of the fit. This method has been implemented first in MATLAB and then adapted to Python. Random coincidences correction is also necessary since the effect is not taken into account when fitting the charge distributions. Figure 6.25 shows the efficiency obtained for all RPC planes for a data sample of the TRISTAN detector.

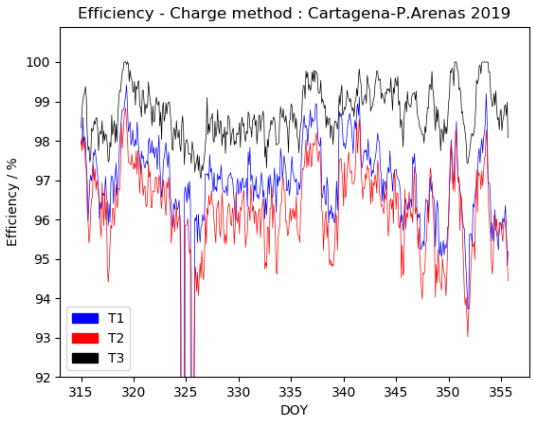

Figure 6.25: The efficiency of T1, T2, and T3 given by the charge method.

6.7 EVENT RECONSTRUCTION

Tracking CR particles together with calibration are the main tasks before performing the data analysis. The determination and study of the trajectories of the charged particles that leave a footprint in the detector can be done using different methods. TimTrack (acronym of Timing and Tracking) is the algorithm developed within the framework of the TRASGO project in order to reconstruct CR events. Knowing the trajectories of the particles is important to identify their nature and to perform a detailed physics analysis.

TimTrack allows the tracking of particles using both spatial and temporal variables in one step, and it is based on the least-squares method (LSM). As a result, a description of the method is done using a full matrix formalism, which gives all the kinematical information of a particle in an object called saeta (SmAllest sEt of daTA). A saeta is a vector that contains the minimum set of parameters required to describe the trajectory of a particle:

$$\mathbf{s} = (X_0, X', Y_0, Y', T_0, S) . \qquad (6.18)$$

USC UNIVERSIDADE DE SANTIAGO DE COMPOSTELA

where (X_0, Y_0) are the coordinates of the particle at the reference plane $z = 0$, (X', Y') are the slopes projected onto X-Z and Y-Z planes, respectively, T_0 is the time at which the particle crossed the reference plane, and S is the slowness, i.e., the inverse of the velocity of the incident particle.

The parameters of a saeta are obtained by minimizing the distance between the model and the experimental data due to the fact that TimTrack is based on LSM. A detailed explanation of the algorithm can be found in [113, 114]. The model developed for the event reconstruction of both TRISTAN and TRAGALDABAS is a non-linear model **m**(**s**) with the following equations:

$$\begin{aligned} \mathrm{m_x} &= \mathrm{X_0} + \mathrm{X'} \cdot \mathrm{z} \\ \mathrm{m_y} &= \mathrm{Y_0} + \mathrm{Y'} \cdot \mathrm{z} \\ \mathrm{m_t} &= \mathrm{T_0} + \mathrm{S} \cdot \mathrm{k} \cdot \mathrm{z} \end{aligned} \tag{6.19}$$

where *k* is the module of the direction vector defined by the projected slopes as follows:

$$\mathrm{k}^2 = \left(1 + \mathrm{X'}^2 + \mathrm{Y'}^2\right). \tag{6.20}$$

A saeta consists of the parameters that fulfill the minimum condition of the chi-square, and can be calculated by the following equation:

$$\mathbf{s} = \mathbf{K}^{-1} \cdot \mathbf{a}\,, \tag{6.21}$$

where $\boldsymbol{K}$ is the configuration matrix, which is always a squared symmetric definite positive matrix. The inverse of $\boldsymbol{K}$ is known as the error matrix because it contains the uncertainties of the parameters that form a saeta. The vector $\boldsymbol{a}$ is called the reduced data vector. It compresses the initial data of dimension n_d into a vector of dimension n_s, which is equal to the number of parameters in a saeta. The sum of the individual configuration matrices and reduced data vectors in a detector composed of different detection volumes, produce the total $\boldsymbol{K}$ matrix and total $\boldsymbol{a}$

USC UNIVERSIDADE DE SANTIAGO DE COMPOSTELA

vector. TRISTAN and TRAGALDABAS saetas are obtained as follows:

$$\mathbf{s} = \left(\sum_{\mathrm{i}}^{\mathrm{n}} \mathbf{K}_{\mathrm{i}} \right)^{-1} \cdot \left(\sum_{\mathrm{i}}^{\mathrm{n}} \mathbf{a}_{\mathrm{i}} \right), \tag{6.22}$$

where n is the number of RPC planes. The non-zero elements of the individual 6×6 matrix and the 6×1 vector applied per plane are given by Equations 6.23 and 6.24, respectively.

$$\begin{aligned}
\mathrm{K}_{i_{11}} &= \mathrm{w_x} \\
\mathrm{K}_{i_{12}} &= \mathrm{w_x}\, \mathrm{z_i} \\
\mathrm{K}_{i_{22}} &= \mathrm{w_x}\, \mathrm{z_i^2} + \mathrm{S^2}\, \mathrm{w_t}\, \mathrm{X'^2}\, \mathrm{z_i}^2\, \mathrm{k^{-2}} \\
\mathrm{K}_{i_{24}} &= \mathrm{S^2}\, \mathrm{w_t}\, \mathrm{X'}\, \mathrm{Y'}\, \mathrm{z_i}^2\, \mathrm{k^{-2}} \\
\mathrm{K}_{i_{25}} &= \mathrm{S}\, \mathrm{w_t}\, \mathrm{X'}\, \mathrm{z_i}\, \mathrm{k^{-1}} \\
\mathrm{K}_{i_{26}} &= \mathrm{S}\, \mathrm{w_t}\, \mathrm{X'}\, \mathrm{z_i}^2 \\
\mathrm{K}_{i_{33}} &= \mathrm{w_y} \\
\mathrm{K}_{i_{34}} &= \mathrm{w_y}\, \mathrm{z_i} \\
\mathrm{K}_{i_{44}} &= \mathrm{w_y}\, \mathrm{z_i^2} + \mathrm{S^2}\, \mathrm{w_t}\, \mathrm{Y'^2}\, \mathrm{z_i}^2\, \mathrm{k^{-2}} \\
\mathrm{K}_{i_{45}} &= \mathrm{S}\, \mathrm{w_t}\, \mathrm{Y'}\, \mathrm{z_i}\, \mathrm{k^{-1}} \\
\mathrm{K}_{i_{46}} &= \mathrm{S}\, \mathrm{w_t}\, \mathrm{Y'}\, \mathrm{z_i}^2 \\
\mathrm{K}_{i_{55}} &= \mathrm{w_t} \\
\mathrm{K}_{i_{56}} &= \mathrm{w_t}\, \mathrm{z_i}\, \mathrm{k} \\
\mathrm{K}_{i_{66}} &= \mathrm{w_t}\, \mathrm{z_i}^2\, \mathrm{k^2}
\end{aligned} \tag{6.23}$$

$$\mathbf{a}_{\mathrm{i}} = \begin{pmatrix} \mathrm{w_x}\, \mathrm{x_i} \\ \mathrm{w_x}\, \mathrm{x_i}\, \mathrm{z_i} + \mathrm{S}\, \mathrm{w_t}\, \mathrm{X'}\, \mathrm{z_i}\, \mathrm{T}\, \mathrm{k^{-1}} \\ \mathrm{w_y}\, \mathrm{y_i} \\ \mathrm{w_y}\, \mathrm{y_i}\, \mathrm{z_i} + \mathrm{S}\, \mathrm{w_t}\, \mathrm{Y'}\, \mathrm{z_i}\, \mathrm{T}\, \mathrm{k^{-1}} \\ \mathrm{w_t}\, \mathrm{T} \\ \mathrm{w_t}\, \mathrm{z_i}\, \mathrm{T}\, \mathrm{k} \end{pmatrix} \tag{6.24}$$

USC UNIVERSIDADE DE SANTIAGO DE COMPOSTELA

and

$$T = t_i + S\,X'^2\,z_i\,k^{-1} + S\,Y'^2\,z_i\,k^{-1} \qquad (6.25)$$

Due to the symmetry of the configuration matrix, the $K_{i\,jk}$ elements are equal to the $K_{i\,kj}$. Parameters (x_i, y_i, t_i) are the experimental measurements at plane *i,* whose position is fixed at z_i (Figure 6.26).

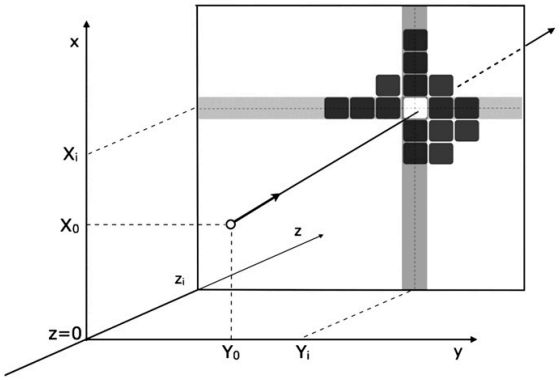

Figure 6.26: Pads provide two coordinates and a time. (Reprinted from [113], with permission from Elsevier)

To solve Equation 6.22 an iterative process is carried out since the configuration matrix and the reduced data vector depend on the parameters *S,* $X'$and Y'. The iterative process starts with an initial solution called input saeta, which is the trajectory defined by the upper and lower plane hit coordinates. The process stops when the Euclidean module of the solution differs less than 10^{-5} from the previous one. This model has been implemented in the existing TRAGALDABAS software as a new class called *trpcsaeta*. Even though the same model has been included for TRISTAN as *ttracking* the data presented in this work has no time constraint in the time of flight of the events. Thus, the model becomes more simple and can be derived from Equations 6.23 and 6.24 removing the time component. In this case, Equation 6.22 has an exact solution, which is obtained directly without performing an iterative process. In Figure 6.27, the main parameters obtained by applying the aforementioned method, are shown.

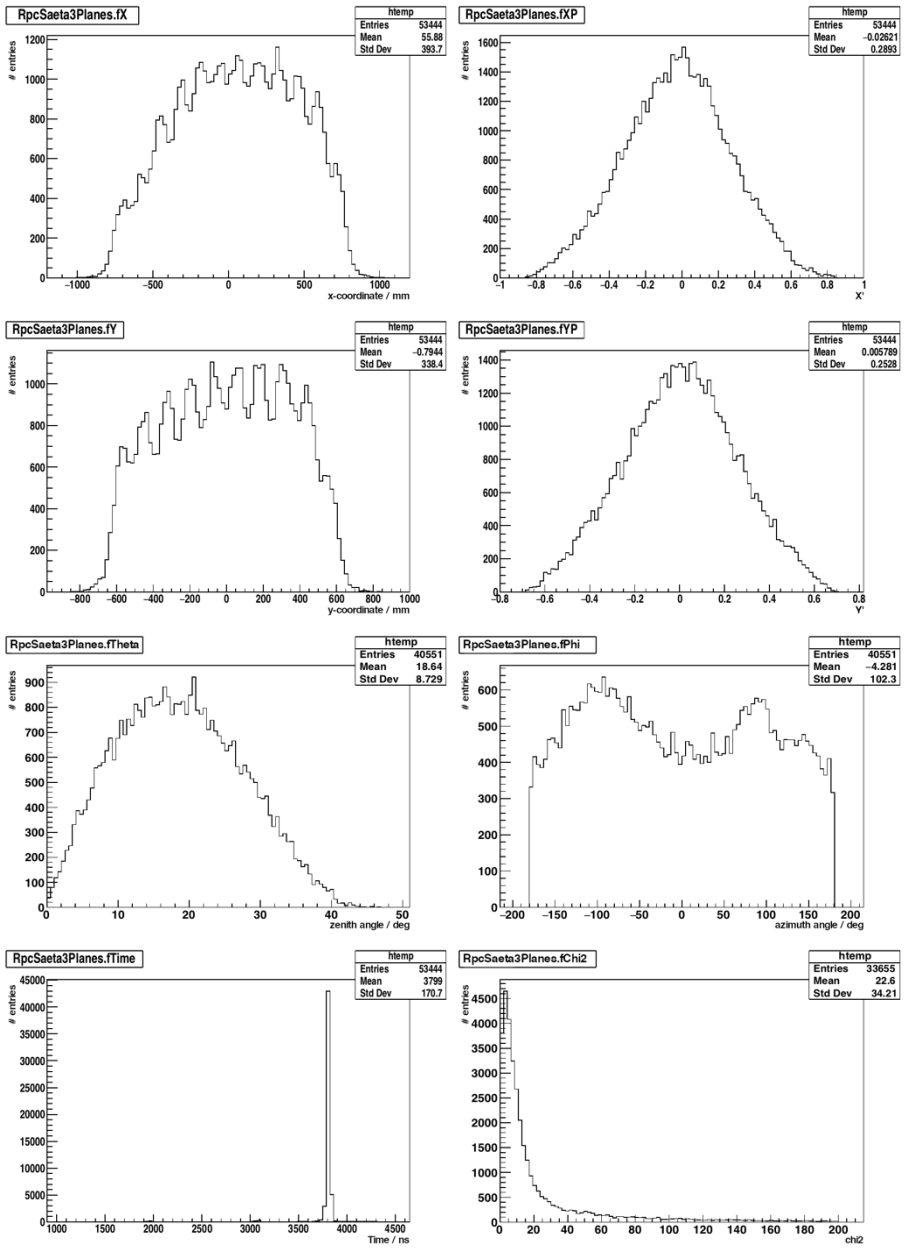

Figure 6.27: Main information available for all reconstructed saetas. Position on xy-plane, slope, zenith and azimuth angles, time and chi-square distribution.

USC
UNIVERSIDADE DE SANTIAGO DE COMPOSTELA

Saetas are constructed with the charge-time calibrated hits. Event reconstruction provides information about the rate of CRs for different angular sectors and multiplicities. Multiplicity refers to the number of reconstructed tracks a CR event has. CR data must be calibrated by the algorithms and methods described throughout this chapter before being analyzed or correlated with variables like the magnetic field, pressure, and temperature.

6.8 PERFORMANCE

The high efficiency and excellent time resolution of RPCs, together with the low cost of fabrication and hassle-free maintenance, make them a good candidate for tracking and timing purposes in high-energy physics experiments. To evaluate the capability of an RPC-based detector, position, time, and angular resolutions have to be provided. These parameters have been calculated by running a Monte Carlo simulation for both detectors. A Python program called *tgenedigitana* has been developed for such a purpose. Events are generated under the condition of having one fired cell or hit per plane in the same way as explained in Section 6.2. Ten thousand saetas are created and digitized to extract the coordinates and time on each detector's plane. Then, the TimTrack algorithm explained in Section 6.7 takes these variables and reconstructs the saeta, giving the set of six parameters shown in Equation 6.18. The difference between reconstructed and simulated parameters gives the residuals. Residuals of position, time, and zenith angle are used to estimate the global resolution of each detector. We assume that the distributions of the residuals can be approximated by a Gaussian, to fit the histograms and get the sigma. Table 6.3 shows the global resolutions obtained for both detectors by applying the TimTrack reconstruction algorithm, and in parenthesis, the first significant digits of the standard uncertainties.

Table 6.3: Resolutions obtained for each detector after TimTrack.

Detector	σ_Θ / deg	σ_t / ps	σ_x / mm	σ_y / mm
TRISTAN	6.35 (4)	272 (1)	64.8 (3)	62.4 (3)
TRAGALDABAS	1.45 (1)	133 (1)	25.8 (2)	25.0 (2)

USC UNIVERSIDADE DE SANTIAGO DE COMPOSTELA

6.8.1 Angular resolution

The angular resolution obtained for both detectors is shown in Figure 6.28. TRAGALDABAS has a better resolution than TRISTAN due to its higher granularity for the same active volume, and a longer distance between RPC planes. The simulation carried out provide an angular resolution $\sigma_\theta = 1.45 \pm 0.01$ degrees for the first, and $\sigma_\theta = 6.35 \pm 0.04$ degrees for the second, with a notable deviation from the gaussian far from the mean value.

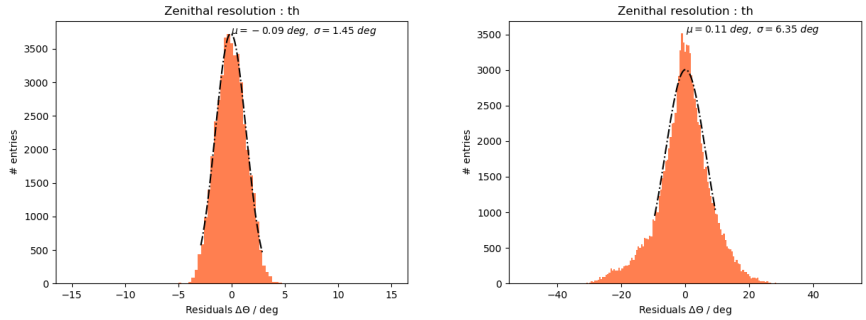

Figure 6.28: Theta residuals fit. Left) TRAGALDABAS. Right) TRISTAN.

6.8.2 Time resolution

The estimation of the time resolution involves the time of flight and the time it takes to propagate the signal from the impact point to the center of the cell where the read-out is performed. Taking into account both times we obtained a global time resolution $\sigma_t = 133 \pm 1$ ps for TRAGALDABAS, and $\sigma_t = 272 \pm 1$ ps for TRISTAN.

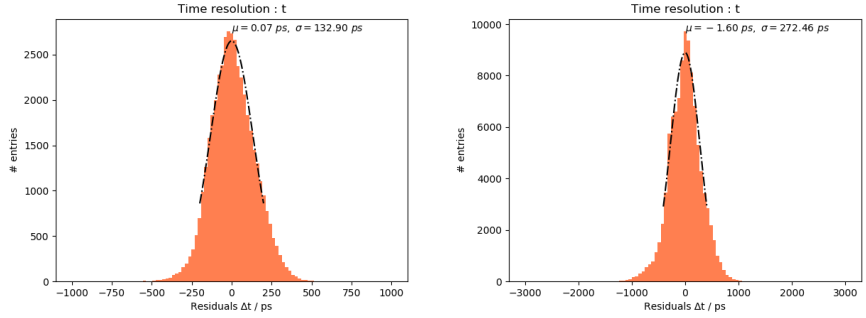

Figure 6.29: Time residuals fit. Left) TRAGALDABAS. Right) TRISTAN.

USC UNIVERSIDADE DE SANTIAGO DE COMPOSTELA

The time resolution is better for the TRAGALDABAS detector due to its geometry (Figure 6.29). In the same way, as for the angular resolution, the higher granularity or smaller pad size offers the best results for the same RPC dimensions.

6.8.3 Position resolution

Pad size determines the position resolution for both detectors. The simulation carried out provides a position resolution in x-coordinate $\sigma_x = 25.8 \pm 0.2$ mm for TRAGALDABAS, and $\sigma_x = 64.8 \pm 0.3$ mm for TRISTAN. For the y-coordinate the results are $\sigma_y = 25.0 \pm 0.2$ mm for the first, and $\sigma_y = 62.4 \pm 0.3$ mm for the second (Figure 6.30).

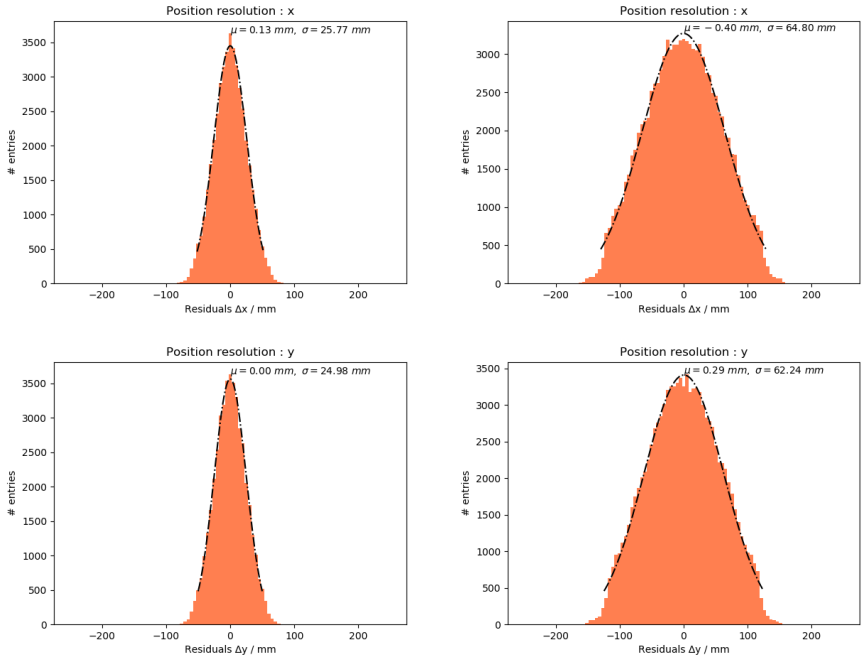

Figure 6.30: Position residuals fit. Left) TRAGALDABAS. Right) TRISTAN.

USC
UNIVERSIDADE
DE SANTIAGO
DE COMPOSTELA

USC
UNIVERSIDADE
DE SANTIAGO
DE COMPOSTELA

7 RESULTS

Data analysis is the final stage of the detector's data processing, and it is when the capabilities of the whole system are verified. This chapter shows the final results and corrections of the calibrated data by different external variables. The dependency of the rate of CRs of TRISTAN and TRAGALDABAS on the barometric pressure, atmospheric temperature, cutoff rigidity, and space weather events has been studied in detail.

7.1 INTRODUCTION

The natural continuation of the calibration and reconstruction processes, explained in the previous chapter, is the analysis of the data. In this chapter, a detailed description of the data-taking campaigns of TRISTAN and TRAGALDABAS used in this work, and the final results obtained using the calibrated and corrected data, are given. The development of algorithms suitable for all periods has been challenging, due to the different conditions under which the detectors have been operating. Several approaches have been tried out before finding the best calibration parameters, which have been applied to the raw data in order to reconstruct the CR events. However, the calibrated data cannot be used directly to search for correlations with other variables before correcting it by the local environmental conditions. CRs are affected by the Earth's atmosphere, as has been introduced in Section 1.5. Hence, a correction of the calibrated data is needed in order to study the effects of the cutoff rigidity and the conditions at different atmospheric layers for TRISTAN and TRAGALDABAS data. Both detectors have been described, in detail, in Chapter 3, and the main difference between them is that TRAGALDABAS has been designed to operate as a static station, whereas TRISTAN performed several latitudinal surveys before being converted into a static station at the BAE-JCI.

USC
UNIVERSIDADE DE SANTIAGO DE COMPOSTELA

7.2 DATA-TAKING CAMPAIGNS

Even though the detectors used in this thesis are based on the same technology, and their layouts are very similar, the data analysis differs slightly depending on the operating conditions. The data-taking campaigns studied in this chapter correspond to all TRISTAN available data, which is the main task of this work, and a sample of 2015 TRAGALDABAS data because of the information it has concerning solar modulation.

7.2.1 TRISTAN

The data sample of this detector includes three latitudinal surveys, which were carried out in 2018 and 2019, and two static CR measurements at Santiago de Compostela and Antarctica in 2019 and 2020, respectively. Paths and locations are shown in Figure 7.1. TRISTAN was commissioned in the LIP Coimbra to guarantee the detector's integrity and stability before the first latitudinal journey. In the Appendix, the figures of all slow control variables are available to compare the different operating conditions of the most important variables of the detector during the numerous data-taking campaigns.

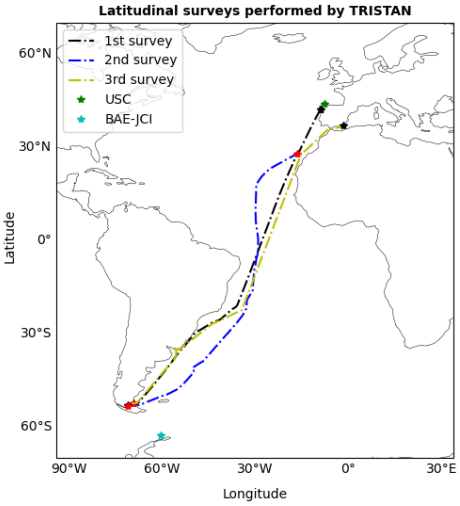

Figure 7.1: TRISTAN latitudinal surveys and static locations. The black and red stars mark the start and end points of the different journeys, whereas the green and cyan stars indicate the static locations.

7.2.1.1 Latitudinal survey 2018

The first latitudinal scan was performed between November 16th and December 12th, 2018. The detector was installed in a thermally controlled room onboard the Sarmiento de Gamboa vessel at Vigo, Spain (42º14'13" N, 8º43'59" W) below the deck. After almost one month of registering CR events across the Atlantic Ocean, the data acquisition was stopped at Punta Arenas, Chile (53º09'17" S, 70º54'41" W). It is important to bear in mind that TRISTAN is part of ORCA, and this was the first time an experiment of this kind was carried out. Yearly latitudinal surveys with a neutron monitor were performed between 1994 and 2007 from Seatle, United States, to McMurdo, Antarctica [115]. However, none of them have a system like ORCA, which combines neutron, muon, and electron measurements providing more information about the secondary CRs, for example, directionality.

The dates of this survey correspond to a range in the day of the year (DOY) from 320 to 346. TRISTAN ran smoothly from Vigo to approximately the equator (DOY 330) when the air conditioning system (AC) of the Sarmiento de Gamboa suffered terminal damage, which couldn't be fixed.

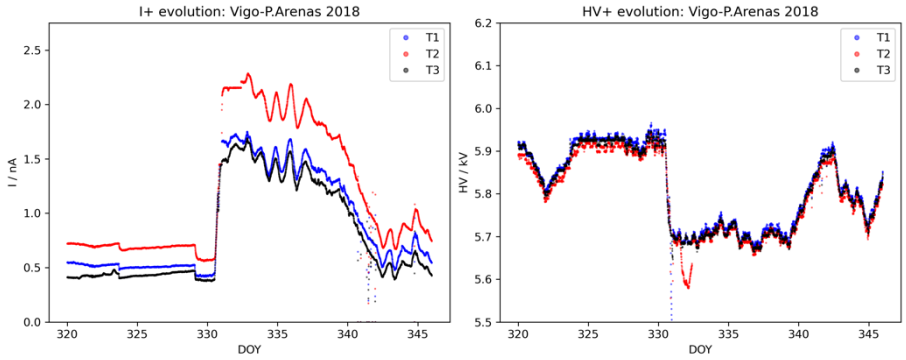

Figure 7.2: First survey slow control. Left) T3 background current growth caused by an abrupt increase of the temperature of more than 10 ºC. Right) T3 HV behavior as a function of DOY shows the drop caused by the saturation of the currents after the AC failure of DOY 330 and DOY 340 oscillations.

USC UNIVERSIDADE DE SANTIAGO DE COMPOSTELA

The AC failure caused a dramatic increase in the temperature due to the extreme environmental conditions of the equator region, which affected the background currents of the RPCs, among other variables (Figure 7.2). The HV dynamic adjustment of the HV PS explained in Section 4.5.2 avoided unrecoverable damage to the RPCs by reducing the HV value when the currents reached the saturation limit. The CR data registered at the time currents of the T2 plane were limiting (DOY 331) has been removed from the analysis. DOY 341 has been discarded too because of the high oscillations of the HV. Another consequence of the currents' increase can be seen in Figure 7.3, where the self-trigger rate of the T3 plane and the number of random or accidental coincidences, calculated by Equations 6.7 and 6.8, are represented. The efficiency obtained by the three different methods described in Section 6.6 has to be corrected by the random coincidences effect to suppress the undesired noise from the analysis.

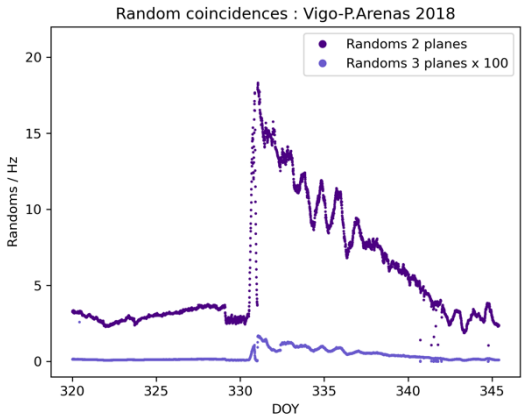

Figure 7.3: Effect of randoms in the first survey for two and three planes. Random coincidences for three planes are multiplied by 100 for visualization.

Although the gas flow was reduced to half of its average value at the end of the journey, that data was used for the analysis due to the well-operating conditions of the RPCs. At Punta Arenas, the detector was turned off and kept in the thermalized room while Sarmiento de Gamboa assisted in other experiments in the surroundings of BAE-JCI, and it was turned on at the start of the next survey.

USC UNIVERSIDADE DE SANTIAGO DE COMPOSTELA

7.2.1.2 Latitudinal survey 2019-I

The return leg of the two-way latitudinal survey that started in 2018 took place between February 28th and April 9th, 2019, i.e., from DOY 59 to 99. At this time, TRISTAN and ORCA were operating separately as the second was installed in December 2018 at BAE-JCI (62º39'46" N, 60º23'20" W).

Knowing the conditions of the AC system and its non-functional state since the previous journey, the saturation limit of the currents was increased to overcome the high-temperature region without losing data. Nevertheless, the appearance of new issues related to the reboot of the ODROID first and then to HLD storage reduced the data sample to the range of DOY between 59 and 82. The ODROID weekly reboot explained in Section 4.7.1 failed to restore the detector to an operative status on DOY 63–64. In addition, since DOY 82 the HLD storage failed due to an unknown reason, causing the loss of two weeks of data. The information of all subsystems could be registered and stored, allowing us to understand the detector's response until it arrived in Vigo on DOY 99. Figure 7.4 shows the background currents and the HV of the T3 plane during this trip. The evolution of both variables as a function of the DOY shows a smooth variation with no abrupt changes.

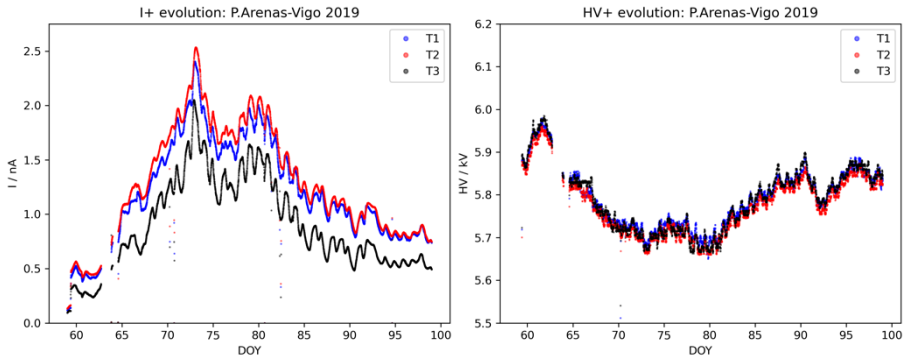

Figure 7.4: Second survey slow control. Left) T3 background current changes due to temperature oscillations. Right) T3 HV behavior as a function of DOY.

USC UNIVERSIDADE DE SANTIAGO DE COMPOSTELA

The effect of the random coincidences is still relevant because the temperature rose more than 15 ºC from Punta Arenas to the equator, where it reached a maximum value of 35 ºC. Figure 7.5 shows its evolution from DOY 59 to 82, which is the available range of reconstructed data due to the aforementioned problems.

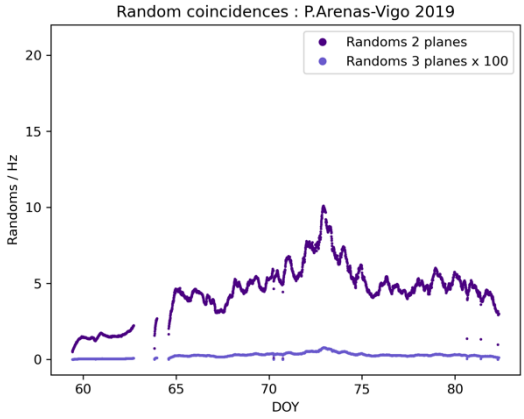

Figure 7.5: Effect of randoms in the second survey for two and three planes. Random coincidences for three planes are multiplied by 100 for visualization.

Upon its arrival in Vigo, the detector worked without the need for operator-driven assistance, showing the effectiveness of its design to operate in Antarctica as an almost-fully autonomous detector. TRISTAN was unmounted and carried to Santiago de Compostela, where it was mounted back, and started a new data-taking campaign in October of the same year.

7.2.1.3 Latitudinal survey 2019-II

Onboard the Spanish oceanographic research vessel, called BIO Hespérides, TRISTAN performed a final latitudinal scan of CR flux. The last journey started on November 11th, 2019, in Cartagena, Spain, (37º36'00" N, 0º59'00" W), and finished on December 21st, 2019, in BAE-JCI (62º39'46" N, 60º23'20" W). These dates correspond to DOY 315–355, which cover 40 days, being this data sample the longest of the three surveys. The detector was installed in a non-thermalized

USC UNIVERSIDADE DE SANTIAGO DE COMPOSTELA

laboratory on the first deck of BIO Hespérides. Regardless of the absence of temperature and humidity stabilization by an AC system, the background currents were kept under control below 1 nA by increasing the gas flow slightly for this trip. The fact that the detector was placed over a desk improved the air renewal, so the temperature changes inside the RPCs were not as abrupt as in the previous surveys. Besides the oscillations due to the dynamic adjustment by pressure and temperature changes, the HV was stable at around 5.9 kV as it can be seen in Figure 7.6.

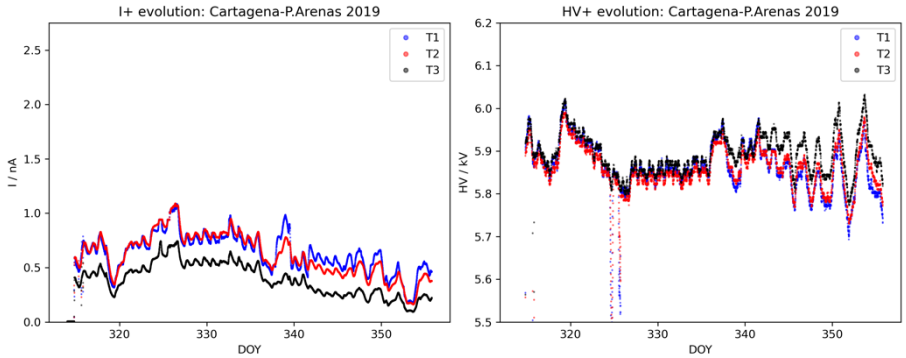

Figure 7.6: Third survey slow control. Left) T3 background current changes due to temperature oscillations. Right) T3 HV behavior as a function of DOY.

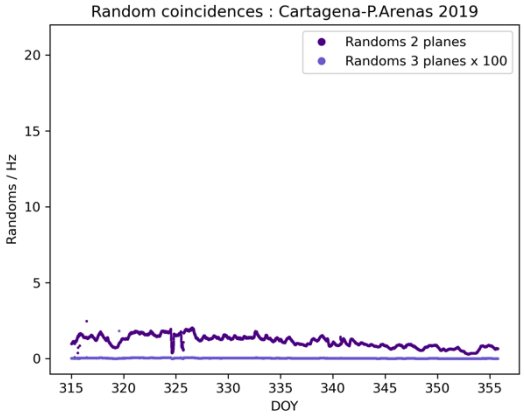

Figure 7.7: Effect of randoms in the third survey for two and three planes. Random coincidences for three planes are multiplied by 100 for visualization.

USC UNIVERSIDADE DE SANTIAGO DE COMPOSTELA

In contrast to the high impact that the random coincidences have on the efficiency calculation for the first two data-taking campaigns, in this one, their effect is almost negligible (Figure 7.7). Therefore, because of the good quality of the registered CR data, this sample was used to improve and develop all calibration and correction algorithms and methods. After completing this latitudinal journey, TRISTAN was installed in Antarctica to measure CR as a permanent station.

7.2.1.4 Santiago 2019

Between the two latitudinal surveys performed in 2019, a new run of CR measurements was carried out using TRISTAN as a static station at Santiago de Compostela, Spain (~ 260 m a.s.l.). It took place from October 14th to November 5th, DOY 287 and 309, respectively. TRISTAN was mounted in a thermalized laboratory on the ground floor of a two-floor building at the Faculty of Physics of the USC (42º52'34" N, 8º33'37" W). In this way, the concrete of the floors above the detector reduced the number of low-energy particles traversing the RPCs.

In Figures 7.8 and 7.9, the stability of the detector in terms of the most important variables can be seen. The low background currents, the stable HV values, and the low number of random coincidences (below 3 Hz) guarantee a good quality of this data sample.

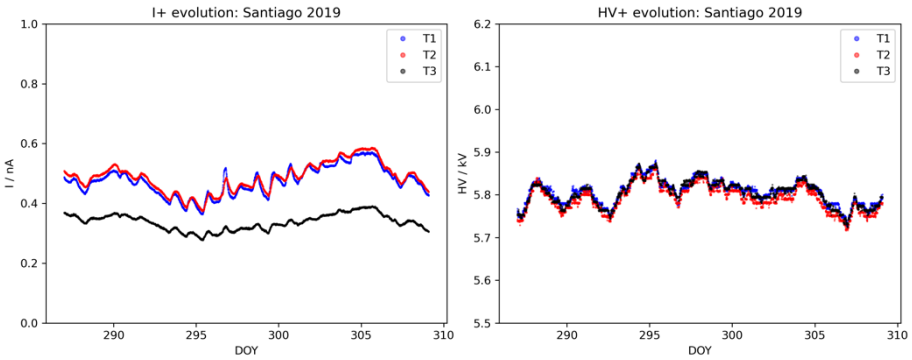

Figure 7.8: Santiago slow control. Left) T3 background current changes due to temperature oscillations. Right) T3 HV behavior as a function of DOY.

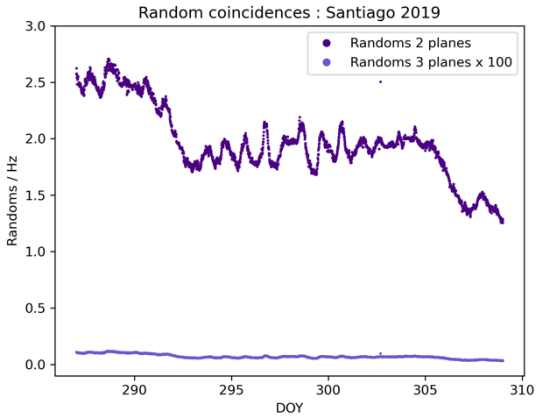

Figure 7.9: Effect of randoms in Santiago for two and three planes. Random coincidences for three planes are multiplied by 100 for visualization.

On November 5th, 2019, the detector was unmounted and transported to Cartagena for its installation onboard BIO Hespérides to start the last one of the three trips along the Atlantic Ocean.

7.2.1.5 Antarctica 2020

Finally, after completing the last latitudinal scan, TRISTAN was placed in Antarctica in the facilities of BAE-JCI (62º39'46" N, 60º23'20" W), at approximately 14 m a.s.l. Thus, TRISTAN joined the other set of ORCA detectors installed in late 2018. Even though we arrived on December 21st at the base, the detector couldn't be set up until December 27th. The first days after the installation of TRISTAN were used to check its integrity with the HV dynamic adjustment turned off. Figure 7.10 shows the evolution of the currents and HV, where the constant value at negative DOY, i.e., the last days of 2019, corresponds to such a period. Therefore, the data registered until January 1st, 2020, had to be removed from the analysis, as the detector was not running under correct operating conditions.

The data-taking period ended on January 28th, with the end of the first phase of the Spanish Antarctic campaign. The low temperature in Antarctica favors noise reduction, so the correction by random coincidences is insignificant, as shown in Figure 7.11.

USC UNIVERSIDADE DE SANTIAGO DE COMPOSTELA

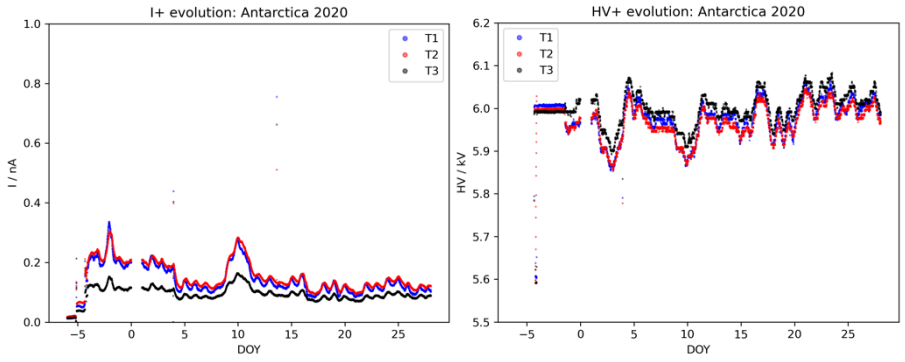

Figure 7.10: Antarctica slow control. Left) T3 background current changes due to temperature oscillations. Right) T3 HV behavior as a function of DOY. Negative values of DOY represent the last days of the previous year.

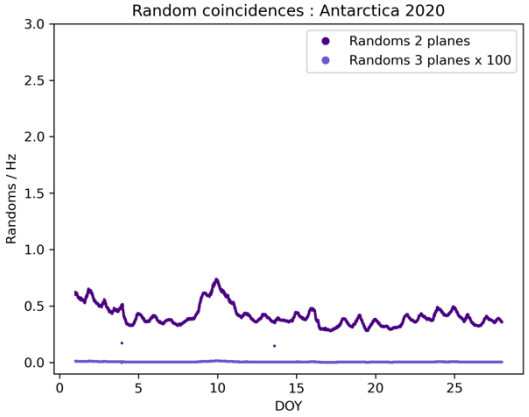

Figure 7.11: Effect of randoms in Antarctica for two and three planes. Random coincidences for three planes are multiplied by 100 for visualization.

During this period, the bubbler of the T1 plane ran out of vaseline and had to be refilled. It was the only issue and didn't affect the data registration. This figure and the complete set of slow control figures can be seen in the Appendix. The figures of surveys and static measurements are on the same scale to enable easy comparison of the quality of the data for similar campaigns.

7.2.2 TRAGALDABAS

Many data-taking campaigns have been carried out since the installation of TRAGALDABAS in 2015 at the Faculty of Physics of the USC, Spain (42º52'34" N, 8º33'37" W). Multiple hardware and software updates have been implemented in the last years to improve the detector's stability. The detector is taking data since March 3rd, 2022, under constant surveillance to ensure the best data quality for future analysis. Nevertheless, the data studied in this work was taken from June 1st to August 1st, 2015 (DOY 152–213) with two RPC planes (T2-T4) in coincidence. For this first analysis, only the events with the same number of hits in both trigger planes have been taken into account, which rose to unambiguous tracks. This data sample is of special interest concerning solar physics because a strong geomagnetic storm materialized into an intense Forbush Decrease (FD).

7.3 Raw data processing

Correct treatment and understanding of the raw data are the keys to a good analysis. Thus, the signal calibration algorithms, which provide the calibration constants, determine the quality of the reconstructed data. Even a non-stable run can be recovered by calibration techniques. After the reconstruction, raw data must be calibrated before continuing with further studies. The main results of this process are presented in this section. All calibration and reconstruction methods have been explained in detail in Chapter 6.

7.3.1 Event reconstruction

The CR data measurements of the different detectors and periods have been processed similarly. TimTrack algorithm, whose explanation was given in Section 6.7, has been implemented in the reconstruction software of both detectors. CR events are analyzed individually to extract the number of unambiguous tracks compatible with the speed of light, also known as track multiplicity. The data acquisition registers a rate of about 13 and 9 million events per day in TRISTAN and TRAGALDABAS, respectively. The detectors' trigger configuration has been described in Section 4.7.

USC
UNIVERSIDADE DE SANTIAGO DE COMPOSTELA

TimTrack gives all saetas that are accepted for all combinations of hits within the same event. The read-out of the hit signal takes place at the center of the pad, so the input uncertainties of TimTrack are calculated from the uniform distribution of probability as follows:

$$\sigma_{x,y} = \frac{l_{x,y}}{\sqrt{12}}, \tag{7.1}$$

where $l_{x,y}$ are the dimensions of the pads. Tracks are produced by filtering saetas and removing the ones that share a hit. First, the saeta with the lowest chi-square is stored. Then, this saeta is compared to the remaining saetas in the list, and saetas that use one of its hits are rejected. The process continues until no saetas are available, providing a clean matrix of unambiguous tracks. Finally, only the tracks with a chi-square below a certain threshold are considered.

The percentage of events with track multiplicity equal to one (M1) constitutes 99% of the total number of reconstructed tracks, and events with a track multiplicity of two (M2) wrap around 0.8%. The remaining 0.2% is comprised of higher multiplicities (MH).

Zenith and azimuth angles of the tracks are calculated by using the slopes (X', Y') given by TimTrack. Based on the angular distribution of CR muons and the acceptance of the detectors, the rate has been split into different zenithal sectors. In the case of TRISTAN, the degree intervals that have been chosen are: (0, 25), (25, 35), (35, 45), (45, 55), and (55, 65). For this analysis, no distinction was made, and all intervals were analyzed together. The high granularity of TRAGALDABAS made the selection of narrower intervals possible. The degree intervals that have been selected for this detector are: (0, 13), (13, 18), (18, 23), (23, 27), (27, 30), and (30, 60). The analysis of TRAGALDABAS data is not as deep as the performed for TRISTAN data, and that is the reason why only M1 tracks with a zenith angle below 30 degrees have been studied.

Rates of M1, M2, and MH have been averaged and stored in 10-minute intervals. This data needs calibration before being correlated with other external variables such as rigidity, pressure, or temperature.

USC UNIVERSIDADE DE SANTIAGO DE COMPOSTELA

7.3.2 Calibration

The first stages of this process consist in obtaining the charge and calibration constants applied to the unpacked data and the tracking. The next step in raw data processing involves the calibration by active and dead times, random coincidences, and efficiency.

Active time is a measure of the time the detector was taking data during a certain period, which in our case is a 10-minute interval. Hence, it defines the real-time over which the raw data is averaged instead of the fixed 10 minutes. The dead time correction is negligible as it has been justified in Section 6.5. Random coincidences' impact on the reconstructed rate has been introduced in the description of every data-taking campaign. Efficiencies obtained by the three different methods, already presented in Section 6.6, have been corrected by this effect and will be displayed throughout this section.

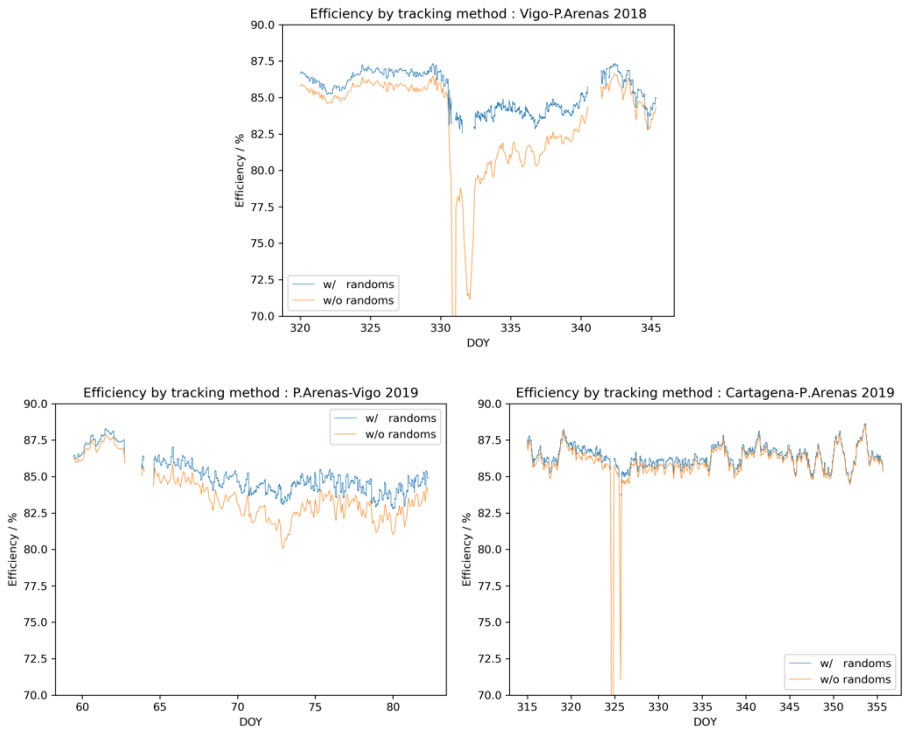

Figure 7.12: Efficiencies of the latitudinal scans given by the tracking method with (w/) and without (w/o) randoms' calibration.

USC UNIVERSIDADE DE SANTIAGO DE COMPOSTELA

Significant differences can be observed in Figure 7.12. Results show diverse behaviors because of the contrasting working conditions that characterize each latitudinal scan. The explanation of the efficiency drops is straightforward: high temperatures imply high background currents, which increases the noise rate that causes the efficiency loss. This is clearly noticeable in the first survey when the AC failure led to an abrupt temperature growth on DOY 330. According to the environmental sensors inside the RPCs, the temperature increased from 19 ºC to 30 ºC in just 8 hours. After that, the temperature descended on the way to Punta Arenas. Moreover, the lack of data on DOY 331 is owed to the saturation of the currents in the T2 plane.

Calibrating by random coincidences improve the efficiency curve, mitigating the effects of the unstable environmental conditions where the detector is located. Efficiency curves, with and without randoms' correction, become closer for periods of steady temperature oscillations like in Antarctica (Figure 7.13).

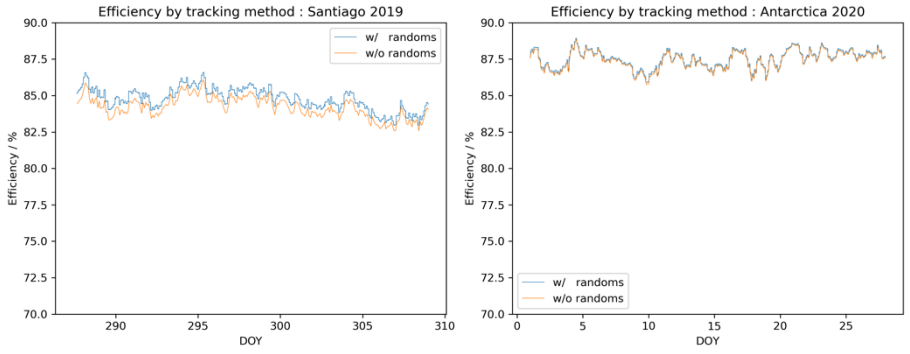

Figure 7.13: Efficiencies of the static measurements given by the tracking method with (w/) and without (w/o) randoms' calibration.

TRAGALDABAS data sample has been calibrated beforehand, so our analysis of this data sample starts in the next section with the atmospheric corrections. For its calibration, a mask containing the dead and noisy cells, which was created manually, has been applied to the unpacked data to guarantee the best event reconstruction.

The charge study provides an individual efficiency for each RPC in contrast to the tracking method, which only gives the value for T2 due to the trigger configuration of TRISTAN. Results of this method show the same features as those obtained by tracking (Figure 7.14).

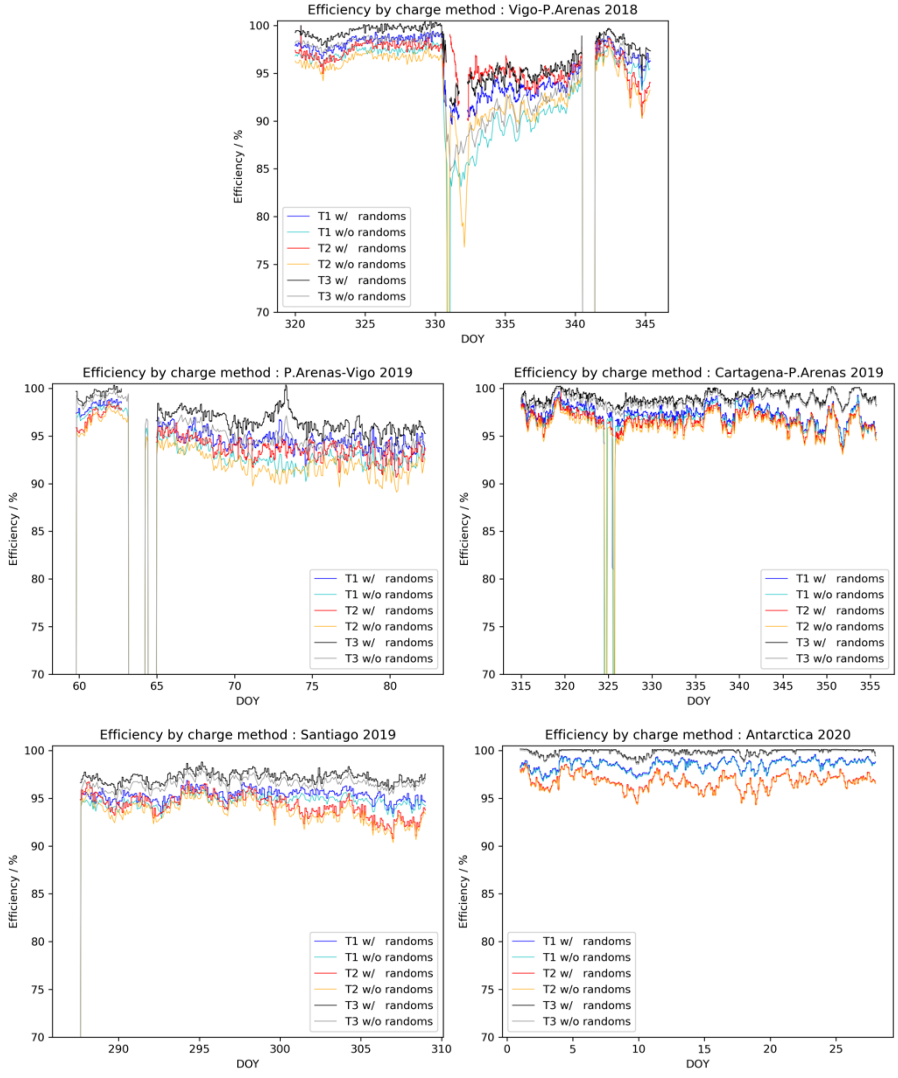

Figure 7.14: Efficiencies of the latitudinal surveys and the static measurements given by the charge study with (w/) and without (w/o) randoms' calibration.

USC UNIVERSIDADE DE SANTIAGO DE COMPOSTELA

Finally, efficiencies arising from the application of the PCA to the slow control variables already mentioned in Section 6.6.2 are shown in Figure 7.15. A description of the feature variables used and the equations extracted from the PCA will be explained afterward.

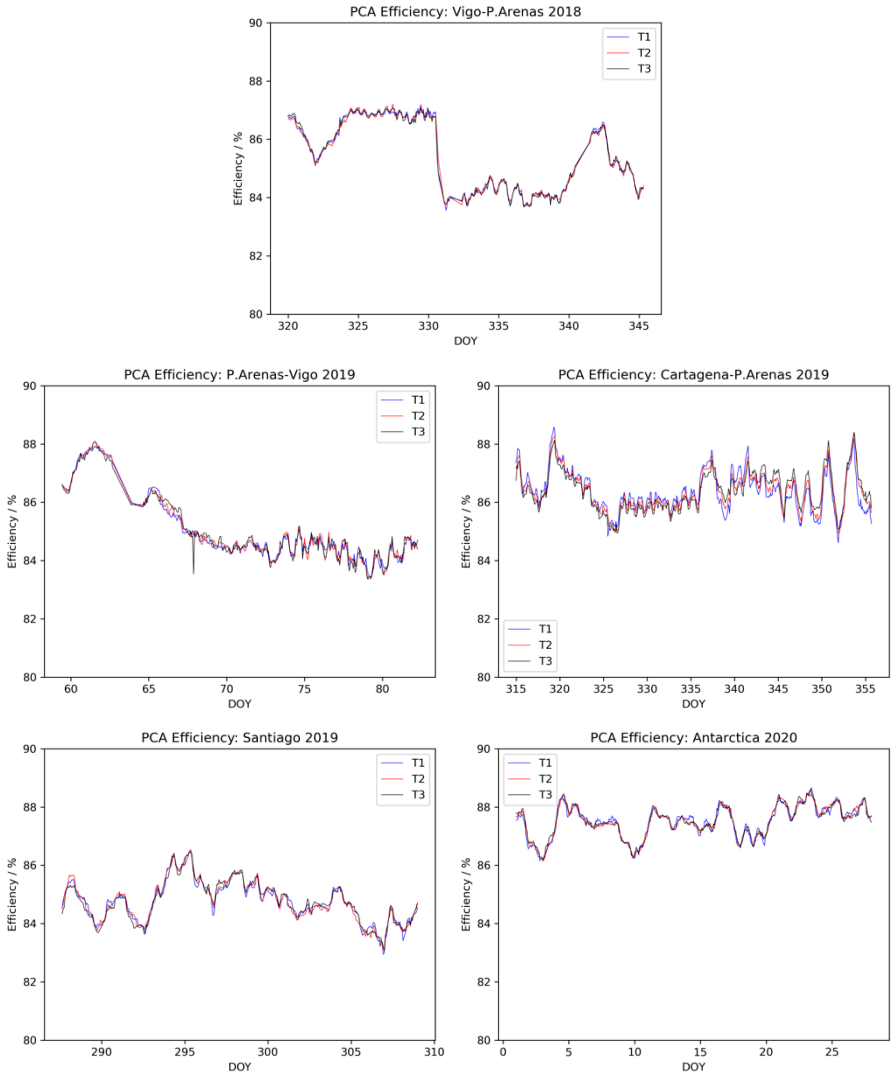

Figure 7.15: Efficiencies of the latitudinal surveys and the static measurements given by the PCA with (w/) and without (w/o) randoms' calibration.

PCA inputs include the T2 slow control variables and the target. The target variable is the efficiency provided by the tracking method and calibrated by random coincidences. A dimensionality reduction has been performed, reducing the number of variables from five to just two. The first two PCs explain around 90% of the variance (~ 60% the PC1 and ~ 30% the PC2), and the following components account for small oscillations. Tables 7.1 and 7.2 contain the first eigenvectors of the projection matrix used to get the transformed featured data.

Table 7.1: First two eigenvectors of the three latitudinal surveys.

Variable	LS1-PC1	LS1-PC2	LS2-PC1	LS2-PC2	LS3-PC1	LS3-PC2
Temperature	-0.516	0.185	-0.546	-0.116	-0.543	-0.254
Pressure	0.191	0.931	-0.021	-0.933	-0.425	0.513
Hunidity	0.430	-0.132	-0.350	0.309	-0.433	0.183
HV	0.519	0.169	0.545	-0.073	0.110	0.789
Current	-0.493	0.230	-0.531	-0.124	-0.570	-0.127

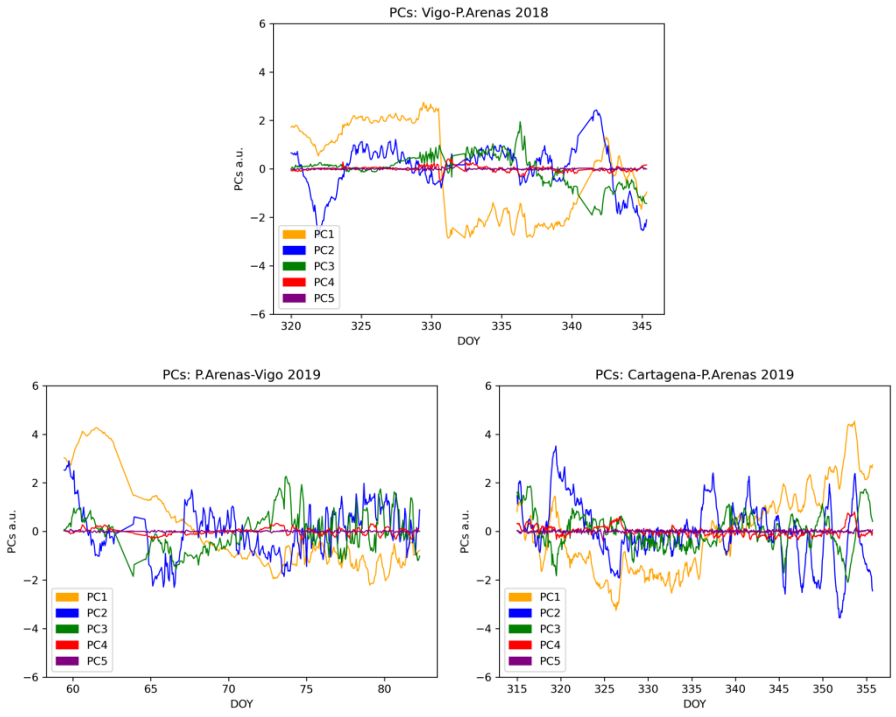

Figure 7.16: Original variables projected onto the PC space during the latitudinal surveys.

USC UNIVERSIDADE DE SANTIAGO DE COMPOSTELA

The behavior of the PCs calculated for all sets of data is shown in Figures 7.16 and 7.17. Comparing them to the aforementioned efficiencies sheds light on which ones have a higher correlation with the target. PCA is just a mathematical transformation, and the sign of the PC scores is meaningless. The interpretation of the results stays exactly the same.

Table 7.2: First two eigenvectors of the two static measurements.

Variable	SM1-PC1	SM1-PC2	SM2-PC1	SM2-PC2
Temperature	-0.549	-0.151	-0.589	-0.221
Pressure	0.061	-0.753	0.057	-0.846
Hunidity	-0.523	-0.164	0.151	-0.133
HV	0.348	-0.600	0.537	-0.391
Current	-0.548	-0.156	-0.582	-0.255

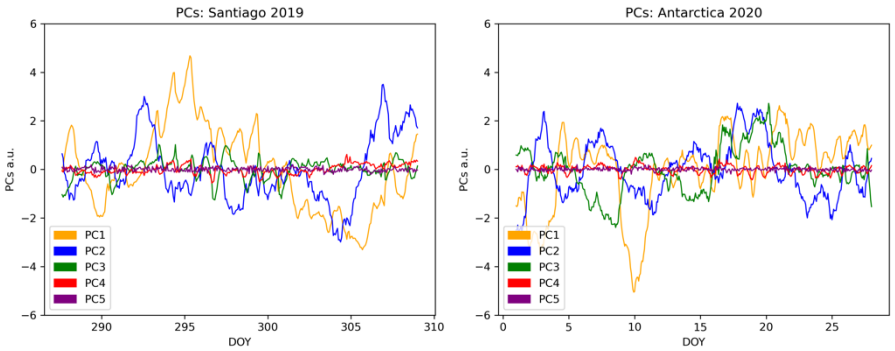

Figure 7.17: Original variables projected onto the PC space during the static measurements.

Efficiencies already illustrated in Figure 7.15 have been computed by performing 2-dimensional fits of the corresponding PC1 (p_1) and PC2 (p_2) in the following way:

$$f(p_1, p_2) = a_0 p_1 + a_1 p_2 + a_2 p_1 p_2 + a_3 \,. \qquad (7.2)$$

Fits yield the a_i coefficients and their associated standard uncertainties. A summary of the results for all periods can be found in Table 7.3, where the first significant digits of the standard uncertainties are in parenthesis. An example of the fits has been shown in Figure 6.23.

Table 7.3: Coefficients and standard uncertainties of the 2-dimensional fits.

Data samples	a_0	a_1	a_2	a_3
Survey 2018	0.61 (1)	0.24 (2)	0.021 (9)	85.46 (2)
Survey 2019-I	0.65 (1)	-0.18 (2)	-0.004 (2)	85.07 (2)
Survey 2019-II	0.17 (1)	0.47 (1)	0.007 (3)	86.38 (1)
Santiago 2019	0.31 (1)	-0.33 (1)	0.009 (5)	84.76 (2)
Antarctica 2020	0.27 (1)	-0.25 (1)	-0.009 (4)	87.51 (1)

The scores of the coefficients are characteristic of each campaign because of the different operating conditions. The coefficients, the slow control variables of T1 and T3 planes, and the projection matrix resulting from the PCA give the efficiency of each RPC. Since the RPCs are nonidentical, their response to the external conditions differs. As for the charge method, this method allows the estimation of the individual efficiencies.

7.3.3 Raw vs. calibrated data

The calibration process is completed with the production of the calibrated data. Raw data are divided by the efficiency of the whole detector, which is the product of the individual efficiencies of each RPC. In addition, the acceptance factor that limits the efficiency evaluated by the tracking method to around 90% has been taken into account to generate the calibrated data. The guard electrodes cover about 10% of the total RPC active area, so their impact is considerable. Hereinafter, the calibrated data have been constructed by using the efficiency determined by the tracking method with randoms' correction.

A comparison between raw and calibrated data is displayed in Figure 7.18. The black curve symbolizes the raw data, whereas the red stands for the calibrated. Some peculiarities exist for each data-taking period. The ones of major significance have already been introduced in Section 7.2 and are mainly related to the latitudinal surveys. Furthermore, the lack of data from DOY 338 to 341 in the journey from Cartagena to Punta Arenas is related to a temporary stop in Montevideo, Uruguay. These data have been discarded due to the unstable conditions of the RPCs in terms of temperature and currents. Most likely related to a change in the power supply of the ship.

USC UNIVERSIDADE DE SANTIAGO DE COMPOSTELA

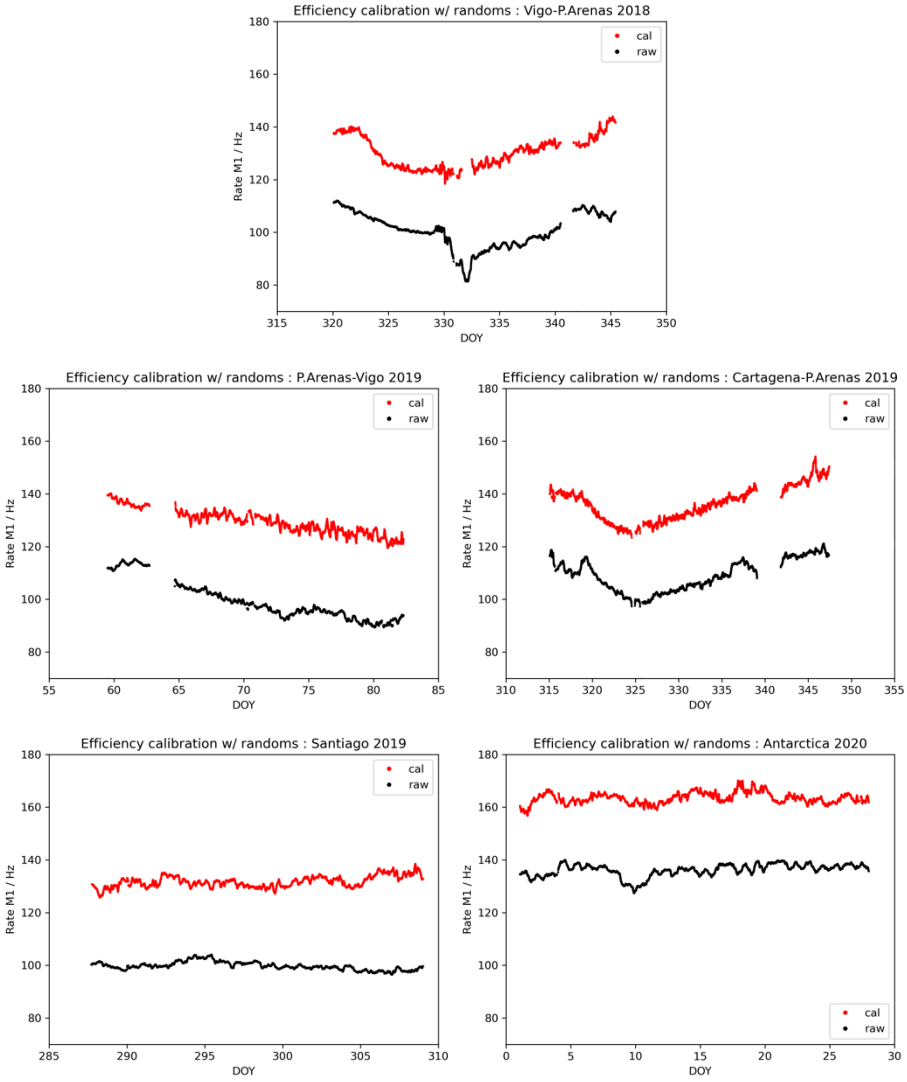

Figure 7.18: TRISTAN raw vs. calibrated M1 data.

A moving average smoothing with a window of two hours has been applied to the 10-minute data. Effects such as the efficiency falloff in the first trip are almost completely amended with the calibration algorithms developed in this thesis.

Analogous results have been assessed by the alternative charge and PCA methods. Rate minimum-maximum ranges coming from the calibration have been estimated by comparing the calibrated data resulting from the three methods. These ranges define the extreme differences between rates given by the tracking method and the others.

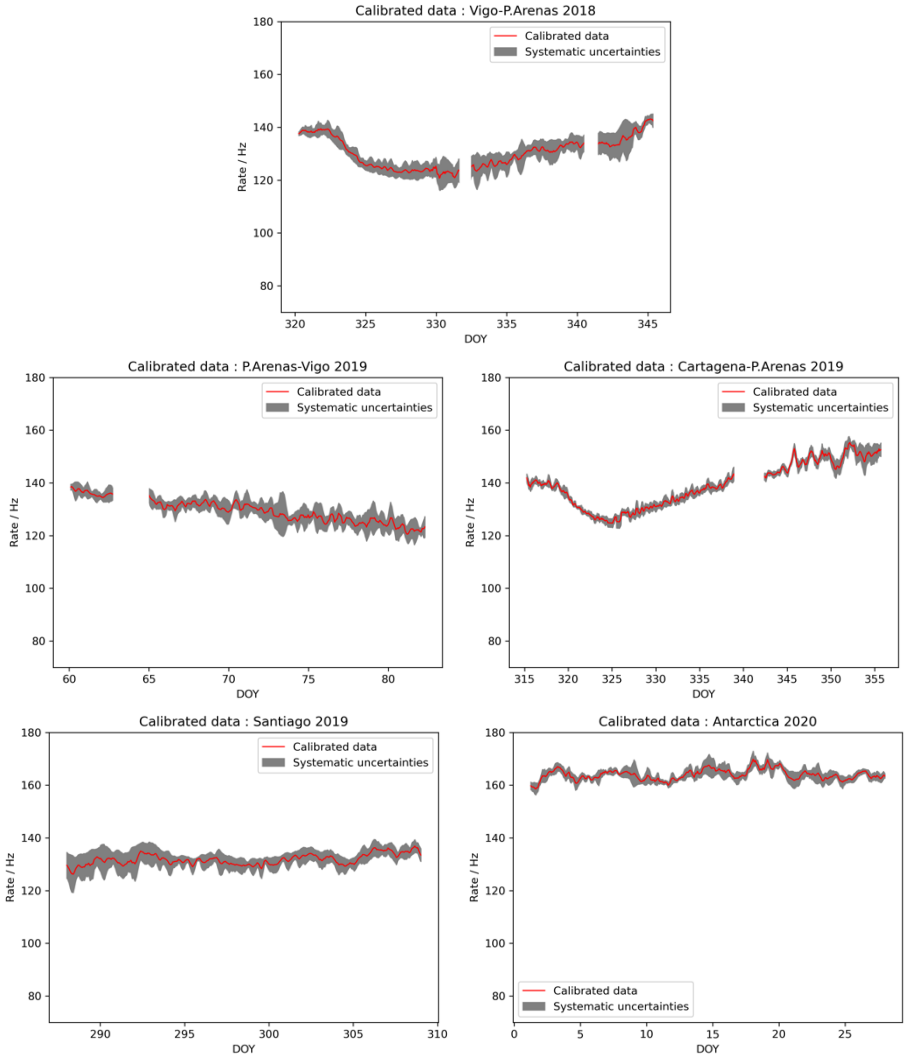

Figure 7.19: TRISTAN calibrated M1 data.

USC UNIVERSIDADE DE SANTIAGO DE COMPOSTELA

The hourly averages of the calibrated data for all campaigns are shown in Figure 7.19. A smoothing of the data with a moving 6-hour window has been performed. Shadow bands represent the minimum-maximum ranges. It is important to bear in mind that the tracking method with the randoms' calibration was the reference to obtain the minimum-maximum ranges.

Statistical uncertainties of the rate are not included in the plots. However, to compute them, we utilize the fact that the rates follow a Poisson distribution. Therefore, the bin of a histogram has an uncertainty given by the square root of its entries. As a consequence, the 10-minute rates have a statistical uncertainty of the order of magnitude of ~ 0.5 Hz.

Systematic uncertainties can be inferred by the use of the rates obtained through the three aforementioned methods. Considering the average of the three rates the systematic uncertainties are below 3 Hz.

Once the new set of data has been produced, we can proceed to analyze the influence of the external variables. To evaluate the quality of the calibrated data, we have studied their correlations with the atmospheric conditions and the cutoff rigidity.

7.4 ATMOSPHERIC CORRECTIONS

Specific features that appear in raw data, whose origin is related to changes in the working conditions of the detector, are removed with the calibration. Nevertheless, these are not the only corrections that must be made to the registered data. Atmospheric or meteorological effects on secondary CRs have to be taken into account for further studies of the measured CR flux. The well-known pressure and temperature effects explained in Section 1.5.2 are the most important corrections to be applied.

The relationship between calibrated data and atmospheric conditions will be studied in this section. The barometric effect will be quantified for both detectors, whereas the analysis of the temperature effect will only be introduced. Future projects will be able to study in detail this effect, but first, particle identification algorithms must be created to distinguish between electrons and muons.

USC UNIDADE SANTIAGO COMPOSTELA

The ground-level atmospheric data have been supplied by Sarmiento de Gamboa and BIO Hespérides instruments for the latitudinal surveys. The same information has been extracted for Santiago and Antarctica measurements from the databases of MeteoGalicia and Agencia Estatal de Meteorología (AEMET), respectively [82, 116]. AEMET station is placed less than 100 m from the location of TRISTAN.
Information about the atmospheric layers has been retrieved from Copernicus Climate Data Store (CDS) reanalysis, ERA5, for the 1979-present period [117]. ERA5 is the fifth generation of the European Centre for Medium-Range Weather Forecast (ECMWF) reanalysis for global climate. Reanalysis combines observations with model data into a global dataset. ERA5 hourly atmospheric data such as vertical temperature and geopotential height at 37 isobaric levels. From higher to lower atmosphere, the pressure levels (in hPa) are the following: 1, 2, 3, 5, 7, 10, 20, 30, 50, 70, 100, 125, 150, 175, 200, 225, 250, 300, 350, 400, 450, 500, 550, 600, 650, 700, 750, 775, 800, 825, 850, 875, 900, 925, 950, 975, and 1000.
Atmospheric data have been resampled to 6-hour values for TRISTAN due to the diversity in the frequency of the measurements (1 minute Sarmiento de Gamboa, 1 hour BIO Hespérides, 10 minutes MeteoGalicia and AEMET, and 1 hour ERA5).

7.4.1 Barometric effect

The effect of the atmospheric pressure explains the impact of the atmospheric mass above the detector, and it is usually referred to as the barometric effect. As it is the dominant effect on the secondary CR flux, it has to be removed first to study subtler effects.

To quantify this effect and determine the barometric coefficient (β) for TRISTAN, we have used the data of Santiago and Antarctica exclusively. Pressure and rate of CRs are connected by Equation 1.11. The barometric coefficient represents how much the pressure affects the measured rate of secondary CRs. The β-coefficients have been obtained by linear regression between the experimental variations of M1 rate and atmospheric pressure. Periods highly influenced by the solar, interplanetary, and geomagnetic fields have been ignored to do so. Since the available data samples of TRISTAN contain around a month

USC UNIVERSIDADE DE SANTIAGO DE COMPOSTELA

of data each, this avoids the long-term variations not related to the pressure. For the same reason, only the data of July has been used to calculate the barometric coefficient of TRAGALDABAS. Figures 7.20 and 7.21 show the results of the regression for the different detectors and periods. To minimize the impact of the outliers in the determination of the coefficients, we have used a robust linear regression. This algorithm is called RANSAC, which is the acronym for RANdom SAmple Consensus. First, a random sample of inliers is selected to train the model. Then, the other points are tested against the trained model, and the ones that fall within a certain tolerance are the new inliers. The process continues until the residuals are minimum or a maximum number of iterations is reached.

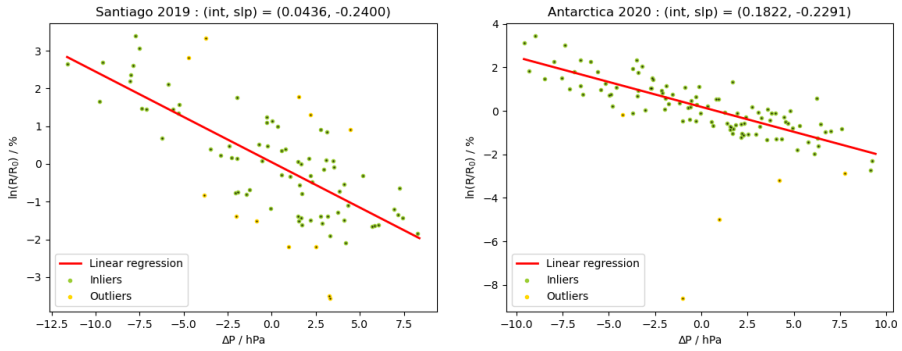

Figure 7.20: TRISTAN regression result, and M1 barometric coefficient.

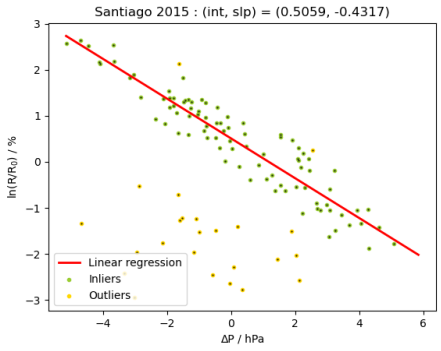

Figure 7.21: TRAGALDABAS regression result, and M1 barometric coefficient.

A summary of the coefficients, derived from the linear regressions, can be found in Table 7.4, where the first significant digits of the standard uncertainties are in parenthesis. The data of the latitudinal surveys have been corrected by the average of TRISTAN coefficients.

Table 7.4: M1 barometric coefficients for the different detectors and periods.

Data samples	β / % hPa	Intercept / %
TRISTAN - Santiago	-0.24 (3)	0.04 (1)
TRISTAN - Antarctica	-0.23 (3)	0.18 (5)
TRAGALDABAS - Santiago	-0.43 (5)	0.51 (6)

The estimation of the barometric coefficient for the detectors that compose the Global Muon Detector Network (GMDN) brings a logarithmic dependency with the cutoff rigidity (R_c) [118].

$$\langle\beta\rangle = -0.167 + 0.019 \ln(\langle R_c \rangle) . \quad (7.3)$$

Although the use of the cutoff rigidities of Santiago ($\sim$ 6 GV) and Antarctica ($\sim$ 2.5 GV) in Equation 7.3 does not match the results of Table 7.4, this is due to the different detectors' layout, counting threshold, and acceptance. The four detectors of the GMDN use plastic scintillators, whereas TRASGOs are based on RPCs. The origin of the deviations between TRISTAN and TRAGALDABAS data in Santiago is most likely related to the event reconstruction. The sample of the second has been taken with just two planes in coincidence and no lead in between them, which has high contamination of electrons that are very sensitive to the atmospheric conditions.

7.4.2 Temperature effect

The remaining variations of the CR flux that are still present after the elimination of the pressure correlation are linked to the temperature effect. There are a large number of diverse methods to correct the flux of secondary CRs in the literature, but none of them is considered universal [45]. The characteristics of each detector make them more suitable for one or another method. All methods have a similar approach and are based on temperature observations at different altitudes. TRISTAN static locations have been used to study the influence of the

USC UNIVERSIDADE DE SANTIAGO DE COMPOSTELA

temperature on the CR flux. Two examples of the vertical profile of the temperature from 1000 to 10 hPa for the two locations are shown in Figure 7.22. This figure illustrates a remarkable feature of the tropopause (minimum temperature region), which is the difference in altitude or pressure level between the two hemispheres [119].

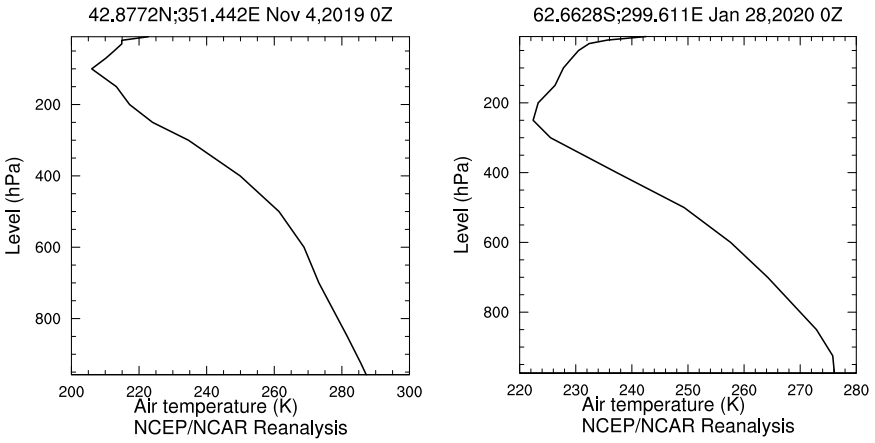

Figure 7.22: Example of the vertical temperature profile on the last day of left) Santiago, and right) Antarctica data-taking campaigns.

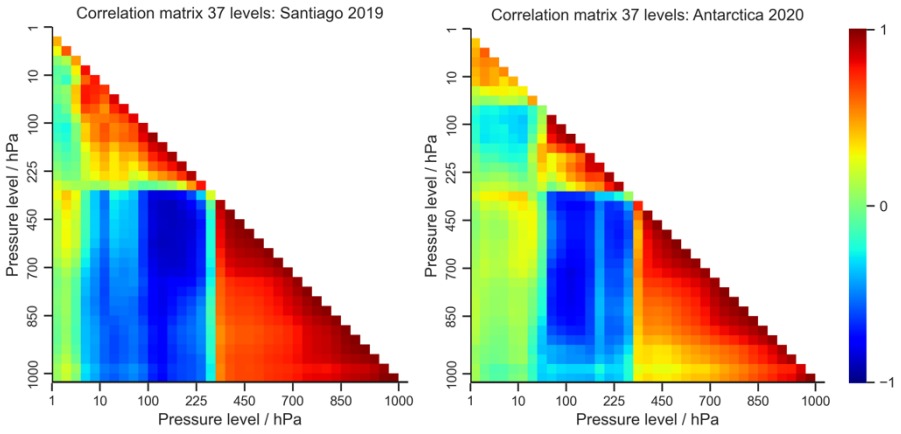

Figure 7.23: Parwise correlations between temperatures of all pressure levels, during left) Santiago, and right) Antarctica data-taking campaigns.

As it has been done for the barometric effect, a linear regression method has been used, according to Equation 1.12, to get the temperature coefficients. This equation can be written as follows:

$$\left(\frac{\Delta N}{N_0}\right)_T = \sum_i \alpha_{T_i} \Delta T_i \,, \tag{7.4}$$

where $\Delta N/N_0$ is the relative variation of the measured CR rate, α_{T_i} is the temperature coefficient of the atmospheric layer i, and ΔT_i is the variation of the temperature of the same layer with respect to the mean.

The correlations between the relative variations of the rate and the temperature have been analyzed. But first, the strong correlation of the temperatures of the atmospheric layers required the preparation of a new set of uncorrelated variables. The correlation matrix for the 37 pressure levels in Santiago and Antarctica can be seen in Figure 7.23.

A PCA has been performed to remove the correlations and obtain the temperature coefficients. This method was already described mathematically in Section 6.6.2. The projection matrix (W) has been formed with just the first 3 out of 37 eigenvectors, considering that they explain approximately 80% of the variance. Applying W to project the original variables onto the new subspace gives the desired uncorrelated variables. A linear regression has been used to get the coefficients that correlate these new variables with the M1 rate measured by TRISTAN. The coefficients calculated for the new subspace (α_s) are transformed back to the original space in the following way:

$$\alpha_T = W\alpha_s \,, \tag{7.5}$$

where α_T are the temperature coefficients defined in Equation 7.4.

The results obtained for the static measurements carried out by TRISTAN in Santiago de Compostela and Antarctica are presented in Figures 7.24. In this figure, the two effects that contribute to the temperature modulation of the CR flux can be observed.

USC
UNIVERSIDADE DE SANTIAGO DE COMPOSTELA

The fact that the temperature increases at around 200 hPa and also in the lower atmosphere means that the M1 rate of TRISTAN includes both muons and electrons. This highlights the need to implement the particle identification algorithm that is under development in our group.

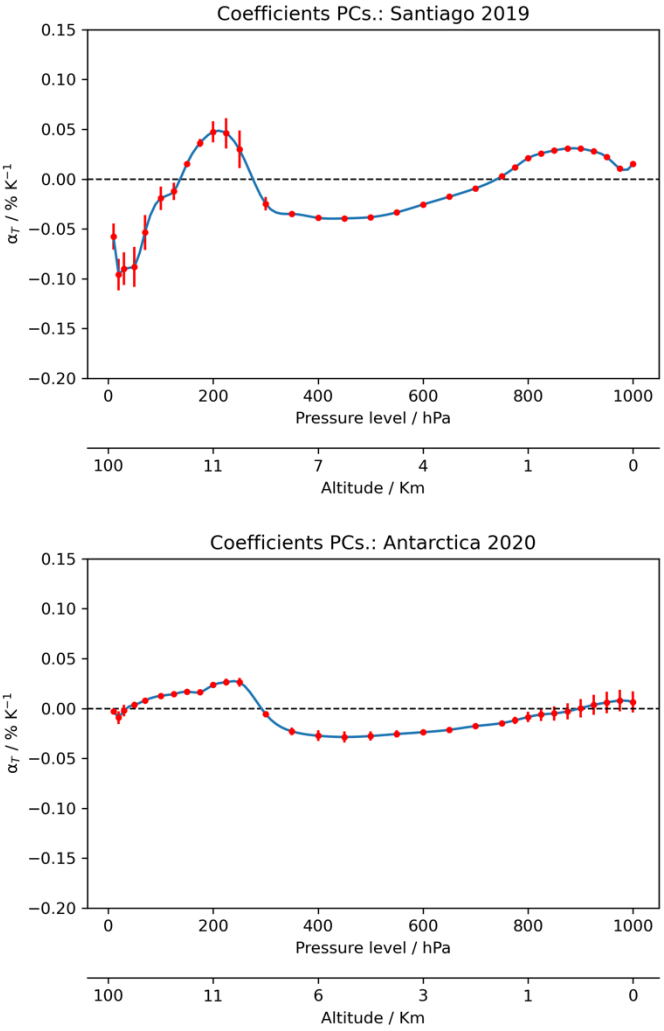

Figure 7.24: Temperature coefficients at 37 pressure levels for Santiago (top) and Antarctica (bottom) data-taking campaigns.

Regardless of having calculated the temperature coefficients for the different atmospheric layers, data samples have not been corrected by such an effect. The main reason is that several correction algorithms have to be tested before deciding which one suits better to our detector. A correction of the data by the ground temperature has been attempted, but no clear correlation has been found. Moreover, the atmospheric correction to the data of the latitudinal scans is very challenging, as many corrections have to be performed due to the ship's movement.

7.4.3 Calibrated vs. corrected data

The correction process that involves the atmospheric conditions is finalized with the production of the corrected data. On the one hand, the barometric effect has been removed from the data successfully. On the other hand, the correction by ground temperature has not been made due to the inconclusive results caused by the high point dispersion.

Effects of the barometric correction on the calibrated data are shown in Figures 7.25 and 7.26 for TRAGALDABAS and TRISTAN, respectively. The negative correlation between pressure and rates is manifested in these figures. Secondary CRs suffer more collisions on the way to the surface when the pressure is higher than the average value, so the registered rate decreases, and vice-versa.

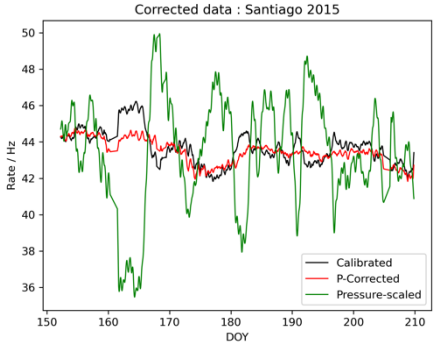

Figure 7.25: TRAGALDABAS calibrated vs. pressure corrected M1 data.

USC
UNIVERSIDADE DE SANTIAGO DE COMPOSTELA

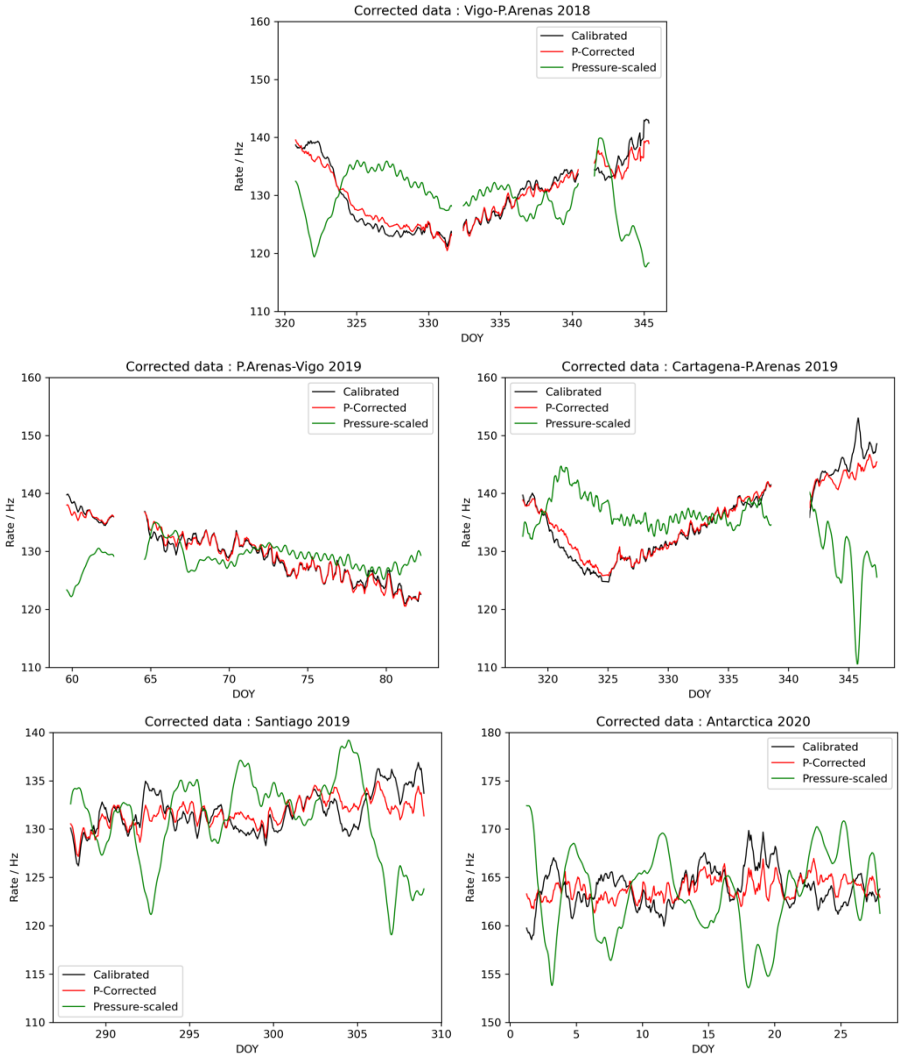

Figure 7.26: TRISTAN calibrated vs. pressure corrected M1 data.

A smoothing of the hourly calibrated data with a moving 6-hour window has been performed. Pressure values have been scaled to the mean rate to visualize how the rate oscillations are flattened by applying this correction. The influence of the magnetic field and solar activity on the corrected data is discussed in the next section.

7.5 INFLUENCE OF GEOMAGNETIC FIELD AND SOLAR ACTIVITY

Once the data have been corrected and the most relevant atmospheric effects have been removed, the influence of magnetic field and solar activity can be investigated. The nature of CRs makes them vulnerable to being scattered and deflected by the magnetic fields they traverse (Section 1.3). Therefore, only the ones with the highest energies can travel through the galactic magnetic field (GMF) and continue unimpeded, crossing the geomagnetic field. CRs require a minimum value of their magnetic rigidity to reach each point in the magnetosphere. Besides, solar activity may perturb the solar wind and the heliospheric magnetic field (HMF) through the emission of solar flares (SF) and coronal mass ejections (CMEs). Both might cause geomagnetic storms when interacting with the Earth's magnetosphere. A CME that sweeps past Earth shields it from CRs, causing a FD. Additionally, the weak minimum on the geomagnetic field in the South Atlantic Anomaly (SAA) region is particularly problematic at high altitudes as a result of the radiation increase.

7.5.1 Cutoff rigidity

Unprecedented series of TRISTAN measurements in a wide range of latitudes (~ 90º) give information about the relationship between the corrected rates and the cutoff rigidity. For the latitudinal survey of 2018, TRISTAN operated alongside the other detectors that compose ORCA. ORCA team provided us with the data taken by NEMO, i. e., by the three neutron monitors without shielding (BNM) and the three standard neutron monitors (NM64). The barometric coefficients used by ORCA team to correct the BNM and NM64 rates were –0.75% hPa and –0.72% hPa, respectively [120]. TRISTAN and NEMO data will be examined side by side to find the rigidity coefficients.

A world grid of cutoff rigidity has been prepared to understand the behavior of the rates with the rigidity (Figure 7.27). The 12th generation of the International Geomagnetic Reference Field (IGRF) has been used to create the tables of 2020 in [121]. The resolution of the original grid was 5° in latitude and 15° in longitude, and it was interpolated to create a $1° \times 1°$ resolution grid. Coordinates of the path followed by the Sarmiento de Gamboa vessel have been taken from the Marine

USC UNIVERSIDADE DE SANTIAGO DE COMPOSTELA

Technology Unit (UTM) data center [122]. For the last journey, coordinates were given by BIO Hespérides personnel.

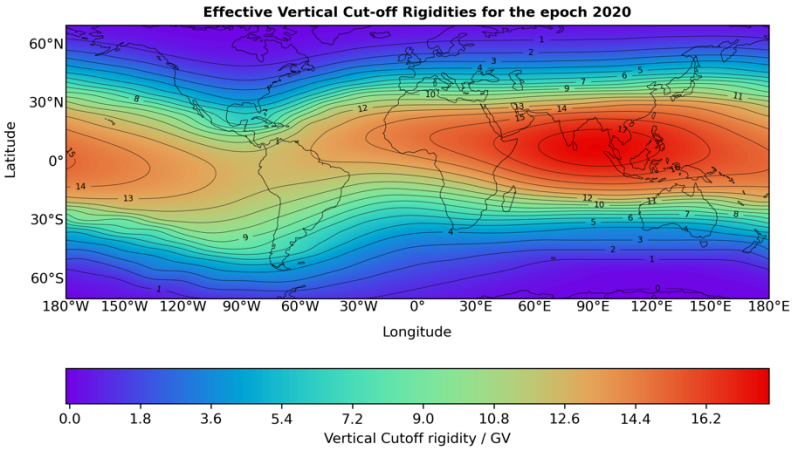

Figure 7.27: World map of vertical cutoff rigidities for the epoch 2020.

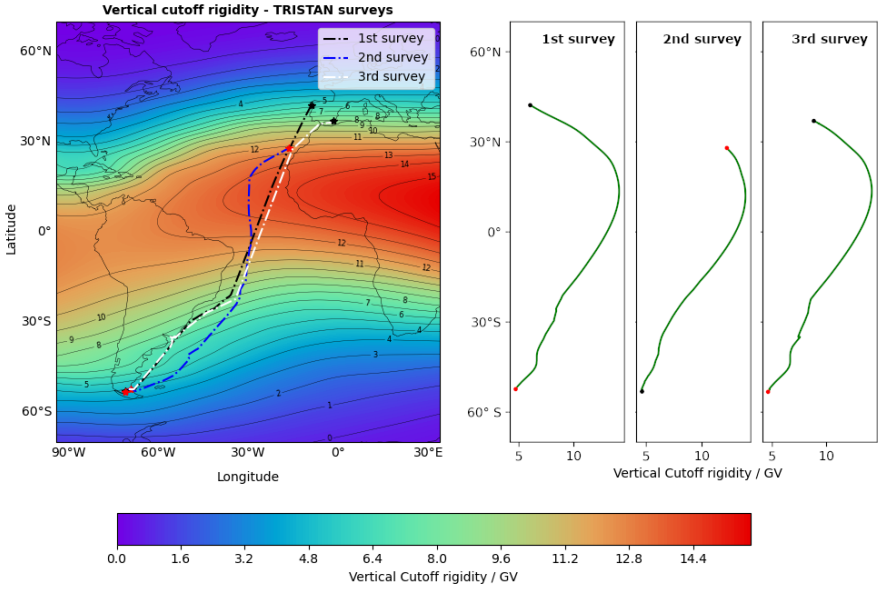

Figure 7.28: Coordinates and vertical cutoff rigidity for the latitudinal surveys. Black and red stars mark the start and end points of the different journeys.

Side-by-side plots of the vertical cutoff rigidity are presented in Figure 7.28 for the three latitudinal scans. Rigidity projections can be compared to the corrected data in Figure 7.29. The CR flux is reduced (∼ 12%) as we approach the zone of the path where the rigidity is maximum, at approximately (14º0'59" N, 20º23'28" W). From then on, a recovery of the rate is observed. At high latitudes in both hemispheres, the contribution of low energy secondary CRs increases between 10–15% with respect to the values at maximum rigidity.

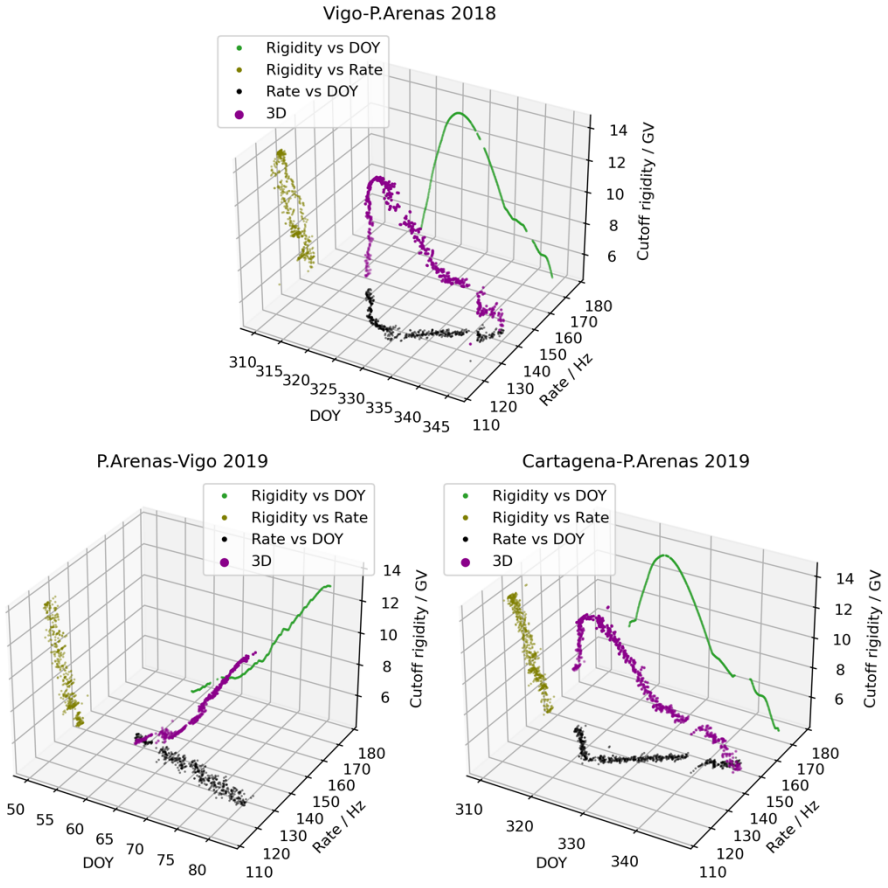

Figure 7.29: TRISTAN 3-dimensional (3D) plots of DOY, rate, and cutoff rigidity. Lateral and bottom panels show the different projections.

USC UNIVERSIDADE DE SANTIAGO DE COMPOSTELA

Normalized counting rates registered by the three BNM and the three NM64 neutron monitors, of which the NEMO system is composed, are shown in Figure 7.30. In this figure, the robustness and consistency of neutron monitor observations can be checked for the first latitudinal survey.

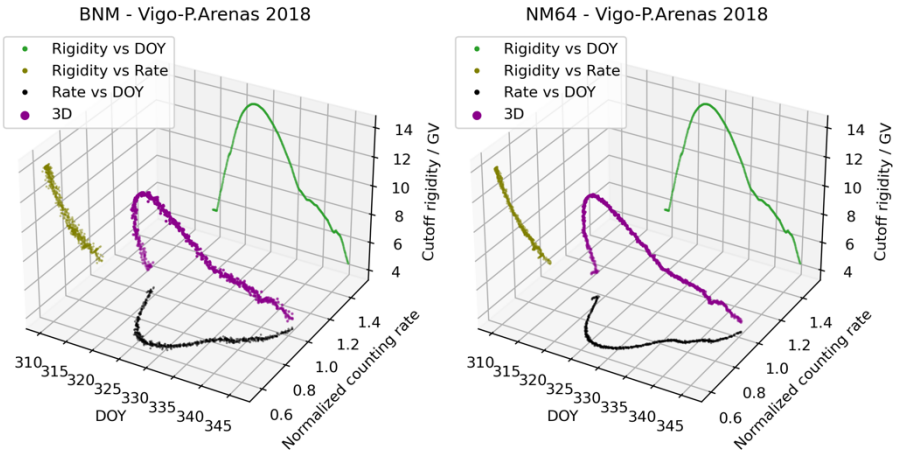

Figure 7.30: NEMO 3-dimensional (3D) plots of DOY, rate, and cutoff rigidity. Lateral and bottom panels show the different projections.

Neutron monitor observations carried out by NEMO have been analyzed complementary to TRISTAN data. The observational range of primary CRs for neutron monitors extends from the lowest energies accessible at the ground up to around 50 GeV. Surface directional muon detectors, like TRISTAN, are sensitive to energies between approximately 10 GeV and several hundred GeV. TRISTAN detects mainly muons but also exists a contribution of electrons of a few percent.

The dominant modulation processes seen by neutron monitors and muon telescopes are similar at the low energies of the muon observational range. Nevertheless, the data correction for local atmospheric effects is more sophisticated for muon detectors than for neutron monitors. A correction by the barometric effect is enough in the case of neutron monitors, but the positive and negative temperature effects only affect muon detectors.

Having explained the atmospheric corrections applied to TRISTAN in the previous section, it should be noted that a joint analysis with NEMO data has been performed. The study aims to evaluate and compare the response of both detectors to cutoff rigidity changes. As can be seen in Figures 7.29 and 7.30, the rates behave differently as a function of the cutoff rigidity. The rigidity coefficients or η-coefficients have been obtained by performing a linear regression to TRISTAN data and using the Dorman function for NEMO data [123]. The usage of these regressions is based on the minimization of the root-mean-square error (RMSE).

A summary of the regression results, displayed in Figures 7.31, 7.32, and 7.33, can be found in Table 7.5, where the first significant digits of the standard uncertainties are shown in parenthesis. The data sample of the survey 2018 has been divided into Northern-Southern Hemisphere (NH-SH) due to the deviation observed (Figure 7.29).

Table 7.5: TRISTAN rigidity coefficients for the different periods.

Data samples	η / GV	Intercept
Survey 2018 - NH	-0.0130 (7)	1.083 (8)
Survey 2018 - SH	-0.0130 (9)	1.058 (9)
Survey 2019-I	-0.0120 (5)	1.045 (4)
Survey 2019-II	-0.0130 (5)	1.063 (5)

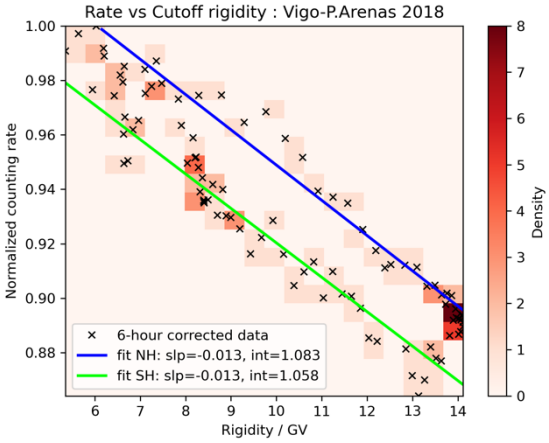

Figure 7.31: TRISTAN regression result and rigidity coefficients for the first latitudinal survey. Normalized M1 rate vs. cutoff rigidity.

USC UNIVERSIDADE DE SANTIAGO DE COMPOSTELA

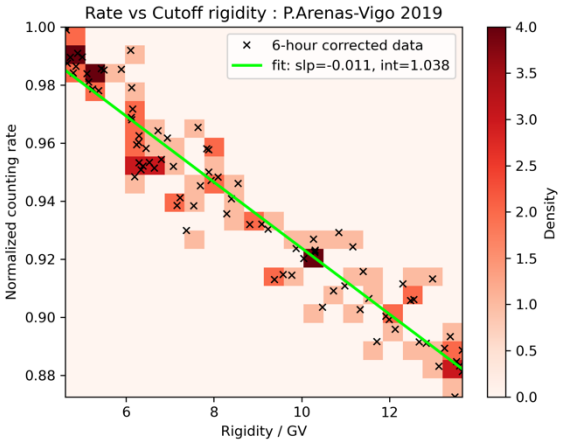

Figure 7.32: TRISTAN regression result and rigidity coefficients for the second latitudinal survey. Normalized M1 rate vs. cutoff rigidity.

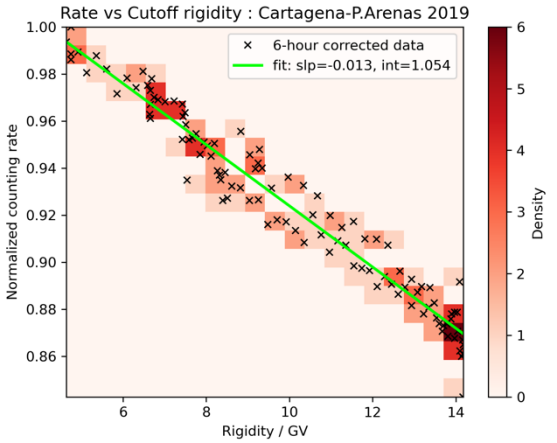

Figure 7.33: TRISTAN regression result and rigidity coefficients for the third latitudinal survey. Normalized M1 rate vs. cutoff rigidity.

Rigidity coefficients differ slightly between surveys. However, the values are compatible, with the given uncertainties, for all latitudinal scans. The discrepancy between NH and SH might be related to the variations in the atmospheric conditions since the two atmospheres are different [119]. The study of this feature is not straightforward since we have to remove the atmospheric effect first.

Regarding NEMO, the dependency of the counting rates with the cutoff rigidity can be approximated by the Dorman function:

$$N = N_0(1 - \exp(-\alpha R_c^{-\kappa})), \quad (7.6)$$

where N_0, α, and κ are free parameters [123]. Despite not having physical content, this parameterization describes the integral response function (N) in good agreement with the observations.

Table 7.6 summarizes the results obtained for the two sets of monitors, BNM and NM64. Standard uncertainties associated with the coefficients are shown in parenthesis. The origin of the differences between the coefficients of both detectors relies on their different thresholds. BNM set is sensitive to neutrons below 50 eV, whereas the NM64 is to neutrons above 100 MeV due to its lead shielding. Figures 7.34 and 7.35 present the behavior of NEMO as a function of the cutoff rigidity.

Table 7.6: NEMO rigidity coefficients for the different neutron monitors.

Data samples	N_0	α	κ
BNM	1.35 (5)	4.5 (5)	0.78 (2)
NM64	1.11 (1)	8.4 (3)	0.90 (1)

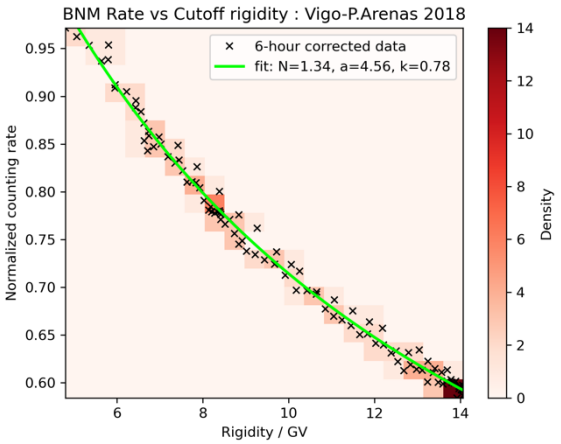

Figure 7.34: NEMO-BNM regression result and rigidity coefficients for the first latitudinal survey. Normalized rate vs. cutoff rigidity.

USC
UNIVERSIDADE DE SANTIAGO DE COMPOSTELA

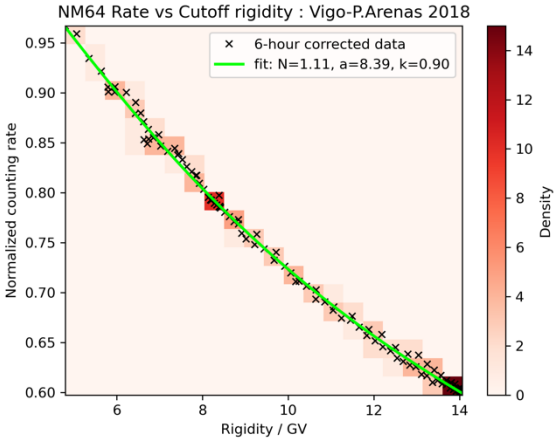

Figure 7.35: NEMO-NM64 regression result and rigidity coefficients for the first latitudinal survey. Normalized rate vs. cutoff rigidity.

ORCA detectors, TRISTAN and NEMO, are complementary, and the whole system covers a wide range of observational energies. Cutoff rigidity affects more NEMO than TRISTAN rate because of the energy of the particles each one detects. Neutron monitors' rate decreases around 30% between Vigo to the equator, whereas for TRISTAN, the maximum reduction is about 15%.

7.5.2 Solar activity

Magnetic field disturbances in the ISM affect the propagation of GCR. Long- and short-term modulation of the GCR intensity has been introduced in Section 1.4. The chance of extreme space weather events such CMEs varies within and between solar cycles. Continuous monitoring of the GCR intensity exposes the decrease of its magnitude associated with geomagnetic storms, the so-called FD. Typical events show a sudden reduction of the GCR intensity (3–20%) within a few hours from the arrival of a CME to the Earth's magnetosphere. The Earth is shielded from low-energy galactic cosmic radiation by the bow shock at the front of the magnetic cloud. The recovery period to the previous GCR intensity can take days or even weeks and depends on the strength of the CME emitted.

One of the top fifty geomagnetic storms since 1994 occurred during the solar cycle 24 in the summer solstice of 2015. Four CMEs erupted from sunspot AR2371 between June 18th and 23rd, associated with M-class SF. A CME of these characteristics reaches the Earth approximately three days after being emitted. The first impact of the interplanetary shock wave on June 21st did not produce a geomagnetic storm. It was not until the third shock impact on June 22nd, when ground detectors registered a GCR intensity decrease, the FD. A G4-class geomagnetic storm took place on June 22nd and 23rd as a result of the superposition effects of the impact of the multiple CMEs on the Earth's magnetosphere. Moreover, a G2-class geomagnetic storm occurred on June 24th. The storm scale can be found in the National and Oceanic Atmospheric Administration (NOAA) [124].

The effects of the above-mentioned geomagnetic storms on TRAGALDABAS data will be reported, as well as the changes they caused on the magnetic field components, the planetary K-index (Kp), and the Disturbance Storm-Time index (Dst).

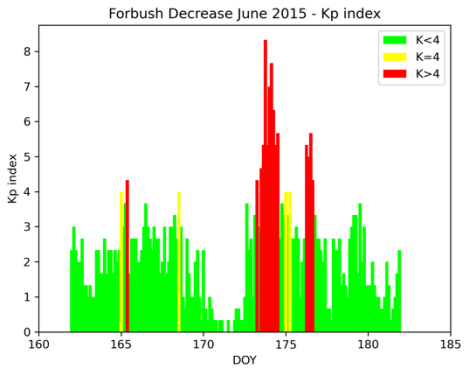

Figure 7.36: Kp index evolution during the geomagnetic storms of June 2015.

The Kp index accounts for the magnetic effects of solar particle radiation, and it is the global geomagnetic activity index [125]. Measurements from ground-based magnetometers in several countries (Australia, Canada, Germany, United Kingdom, and the United States) are put together to determine the Kp index. A value below four indicates

USC UNIVERSIDADE DE SANTIAGO DE COMPOSTELA

quiet or low levels of geomagnetic activity, equal to four refers to moderate, and above four means high geomagnetic activity or geomagnetic storm. The higher the Kp-index is, the more severe the storm. Figure 7.36 shows the Kp-index during the geomagnetic storms of June 2015. The GFZ (GeoForschungZentrum) Helmholtz Centre Potsdam is our data source of the Kp-index [125]. The geomagnetic storm on June 22nd was severe, i.e., Kp between 7.67 and 8.67.

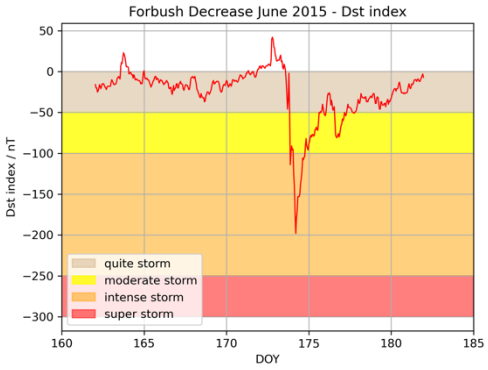

Figure 7.37: Dst-index evolution during the geomagnetic storms of June 2015.

The Dst index measures the intensity of the ring current and is based on the variation of the horizontal component of the Earth's magnetic field near the equator region. It is expressed in nanotesla and is a measure of the severity of geomagnetic storms. Contrary to the Kp index, low values of the Dst imply a high accumulation of energy in the Earth's magnetosphere. The evolution of the Dst index during the storms of June 2015 is shown in Figure 7.37. The minimum value in this period was around 200 nT which indicates the strength of this geomagnetic storm. Dst index used in this document was provided by the World Data Center for Geomagnetism, Kyoto [126].

Earth's magnetic field components, north (B_X), east (B_Y), and vertical (B_Z) are shown in Figure 7.38 together with the total intensity (B_F). Upon the arrival of the third interplanetary shock originated by the CMEs, oscillations in the components can be observed. Data provided by L'Observatori de l' Ebre [127].

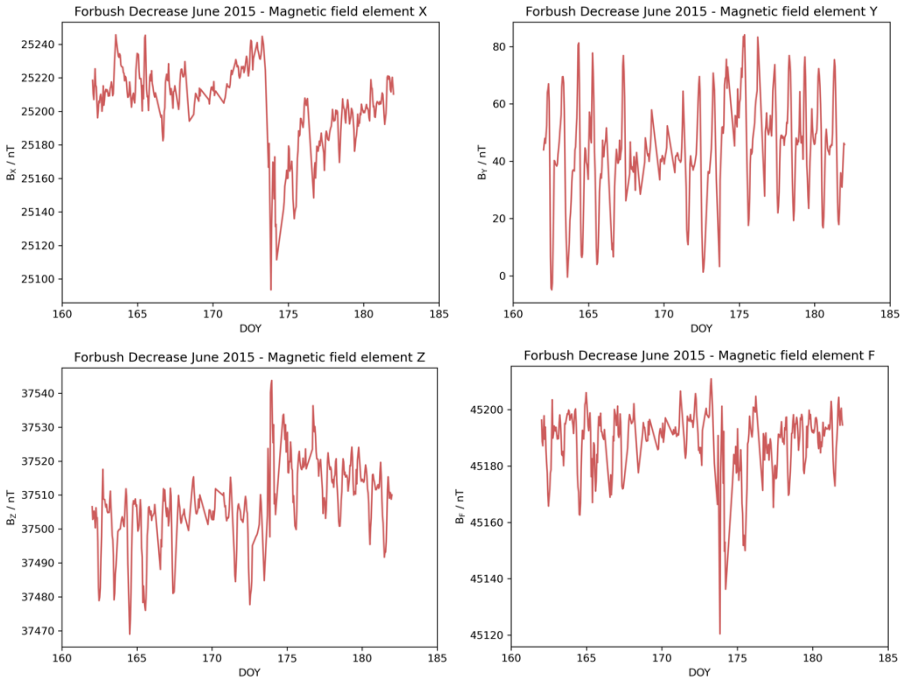

Figure 7.38: Evolution of the components (X,Y,Z, and F) of the magnetic field during the geomagnetic storms of June 2015.

The analysis of TRAGALDABAS measured data in the course of the aforementioned geomagnetic storms yields promising results. The successive interplanetary shocks acted like a barrier shielding the detector from GCRs. A depression in the relative variation of the M1 rate has been observed. Its start is in temporal coincidence with the impact of the first shock on June 21st (DOY 172). Therefore, a FD has been detected, and its amplitude reached up to 4%.

Figure 7.39 shows the relative variation of the M1 rate during the geomagnetic storms of June 2015, which manifest a good temporal correlation with the Kp index, Dst index, and the Earth's magnetic field that have been previously described (Figures 7.36, 7.37, and 7.38). The effect of the storms starts to disappear gradually after June 26th (DOY 177), and the counting rate is back to the pre-FD state on July 1st (DOY 182).

USC UNIVERSIDADE DE SANTIAGO DE COMPOSTELA

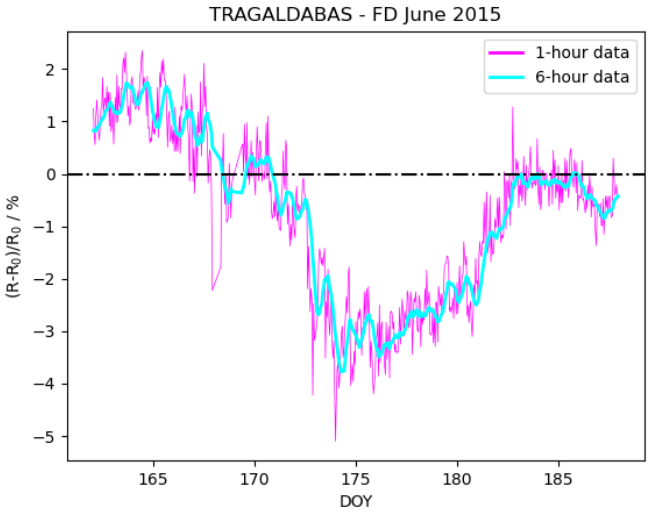

Figure 7.39: Relative variation of the M1 rate measured by TRAGALDABAS during the geomagnetic storms of June 2015, i.e., the FD.

TRAGALDABAS detector is sensitive to space weather effects that imply a rate reduction of a few percent. The FD amplitude given by this detector can be compared with other results in [38, 128, 129].

7.5.3 SAA

As it was stated in Section 1.3.4.2, the SAA is a region over South America and the South Atlantic that extends to South Africa. It covers the latitudes from the equator to the 50ºS parallel. Earth's magnetic field is strongly decreasing with time in this area which modulates the CR flux measured on the surface. Changes in the geomagnetic field affect the trajectory of the CRs, so more particles are detected due to the above-mentioned reduction of the cutoff rigidities. However, this effect is small, around a 1.5% increase in neutron monitor counting rate per year [130]. Because of that, TRISTAN data have to be analyzed very carefully to remove all contributions of the atmospheric conditions and ship motions. A possible approach to SAA analysis is the study of the east-west effect. New efficiencies at different zenithal angles should be calculated to calibrate the data accordingly.

USC UNIDADE SANTIAGO DE COMPOSTELA

7.6 EXTENDED MULTIPLICITY STUDY

TRASGO detectors are characterized by their high granularity and good position-time resolution. This configuration enables multiparticle detection and separation between muons, electrons, and gammas. The different signals or stamps that particles leave in the active size of TRISTAN are diagramed out in Figure 7.40.

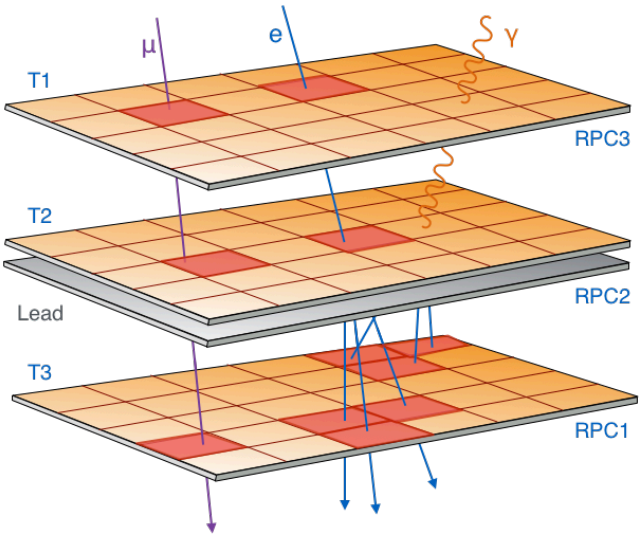

Figure 7.40: Particles' signals across the active size of TRISTAN. A lead layer is placed between T2 and T3 and covers, exclusively, the 12 central pads.

Multiplicity studies involve the data acquired by TRISTAN during the third latitudinal survey and the two static measurements. The steps followed in this section have already been explained throughout this chapter for M1. The barometric effect, and the influence of the cutoff rigidity, will be analyzed for multiplicity two (M2) and multiplicity higher than two (MH). These multiplicities have no restriction on the number of hits per plane and have been constructed based on the number of unambiguous tracks. The calibration of M2 and MH rates has been done like for M1. Multiplicities higher than one are related to electromagnetic showers produced by muon decays in the last kilometers of the atmosphere above the detector. The higher the multiplicity, the higher the energy of the primary CR.

USC UNIVERSIDADE DE SANTIAGO DE COMPOSTELA

7.6.1 Barometric effect

The impact of the atmospheric mass above a detector differs for the different multiplicities. To determine the barometric coefficients of M2 and MH, we have used the data of Santiago and Antarctica (Figure 7.41). As it can be seen in Table 7.7, the β-coefficient increases with multiplicity. TRASGOs detect multiple particles when high-energy muon decay takes place in the last few kilometers above them because the electromagnetic showers they produce are very narrow.

Table 7.7: TRISTAN M2 and MH barometric coefficients.

Data samples	β_{M2} / % hPa	β_{MH} / % hPa
Santiago	-0.32 (4)	-0.45 (5)
Antarctica	-0.32 (4)	-0.44 (4)

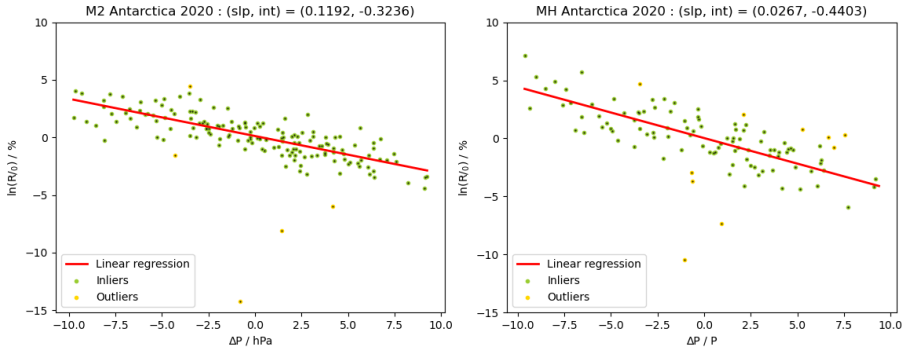

Figure 7.41: Barometric effect observed on M2 and MH rates for Antarctica.

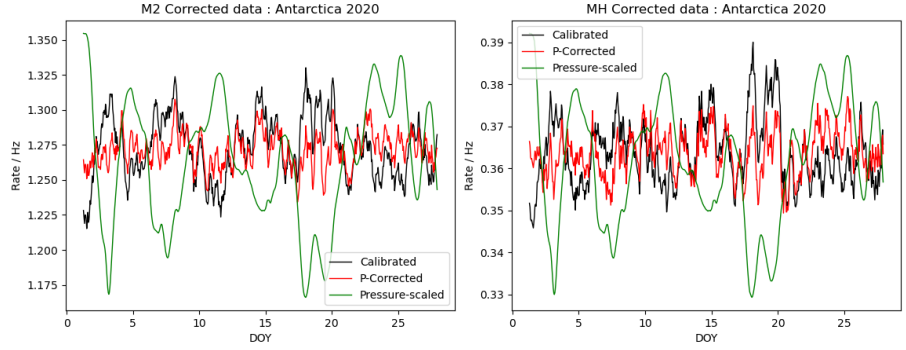

Figure 7.42: Corrected M2 and MH rates for Antarctica.

Effects of the barometric correction on the M2 and MH calibrated data are shown in Figures 7.42 and 7.43 for the two static measurements and the third latitudinal survey, respectively. The average between Santiago and Antarctica coefficients has been used to correct the data of the third journey.

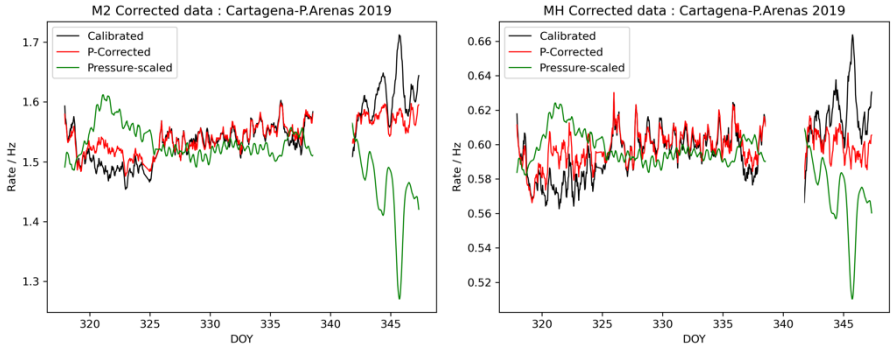

Figure 7.43: Corrected M2 and MH rates for the thid latitudinal survey.

A smoothing of the hourly calibrated data with a moving 6-hour window has been performed. Pressure has been scaled to the mean rate to visualize how the oscillations are flattened by applying this correction.

7.6.2 Cutoff rigidity dependency

Event or track multiplicities give us information about the energy of the primary CR that produced the secondaries we detect on the surface. A simple demonstration concerns the cutoff rigidity and the rate of M2 and MH measured by TRISTAN in the last journey. The rigidity coefficients or η-coefficients have been estimated following the same procedure as for M1. Results are summarized in Table 7.8, where the first digits of the standard uncertainties are given in parenthesis.

Table 7.8: M2 and MH rigidity coefficients for the last latitudinal survey.

Data samples	η / GV	Intercept
Survey 2019-II - M2	-0.0045 (4)	1.000 (4)
Survey 2019-II - MH	-0.0007 (5)	0.956 (6)

USC UNIVERSIDADE DE SANTIAGO DE COMPOSTELA

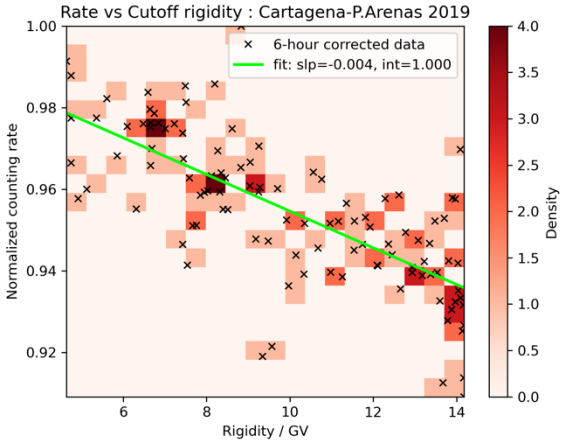

Figure 7.44: TRISTAN regression result and rigidity coefficients for the third latitudinal survey. Normalized M2 rate vs. cutoff rigidity.

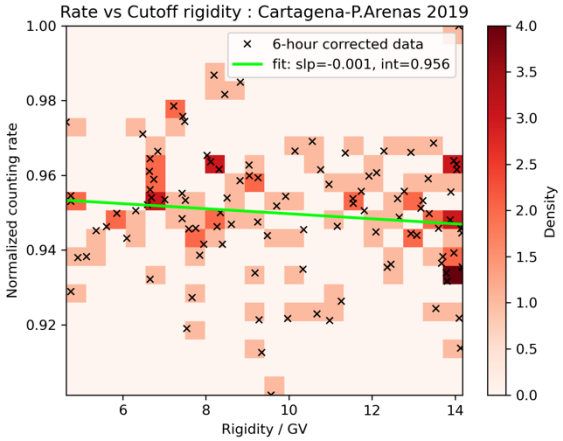

Figure 7.45: TRISTAN regression result and rigidity coefficients for the third latitudinal survey. Normalized MH rate vs. cutoff rigidity.

A direct comparison of the rigidity coefficients for M1, M2, and MH demonstrates that high multiplicities come from high-energy primary CRs, as we expected. The η-coefficient decreases with multiplicity. The data of the latitudinal surveys are very valuable for the study of the energies associated with each multiplicity and offer new possibilities concerning the magnetic fields and the atmosphere.

USC
UNIVERSIDADE
DE SANTIAGO
DE COMPOSTELA

USC
UNIVERSIDADE
DE SANTIAGO
DE COMPOSTELA

CONCLUSIONS

In the present work, we have reported the tasks that have been carried out to guarantee the best quality of the CR data registered by TRISTAN and TRAGALDABAS. All the essential aspects required to run an experiment of this kind have been covered, from the assembly or installation of the detector to the analysis of the data. The similarities between the two detectors allow everything learned with one to be applied to its counterpart.

TRISTAN has been installed in Antarctica at BAE-JCI with great success. The unprecedented latitudinal surveys it has performed have meant that almost all of our resources have been focused on achieving the best data quality. To accomplish that, we have developed the calibration, reconstruction, and analysis algorithms. Unpacked data have been calibrated by charge and time of flight, which allowed data filtering to reduce the noise-to-signal ratio. The data produced by applying the calibration constants have been calibrated, also by the efficiency. Besides a unique efficiency calibration method, we have developed three. Comparing the calibrated data obtained through these three techniques, we have calculated the systematic uncertainties of the calibration process as well as the minimum-maximum range. We observed that for periods when the operating conditions were extreme, the efficiency was not enough to remove some effects, for example, in the first latitudinal scan. Hence, a new correction method based on the number of random coincidences has been implemented successfully to overcome this.

The barometric and temperature effects have been studied after finishing the calibration process. The analysis of the data taken by TRISTAN in Santiago de Compostela and Antarctica has yielded a barometric coefficient of –0.23% hPa, and the temperature coefficients have shown a positive correlation with the tropopause region.

USC
UNIVERSIDADE DE SANTIAGO DE COMPOSTELA

Moreover, various tools have been created to compute the cutoff rigidity everywhere. The relationship between the pressure-corrected data and the cutoff rigidity has been explored, showing compatible coefficients for the two complete surveys. These coefficients have been compared with the results obtained for the neutron data measured by NEMO.
TimTrack has been implemented as the event reconstruction algorithm for both detectors. We have filtered the saetas by their chi-square to extract only the unambiguous tracks. In addition, a Monte Carlo simulation has been carried out to determine the acceptance and the reconstruction resolutions of both detectors. It should be noted that the achieved time resolutions for TRAGALDABAS and TRISTAN have been below 200 and 300 ps, respectively.
Regarding TRAGALDABAS, several updates concerning hardware and software have been made to improve its integrity and stability. We have instrumented and commissioned the fourth plane in late 2021/early 2022. Most of the existing codes have been adapted to the new layout, and the new trigger configuration files have been created. A self-trigger run of a few minutes is performed daily via cron to check the RPC conditions. The high voltage (HV) dynamic adjustment has been configured to maintain the reduced electric field inside the gap constant at 228 Td. We have kept a rigorous control of the detector, and the noisy and dead channels have been replaced. For this reason, the slow control and monitoring system (SCMS) is one of the most important systems. Due to the hardware upgrades, the Nagios sensors that retrieve the information of the log files had to be improved. Apart from Nagios, which is also used to send the alarms when a variable goes beyond a certain threshold, Grafana provides graphs of the detector's operating conditions. A set of dashboards has been customized to show all the slow control variables of each plane. Additionally, our group has developed a graphical user interface (GUI), called CellViewer, to represent the raw rates, hits, and reconstructed saetas by way of cell maps.
In conjunction with TRISTAN data analysis, a data sample of TRAGALDABAS has been examined because of its interest in solar physics and space weather events. The study of the barometric effect has given a coefficient of −0.43% hPa, which almost doubles the TRISTAN value. However, this discrepancy is most likely related to

USC UNIDADE SANTIAGO COMPOSTELA

the different layouts of the detectors and the energies they observed. We have investigated the behavior of the global geomagnetic index and the components of the Earth's magnetic field during the geomagnetic storms that occurred in mid-June 2015. The inspection of TRAGALDABAS data in the course of these storms has revealed a sudden depression in the rate followed by a gradual recovery, i.e., a Forbush decrease (FD) has been observed. We have estimated that its amplitude reached up to 4%. The joint analysis of the different indices has shown a good temporal correlation between the rate and the different indices.

A preliminary analysis of the barometric effect and the influence of the cutoff rigidity on events with multiplicities higher than one has been carried out. Results have yielded an increasing barometric coefficient and decreasing rigidity coefficient as multiplicity grows. This behavior confirms what was expected, that high-multiplicity events come from EAS created by high-energy primary CRs.

To conclude, this thesis presents the results of the rate of multiplicity equal to one (M1), which refers to events with only one unambiguous reconstructed track. These events constitute around 99% of the total. Nevertheless, the advantage of the TRASGOs over other detectors such as neutron monitors or standard muon telescopes is their capability to detect events of different multiplicities or bundles of particles. Further studies should be necessary to understand the behavior of the rates of multiplicity two (M2) and higher (MH). These rates have already been constructed and divided into several zenithal and azimuthal intervals, which allows the investigation of the angular dependency in the region of the South Atlantic Anomaly (SAA). Furthermore, the particle identification algorithms under development in our group may allow us to separate muons and electrons. It has been demonstrated that TRISTAN and TRAGALDABAS can operate autonomously and that both are sensitive to atmospheric and space weather effects. Therefore, TRASGO detectors could be an alternative to other technologies such as neutron monitors and muon telescopes.

USC
UNIVERSIDADE DE SANTIAGO DE COMPOSTELA

USC
UNIVERSIDADE
DE SANTIAGO
DE COMPOSTELA

RESUMO EN GALEGO

Os raios cósmicos seguen a ser unha fonte permanente de misterios, a pesar de ser descubertos por Victor Hess hai máis de cen anos. A radiación cósmica primaria chega de igual maneira dende todas as direccións á Terra e dá unha mostra de materia provinte de algún dos procesos astrofísicos máis enerxéticos na natureza. A maioría dos raios cósmicos son núcleos atómicos cargados relativistas, principalmente protóns (∼ 86%), partículas alfa (∼ 11%) e unha contribución de núcleos pesados e electróns que son orixinados no espazo exterior. Este tipo de radiación, está exposta a alteracións nas súas traxectorias dende a fonte na que se producen ata onde os detectamos. A atmosfera da Terra é bombardeada continuamente por estas partículas altamente enerxéticas. A primeira interacción dos raios cósmicos cos núcleos atmosféricos ocorre tipicamente entre os 10 e os 30 km de altura sobre o nivel do mar. Estas interaccións consisten en colisións de moi alta enerxía que producen partículas secundarias como por exemplo protóns, neutróns e pións. Ditas novas partículas poden interaccionar de novo na atmosfera dando lugar a o que se coñece como cascadas de partículas ou "Extensive Air Showers" (EAS). Unha cascada deste tipo pódese descompoñer en tres compoñentes: hadrónica, muónica e electromagnética. A medida que unha EAS avanza en dirección á superficie da Terra, as compoñentes vanse reproducindo ata que a enerxía das partículas secundarias non é suficiente para continuar co proceso. Unicamente unha parte destas cascadas chega á superficie antes de ser absorbida pola atmosfera. O número de partículas detectadas será maior para raios cósmicos primarios de moi alta enerxía que para os de menor enerxía, posto que para estes a maior parte da EAS será completamente absorbida. O capítulo primeiro presenta ó lector o tema dos raios cósmicos, e explica as súas principais propiedades. Tamén se trata

USC
UNIVERSIDADE DE SANTIAGO DE COMPOSTELA

a influenza que os diversos campos magnéticos que atravesan e a atmosfera terrestre exercen sobre eles antes de ser detectados.
Hoxe en día dispoñemos de unha ampla variedade de técnicas que permiten a detección de raios cósmicos. O método empregado para medir os fluxos de diferentes partículas, depende tanto da súa enerxía coma da súa natureza, ademais do lugar no que se leva a cabo a medida. Entre todas as posibilidades, os detectores de gas ionizante tales como as "Resistive Plate Chambers" (RPC), son empregados mundialmente en múltiples experimentos. Isto débese á súa capacidade tanto para o seguimento das traxectorias das diferentes partículas como para facer medicións do seu tempo de voo. O desenrolo dunha nova xeración de detectores de raios cósmicos baseado neste tipo de tecnoloxía, permite o estudo das partículas secundarias producidas nas cascadas atmosféricas. Esta nova familia de detectores son os chamados TRASGOs (acrónimo de "TRAck reconStructinG bOx"), cuxas características principais son unha alta granularidade e unhas moi boas resolucións tanto en posición como en tempo. Un TRASGO está capacitado para rexistrar varias partículas que inciden ó mesmo tempo no seu volume activo, e ademais permite identificar se son muóns, protóns ou electróns. O capítulo segundo introduce a teoría na que se basean os detectores de gas ionizante, describindo os procesos de interacción radiación materia e os seus principios de operación. Posteriormente no capítulo terceiro, introdúcese o proxecto TRASGO comezando coa motivación e descrición dos diversos detectores que están tanto en funcionamento como en desenrolo na actualidade.
O proxecto TRASGO ten como finalidade ofrecer información de forma regular sobre os raios cósmicos que normalmente non permiten outras clases de detectores. A reconstrución dos eventos ou cascadas rexistradas podería permitirnos estimar a enerxía do raio cósmico primario que orixinou a EAS. Ademais, se engadimos a identificación de partículas que atravesan o detector, teríamos acceso á avaliación dos efectos atmosféricos, do campo magnético terrestre e da modulación solar. Todos estes efectos inflúen ou modulan o fluxo de raios cósmicos que detectamos na Terra. No proxecto TRASGO encádranse os detectores TRISTAN e TRAGALDABAS nos que se basea esta tese. Por unha banda, TRISTAN (TRasgo para InveSTigacións Antárticas)

USC UNIVERSIDADE DE SANTIAGO DE COMPOSTELA

levou a cabo unha serie de medidas de raios cósmicos recorrendo un rango de case 90º de latitude. Estas medidas teñen un carácter inédito e son únicas no mundo para un detector de este tipo, as cales permiten o estudo do fluxo medido e a súa dependencia coa rixidez de corte e a atmosfera. Despois de percorrer ata en tres ocasións o océano atlántico dende España ata Punta Arenas en Chile, foi instalado na Base Antártica Española Juan Carlos I (BAE-JCI). Este detector está composto por tres planos RPC en disposición horizontal con trinta células de detección cada un. Cada plano ten un área de aproximadamente 1.8 m^2 e foron deseñados polo LIP de Coimbra. Entre o segundo e terceiro plano contando dende arriba engadiuse 1 cm de chumbo, que abarca as doce células centrais, para filtrar as partículas por enerxías e fomentar a producción de cascadas electromagnéticas. O detector foi instalado nos buques oceanográficos Sarmiento de Gamboa e BIO Hespérides para os escaneados latitudinais e transporte á Antártida, como parte do Observatorio de Raios Cósmicos Antártico (ORCA). Por outra banda, TRAGALDABAS (acrónimo de "TRAsGo for the AnaLysis of the nuclear matter Decay, the Atmosphere, the earth B-field And the Solar activity") é unha estación fixa que ten como sede a Facultade de Física da Universidade de Santiago de Compostela dende 2015. Ata catro planos RPC de cento vinte células, xunto con unha capa de 1 cm de chumbo entre o terceiro e cuarto plano, forman este detector. Cada plano ten un área de aproximadamente 1.8 m^2 como no caso de TRISTAN e tamén foron deseñados polo LIP de Coimbra. Este detector estuda os efectos do clima espacial e da atmosfera principalmente. O capítulo cuarto recolle en detalle os sistemas electrónicos esenciais para a construción dun TRASGO, así como os esquemas de alimentación e de transferencia de datos entre os diversos compoñentes.

Como ocorre en calquera experimento de física de altas enerxías, a monitorización e o control dos compoñentes é unha peza fundamental para garantir a estabilidade e integridade do detector. As condicións de traballo teñen que ser as correctas para que a calidade dos datos sexa óptima. Por este motivo, os detectores TRISTAN e TRAGALDABAS teñen un sistema de control propio e múltiples ferramentas de visualización das diversas variables de control. O capítulo quinto describe as ferramentas deseñadas para tal fin.

USC
UNIVERSIDADE DE SANTIAGO DE COMPOSTELA

A vixilancia do detector non é o único necesario para obter uns bos datos. Unha vez tomadas as medidas de raios cósmicos nas mellores condicións, os datos teñen que ser calibrados e reconstruídos para que a interpretación dos resultados sexa a correcta. As primeiras etapas da calibración consisten na filtración tanto por medio da carga depositada como do tempo de voo. Os datos filtrados calíbranse posteriormente por tempo activo e tempo morto, xunto co número de coincidencias aleatorias. A última fase consiste na calibración por eficiencia do detector. Esta depende de diversos factores e non sempre é constante, o cal afecta directamente á taxa de raios cósmicos medida. O capítulo sexto describe os algoritmos de calibración e reconstrución empregados e deseñados para TRISTAN e TRAGALDABAS.

Analizando conxuntamente os datos rexistrados de raios cósmicos con variables externas serve como mostra da calidade das medidas. O principal efecto que se ten que eliminar para estudar outros mais sutís é o efecto da presión. Coñecido como efecto barométrico achega información da masa atmosférica que atravesan os raios cósmicos ata impactar no detector. Unha vez corrixidos os datos e eliminada a dependencia con esta variable, poderase investigar a influencia da temperatura das diferentes capas da atmosfera da Terra, a modulación solar ou a rixidez de corte. O capítulo sétimo mostra os coeficientes que relacionan a presión, a temperatura de atmosfera terrestre e a rixidez de corte obtidos para TRISTAN. Ademais, inclúe a corrección por presión aplicada ao detector TRAGALDABAS e o estudo dos seus datos xa corrixidos durante unha potente tormenta xeomagnética.

A tese que aquí se presenta informa das tarefas que foron levadas a cabo para garantir a mellor calidade dos datos de raios cósmicos rexistrados por ambos os dous detectores, TRISTAN e TRAGALDABAS. Todos os aspectos fundamentais para o desenrolo dun experimento desde tipo foron cubertos, dende a ensamblaxe ou instalación do detector ata a análise minuciosa dos seus datos. As semellanzas entre os dous detectores descritos favorecen que todo o aprendido cun deles serva para ser aplicado no outro unicamente cambiando a xeometría no software.

A instalación do detector TRISTAN na Antártida, que levamos a cabo a finais do ano 2019 e comezos do 2020, concluíuse con éxito a pesar das dificultades que supoñía. Os barcos Sarmiento de Gamboa e

USC UNIVERSIDADE DE SANTIAGO DE COMPOSTELA

BIO Hespérides foron os portadores do detector durante os viaxes polo océano atlántico. O carácter único das medidas tomadas nos escaneados latitudinais fixeron que os nosos recursos se centrasen en conseguir a mellor calidade posible dos datos. Con este obxectivo, creáronse os programas de calibración, reconstrución e análise aquí descritos.

En primeiro lugar os datos foron desempaquetados e filtrados pola carga depositada. Isto, consistiu na mellora da proporción sinal-ruído. Calculáronse os pedestais ou umbrais de corte diariamente para cada unha das células das que están formados os detectores, eliminando todas aquelas cargas que quedaban por debaixo dos mesmos. A sincronización das sinais temporais proporcionadas polas células levouse a cabo mediante un algoritmo iterativo que centra as distribucións das diferenzas de tempo entre elas. Esta calibración é necesaria para eliminar os efectos das diferentes lonxitudes dos cables e así facer selección de trazas con diferentes tempos de voo. Aínda que o tempo de voo non se empregou para filtrar os datos de TRISTAN, as constantes de calibración almacenáronse diariamente. Unha vez calculadas as constantes, os datos extraídos do detector foron corrixidos pola eficiencia.

Ata tres métodos de calibración por eficiencia foron deseñados nesta tese, os cales foron denominados como os métodos de ”tracking”, “PCA”, e “charge”. Os tres métodos teñen en conta diferentes parámetros e os pasos seguidos para aplicalos atópanse no capítulo sexto. A elaboración de tres métodos en lugar de un único, permite facer unha estimación das incertezas sistemáticas asociadas ó proceso de calibración completo, así como definir uns rangos mínimo e máximo entre os cales se atopará a nosa taxa de raios cósmicos unha vez calibrada.

As observacións dos datos calibrados pola eficiencia cando as condicións de traballo foron extremas, diagnosticaron que esta non era suficiente como para rexeitar todo aquel efecto non producido por raios cósmicos. En particular, durante a primeira viaxe dende Vigo, España, ata Punta Arenas, Chile, o aire acondicionado do Sarmiento de Gamboa avariouse. Este problema desencadeou que na sala na que se instalou TRISTAN, a temperatura pasase de estar regulada a incrementarse drasticamente. O incremento de temperatura afecta directamente o funcionamento do detector, xa que supón un aumento dos niveis de ruído electrónico e por tanto do número de coincidencias accidentais

USC
UNIVERSIDADE DE SANTIAGO DE COMPOSTELA

ou aleatorias. A adquisición dun evento realízase cos planos 1 e 3 en coincidencia. Para solucionar este problema e a consecuente perda na calidade dos datos, creouse un novo método que ten en conta os efectos das coincidencias aleatorias na taxa. Esta corrección adicional permitiu unha reconstrución case óptima dos datos afectados dende a devandita avaría ata o destino final.

Os datos xerados tras o proceso de calibración, aínda tiveron que ser corrixidos polos ben coñecidos efectos de presión e de temperatura. No caso da presión, cando esta aumenta os muóns producidos nas cascadas atmosféricas teñen unha maior probabilidade de interaccionar con un núcleo da atmosfera que de desintegrarse contribuíndo a compoñente electromagnética. Isto, tradúcese nunha diminución na taxa medida. O efecto contrario ocorre coa temperatura, e cando esta aumenta os muóns teñen unha maior probabilidade de desintegrarse que de colisionar polo camiño, co cal a taxa detectada aumenta. A análise do efecto barométrico para TRISTAN deixou como resultado un coeficiente de -0.23% hPa. O cálculo do coeficiente barométrico realizouse para os datos que este detector rexistrou en Santiago de Compostela e na Antártida, e posteriormente eliminouse o efecto nos datos das múltiples viaxes. Os coeficientes para a temperatura mostraron unha correlación positiva na rexión da tropopausa e tamén nas capas máis baixas da atmosfera. No caso da temperatura, os seus efectos non se corrixiron nos datos debido a que primeiro é necesario entender cal dos métodos coñecidos se adapta máis a este detector, xa que ningún deles é universal. Os datos corrixidos pola presión foron estudados coa rixidez de corte. Para iso, creáronse diversas ferramentas que permiten calcular a rixidez de corte en calquera coordenadas a unha altitude de aproximadamente 20 km sobre o nivel do mar con alta precisión.

Explorando a relación entre rixidez e taxa observouse a compatibilidade entre coeficientes obtidos para todas as viaxes, en particular para as dúas que se fixeron completas. A dispoñibilidade dunha mostra de datos doutro experimento de ORCA chamado NEMO, que se encarga de medidas de fluxo de neutróns na superficie, fixo posible a comparación entre os datos dos dous detectores.

USC UNIDADE SANTIAGO COMPOSTELA

O algoritmo TimTrack foi o implementado como método de reconstrución nos dous detectores TRISTAN e TRAGALDABAS. No caso do primeiro, as traxectorias reconstruídas foron filtradas polo seu chi cadrado e polas células impactadas. Deste xeito, a mostra de datos final só contiña traxectorias non ambiguas ou para as que se usase en mais dunha ocasión a mesma célula. A aceptancia dos detectores foi calculada mediante a simulación mediante métodos Monte Carlo. Unha segunda simulación do rendemento ofertado polos dous detectores proporcionou unhas resolucións temporais de aproximadamente 200 e 300 ps para TRAGALDABAS e TRISTAN respectivamente.

En canto ó TRAGALDABAS, fixéronse varias actualizacións en canto ó hardware e ó software que serviron para mellorar a súa estabilidade e integridade. O último plano RPC dos que dispón este detector foi equipado a finais de 2021 e comezos de 2022. A maioría dos códigos existentes foron adaptados a esta nova distribución e os ficheiros de configuración do novo trigger foron creados. Tamén se implementou un modo de self-trigger que se executa unha vez cada día e que permite coñecer as condicións internas das RPC. O sistema alto voltaxe foi modificado para que manteña a mesma ganancia incluso con cambios de presión e temperatura, pasando de ser fixo a ser un axuste dinámico en función destas variables. Eliminároronse todas as células ruidosas do detector previa instalación da última RPC. Para isto, o sistema de control, monitorización e visualización foi de gran relevancia. Aínda que os cambios introducidos fixeron que fose necesario actualizar e elaborar novos códigos de lectura dos datos aportados polas RPC. Os dous sistemas de control que se empregan son Nagios e Grafana, que se describen no capítulo quinto. Nagios úsase para o envío de alarmas en canto unha variable sae do seu rango de traballo e Grafana é a ferramenta de visualización. Neste marco creáronse varios bloques de gráficos que mostran todas as variables críticas de cada un dos planos. Engadiuse unha interface gráfica deseñada unicamente para este tipo de detectores, chamada "CellViewer", que fai posible a representación dos datos reconstruídos en tódolos niveles (hit, raw, saeta).

Conxuntamente coa análise dos datos de TRISTAN, examinouse unha mostra de datos de TRAGALDABAS por mor do seu interese no ámbito do clima espacial. A relación da taxa de raios cósmicos medida

USC UNIVERSIDADE DE SANTIAGO DE COMPOSTELA

con este detector arroxou un coeficiente barométrico de −0.43% hPa. Este resultado case dobra o valor obtido para TRISTAN. O máis probable é que esta discrepancia estea relacionada coa diferente configuración dos dous detectores e as enerxías que observaron. Para os estudos de clima espacial, investigamos o índice global xeomagnético e as compoñentes do campo magnético da Terra durante as tormentas xeomagnéticas que aconteceron a mediados de xuño do ano 2015. A inspección dos datos de TRAGALDABAS durante o transcurso destas tormentas revelou unha depresión ou diminución repentina da taxa seguido dunha recuperación gradual, é dicir, observouse o coñecido efecto chamado "Forbush decrease" (FD). Analizando simultaneamente os diferentes índices de campo atopouse que tanto estes como a taxa sufrían os efectos en coincidencia temporal. Determinouse unha amplitude do FD de ata un 4%, valor que se pode comparar no texto principal con outros resultados obtidos por diferentes tipos de detectores.

Por último levouse a cabo un estudo preliminar do efecto barométrico e a influencia da rixidez de corte en eventos con multiplicidades maiores de un. O termo multiplicidade da conta do número de traxectorias reconstruídas que son compatibles coas condicións impostas de filtrado. Os resultados mostraron un aumento da dependencia coa presión a medida que a multiplicidade se fai maior, así como unha diminución da dependencia coa rixidez de corte. Este comportamento cumpre co esperado, xa que as cascadas de alta multiplicidade son orixinadas na interacción de raios cósmicos primarios de alta enerxía coa atmosfera.

Para rematar, esta tese presenta principalmente os resultados da taxa de multiplicidade igual a un, tamén chamada M1, a cal foi construída a partir de traxectorias inequívocas. A taxa de M1 supón ó redor do 99% da taxa total rexistrada polos detectores TRISTAN e TRAGALDABAS. Aínda que a vantaxe deste tipo de detectores respecto a outros como por exemplo os monitores de neutróns ou telescopios de muóns estándar, é a súa capacidade para detectar simultaneamente un gran número de partículas. A porcentaxe de eventos de multiplicidade dous estimouse sobre o 0.8%, mentres que o 0.2% restante se divide entre as diferentes multiplicidades maiores. Para comprender a información

USC
UNIVERSIDADE DE SANTIAGO DE COMPOSTELA

contida nas altas multiplicidades serán necesarios estudos máis profundos, principalmente de multiplicidade dous e maior que dous. Estas taxas foron construídas da mesma forma que M1 e agrupáronse por sectores angulares, o cal deixa practicamente todo preparado para analizar a dependencia angular na rexión da Anomalía do Atlántico Sur (SAA). Ademais, os algoritmos de identificación de partículas que se atopan en desenrolo no noso grupo de investigación pretenden separar muóns de electróns para o estudo dos efectos da temperatura da atmosfera entre outros. Nesta tese demostramos como TRISTAN e TRAGALDABAS poden traballar de forma autónoma e que ambos os dous son sensíbeis a efectos de clima espacial e tempo atmosférico. Polo tanto, os detectores tipo TRASGO poderían ser unha tecnoloxía alternativa os monitores de neutróns e telescopios de muóns tradicionais.

USC
UNIVERSIDADE DE SANTIAGO DE COMPOSTELA

USC
UNIVERSIDADE
DE SANTIAGO
DE COMPOSTELA

APPENDIX

In this appendix the we show the most relevant figures corresponding to the slow control variables of TRISTAN detector during the different data-taking campaigns. The background currents and the HV can be found in Chapter 7.

Latitudinal survey 2018

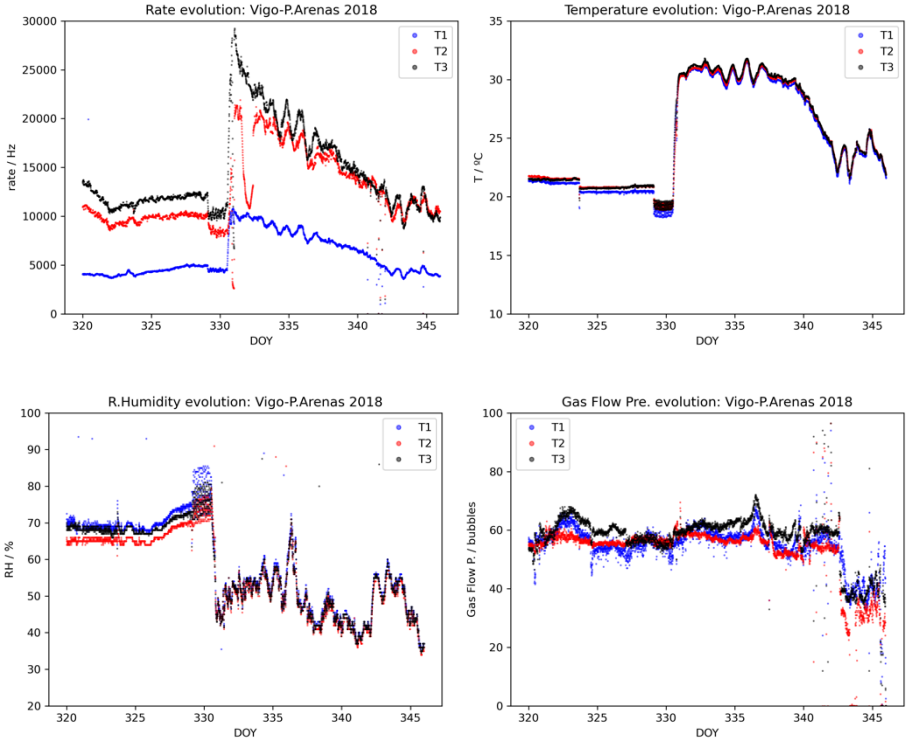

USC UNIVERSIDADE DE SANTIAGO DE COMPOSTELA

Latitudinal survey 2019-I

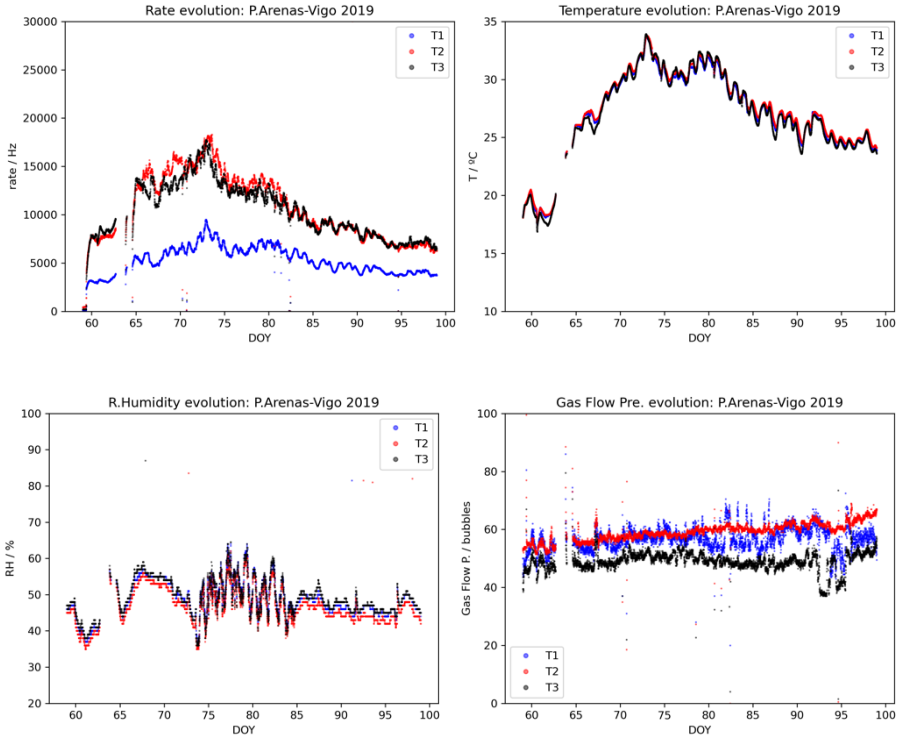

Latitudinal survey 2019-II

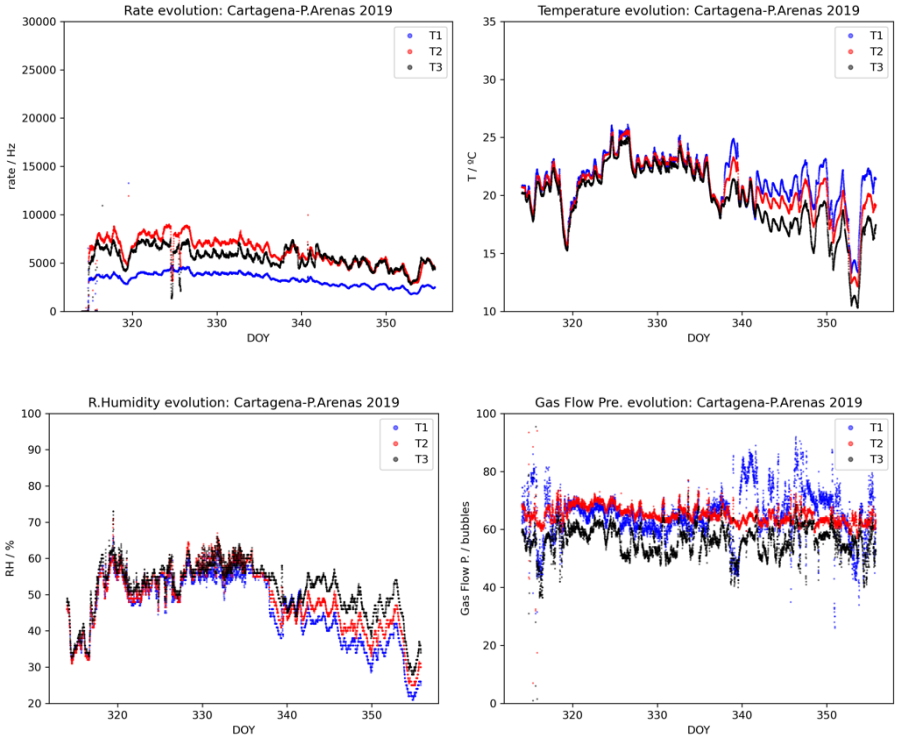

USC
UNIVERSIDADE DE SANTIAGO DE COMPOSTELA

Santiago de Compostela 2019

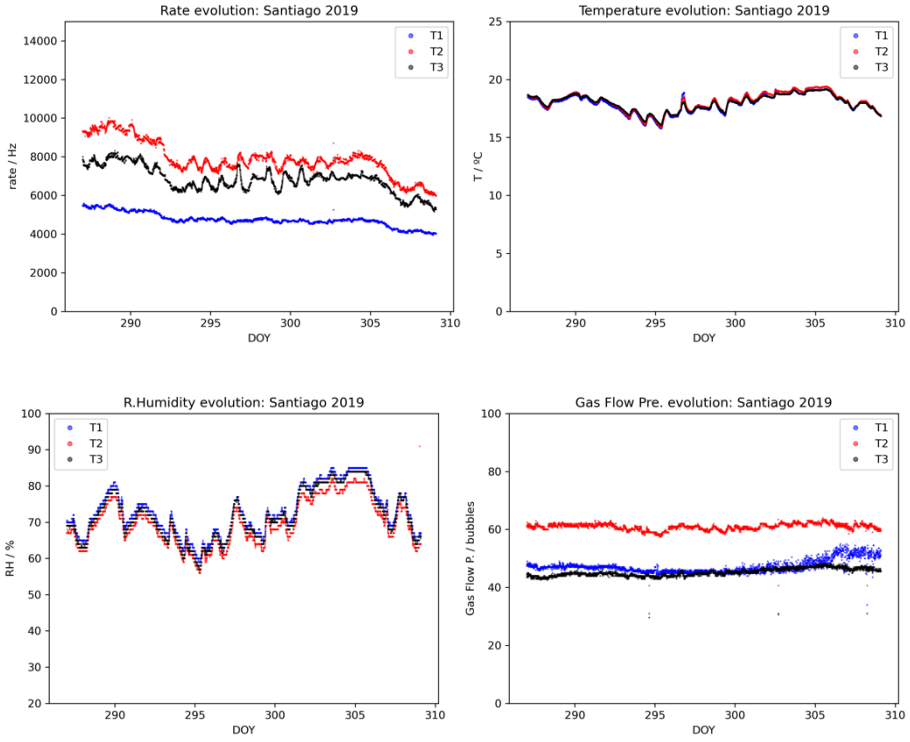

Antarctica 2020

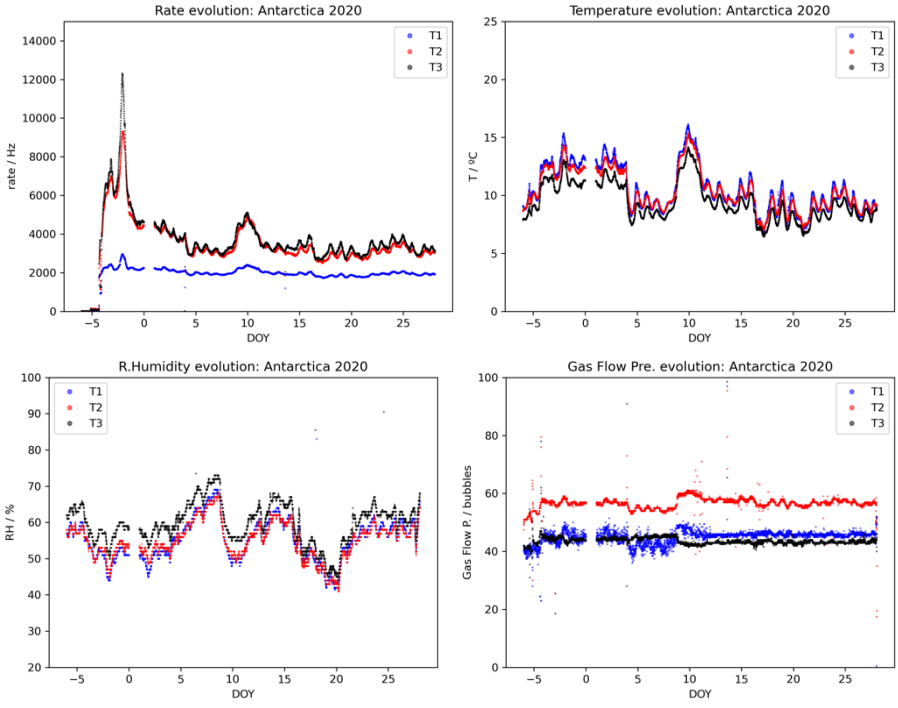

USC
UNIVERSIDADE DE SANTIAGO DE COMPOSTELA

USC
UNIVERSIDADE
DE SANTIAGO
DE COMPOSTELA

BIBLIOGRAPHY

[1] Rutherford, E. Radio-activity. 1st ed. Cambridge University Press, 1904.
[2] Elster J., Geitel H. Weitere Versuche über die Elektricitäts-zerstreuung in abgeschlossenen Luftmengen. Phys. Zeit. 2 (1901), 560–563.
[3] Wulf, T. Beobachtungen über die Strahlung hoher Durchdringungs-fähigkeit auf dem Eiffelturm. Phys. Zeit. 11 (1910), 811–813.
[4] Pacini, D. La radiazione penetrante alla superficie e in seno alle acque. Nuovo Cimento, 3, (1912), 93–100.
[5] Hess, F. V. Über Beobachtungen der durchdringendern Strahlung bei sieben Freiballon-fahrten Phys. Zeit. 13 (1912), 1084–1091.
[6] Millikan, R. A., Cameron, G. H. High Frequency Rays of Cosmic Origin. Phys. Rev. 28 (1926), 851–868.
[7] Beatty, J. J., Westerhoff, S. The Highest-Energy Cosmic Rays. Ann. Rev. Nucl. Part. Sci. 59 (2009), 319–345.
[8] Becker, J., Merten, L. Closing in on the origin of Galactic cosmic rays using multimessenger information. Phys. Rep. 872 (2020), 1–98.
[9] Beringer, J. et al. Particle Data Group. Phys. Rev. D. 86 (2012), 010001.
[10] Greisen, K. End to the Cosmic-Ray Spectrum?. Phys. Rev. Lett. 16 (1966), 748–750.
[11] Rauch, B. F., Walsh, N. E., Zober, W. V. The Trans-Iron Galactic Element Recorder for the International Space Station (TIGERISS). PoS. 395 (2021), 87–96.
[12] Reeves, H. On the origin of the light elements (Z<6). Rev. Mod. Phys. 66 (1994), 193–216.
[13] Fermi, E. On the Origin of the Cosmic Radiation. Phys. Rev. 75 (1949), 1169–1174.
[14] Krymskii, G. F. A regular mechanism for the acceleration of charged particles on the front of a shock wave. Dokl. Acad. Nauk. SSSR. 234 (1977), 1306–1308.

USC
UNIVERSIDADE DE SANTIAGO DE COMPOSTELA

[15] Axford, W. I., Leer, E., Skadron, G. The Acceleration of Cosmic Rays by Shock Waves. 15th ICRC Plovdiv, Bulgaria, AIP Proc. 11 (1978), 132–137.
[16] Bell, A. R. The acceleration of cosmic rays in shock fronts. MNRAS, 182 (1978), 443–455.
[17] Blandford, R. D., Ostriker, J. P. Particle acceleration by astrophysical shocks. Astrophys. J. 221 (1978), L29–L32.
[18] Hillas, A. M. The Origin of Ulta-High-Energy Cosmic Rays. Ann. Rev. Astron. Astrophys. 22 (1984), 425–444.
[19] Strong, A. W., Moskalenko, I. V., Ptuskin, V. S. Cosmic-Ray Propagation and Interactions in the Galaxy. Ann. Rev. Nucl. Part. Sci. 57 (2007), 285–327.
[20] Kronberg, P.P. Extragalactic magnetic fields. Rep. Prog. Phys. 57 (1994), 325–382.
[21] Beck, R. Cosmic Magnetic Fields: Observations and Prospects. AIP Conf. Proc. 1381 (2011), 117–136.
[22] Rand, R. J., Kulkarni, S. R. The local Galactic magnetic field. Astrophys. J. 15 (1989), 760–772.
[23] Stanev, T. High Energy Cosmic Rays. Springer Praxis Books, 2010.
[24] Bütikofer, R. Cosmic Ray Particle Transport in the Earth's Magnetosphere. In: Solar particle radiation storms forecasting and analysis. Astrophys. Space Sci. Lib. 444 (2018), 79–94.
[25] Johnson, T .H. The Azimuthal Asymmetry of the Cosmic Radiation. Phys. Rev. 43 (1933), 834–835.
[26] Dorman, L. Cosmic Rays in Magnetosphere of the Earth and other Planets. Astrophys. Space Sci. Lib. 358 (2009).
[27] Cordaro, E. G., Gálvez, D., Laroze, D. Observation of intensity of cosmic rays and daily magnetic shifts near meridian 70° in the South America. JASTP. 142 (2016), 72–82.
[28] Pavón-Carrasco, F. J., De Santis, A. The South Atlantic Anomaly: The Key for a Possible Geomagnetic Reversal. Front. Earth Sci. 4 (2016), 40.
[29] Smart, D.F., Shea, M. A. Galactic Cosmic Radiation and Solar Energetic Particles. In: Handbok of Geophysics and The Space Environment. US Air Force Geophysics Laboratory. 6 (1988), 1–29.

USC
UNIDADE DE XACOBEO SANTIAGO DE COMPOSTELA

[30] Coetzee, W. F. et al. Cutoff rigidities and latitude dependence of muons at 307 g/cm2 in inclined directions. Acta Phys. Acad. Sci. Hung. 19 (1970), 559–563.
[31] Potgieter, M. S. Solar Modulation of Cosmic Rays. Living Rev. Sol. Phys. 10 (2013), 3.
[32] Forbush, S. E. World-Wide Cosmic-Ray Variations, 1937–1952. Geophys. Res. J. 59 (1954), 525–542.
[33] Thomas, S. R., Owens, M. J., Lockwood, M. The 22-Year Hale Cycle in Cosmic Ray Flux – Evidence for Direct Heliospheric Modulation. Sol. Phys. 289 (2014), 407–421.
[34] Alania, M. V., Modzelewska, R., Wawrzynczak, A. On the Relationship of the 27-day Variations of the Solar Wind Velocity and Galactic Cosmic Ray Intensity in Minimum Epoch of Solar Activity. Sol. Phys. 270 (2011), 629–641.
[35] Ross, E., William J. C. The Behaviour of Galactic Cosmic-Ray Intensity During Solar Activity Cycle 24. Sol. Phys. 294 (2019), 8.
[36] Forbush, S. On the effects in the cosmic ray intensity observed during magnetic storms. Phys. Rev. 51 (1937), 1108–1109.
[37] Consolandi, C. Primary Cosmic Ray Proton Flux Measured by AMS-02. arXiv:1402.0467v2 [astro-ph.HE] (2019).
[38] Huang, D. et al. Analysis of Forbush decreases observed using a muon telescope in Antarctica starting on 21 June 2015. Chin. Phys. C. 42 (2018), 125001.
[39] Grieder, P. K. F. Cosmic Rays at Earth: Researcher's reference, manual and data book. Elsevier Science, 2001.
[40] Gosse, J. C., Phillips, F. M. Terrestrial in situ cosmogenic nuclides: theory and application. Quat. Sci. Rev. 20 (2001), 1475–1560.
[41] Linsley, J. Mini and super mini arrays for the study of highest energy cosmic rays. 19th ICRC San Diego, United States. 3 (1985), 434–437.
[42] Hillas, A. M. Some recent developments in cosmic rays. Phys. Rep. 20 (1975), 59–136.
[43] Duperier, A. On the positive temperature effect of the upper atmosphere and the process of meson production. JASTP. 1 (1951), 296–310.

USC
UNIVERSIDADE DE SANTIAGO DE COMPOSTELA

[44] Blackett, P. M. S. On the Instability of the Barytron and the Temperature Effect of Cosmic Rays. Phys. Rev. 54 (1938), 973–974.
[45] Mendonça, R. R. S. et al. The Temperature Effect in Secondary Cosmic Rays (Muons) Observed at Ground: Analysis of the Global Muon Detector Network Data. Astrophys. J. 830 (2016), 88.
[46] Maeda, K., Wada, M. Atmospheric temperature effect upon cosmic ray intensity at sea level. Sci. Res. J. 48 (1954), 71–79.
[47] Dorman, L. Meteorological effects of cosmic rays. Nauka, 1972.
[48] Sagisaka, S. Atmospheric effects on cosmic-ray muon intensities at deep underground. Nuovo Cimento C, 9, (1986), 809–828.
[49] Dmitrieva, A. N., Kokoulin, R. P., Petrukhin, A. A., Timashkov, D. A. Corrections for temperature effect for ground-based muon hodoscopes. Astrop. Phys. 34 (2011), 401–411.
[50] Abrahão, T. et al. Cosmic-muon characterization and annual modulation measurement with Double Chooz detectors. Cosm. Astrop. Phys. J. 2017 (2017), 002–017.
[51] An, F. et al. Seasonal Variation of the Underground Cosmic Muon Flux Observed at Daya Bay. Cosm. Astrop. Phys. J. 2018 (2018), 001.
[52] Tilav, S. Atmospheric variations as observed by IceCube. arXiv:1001.0776v2 [astro-ph.HE] (2010).
[53] Adamson, P. et al. Observation of muon intensity variations by season with the MINOS far detector. Phys. Rev. D. 81 (2010), 12001.
[54] Agostini, M. et al. Modulations of the Cosmic Muon Signal in Ten Years of Borexino Data. Cosm. Astrop. Phys. J. 2019 (2019), 002–046.
[55] Sutton, E. C. Observational Astronomy: Techniques and Instrumentation. Cambridge University Press. 2011.
[56] Spiro, M., Aubourg, E., Palenque-Delabrouille. Review on experimental particle astrophysics. In: Surveys in High Energy Physics. Taylor and Francis Online. 15 (2000), 1–36.
[57] Sauli, F. Gaseous Radiation Detectors: Fundamentals and Applications. Cambridge University Press, 2014.
[58] Tanabashi, M. et al. Particle Data Group. Phys. Rev. D. 98 (2019), 030001.

USC
UNIDADE DE XESTIÓN DE COMPOSTELA

[59] Leroy, C., Rancoita, P. Principles of Radiation Interaction in Matter and Detection. 2nd ed. Prikladnaia Mekhanika, 2009.
[60] Rinard, P. Neutron interactions with matter. Passive nondestructive assay of nuclear materials. (1991), 375–377.
[61] William, L. Techniques for nuclear and particle physics experiments: a how-to approach. 2nd ed. Springer, 1994.
[62] Hilke, H. J., Riegler, W. Gaseous Detectors. In: Particle Physics Reference Library Volume 2: Detectors for Particles and Radiation. Springer, 2020.
[63] Abbrescia, M., Peskov, V., Fonte, P. Resistive Gaseous Detectors: Designs, Performance, and Perspectives. 1st ed. Wiley, 2018.
[64] Lippmann, C., Riegler, W. Detector physics of resistive plate chambers. IEEE Nucl. Sci. Symp. Conf. Rec. 1 (2002), 600–604.
[65] Townsend, J. S. The Theory of Ionisation of Gases by Collision. Nature. 85 (1911), 400–401.
[66] Davydov, Y. I. On the First Townsend Coefficient at High Electric Field. IEEE Trans. Nucl. Sci. 53 (2006), 2931–2935.
[67] Lippmann, C., Riegler, W. Space charge effects in Resistive Plate Chambers. Nucl. Instr. and Meth. A. 517 (2004), 54–76.
[68] Fonte, P., Peskov, V., Ramsey, B. D. Streamers in MSGC's and other gaseous detectors. ICFA Instrum. Bull. 15 (1997), 1.
[69] Santonico, R., Cardarelli, R. Development of resistive plate counters. Nucl. Instr. and Meth. 187 (1981), 377–380.
[70] Konecki, M. The RPC based trigger for the CMS experiment at the LHC. JINST. 9 (2014), C07002.
[71] ALICE Collaboration et al. Performance of the RPC-based ALICE muon trigger system at the LHC. JINST. 7 (2012), T12002.
[72] Belver, D. et al. The HADES inner TOF wall. Nucl. Instr. and Meth. A. 602 (2009), 687–690.
[73] Ying, J. et al. Study of an avalanche-mode resistive plate chamber. J. Phys. G: Nucl. Part. Phys. 26 (2000) 1291–1298.
[74] Riegler, W. Induced signals in resistive plate chambers. Nucl. Instr. and Meth. A. 491 (2002), 258–271.

USC
UNIVERSIDADE DE SANTIAGO DE COMPOSTELA

[75] Ramo, S. Currents Induced by Electron Motion. Proc. IRE. 27 (1939), 584–585.
[76] Riegler, W., Veenhof, R., Lippmann, C. Detector physics and simulation of resistive plate chambers. Nucl. Instr. and Meth. A. 500 (2002), 144–162.
[77] Belver, D. et al. TRASGO: A proposal for a timing RPCs based detector for analyzing cosmic ray air showers. Nucl. Instr. and Meth. A. 661 (2012), S163–S167.
[78] Garzón, J. A. TRASGOS: Towards a New Standard for the Regular Measurement of Cosmic Rays. Phys of Atom. Nuclei. 83 (2020), 453–462.
[79] García-Castro, D. et al. TRASGO Project. Present Status and Results. Phys. of Atom. Nucl. 84 (2021), 1070–1079.
[80] Blanco, A. et al. TRAGALDABAS: a new RPC based detector for the regular study of cosmic rays. JINST. 9 (2014), C09027.
[81] Garzón, J. A. et al. TRAGALDABAS. First results on cosmic ray studies and their relation with the solar activity, the Earth magnetic field and the atmospheric properties. arXiv:1701.07277v1 [astro-ph.HE] (2017).
[82] MeteoGalicia. www.meteogalicia.gal
[83] LIP Coimbra. www.coimbra.lip.pt
[84] Abreu, P. et al. MARTA: A high-energy cosmic-ray detector concept with high-accuracy muon measurement. Eur. Phys. J. C. 78 (2018), 333.
[85] Saraiva, J. et al. The TRISTAN detector - 2018–2019 Latitude Survey of Cosmic Rays. arXiv:2004.13615v4 [physics.ins-det] (2020)
[86] García-Castro, D. The TRISTAN detector. Cosmic ray survey between latitudes 38ºN and 53ºS along the Atlantic Ocean. PoS. 399 (2021).
[87] Ministerio de Ciencia e Innovación. Buques Oceanográficos. www.ciencia.gob.es/ca/Organismos-y-Centros/Comite-Polar-Espanol/Buques-Oceanograficos
[88] Hidronav Technologies. www.hidronav.com
[89] Blanco, J. J. et al. ORCA (Antarctic Cosmic Ray Observatory): 2018 latitudinal survey. PoS. 1059 (2019).
[90] Cuenca-García, J. J. Simulation and reconstruction algorithms for a commercial muon tomography system. PhD thesis, USC. 2018.

USC
UNIVERSIDADE DE SANTIAGO DE COMPOSTELA

[91] Belver, D. The Front-End Electronics of the HADES timing RPCs wall: design, development and performances analysis. PhD thesis, USC. 2009.
[92] Gil, A. Electronic developments for the HADES RPC Wall. PhD thesis, Universitat de València. 2010.
[93] Anghinol, F. et al. NINO: an ultra-fast and low-power front-end amplifier/discriminator ASIC designed for multigap resistive plate chamber. Nucl. Instr. and Meth. A. 533 (2004), 183–187.
[94] Christiansen, J. HPTDC. Digital Microelec. Group, CERN.
[95] Traxler, M. et al. A general purpose trigger and readout board for HADES and FAIR-experiments. GSI Sci. Rep. 2007–1, 2006.
[96] Traxler, M. et al. A compact system for high precision time measurements (< 14 ps RMS) and integrated data acquisition for a large number of channels. JINST. 6 (2011), C12004.
[97] Lopes, L. et al. Outdoor Field Experience with Autonomous RPC Based Stations. JINST. 11 (2016), C09011.
[98] Abbrescia, M. et al. Eco-friendly gas mixtures for Resistive Plate Chambers based on Tetrafluoropropene and Helium. JINST. 11 (2016), P08019.
[99] Lopes, L., Assis, P., Blanco, A., Fonte, P., Pimenta, M. Towards Sealed Resistive Plate Chambers. arXiv:2006.08291v1 [physics.ins-det] (2020).
[100] CESGA. www.cesga.es
[101] Adamczewski-Musch, J., Essel, H.G., Kurz, N., Linev, S. Dataflow engine in DAQ backbone DABC. IEEE Transactions on Nuclear Science. 57 (2010), 614–617.
[102] Adamczewski-Musch, H.G., Kurz, N., Linev, S. Developments and applications of DAQ framework DABC v2. J. Phys. Conf. Ser. 664 (2015), 082027.
[103] Nagios. www.nagios.org
[104] PNP4Nagios. docs.pnp4nagios.org
[105] Grafana. grafana.com
[106] ROOT. root.cern

USC
UNIVERSIDADE DE SANTIAGO DE COMPOSTELA

[107] Belver, D. et al. Performance of the Low-Jitter High-Gain/Bandwidth Front-End Electronics of the HADES tRPC Wall. Nucl. Sci. IEEE Transactions. 57 (2010), 2848–2856.
[108] Kornakov, G. New advances and developments on the RPC TOF Wall of the HADES experiment at GSI. PhD thesis, USC. 2012.
[109] Alvarez-Pol, H. et al. A large area timing RPC prototype for ion collisions in the HADES spectrometer. Nucl. Instr. and Meth. A. 533 (2004), 277–282.
[110] Janossy, L. Rate of n-fold Accidental Coincidences. Nature. 153 (1944), 165.
[111] Knoll, G. F. Radiation Detection and Measurement. JohnWiley and Sons, 2010.
[112] Jolliffe, I. T. Principal Component Analysis. Springer, 2002.
[113] Garzón, J. A., Cabanelas, P., González-Díaz, D., Kurtukian-Nieto. TimTrack: A new concept for the tracking of charged particles with timing detectors. Nucl. Instr. and Meth. A. 629 (2011), 311–322.
[114] Garzón, J. A., Cabanelas, P. TimTrack: A matrix formalism for a fast time and track reconstruction with timing detectors. Nucl. Instr. and Meth. A. 661 (2012), S210–S213.
[115] Nuntiyakul, W., et al. Latitude survey investigation of galactic cosmic ray solar modulation during 1994–2007. Astrophys. J. 795 (2014), 11.
[116] AEMET. opendata.aemet.es
[117] Hersbach, H., et al. ERA5 hourly data on pressure levels from 1979 to present. Copernicus Climate Change Service (C3S) Climate Data Store (CDS). 2018.
[118] Mendonça, R. R. S. et al. Analysis of cosmic rays' atmospheric effects and their relationships to cutoff rigidity and zenith angleusing Global Muon Detector Network Data. Geophys. Res. J. Space Phys. 124 (2019), 9791–9813.
[119] Rieckh, T., Scherllin-Pirscher, B., Ladstädter, F., Foelsche, U. Characteristics of tropopause parameters as observed with GPS radio occultation. Atm. Meas. Tech. 7 (214), 3947–3958.

USC
UNIDADE DE XUNTA DE COMPOSTELA

[120] Blanco, J. J., et al. Cosmic ray observations from Livingston Island. Adv. Space Res. 69 (2022), 3514–3524.
[121] Gerontidou, M., et al. World grid of cosmic ray vertical cut-off rigidity for the last decade. Adv. Space Res. 67 (2021), 2231–2240.
[122] UTM data center. data.utm.csic.es/set/sdg/20181116/, and data.utm.csic.es/set/sdg/20190227/
[123] Dorman, L. Coupling and barometer coefficients for measurements of cosmic ray variations at altitudes of 260–400 mb. 11th ICRC Budapest, Hungary. 2 (1970), 233–236.
[124] NOAA. swpc.noaa.gov/noaa-scales-explanation
[125] GFZ Helmholtz Centre Potsdam. gfz-potsdam.de/en/kp-index
[126] World Data Center for Geomagnetism, Kyoto. wdc.kugi.kyoto-u.ac.jp/wdc/Sec3.html
[127] L'Observatori de l' Ebre. obsebre.es
[128] Augusto, C. R. A., et al. Summer Solstice Storm: One of the major geomagnetic storms of solar cycle 24 observed at ground level. Sol. Phys. 293 (2018), 84.
[129] Fauth, A., Vieira de Souza, H. Observation of the Forbush decrease of 22 June 2015 with the LAGO detector in Brazil. PoS. 130 (2017).
[130] Cordaro, E. G., Venegas-Aravena, P., Laroze, D. Variations of geomagnetic cutoff rigidity in the southern hemisphere close to 70ºW (South-Atlantic Anomaly and Antarctic zones) in the period 1975–2010. Adv. Space Res. 63 (2019), 2290–2299.

USC
UNIVERSIDADE DE SANTIAGO DE COMPOSTELA

USC
UNIVERSIDADE
DE SANTIAGO
DE COMPOSTELA

USC
UNIVERSIDADE
DE SANTIAGO
DE COMPOSTELA

TRASGOs are a new generation of cosmic ray detectors to study the influence of the Earth's magnetic field and the atmosphere on the cosmic ray flux. This thesis presents the calibration, reconstruction, and analysis algorithms developed for two TRASGOs: TRISTAN and TRAGALDABAS. TRISTAN performed a series of unprecedented latitudinal surveys before being installed in Antarctica at the Spanish Antarctic Base JCI, and TRAGALDABAS is located in Santiago de Compostela. We have investigated the effects of the barometric pressure, atmospheric temperature, and cutoff rigidity on the cosmic ray data as well as the correlation with space weather events.